

DIRECT SEARCH FOR HIGGS BOSON IN LHCb AND CONTRIBUTION TO THE DEVELOPMENT OF THE VERTEX DETECTOR

THÈSE N° 3868 (2007)

PRÉSENTÉE LE 26 OCTOBRE 2007

À LA FACULTÉ DES SCIENCES DE BASE

Laboratoire de physique des hautes énergies 1

SECTION DE PHYSIQUE

ÉCOLE POLYTECHNIQUE FÉDÉRALE DE LAUSANNE

POUR L'OBTENTION DU GRADE DE DOCTEUR ÈS SCIENCES

PAR

Laurent LOCATELLI

physicien diplômé de l'Université de Lausanne
de nationalité suisse et originaire de Le Locle (NE)

acceptée sur proposition du jury:

Prof. R. Schaller, président du jury

Prof. A. Bay, directeur de thèse

Dr F. Courbin, rapporteur

Prof. C. Matteuzzi, rapporteur

Dr B. Pietrzyk, rapporteur



ÉCOLE POLYTECHNIQUE
FÉDÉRALE DE LAUSANNE

Lausanne, EPFL

2007

Abstract

The LHCb experiment (Large Hadron Collider beauty) is one of the four experiments under construction at the LHC (Large Hadron Collider) at CERN near Geneva. It is planned to start in 2007 and its goal is the study of b -quark physics. The LHC is a circular accelerator in which collide protons-protons at a center-of-mass energy of $\sqrt{s} = 14$ TeV. This generates a large number of high energy $b\bar{b}$ pairs which are predominantly produced in the same forward cone. The LHCb detector is therefore a forward single arm spectrometer designed to exploit the large $b\bar{b}$ production cross section ($\sigma_{b\bar{b}} \sim 500 \mu\text{b}$) and to perform precise measurements of CP violation in b -hadrons decays.

One of the actual greatest challenges in High Energy Physics is the discovery of the Higgs boson which is responsible for the Model Standard particles mass generation through the Spontaneous Symmetry Breaking process. The Higgs mass is not known and cannot be predicted by the theory. However the recent results of LEP at CERN have shown that $m_{H^0} > 114 \text{ GeV}/c^2$. Below $\sim 150 \text{ GeV}/c^2$ the Higgs decay into two b -quarks $H^0 \rightarrow b\bar{b}$ dominates. The two quarks emitted back-to-back in the H^0 rest frame form a string which fragments, giving rise to hadronization in jets containing b -hadrons.

The aim of this thesis is to assess the feasibility to discover a Higgs boson with intermediate mass at LHCb by using the detector sensibility to b -hadrons in order to reconstruct these jets using jets reconstruction algorithms. The study is focused on the mechanisms in which the Higgs boson is produced in association with a gauge boson decaying leptonically $H^0 + W^\pm \rightarrow b\bar{b} + \ell\nu_\ell$ and $H^0 + Z^0 \rightarrow b\bar{b} + \ell^+\ell^-$ for Higgs masses in the range 100 - 130 GeV/c^2 . The gauge bosons decay produces hard leptons quite often isolated from the b -jets. Hence an isolated lepton with high transverse momentum is required in order to reject the large QCD background. Several important background channels which also provide two b -quarks and an isolated lepton - like $t\bar{t} \rightarrow W^+b W^-\bar{b}$, $Z^0 + W^\pm \rightarrow b\bar{b} + \ell\nu_\ell$, $Z^0 + Z^0 \rightarrow b\bar{b} + \ell^+\ell^-$, $W^\pm + b$ -jets, $Z^0 + b$ -jets and generic $b\bar{b}$ - are studied in parallel. The idea is to find observables which behave differently for backgrounds and Higgs signal and to exploit these differences in the framework of a neural network, precisely in order to discriminate background from signal.

The LHCb experiment needs a high capability to identify b -hadrons despite their very short lifetime $\tau_B \sim 1.5 \cdot 10^{-12}$ s. The Vertex Locator (VeLo) is a sub-detector placed around the p - p interaction point which has to provide accurate measurements of the b -hadrons production and decay points by reconstructing secondary vertices.

The second part of this thesis is a technical contribution to the development of the VeLo analogue transmission line. It consists in testing several hardware and software methods to improve the VeLo analogue transmission between the on-detector part of the readout and the off-detector electronics. Because the ~ 60 m line introduces an important attenuation, several cables and line drivers configurations with frequency and gain compensation are studied in order to obtain the best results in terms of signal-to-noise ratio and channel crosstalk. The different contributions to the noise are also studied and an estimation of the contribution due to the Beetle pipeline non-uniformity is given in order to see if a specific correction is needed or if it can be suppressed by a standard common noise correction procedure.

Keywords:

CERN, LHCb, high energy physics, Standard Model, Higgs boson, jets reconstruction, neural network.

Résumé

L'expérience LHCb (Large Hadron Collider beauty) est une des quatre expériences en cours de construction au grand collisionneur de hadrons LHC au CERN près de Genève. Le début de son exploitation est prévue pour 2007 et son but est l'étude de la physique des quarks b . Le LHC est un accélérateur circulaire dans lequel collisionnent des protons à une énergie dans le centre de masse de $\sqrt{s} = 14$ TeV. Cela génère un grand nombre de paires $b\bar{b}$ de haute énergie produite dans un même cône. De ce fait, le détecteur LHCb est un spectromètre à bras unique conçu pour exploiter la grande section efficace de production de paires $b\bar{b}$ ($\sigma_{b\bar{b}} \sim 500 \mu\text{b}$) et pour réaliser des mesures précises de la violation CP dans les désintégrations des hadrons B .

Un des plus grands challenges actuels de la physique des hautes énergies est la découverte du boson de Higgs, responsable de la génération de la masse des particules dans le Modèle Standard via le processus de la brisure spontanée de symétrie. La masse du Higgs n'est pas connue et ne peut être prédite par la théorie. Néanmoins, les récents résultats obtenus par le LEP au CERN ont montré que $m_{H^0} > 114 \text{ GeV}/c^2$. En dessous de $\sim 150 \text{ GeV}/c^2$, la désintégration $H^0 \rightarrow b\bar{b}$ du Higgs en deux quarks b domine. Les deux quarks - émis dos à dos dans le référentiel du H^0 - forment alors une corde qui se fragmente pour hadroniser sous forme de jets contenant, entre autres, des hadrons B .

Le but de cette thèse est d'estimer la faisabilité de découvrir un boson de Higgs de masse intermédiaire à LHCb en tirant profit de la sensibilité du détecteur envers les hadrons B afin de reconstruire ces jets. L'étude se focalise sur les mécanismes dans lesquels le boson de Higgs est produit en association avec un boson de gauge se désintégrant leptoniquement $H^0 + W^\pm \rightarrow b\bar{b} + \ell \nu_\ell$ et $H^0 + Z^0 \rightarrow b\bar{b} + \ell^+ \ell^-$, pour des masses du Higgs de l'ordre de 100 - 130 GeV/c^2 . La désintégration des bosons de gauge produit des leptons souvent isolés par rapport aux jets. De ce fait, la présence d'un lepton isolé avec une grande quantité de mouvement transverse est requise afin de rejeter l'énorme bruit de fond QCD. Plusieurs importants canaux de bruit de fond fournissant également deux quarks b et un lepton isolé - comme $t\bar{t} \rightarrow W^+ b W^- \bar{b}$, $Z^0 + W^\pm \rightarrow b\bar{b} + \ell \nu_\ell$, $Z^0 + Z^0 \rightarrow b\bar{b} + \ell^+ \ell^-$, $W^\pm + b\text{-jets}$, $Z^0 + b\text{-jets}$ ainsi que le bruit de fond générique $b\bar{b}$ - sont étudiés en parallèle. L'idée est de trouver des

observables qui se comportent différemment pour le bruit de fond et le signal Higgs, et d'exploiter ces différences dans le cadre d'un réseau de neurones, précisément afin de discriminer le bruit de fond du signal.

L'expérience LHCb nécessite une grande capacité à identifier les hadrons B malgré leur très courte durée de vie $\tau_B \sim 1.5 \cdot 10^{-12}$ s. Le détecteur de vertex VeLo est un sous-détecteur placé autour du point d'interaction p - p conçu pour fournir des mesures précises des lieux de production et de désintégration des hadrons B en reconstruisant les vertex secondaires.

La seconde partie de cette thèse est une contribution technique au développement de la ligne de transmission analogique du VeLo. Plusieurs méthodes hardware et software sont testées afin d'améliorer la transmission analogique du VeLo entre la partie de lecture sur le détecteur et l'électronique hors détecteur. La ligne d'environ 60 m induit une importante atténuation du signal. Plusieurs configurations de câbles et de line drivers avec compensation de gain et de fréquence sont étudiées afin d'obtenir les meilleurs résultats en termes de signal sur bruit et de propagation du signal entre canaux. Les différentes contributions au bruit sont également étudiées. En particulier, une estimation de la contribution due à la non-uniformité du pipeline du Beetle est donnée afin d'établir si une correction spécifique est nécessaire ou si une procédure standard de suppression du bruit commun est suffisante.

Mots-clés:

CERN, LHCb, physique des hautes énergies, Modèle Standard, boson de Higgs, reconstruction de jets, réseau de neurones.

Remerciements

D'une manière générale, je voudrais remercier le Laboratoire de Physique des Hautes Energie de l'Ecole Polytechnique Fédérale de Lausanne pour m'avoir permis de réaliser cette thèse de doctorat dans d'excellentes conditions. En particulier, je tiens à exprimer ma gratitude à son directeur, le Professeur Aurelio Bay, qui, malgré ses importantes tâches administratives, a toujours su trouver le temps pour m'aiguiller dans mon travail de recherche.

Je remercie également mes collègues de bureau Federica Legger et Guido Haefeli pour leur support et leur aide durant mon travail sur le VeLo et le TELL1. Un grand merci à Benjamin Carron, Jérémie Borel, Pawel Jalocha ainsi que le groupe de recherche sur le VeLo au CERN pour leur collaboration sur ce projet. Par la même occasion, je remercie les électroniciens Raymond Frei et Guy Masson pour leur disponibilité et leurs explications dans ce domaine qui n'est malheureusement pas ma spécialité.

Un immense merci à Charles Currat dont la thèse de doctorat m'a été fort utile durant mon travail sur le boson de Higgs. Dans un même temps, je remercie mes collaborateurs du groupe de recherche sur les jets au CERN: Frederic Teubert et José Angel Hernando Morata du CERN, Bolek Pietrzyk et Victor Coco du Laboratoire d'Annecy-le-Vieux de Physique des Particules, Clara Mateuzzi et Nelli Pukhaeva de l'Université de Milan ainsi qu'Ivan Belyaev de l'Université de Syracuse (USA).

Un grand merci également à Japhet Bagilishya, responsable informatique du BSP, ainsi qu'à ses successifs "délégués" du LPHE Hubert Degaudenzi, Olivier Dormond et Christian Jacoby pour leur disponibilité et leur aide précieuse à résoudre les nombreuses difficultés informatiques qui ont jalonné ces cinq années de travail.

Je remercie encore tous les membres du LPHE pour la bonne ambiance qui règne à l'institut, les adorables secrétaires Erika Luthi et Esther Hofmann pour leur dévouement et leur bonne humeur communicative, avec une pensée particulière pour Monique Romaniszin. Merci aussi à Maurice Gailloud pour sa collaboration durant mon travail d'assistanat.

Je tiens à remercier également l'ensemble de l'équipe de football du LPHE, Luc Hinz, Martin Rey, Dario Zurcher, Luis Fernandez, Andrea Scarabosio et Luc Simon avec qui nous avons participé à deux championnats de l'EPFL et qui m'ont ainsi

permis d'exercer un minimum d'activités sportives et de décompresser entre midi et deux heures dans mon sport favori.

Je remercie finalement mes parents, mon frère et le reste de ma famille en Suisse et en Italie, ainsi que mes nombreux amis et amies parmi lesquels mes successifs colocataires Nicolas, Thomas, Paolo, Antonio, Alexandra et Magdalena.

Lausanne, le 13 août 2007

Contents

1	Theoretical Overview	1
1.1	Overview of the Standard Model	1
1.1.1	Elementary particles	2
1.1.2	Fundamental interactions	8
1.2	CP violation	12
1.3	Higgs Physics	14
1.3.1	The Goldstone model: A simple example of Spontaneous Symmetry Breaking	15
1.3.2	The Higgs Mechanism	18
1.3.3	The Higgs Mechanism in the Standard Model	20
1.3.4	Higgs production	25
1.3.5	Higgs decays	27
2	The LHCb Experiment at CERN	31
2.1	The Large Hadron Collider	32
2.2	The LHCb experiment	36
2.2.1	Vertex Locator	37
2.2.2	Magnet	40
2.2.3	RICH detectors	40
2.2.4	Tracking system	41
2.2.5	Calorimeters	42
2.2.6	Muon detector	42
2.2.7	Front-end electronics and data acquisition system	43
2.2.8	LHCb trigger system	44
3	Higgs boson search in LHCb	49
3.1	Introduction	49
3.2	Generation of Higgs and background events with PYTHIA	51
3.3	LHCb fast simulation	57
3.4	Events selection procedure	59
3.4.1	Preselection	59

3.4.2	Associated boson tagging from isolated lepton	59
3.4.3	Selection cuts	62
3.5	Jet reconstruction algorithms	67
3.5.1	Cone algorithm	67
3.5.2	K_T or “Durham” algorithm	68
3.5.3	Cone and K_T algorithms comparison	71
3.6	Jet energy correction	74
3.7	Investigations for discriminant variables	77
3.7.1	$Z^0 \rightarrow b\bar{b}$ decay products pseudorapidity asymmetry	78
3.7.2	Primary boson reconstruction	83
3.8	Background discrimination using neural networks	86
3.8.1	Multi-Layer Perceptron	87
3.8.2	MLP input parameters	88
3.8.3	Performances for $t\bar{t}$ and irreducible backgrounds suppression with multiple MLPs	91
3.9	Conclusion	108
4	Tests on the VeLo analogue transmission line with the TELL1 prototype RB3	111
4.1	Introduction	111
4.2	Experimental setup	112
4.2.1	Front-End Electronics setup	112
4.2.2	Off-Detector Electronics setup	115
4.2.3	Performances of the RB3 system	117
4.3	Studies of the 60 m transmission line	118
4.3.1	Cable choice and performances	118
4.3.2	Gain and Frequency compensation	122
4.3.3	Performance measurements with the optimal configuration	126
4.4	Noise study	136
4.4.1	Pipeline non-uniformity	136
4.4.2	Contributions to noise	140
4.4.3	Contribution to noise in channels near the header	144
4.5	Conclusion	151
	List of Figures	152
	List of Tables	158
	Bibliography	161

Chapter 1

Theoretical Overview

1.1 Overview of the Standard Model

Already during the Antiquity, people were interested in describing the nature and the matter with fundamental constituents. In the ancient Greece, although not yet observed, the concept of atom, from “atomos” which means indivisible, was introduced to define the smallest elements constituting matter. During the XVIIth and XVIIIth centuries, more elaborated studies were performed to extract their chemical properties. Similarities were found between groups of elements leading to the actual classification proposed by Mendeleev in 1869: *the Periodic Table of Elements*. In 1911, the famous experiment of Rutherford showed that atoms were not the elementary constituents of matter but that they had an internal structure made of a cloud of electrons surrounding a hard nucleus. The electrons carry a negative electric charge while the nucleus has an opposite positive charge giving an overall neutral charge for the atoms in their fundamental state as classified in the periodic table. In 1919, Rutherford discovered that neither the nucleus is an elementary particle. It is actually composed of protons - which carry the positive electric charge - and neutrons. Protons and neutrons are also called *nucleons*. In the sixties, Gell-Mann exhibited an internal structure for the nucleons. The introduction of the concept of *quark* as fundamental particle rewarded him of the Nobel Prize in Physics in 1969. Nowadays, electrons and quarks are still considered as the tiniest particles which compose the matter that surrounds us.

The Standard Model is a theoretical model, mathematically based on the Group theory, that describes the properties of elementary particles - and those of the particles they compose - and the interactions between them. It was elaborated during the XXth century and has not changed much since 1974. The theory is consistent as a lot of Standard Model predictions were experimentally confirmed such as the existence of composite particles.

1.1.1 Elementary particles

In the framework of the Standard Model, the elementary constituents of matter are divided into two categories: the leptons and the quarks. Similitudes exist in the architecture of these categories as they are grouped in three families of two particles each as shown in table 1.1:

		Q [e]	m [MeV/c^2]	L	B
Leptons	e^-	-1	0.511	+1	0
	ν_e	0	$< 3 \cdot 10^{-6}$	+1	0
	μ^-	-1	105.6	+1	0
	ν_μ	0	< 0.19	+1	0
	τ^-	-1	1777	+1	0
	ν_τ	0	< 18.2	+1	0
Quarks	u	$+\frac{2}{3}$	1.5 - 4.0	0	$+\frac{1}{3}$
	d	$-\frac{1}{3}$	4.0 - 8.0	0	$+\frac{1}{3}$
	c	$+\frac{2}{3}$	1150 - 1350	0	$+\frac{1}{3}$
	s	$-\frac{1}{3}$	80 - 130	0	$+\frac{1}{3}$
	t	$+\frac{2}{3}$	4100 - 4400	0	$+\frac{1}{3}$
	b	$-\frac{1}{3}$	$175 \cdot 10^3$	0	$+\frac{1}{3}$

Table 1.1: The Standard Model fundamental particles. The classification contains the three families of leptons and quarks with the electric charge Q , the mass m , the leptonic and baryonic numbers L and B [1].

Lepton comes from the Greek word “leptos” meaning light and, by the fact, designs low masses particles. The electron is the lightest one and, following the law of nature in which the physical systems always seek for the lowest energy states, is the most current. Muons are quite abundant too as they are produced in interactions of high energy cosmic rays with the Earth’s atmosphere. e^- , μ^- and τ^- carry a negative elementary charge $-e$ ($e = 1.602 \cdot 10^{-19}$ C). Their respective companions, the neutrini ν_e , ν_μ and ν_τ are neutral and almost massless¹. Every leptons are characterized by a leptonic number equal to +1 and are fermions of spin 1/2.

¹Neutrini are assumed to be massless in the Standard Model and in the rest of this document. However, the neutrino flavour oscillation was experimentally observed in 1998 by the Super-Kamiokande experiment in Japan. This phenomenon requires neutrini to have non-zero masses (see table 1.1).

The second category of elementary particles is the quarks². The first family, composed by the “up” u and “down” d quarks, is the lightest and therefore the most abundant in nature. Associated by three, they are actually the elementary components of the proton uud and the neutron udd . The second and third families contain heavier quarks, respectively the “charm” c and “strange” s and the “top” t and “bottom” or “beauty” b . Contrary to the leptons, quarks do not carry an entire electric charge: upper quarks u , c and t have a fraction $+2/3$ of the elementary charge e while down quarks d , s and b have $-1/3$. Masses are very difficult to measure because quarks cannot be observed alone. This is due to the nature of the strong interaction, the force that bounds quarks together, as it will be explained later. An evaluation is nevertheless possible by measuring the mass of particles containing quarks and by taking into account the contributions from the composition in quarks and from the interaction itself. Quarks are also fermions of spin $1/2$ and they are characterized by a baryonic number equal to $+1/3$.

The first model proposed by Gell-Mann in 1964 is based on the three lightest quarks u , d and s only. It is mathematically represented by $SU(3)$. The three quarks are arranged bidimensionally following their isospin I_3 and their hypercharge $Y = 2(Q - I_3) = B + S$ in a triplet $\mathbf{3}$ as shown on the left of figure 1.1. The isospin is a physical quantity introduced by W. Heisenberg to explain the fact that proton-proton, proton-neutron and neutron-neutron strong interactions inside the nucleus are quite the same. The idea is to represent the nucleons as two different states of the same particle. This can be directly translated into a spin-like formalism in which the quarks u and d have an isospin $I = 1/2$ with projections $I_3 = +1/2$ and $-1/2$

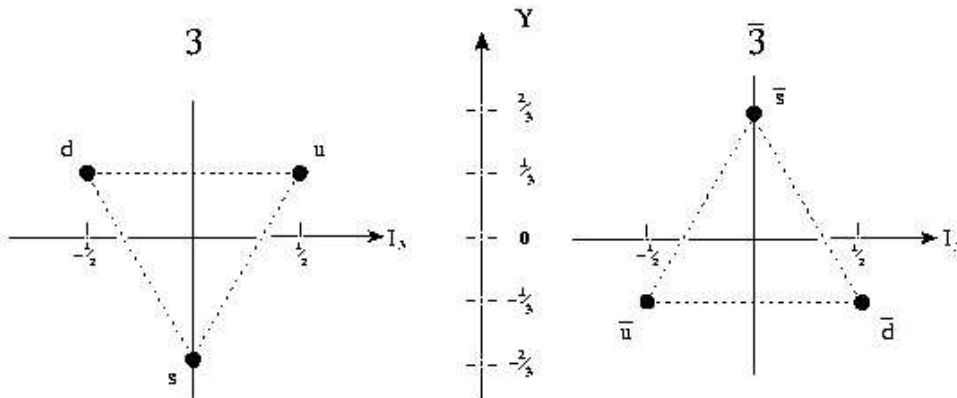


Figure 1.1: $SU(3)$ representations of the quarks and antiquarks triplets $\mathbf{3}$ and $\bar{\mathbf{3}}$.

²The word “quark” was imagined by the novelist James Joyce and adopted by Gell-Mann.

respectively. The other flavours have a null isospin. The hypercharge Y is defined as the sum of the baryonic number B and the strangeness S , a quantum number associated to the quark s uniquely ($S = -1$ for s and 0 for the other flavours).

As previously said, quarks cannot stand alone in the nature. They are associated to other quarks to form compound particles called *hadrons*, from the Greek “hadros” meaning robust or strong. Hadrons are themselves divided into two categories: the *baryons* and the *mesons*.

Baryons - from the Greek word “barys” meaning heavy - are systems of three quarks $q_1q_2q_3$, the lightest of them being the proton and the neutron. Their total baryonic number is $3 \cdot (+1/3) = +1$. Baryons are fermions of spin $1/2$ or $3/2$ obtained by the composition of three spins $1/2$. A multitude of particles can be created by association of three quarks among the six at disposition. Following the Gell-Mann classification $\mathbf{3}$, $3^3 = 27$ combinations are possible. Each of them corresponds to a different particle, which can be arranged following I_3 and Y in a decuplet $\mathbf{10}$, two octets $\mathbf{8}$, $\mathbf{8}'$ and a singlet $\mathbf{1}$ ($\mathbf{3} \otimes \mathbf{3} \otimes \mathbf{3} = \mathbf{10} \oplus \mathbf{8} \oplus \mathbf{8}' \oplus \mathbf{1}$). The baryons decuplet $\mathbf{10}$ and octet $\mathbf{8}$ are pictured in figure 1.2:

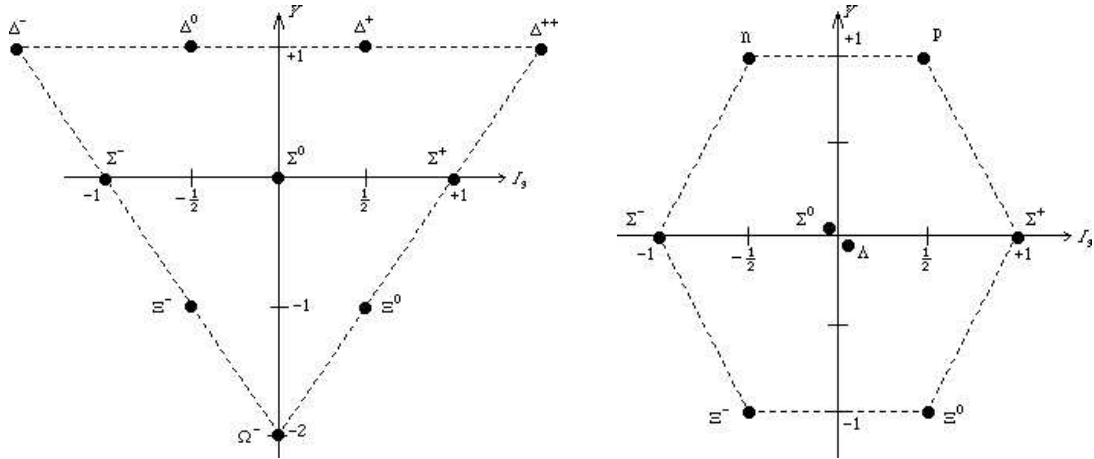
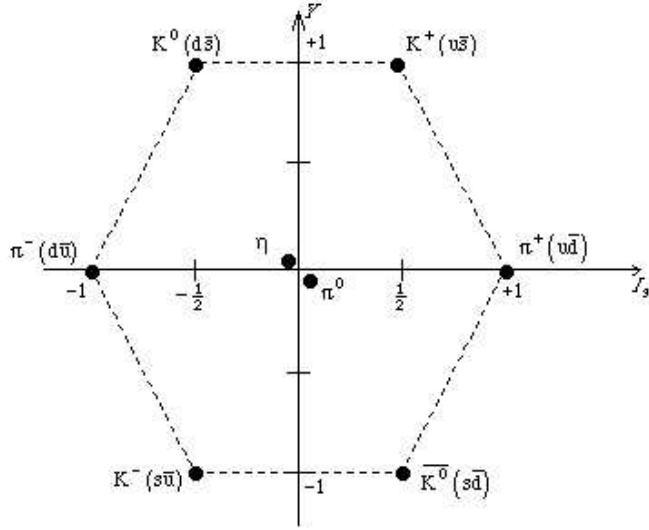


Figure 1.2: Baryons decuplet $\mathbf{10}$ (left) and octet $\mathbf{8}$ (right).

Mesons are bound systems composed of a quark and an antiquark $q_1\bar{q}_2$. They are heavier than leptons and, in principle, lighter than baryons. As a consequence, the origin of the denomination comes from the Greek word “mesos” meaning medium. Their total baryonic number is $(-1/3) + 1/3 = 0$. Contrary to baryons, mesons are bosons of spin 0 or 1 following the composition of two spins $1/2$. In the quark model, the quark triplet $\mathbf{3}$ is associated to the antiquark triplet $\bar{\mathbf{3}}$ (see figure 1.1). The $3^2 = 9$ possible combinations are classified in an octet $\mathbf{8}$ and a singlet $\mathbf{1}$ ($\mathbf{3} \otimes \bar{\mathbf{3}} = \mathbf{8} \oplus \mathbf{1}$) shown in figure 1.3:

Figure 1.3: Mesons octet $\mathbf{8}$.

Until here, only the elementary components of matter have been mentioned. In addition to that, the concept of *antimatter* has to be introduced. Inspired from the Schrödinger equation, P. A. M. Dirac established in 1928 a Lorentz covariant wave equation to describe the time-evolution of elementary particles of spin $1/2$:

$$\boxed{(\gamma^\mu p_\mu - mc) \psi = 0 \quad \mu = 0, 1, 2, 3} \quad \text{Dirac equation} \quad (1.1)$$

where γ^μ are 4×4 matrices and p_μ and m are respectively the energy-momentum four-vector and the mass associated to the wave function ψ . Without going into details, the solution has the form of a double spinor:

$$\psi = \begin{pmatrix} \psi_+ \\ \psi_- \end{pmatrix} \quad \text{with} \quad \psi_+ = \begin{pmatrix} u_1 \\ u_2 \end{pmatrix} \quad \text{and} \quad \psi_- = \begin{pmatrix} u_3 \\ u_4 \end{pmatrix} \quad (1.2)$$

where u_1 and u_2 are solutions with positive energy $+|E|$ while u_3 and u_4 give negative energy $-|E|$. By inverting simultaneously the signs of the energy and the momentum for u_3 and u_4 in (1.1), they can be reinterpreted as particles with positive energy traveling backward in the time:

$$\begin{pmatrix} v_1(E, \vec{p}) \\ v_2(E, \vec{p}) \end{pmatrix} = \begin{pmatrix} u_4(-E, -\vec{p}) \\ u_3(-E, -\vec{p}) \end{pmatrix} \quad (1.3)$$

Physically, as uniquely fermions are considered here, states with negative energy exist but, following the Pauli exclusion principle, are uniformly occupied. A supply

of energy $\Delta E \geq 2 \cdot mc^2$ to the vacuum can excite one of these pseudoparticles so that it becomes a real particle with mass m , electric charge q , energy $+|E|$ and momentum \vec{p} . In the same time remains a hole with same mass m but with opposite characteristics $-q$, $-|E|$ and $-\vec{p}$ as shown in figure 1.4. The hole is called an *antiparticle*. The existence of the antielectron or positron e^+ was predicted by the theory of Dirac and was effectively observed by C. Anderson in 1932. As this theory applies to fermions, it is valid for both leptons and quarks. The corresponding antileptons and antiquarks are exposed in table 1.2.

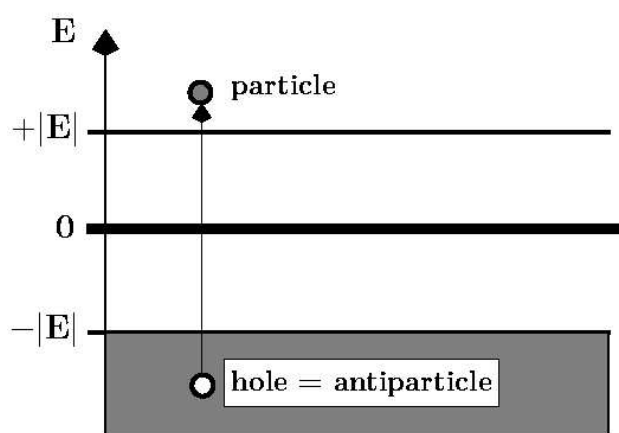


Figure 1.4: Particle-antiparticle pair creation.

In the quark model of Gell-Mann, the three antiquarks \bar{u} , \bar{d} and \bar{s} are arranged in the triplet $\bar{\mathbf{3}}$ shown on the right of figure 1.1. Except for the mass and the spin, most of the antiparticle features - in particular the electric charge Q , the leptonic and baryonic numbers L and B , the isospin I_3 , the strangeness S and the hypercharge Y - are the opposite of the particle ones. Exactly like for matter, antiquarks can combine to form antihadrons. The antibaryons $\bar{q}_1\bar{q}_2\bar{q}_3$ are classified in a decuplet $\bar{\mathbf{10}}$, two octets $\bar{\mathbf{8}}$, $\bar{\mathbf{8}}'$ and a singlet $\bar{\mathbf{1}}$ ($\bar{\mathbf{3}} \otimes \bar{\mathbf{3}} \otimes \bar{\mathbf{3}} = \bar{\mathbf{10}} \oplus \bar{\mathbf{8}} \oplus \bar{\mathbf{8}}' \oplus \bar{\mathbf{1}}$). The antimesons \bar{q}_1q_2 are arranged in an octet $\bar{\mathbf{8}}$ and a singlet $\bar{\mathbf{1}}$ ($\bar{\mathbf{3}} \otimes \mathbf{3} = \bar{\mathbf{8}} \oplus \bar{\mathbf{1}}$).

The theory of Big-Bang describes the formation of the Universe. At the very beginning, the energy density was very high. Following the idea of Dirac, a huge number of particle-antiparticle pairs was created at this epoch. In the same time that Universe expands and cools, the pairs annihilate liberating energy in the form of photons. At the end, the equal quantities of matter and antimatter should have totally annihilated so that the Universe should be empty of matter and filled by radiation. Instead of that, the Universe is not empty of matter. Some theories

		Q [e]	m [MeV/ c^2]	L	B
Antileptons	e^+	+1	0.511	-1	0
	$\bar{\nu}_e$	0	$< 3 \cdot 10^{-6}$	-1	0
	μ^+	+1	105.6	-1	0
	$\bar{\nu}_\mu$	0	< 0.19	-1	0
	τ^+	+1	1777	-1	0
	$\bar{\nu}_\tau$	0	< 18.2	-1	0
Antiquarks	\bar{u}	$-\frac{2}{3}$	1.5 - 4.0	0	$-\frac{1}{3}$
	\bar{d}	$+\frac{1}{3}$	4.0 - 8.0	0	$-\frac{1}{3}$
	\bar{c}	$-\frac{2}{3}$	1150 - 1350	0	$-\frac{1}{3}$
	\bar{s}	$+\frac{1}{3}$	80 - 130	0	$-\frac{1}{3}$
	\bar{t}	$-\frac{2}{3}$	4100 - 4400	0	$-\frac{1}{3}$
	\bar{b}	$+\frac{1}{3}$	$175 \cdot 10^3$	0	$-\frac{1}{3}$

Table 1.2: The Standard Model fundamental antiparticles [1].

explain this observation by introducing bubbles of antimatter traveling in the Universe. Such high concentrations of antimatter should therefore annihilate with the matter surrounding the bubble creating very important sources of light. This was however never observed experimentally which discredits such theories. Actually, it is estimated that, $\sim 10^{-9}$ s after the Big-Bang, for every 10^9 particle-antiparticle pairs created, there was one extra particle. This excess is at the origin of what constitutes the actual material Universe. Understanding the physical processes that led to this asymmetry should precisely explain why the Universe is not empty and composed of matter instead of antimatter. CP violation is one of the ingredient in the understanding of the asymmetry (see section 1.2). Nevertheless, as it is known in the Standard Model, it provides an excess of matter in a much lower proportion than it is really observed. In reality, it could be responsible for the formation of one galaxy at the very most. The explanation has to be found elsewhere or beyond the Standard Model.

The phenomenon of matter excess production is called *baryogenesis*. The necessary conditions for its achievement were first established by A. Sakharov³ in 1967:

³Andreï Sakharov (1921 - 1989) was a Russian nuclear physicist who had to work for the USSR nuclear weapon project at the beginning of the Cold War. He participated to the hydrogen bomb development before turning to activism at the end of the 1950s. He militated in favour of the Human Rights and against nuclear proliferation. He obtained the Nobel Peace Prize in 1975.

- The laws of nature must be biased in such a way that matter and not anti-matter is in excess.
- There must exist processes that do not conserve the leptonic and baryonic numbers.
- These processes must happen out of thermal equilibrium.

The next generation of high-energy experiments will try to answer to these mysteries. In particular, the LHCb experiment at CERN will study CP violation in the B -mesons system.

1.1.2 Fundamental interactions

The description of the Standard Model has to be completed with the interactions between its fundamental particles. Nature counts four fundamental forces: the gravitational, the electromagnetic, the weak and the strong forces.

The gravity is responsible for the attraction of two massive bodies. It was first described by I. Newton in 1687 and then by A. Einstein in its theory of General Relativity. The interaction is mediated by the graviton, a boson of spin 2 introduced in the theory but which has not been observed yet. The graviton is massless, inducing an infinite bearing to the gravitational interaction. The gravitational potential between two bodies of masses m_1 and m_2 separated by a distance r is expressed as:

$$\mathcal{V}_{\text{grav.}}(r) = -G \frac{m_1 \cdot m_2}{r} \quad (1.4)$$

where $G = 6.67 \cdot 10^{-11} \text{ m}^3 \text{ kg}^{-1} \text{ s}^{-2} = 1.32 \cdot 10^{-42} \text{ MeV}^{-1} \text{ fm}$ is the Newton gravitational constant. The adimensional coupling between two protons is about $G m_p^2 / \hbar c \simeq 10^{-38}$. The gravity intensity is the weakest among the four fundamental forces. However, at the human scale or at the scale of the Universe, objects are massive enough so that their motion are totally ruled by the gravity.

The electromagnetic force is responsible for the attraction or the repulsion between charged particles. The theory of electromagnetism - which describes electricity and magnetism together - was formulated in 1864 by J. Maxwell. The vector of the interaction is the massless photon γ implying that the bearing is also infinite. The photon is a boson of spin 1 which energy is characterized by the photon wavelength λ or frequency ν through⁴ $E = h\nu = hc/\lambda$. The electromagnetic potential between two

⁴ $c = 3 \cdot 10^8 \text{ m s}^{-1}$ is the speed of light and $h = 4.136 \cdot 10^{-21} \text{ MeV s}$ is the Planck constant.

particles of charges $Q_1 = q_1 \cdot e$ and $Q_2 = q_2 \cdot e$ separated by a distance r can be written as (with $\hbar = c = 1$):

$$\mathcal{V}_{\text{em}}(r) = -\frac{1}{4\pi\epsilon_0} \frac{Q_1 \cdot Q_2}{r} = -\frac{e^2}{4\pi\epsilon_0} \frac{q_1 \cdot q_2}{r} = -\alpha_{em} \frac{q_1 \cdot q_2}{r} \quad (1.5)$$

where $\alpha_{em} = e^2/4\pi\epsilon_0\hbar c \simeq 1/137$ is the electromagnetic coupling constant and $\epsilon_0 = 8.854 \cdot 10^{-12} \text{ A s V}^{-1} \text{ m}^{-1}$ is the vacuum permittivity. There is a noticeable analogy between (1.4) and (1.5). The mass in gravity plays the role of the electric charge in electromagnetism and they are both combined with a specific constant which represents the strength of the interaction. The photoelectric effect, the Bremsstrahlung and the Compton effect are some examples of the electromagnetic interaction manifestation.

The weak interaction apply to all quarks and leptons including neutrini. The weak mediators are the three massive gauge bosons W^\pm and Z^0 . Their high mass (see table 1.3) implies that the weak force is mainly active at small distance of the order of 10^{-3} fm . The existence of W^\pm and Z^0 is predicted by the Standard Model and their discovery at CERN in 1983 is one of the major success in favour of the theory. As indicated in its name, the strength of the weak interaction is weaker than the strong and electromagnetic force but still higher than the gravity. It is featured by the Fermi coupling constant $G_F/(\hbar c)^3 \simeq 1.166 \cdot 10^{-5} \text{ GeV}^{-2}$. The weak interaction is responsible for the spontaneous decays of heavy quarks and leptons such as:

$$\begin{aligned} t &\rightarrow b \quad W^+ &\rightarrow b \quad e^+ \nu_e \\ \mu^- &\rightarrow W^- \nu_\mu &\rightarrow e^- \bar{\nu}_e \nu_\mu \end{aligned} \quad (1.6)$$

In these examples, a quark or a lepton decays into another quark or lepton respectively, plus a W boson which in turn decays semileptonically into an electron and its associated neutrino. The neutrini have a very low interaction probability which renders them quite undetectable. The fact that they can carry a non negligible energy induces a loss of energy in the event reconstruction. The concept of neutrino was introduced in the model by W. Pauli in 1930 precisely to explain the observed lack of energy in the nuclear β -decays (β refers to electron e^\pm)⁵:

$$\begin{aligned} p &\rightarrow n \quad e^+ \nu_e \\ n &\rightarrow p \quad e^- \bar{\nu}_e \end{aligned} \quad (1.7)$$

The neutrini are uniquely sensitive to the weak force. Their presence provides therefore a clear signature of the weak interaction manifestation.

⁵The experimental discovery of the neutrino by C. Cowan *et al.* in 1956 was rewarded with the 1995 Nobel Prize in Physics.

The strong force acts exclusively on quarks and antiquarks and on the strong mediators, the *gluons*. Gluons are massless spin 1 bosons that can also interact with themselves. Although the gluon is massless, its bearing R is limited to ~ 1 fm, rendering the strong interaction very difficult to observe. It is an attractive force responsible for the quarks confinement inside hadrons. For example, a proton is made of the three quarks uud . The electromagnetic force is attractive between u and d because of the opposite charges of the two quarks, but repulsive between u and u . By considering only the electromagnetic interaction, the proton should therefore explode. However, the repulsive electromagnetic force is largely compensated by the attractive strong force which binds the quarks together. The strong interaction potential between two quarks separated by a distance r is, in the Yukawa form (with $\hbar = c = 1$):

$$\mathcal{V}_{\text{strong}}(r) = -\frac{g_s^2}{4\pi} \cdot \frac{e^{-\frac{r}{R}}}{r} = -\alpha_s \cdot \frac{e^{-\frac{r}{R}}}{r} \quad (1.8)$$

where $\alpha_s = g_s^2/4\pi\hbar c \simeq 0.119$ is the strong coupling constant which characterizes the strength of the interaction. In the Standard Model, the strong interaction is fully described by the Quantum Chromodynamics (QCD), a typical non-abelian gauge theory based on the local gauge symmetry group $SU(3)_c$. In this model, the concept of *colour* is introduced to represent the charge of the interaction, as proposed by O. Greenberg in 1964. In addition to its electric charge, a quark is assigned a colour which can be red r , green g or blue b . At the same time, an antiquark has an anticolour \bar{r} , \bar{g} or \bar{b} . The generators of $SU(3)_c$ are the eight Gell-Mann matrices λ_i with $i = 1, 8$. Hadrons are colour-neutral or white particles. For the baryons $q_1 q_2 q_3$, this is achieved by composing three quarks of three different colours. For the mesons $q_1 \bar{q}_2$, the quark carries a colour and the antiquark its corresponding anticolour. The gluons are doubly coloured: they carry a colour and an anticolour components ($\mathbf{3}_c \otimes \bar{\mathbf{3}}_c = \mathbf{8}_c \oplus \mathbf{1}_c$). Only the eight gluons of the octet $\mathbf{8}_c$ contribute actively to the strong interaction. As coloured particles, gluons also interact with themselves. These self-interactions are considered as second or higher order effects and are mathematically treated within the perturbation theory.

The main features of the four Standard Model fundamental interactions are summarized in table 1.3. They are classified by decreasing order of their intensity from top to down. The interaction mediators are cited together with their mass, spin and bearing.

High energy physicists are inclined to build theories in the most symmetrical way as possible in order to render them aesthetic. In this sense, the Standard Model gauge group, which is the direct product of three groups, is not elegant. Therefore, in addition to the four independent theories describing each of the four fundamental forces, more elaborated models tend to merge interactions together.

interaction	intensity	mediator	m [GeV]	spin	bearing [m]
strong	1	g	0	1	$\leq 10^{-15}$
electromagnetic	10^{-2}	γ	0	1	∞
weak	10^{-5}	W^\pm	80.4	1	10^{-18}
		Z^0	91.2		
gravitational	10^{-38}	graviton	0	2	∞

Table 1.3: The four fundamental interactions in the Standard Model classified by decreasing intensity from top to down, together with the mass, spin and bearing of their mediators.

The Electroweak theory is the unified description of the electromagnetic and the weak interactions. The model established by S. Glashow, A. Salam and S. Weinberg (GWS) was rewarded by the Nobel Prize in Physics in 1979. It postulates an energy threshold above which the two forces are merged into a single electroweak force. The threshold is called the *electroweak unification energy* and is of the order of ~ 1 TeV. Mathematically, the unification is accomplished under a $SU(2)_L \otimes U(1)_Y$ gauge group. The corresponding gauge bosons are the photon of electromagnetism and the W^\pm and Z^0 bosons of the weak force. As it will be explained in section 1.3.3, they acquire mass from the Higgs mechanism through the spontaneous symmetry breaking of the electroweak symmetry from $SU(2)_L \otimes U(1)_Y$ to $U(1)_{\text{em}}$, where $SU(2)_L$ refers to weak isospin with the generators I_W^i ($i = 1, 2, 3$) and $U(1)_Y$ to weak hypercharge with the generator Y_W . The symmetry group $U(1)_{\text{em}}$ remains unbroken, and the massless photon does not interact with the Higgs boson. The generator of $U(1)_{\text{em}}$ satisfies the Gell-Mann - Nishijima relation $Q = \frac{1}{2}Y_W + I_W^3$. Two experimental successes confirmed the GWS electroweak model. The first is the discovery of neutral currents in neutrino scattering by the Gargamelle collaboration in 1973. The second is the discovery of the W^\pm and Z^0 gauge bosons in $p\text{-}\bar{p}$ collisions at CERN in 1983.

Grand Unification or Grand Unified Theory (GUT) aims to merge electroweak and quantum chromodynamics into a unique QCD-electroweak interaction. Similarly to the electroweak model, GUT assumes that all symmetries have the same gauge coupling strength above an extremely high energy threshold of the order of $\sim 10^{13}$ TeV. Finally, beyond the GUT scale, it may also be possible to merge gravity with the other three fundamental interactions into a “theory of everything”.

1.2 CP violation

The parity P inverts every coordinates in a reference frame ($\vec{r} \rightarrow -\vec{r}$, $\vec{r} \in \mathbb{R}^3$). It follows that the momentum \vec{p} is also inverted but the spin, which is the intrinsic kinetic momentum of a particle, remains unchanged. The charge conjugation C inverts the electric charge q of the elementary particles. Basically, a particle is changed into its antiparticle. It is proved that exclusively ν_L and $\bar{\nu}_R$ exist and not ν_R and $\bar{\nu}_L$. The action of P or C on these existing particles leads to non-existent particles:

$$\begin{aligned} P(\nu_L) &= \nu_R & C(\nu_L) &= \bar{\nu}_L \\ P(\bar{\nu}_R) &= \bar{\nu}_L & C(\bar{\nu}_R) &= \nu_R \end{aligned} \quad (1.9)$$

By the fact, both P and C are independently non symmetric for the neutrini. On the other hand, the combined action of C and P becomes a real symmetry:

$$\begin{aligned} CP(\nu_L) &= C(\nu_R) = \bar{\nu}_R \\ CP(\bar{\nu}_R) &= C(\bar{\nu}_L) = \nu_L \end{aligned} \quad (1.10)$$

Nevertheless, CP violation was observed in neutral kaons K^0 and \bar{K}^0 decays in 1964. In the framework of the Standard Model, CP violation in the weak interaction is generated by the 3×3 unitary complex matrix V_{CKM} introduced by Cabibbo, Kobayashi and Maskawa. It represents the relative strengths of the mixing between the down-type and the up-type quarks:

$$V_{\text{CKM}} = \begin{pmatrix} V_{ud} & V_{us} & V_{ub} \\ V_{cd} & V_{cs} & V_{cb} \\ V_{td} & V_{ts} & V_{tb} \end{pmatrix} \quad (1.11)$$

The matrix is uniquely defined by three real parameters and a complex phase. The parameterization proposed by Wolfenstein uses A , λ , ρ and η , among which λ is well known ($\lambda = \sin \theta_c \simeq 0.221$ where θ_c is the Cabibbo angle). It takes the form:

$$V_{\text{CKM}} = V_{\text{CKM}}^{(3)} + \delta V_{\text{CKM}} + \mathcal{O}(\lambda^6) \quad (1.12)$$

where:

$$V_{\text{CKM}}^{(3)} = \begin{pmatrix} 1 - \lambda^2/2 & \lambda & A\lambda^3(\rho - i\eta) \\ -\lambda & 1 - \lambda^2/2 & A\lambda^2 \\ A\lambda^3(1 - \rho - i\eta) & -A\lambda^2 & 1 \end{pmatrix} \quad (1.13)$$

$$\delta V_{\text{CKM}} = \begin{pmatrix} 0 & 0 & 0 \\ -iA^2\lambda^5\eta & 0 & 0 \\ A(\rho + i\eta)\lambda^5/2 & (1/2 - \rho)A\lambda^4 - iA\lambda^4\eta & 0 \end{pmatrix} \quad (1.14)$$

The unitary condition of the CKM matrix:

$$V_{\text{CKM}}^\dagger V_{\text{CKM}} = V_{\text{CKM}} V_{\text{CKM}}^\dagger = \mathbb{1} \quad (1.15)$$

gives nine equations, six of which can be represented as triangles in the complex plane. In particular, two of them are relevant for the B -mesons systems:

$$V_{\text{ud}}V_{\text{ub}}^* + V_{\text{cd}}V_{\text{cb}}^* + V_{\text{td}}V_{\text{tb}}^* = 0 \quad (1.16)$$

$$V_{\text{tb}}V_{\text{ub}}^* + V_{\text{ts}}V_{\text{us}}^* + V_{\text{td}}V_{\text{ud}}^* = 0 \quad (1.17)$$

At $\mathcal{O}(\lambda^3)$, i.e. ignoring δV_{CKM} , both triangles are identical. Eq. (1.16) is represented by the triangle in the left of figure 1.5. Including $\mathcal{O}(\lambda^5)$ terms distorts the triangle like it is shown for eq. (1.17) in the right of figure 1.5:

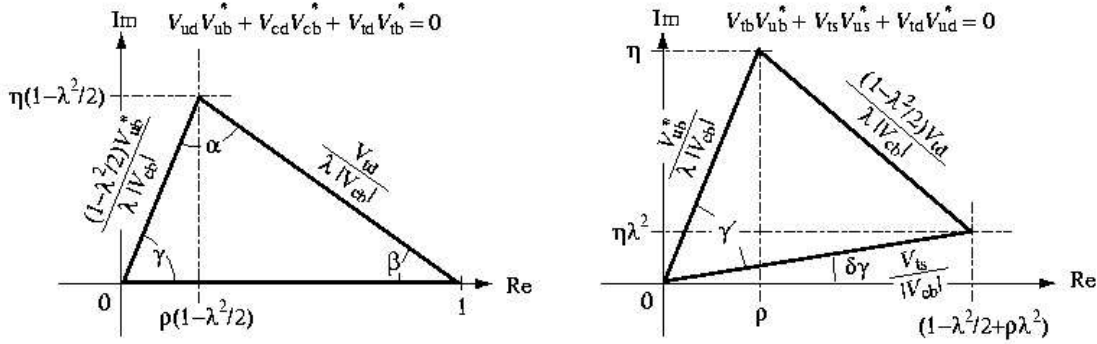


Figure 1.5: Two CKM-triangles corresponding to unitarity relations (1.16) on the left and (1.17) on the right. The Wolfenstein's parameterization is used with approximation at $\mathcal{O}(\lambda^5)$.

Using (1.13), the angles of the CKM-triangles satisfy at $\mathcal{O}(\lambda^3)$:

$$\beta = \arg\left(-\frac{V_{\text{cd}}V_{\text{cb}}^*}{V_{\text{td}}V_{\text{tb}}^*}\right) = -\arg(V_{\text{td}}) \quad (1.18)$$

$$\gamma = \arg\left(-\frac{V_{\text{ud}}V_{\text{ub}}^*}{V_{\text{cd}}V_{\text{cb}}^*}\right) = -\arg(V_{\text{ub}}) \quad (1.19)$$

$$\alpha = \arg\left(-\frac{V_{\text{td}}V_{\text{tb}}^*}{V_{\text{ud}}V_{\text{ub}}^*}\right) \quad (1.20)$$

At $\mathcal{O}(\lambda^5)$ with (1.14):

$$\delta\gamma = \arg(-V_{\text{ts}}V_{\text{us}}^*) = -\arg(V_{\text{ts}}) \quad (1.21)$$

$$\gamma' = \arg\left(-\frac{V_{\text{tb}}V_{\text{ub}}^*}{V_{\text{ts}}V_{\text{us}}^*}\right) \quad (1.22)$$

Two methods emerge to measure the important angles β , γ and $\delta\gamma$. Within the Standard Model, these can be directly measured from CP asymmetries in charge-conjugate decay modes of B -mesons systems. For example:

- β from B_d^0 and $\bar{B}_d^0 \rightarrow J/\psi K_s^0$
- γ from $B_d^0 \rightarrow \bar{D}^0 K_s^{*0}, D^0 K_s^{*0}$ and $\bar{B}_d^0 \rightarrow \bar{D}^0 \bar{K}_s^{*0}, D^0 \bar{K}_s^0$
- $\delta\gamma$ from B_s^0 and $\bar{B}_s^0 \rightarrow J/\psi \phi$

Other decay channels can also help to obtain combinations between these angles:

- $\beta + \gamma (= \pi - \alpha)$ from B_d^0 and $\bar{B}_d^0 \rightarrow \pi^+ \pi^-$
- $\gamma + \delta\gamma$ from B_s^0 and $\bar{B}_s^0 \rightarrow D_s^\pm K^\mp$

On the other hand, the angles can be indirectly obtained by extraction of the lengths sides of the CKM-triangles. Assuming an accurate knowledge of λ , the triangles are completely described by the two parameters ρ and η . As shown in figure 1.5, these can be derived from $|V_{cb}|$, $|V_{ub}|$ and $|V_{td}|$. The first two are determined from inclusive semileptonic B -mesons decays while $|V_{td}|$ can be obtained from the frequency of B_d^0 - \bar{B}_d^0 oscillations.

The comparison between the two methods should confirm or, at contrary, infrim the CKM-model whether the results converge or diverge. Important differences between the two measurements would indicate physics beyond the Standard Model.

Measurements performed in the neutral kaons K^0 and \bar{K}^0 systems are in agreement with the prediction of the CKM model. In the B^0 and \bar{B}^0 systems, there are many more decay modes available, making it very attractive for CP violation studies. Measurements are at present performed in experiments like BaBar, Belle or CDF and will start at LHCb in 2008 in order to improve the knowledge of the CKM-triangles. Figure 1.6 illustrates the experimental constraints on the CKM-triangle and a global fit resulting from various measurements [1]. The shaded 95% CL regions overlap consistently around the global fit region. Future measurements incompatible with this geometry would be a hint for New Physics.

1.3 Higgs Physics

At this point, a question arises concerning the Standard Model: why do the mediators of the weak interaction W^\pm and Z^0 have mass while, for the other interactions, the mediators are massless? In 1964, Peter W. Higgs from the University of Edinburgh and, in parallel, F. Englert and Robert H. Brout from the University of Brussels introduced a new ingredient in the formulation of gauge theories. Exploiting the Spontaneous gauge Symmetry Breaking (SSB), they found a way to give

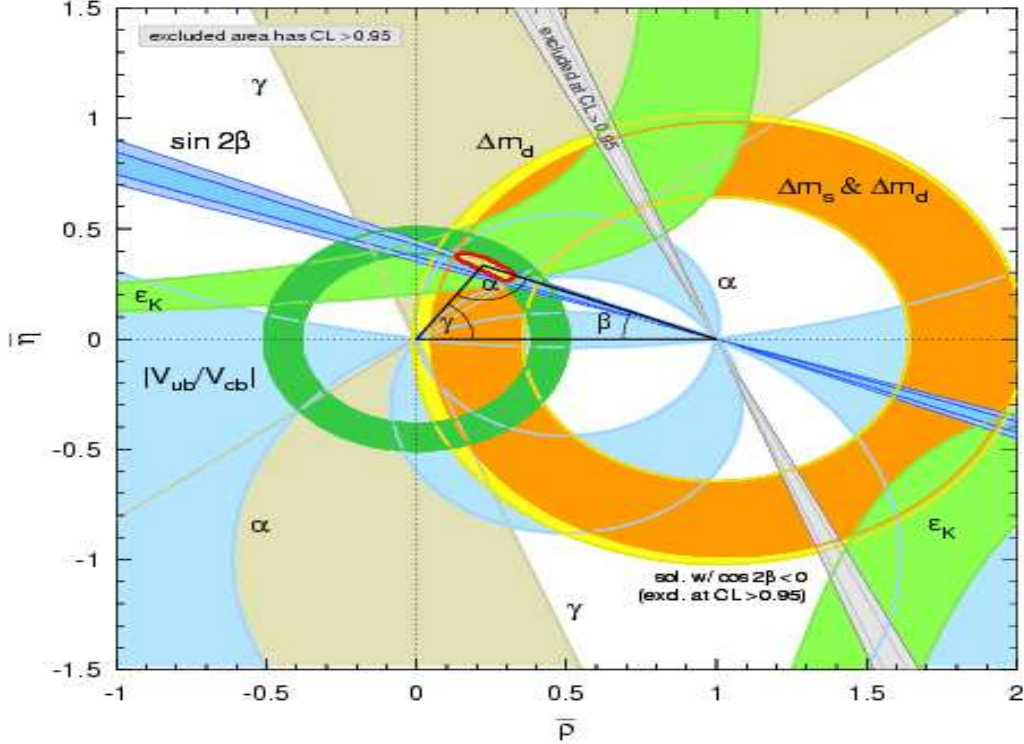


Figure 1.6: Global fit of the unitary CKM-triangle with experimental constraints from various measurements.

mass to some of the Yang-Mills fields, while keeping the theory gauge invariant. This is called the *Higgs Mechanism*.

The fundamental idea is to include in the theory an extra scalar field which does not vanish in the vacuum. As previously said, the vacuum is defined as the state in which all fields have their lowest possible energy. In general, the energy is minimal when the field is null everywhere, that is when the particle has disappeared in the vacuum. As it will be explained in the next sections, the introduced Higgs field is unusual in the sense that its energy is minimal when the field has some uniform value greater than zero. Therefore, Higgs particles exist in any vacuum.

1.3.1 The Goldstone model:

A simple example of Spontaneous Symmetry Breaking

In the Standard Model, the Electroweak theory is formulated as a $SU(2) \otimes U(1)$ gauge theory in which the electroweak interactions between fermions are described by exchange of massless vector bosons.

The Lagrangian density of such free massless boson fields is a composition of the $U(1)$ gauge field B_μ and the three real $SU(2)$ gauge fields W_μ^j , $j = 1, 2, 3$:

$$\mathcal{L} = -\frac{1}{4}B_{\mu\nu}(x)B^{\mu\nu}(x) - \frac{1}{4}W_{\mu\nu}^j(x)W^{j\mu\nu}(x) \quad (1.23)$$

where $B_{\mu\nu}$ and $W_{\mu\nu}^j$ are the field tensors defined as:

$$\begin{aligned} B_{\mu\nu} &= \partial_\mu B_\nu - \partial_\nu B_\mu \\ W_{\mu\nu}^j &= \partial_\mu W_\nu^j - \partial_\nu W_\mu^j \end{aligned} \quad (1.24)$$

By introducing the transformations:

$$\begin{aligned} A_\mu &= \cos \theta_W B_\mu + \sin \theta_W W_\mu^3 \\ Z_\mu &= \sin \theta_W B_\mu - \cos \theta_W W_\mu^3 \\ W_\mu^\pm &= \frac{1}{\sqrt{2}} (W_\mu^1 \mp iW_\mu^2) \end{aligned} \quad (1.25)$$

where the Weinberg angle θ_W is a free parameter, the Lagrangian (1.23) becomes:

$$\mathcal{L} = -\frac{1}{4}F_{\mu\nu}(x)F^{\mu\nu}(x) - \frac{1}{2}F_{W\mu\nu}^\dagger(x)F_W^{\mu\nu}(x) - \frac{1}{4}F_{Z\mu\nu}(x)F_Z^{\mu\nu}(x) \quad (1.26)$$

$F_{\mu\nu}$ is the electromagnetic tensor associated to the photon field A_μ while $F_{W\mu\nu}$ and $F_{Z\mu\nu}$ are the tensors associated to the electroweak fields W^\pm and Z^0 . At this point, the fields W^\pm and Z are still massless but can acquire mass by introducing by hand the terms $m_W^2 W_\mu^\dagger(x)W^\mu(x) + \frac{1}{2}m_Z^2 Z_\mu(x)Z^\mu(x)$ in the Lagrangian (1.26). The problem is that the obtained Lagrangian is no more invariant under $U(1)$ neither $SU(2)$ gauge transformations. This causes the theory to be not renormalizable and hence only appropriate at tree level.

A more suitable scenario using the spontaneous symmetry breaking allows to give mass to the fields W^\pm and Z^0 while retaining the invariance of the $SU(2) \otimes U(1)$ gauge theory. It is called the *Goldstone model*.

For that purpose, a classical Lagrangian density of the form $\mathcal{L} = \mathcal{T} - \mathcal{V}$ is introduced:

$$\mathcal{L} = (\partial^\mu \phi^*)(\partial_\mu \phi) - [\mu^2(\phi^* \phi) + \lambda(\phi^* \phi)^2] \quad (1.27)$$

together with a self-interacting complex scalar field $\phi(x) = \frac{1}{\sqrt{2}}(\phi_1(x) + i\phi_2(x))$. The term $\mathcal{T} = (\partial^\mu \phi^*)(\partial_\mu \phi)$ represents the kinetic energy of the field. The potential energy $\mathcal{V} = \mu^2(\phi^* \phi) + \lambda(\phi^* \phi)^2$ contains a mass term and a self-interaction term with a coupling intensity λ . μ^2 and λ are real constants with $\lambda > 0$.

The vacuum state minimizes the potential energy. Requiring that it is invariant under Lorentz transformations and translations implies that $\phi(x)$ is a constant in the vacuum state. Indeed:

$$\frac{d\mathcal{V}}{d\phi}(\phi_{\min}) = 2\mu^2|\phi_{\min}| + 4\lambda|\phi_{\min}|^3 = 0 \quad \Rightarrow \quad |\phi_{\min}| \cdot (\mu^2 + 2\lambda|\phi_{\min}|^2) = 0$$

If $\mu^2 > 0$, a unique solution $\phi_{\min}(x) = 0$ exists with a minimal potential energy $\mathcal{V}(\phi_{\min}) = 0$. However, if $\mu^2 < 0$, the solution is infinitely degenerate:

$$|\phi_{\min}|^2 = \frac{-\mu^2}{2\lambda} \quad \Rightarrow \quad \phi_{\min}(x) = \sqrt{\frac{-\mu^2}{2\lambda}} \cdot e^{i\theta} \quad \text{with } 0 \leq \theta \leq 2\pi$$

The minima $\phi_{\min}(x)$ stand on a ring of radius $\sqrt{\frac{-\mu^2}{2\lambda}}$ in the (ϕ_1, ϕ_2) complex plane, as shown in figure 1.7:

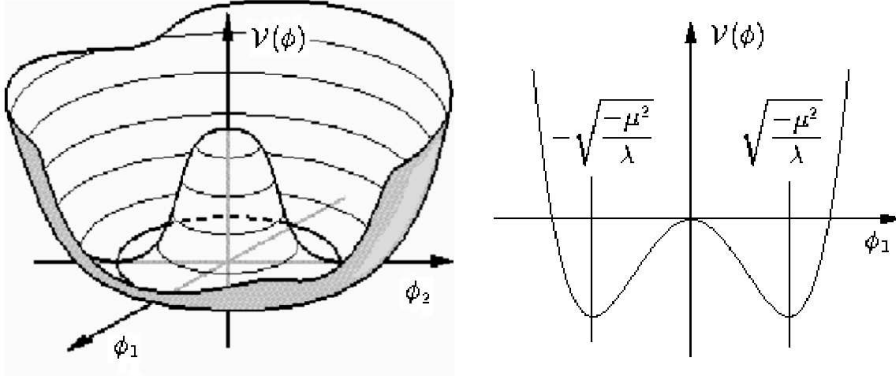


Figure 1.7: Representation in the (ϕ_1, ϕ_2) complex plane of the potential $\mathcal{V}(\phi)$ of a massive and self-interacting complex scalar field $\phi = \phi_1 + i\phi_2$ (*left*) and its projection for $\phi_2 = 0$ (*right*). The shape is like a bottom of bottle with a degenerate minimum lying on a ring of radius $\sqrt{\frac{-\mu^2}{2\lambda}}$.

The invariance of the Lagrangian (1.27) under the global $U(1)$ transformation describing rotations in the complex plane allows to choose $\theta = 0$ without loss of generality. Therefore:

$$\phi_{\min}(x) = \sqrt{\frac{-\mu^2}{2\lambda}} \equiv \frac{v}{\sqrt{2}} \quad \Rightarrow \quad v = \sqrt{\frac{-\mu^2}{\lambda}} \quad (1.28)$$

It has to be noticed that v is real due to the fact that μ^2 is negative. At this point, the components ϕ_1 and ϕ_2 of the complex scalar field can be redefined in terms of σ and η in order to have a better interpretation of the deviations from the vacuum state:

$$\begin{aligned}\phi_1(x) &\rightarrow \sigma(x) + v \\ \phi_2(x) &\rightarrow \eta(x)\end{aligned}\tag{1.29}$$

The complex scalar field becomes $\phi(x) = \frac{1}{\sqrt{2}}(\sigma(x) + v + i\eta(x))$ and the Lagrangian (1.27) can be rewritten as:

$$\begin{aligned}\mathcal{L} &= \frac{1}{2}(\partial^\mu\sigma)(\partial_\mu\sigma) - \lambda v^2\sigma^2 + \frac{1}{2}(\partial^\mu\eta)(\partial_\mu\eta) \\ &\quad - \lambda v\sigma(\sigma^2 + \eta^2) - \frac{1}{4}\lambda(\sigma^2 + \eta^2)^2 + \frac{1}{4}\lambda v^4\end{aligned}\tag{1.30}$$

The terms in the first row of (1.30) represent two real Klein-Gordon fields σ and η . The mass term $\lambda v^2\sigma^2$ implies that the σ boson has a mass $m_\sigma = v\sqrt{2\lambda}$. The η boson is massless and, in agreement to the Goldstone theorem⁶, is a *Goldstone boson*. In the second line, the two first terms correspond to σ - η interactions of different orders. They can be studied with the perturbation theory. The last term is a constant which takes sense only in general relativity as a possible gravitational effect.

To summarize, in the Goldstone model, the Lagrangian density (1.27) describing a massive and self-interacting complex scalar field has a degenerate energy minimum. This breaks spontaneously the $U(1)$ symmetry and creates a perturbative theory with a massive scalar boson.

1.3.2 The Higgs Mechanism

The Goldstone model can be extended to create massive vector bosons in a gauge invariant theory. For that purpose, the covariant derivative $\mathcal{D}_\mu = \partial_\mu + iqA_\mu$ is introduced in the Lagrangian density (1.27) in place of the usual derivative ∂_μ to give:

$$\mathcal{L} = (\mathcal{D}_\mu\phi^*)(\mathcal{D}_\mu\phi) - [\mu^2(\phi^*\phi) + \lambda(\phi^*\phi)^2] - \frac{1}{4}F_{\mu\nu}F^{\mu\nu}\tag{1.31}$$

$F_{\mu\nu} = \partial_\mu A_\nu - \partial_\nu A_\mu$ is the electromagnetic tensor associated to the massless free gauge field of the photon A_μ . The Lagrangian (1.31) is invariant under the $U(1)$ gauge transformations:

$$\begin{aligned}\phi(x) &\rightarrow \phi'(x) = \phi(x) \cdot e^{iq\theta(x)} \\ A_\mu(x) &\rightarrow A'_\mu(x) = A_\mu(x) + \partial_\mu\theta(x)\end{aligned}\tag{1.32}$$

⁶Goldstone theorem: *If a theory has an exact symmetry, such as a gauge symmetry, which is not a symmetry of the vacuum, then the theory must contain a massless boson called Goldstone boson.*

where $\theta(x)$ is any differentiable function. As for the Goldstone model, the complex scalar field can be expressed in terms of σ and η (see (1.29)) and the Lagrangian (1.31) with $\mu^2 < 0$ becomes:

$$\begin{aligned} \mathcal{L} = & \frac{1}{2}(\partial^\mu \sigma)(\partial_\mu \sigma) - \lambda v^2 \sigma^2 + \frac{1}{2}(\partial^\mu \eta)(\partial_\mu \eta) \\ & - \frac{1}{4}F_{\mu\nu}F^{\mu\nu} + \frac{1}{2}q^2 v^2 (A_\mu A^\mu) \\ & + q^2 v \sigma (A_\mu A^\mu) + \frac{1}{2}q^2 (\sigma^2 + \eta^2) (A_\mu A^\mu) + q [\sigma(\partial_\mu \eta) - \eta(\partial_\mu \sigma)] A^\mu \\ & - \lambda v \sigma (\sigma^2 + \eta^2) - \frac{1}{4}\lambda (\sigma^2 + \eta^2)^2 + \frac{1}{4}\lambda v^4 \\ & + qv A^\mu (\partial_\mu \eta) \end{aligned} \quad (1.33)$$

Like in (1.30), the first line represents a scalar boson σ with mass $m_\sigma = v\sqrt{2\lambda}$ and a massless boson η . In the second line is described the vector boson field A_μ which has acquired a mass $m_A = qv$. The third row indicates interactions between the different fields σ , η and A_μ . The fourth one results from σ - η interactions plus a constant, as in (1.30). An undesirable term $qvA^\mu(\partial_\mu \eta)$ remains, which can be interpreted as a perturbative interaction between the gauge field A_μ and η . Furthermore, the Lagrangian (1.30) has four degrees of freedom while the covariant form (1.33) has one more. The appropriate gauge transformation (1.32) allows to absorb it. The unitary gauge:

$$\theta(x) = -\frac{1}{q} \arctan \left(\frac{\phi_2(x)}{\phi_1(x)} \right) \quad (1.34)$$

transforms

$$\phi(x) = \phi_1(x) + i\phi_2(x) = |\phi(x)| \cdot e^{i \arctan \left(\frac{\phi_2(x)}{\phi_1(x)} \right)}$$

in

$$\phi'(x) = \phi(x) \cdot e^{iq\theta(x)} = |\phi(x)| \cdot e^{i \arctan \left(\frac{\phi_2(x)}{\phi_1(x)} \right)} \cdot e^{-iq \cdot \frac{1}{q} \arctan \left(\frac{\phi_2(x)}{\phi_1(x)} \right)} = |\phi(x)|$$

The complex scalar field has now uniquely a real component $H(x) = \sigma(x)$ and can be written as $\phi(x) = \frac{1}{\sqrt{2}}(H(x) + v)$. In the same way, the terms in η in (1.33) are cancelled ($\eta = 0$):

$$\begin{aligned} \mathcal{L} = & \frac{1}{2}(\partial^\mu H)(\partial_\mu H) - \lambda v^2 H^2 - \frac{1}{4}F_{\mu\nu}F^{\mu\nu} + \frac{1}{2}q^2 v^2 (A_\mu A^\mu) \\ & + q^2 v H (A_\mu A^\mu) + \frac{1}{2}q^2 H^2 (A_\mu A^\mu) - \lambda v H^3 - \frac{1}{4}\lambda H^4 + \frac{1}{4}\lambda v^4 \end{aligned} \quad (1.35)$$

Essentially it remains one real massive scalar field H and a massive vector boson A_μ .

In summary, the Higgs mechanism transforms a complex scalar field ϕ (ϕ_1, ϕ_2 : 2 degrees of freedom) and a massless vector field A_μ (two transverse polarization states: 2 d.o.f.) into one massive scalar field H (1 d.o.f.) and one massive vector boson A_μ (a longitudinal and two transverse polarized states: 3 d.o.f.). In a sense, the vector boson has gained a longitudinal mode by absorption of the Goldstone boson. The massive scalar field H is called the *Higgs particle*.

1.3.3 The Higgs Mechanism in the Standard Model

In the framework of the Standard Model, the Higgs mechanism is responsible for the gauge bosons W^\pm and Z^0 , quarks and leptons mass generation. For that purpose, it is extended to $SU(2)_L \otimes U(1)_Y$ symmetry of the GWS electroweak model (see § 1.1.2) [2, 3]. $U(1)_Y$ refers to weak hypercharge involving particles of both chiralities and integers the massless gauge field B_μ . $SU(2)_L$ refers to weak isospin involving only left-handed particles and integers the massless gauge fields triplet W_μ^j . Furthermore, to be valid in the full description of the Standard Model, it has to be invariant under $SU(3)_c$ symmetry which refers to strong interactions between quarks and involves eight gluon gauge fields G_μ^α .

The Lagrangian density includes a complex scalar isodoublet field with a non-zero vacuum expectation value:

$$\phi = \begin{pmatrix} \phi^+ \\ \phi^0 \end{pmatrix} \quad \phi_{\text{vac}} = \begin{pmatrix} 0 \\ v + H \end{pmatrix} \quad (1.36)$$

where H is the physical Higgs field and can be expressed as a sum of four Lagrangian contributions:

$$\mathcal{L}_{\text{SM}} = \mathcal{L}_{\text{GWS}} + \mathcal{L}_{\text{bosons}} + \mathcal{L}_{\text{fermions}} + \mathcal{L}_{\text{QCD}} \quad (1.37)$$

The first term \mathcal{L}_{GWS} concerns the massless gauge fields W_μ^j and B_μ and their interactions with the left-handed (χ_L doublet) and the right-handed (χ_R singlet) fermions in the GWS model. It can be written as:

$$\begin{aligned} \mathcal{L}_{\text{GWS}} = & -\frac{1}{4}W_{\mu\nu}^jW_j^{\mu\nu} - \frac{1}{4}B_{\mu\nu}B^{\mu\nu} \\ & + \bar{\chi}_L\gamma^\mu \left(\partial_\mu - i\frac{g}{2}\tau_jW_\mu^j - i\frac{g'}{2}Y_WB_\mu \right) \chi_L + \bar{\chi}_R\gamma^\mu \left(\partial_\mu - i\frac{g'}{2}Y_WB_\mu \right) \chi_R \end{aligned} \quad (1.38)$$

The first line contains the kinetic terms of the gauge fields with the tensors defined in (1.24). The second line describes the kinetic energy of the fermions and their interactions with the gauge fields. Only left-handed fermions interact with the gauge fields triplet W_μ^j . τ^j are the Pauli matrices and Y_W the weak hypercharge generator. g and g' are the electroweak coupling constants.

The Lagrangian $\mathcal{L}_{\text{bosons}}$ includes the Higgs kinetic term and its potential energy $\mathcal{V}(\phi)$:

$$\mathcal{L}_{\text{bosons}} = \left| \left(\partial_\mu + i \frac{g}{2} \tau_j W_\mu^j + i \frac{g'}{2} Y_W B_\mu \right) \phi \right|^2 - \mathcal{V}(\phi) \quad (1.39)$$

It describes the mutual couplings between the gauge (W^\pm , Z^0 and γ) and the Higgs bosons and is responsible for their mass generation.

The term $\mathcal{L}_{\text{fermions}}$ describes the couplings between the fermions and the Higgs particle - which are also called the *Yukawa couplings* - and is responsible for the fermions mass generation. It is invariant under $SU(2)_L \otimes U(1)_Y$ symmetry and takes the form:

$$\mathcal{L}_{\text{fermions}} = -g_f^u (\bar{\chi}_L^u \phi \chi_R^u + \bar{\chi}_R^u \phi^\dagger \chi_L^u) - g_f^d (\bar{\chi}_L^d \phi \chi_R^d + \bar{\chi}_R^d \phi^\dagger \chi_L^d) \quad (1.40)$$

where ϕ^\dagger is the conjugate of the Higgs doublet (1.36). The coupling constants satisfy the relation:

$$g_f^i = \sqrt{2} \cdot g_f = \sqrt{2} \cdot \frac{m_f}{v} \quad i = u, d \quad (1.41)$$

Finally, the term \mathcal{L}_{QCD} represents the $SU(3)_c$ invariant Lagrangian of the strong interaction:

$$\mathcal{L}_{\text{QCD}} = \sum_{\alpha=1}^8 \left[-G_{\mu\nu}^\alpha \cdot G^{\alpha\mu\nu} + \frac{g_s}{2} (\bar{\psi}_q^j \gamma^\mu \lambda_{jk}^\alpha \psi_q^k) G_\mu^\alpha \right] \quad (1.42)$$

The first term includes the tensors $G_{\mu\nu}^\alpha = \partial_\mu G_\nu^\alpha - \partial_\nu G_\mu^\alpha$ associated to the eight gluon gauge fields G_μ^α and represents the gluons kinetic energies. The second term describes the quark-gluon couplings where ψ_q^j represent the quarks color fields and λ_{jk}^α the Gell-Man matrices which are the $SU(3)_c$ generators. $g_s = \sqrt{4\pi\alpha_s}$ is the strong coupling constant.

The Lagrangian (1.37) is not in its explicitly broken form. It contains a complex scalar isodoublet ϕ and four massless vector bosons W_μ^j and B_μ . The Higgs mechanism transforms them into one real scalar H , three massive vector bosons W^\pm and Z^0 and one massless vector boson γ . Discarding the QCD part and keeping only the electroweak and Higgs parts, the resulting Lagrangian can be written in its spontaneously broken form as:

$$\mathcal{L} = \mathcal{L}_0 + \mathcal{L}_{\text{FB}} + \mathcal{L}_{\text{FH}} + \mathcal{L}_{\text{BB}} + \mathcal{L}_{\text{BH}} + \mathcal{L}_{\text{HH}} \quad (1.43)$$

where:

$$\begin{aligned}
\mathcal{L}_0 = & -\frac{1}{4}F_{\mu\nu}F^{\mu\nu} \\
& -\frac{1}{2}F_{W\mu\nu}^\dagger F_W^{\mu\nu} + m_W^2 W_\mu^\dagger W^\mu \\
& -\frac{1}{4}F_{Z\mu\nu}F_Z^{\mu\nu} + \frac{1}{2}m_Z^2 Z_\mu Z^\mu \\
& + \frac{1}{2}(\partial^\mu H)(\partial_\mu H) - \frac{1}{2}m_H^2 H^2
\end{aligned} \tag{1.44}$$

\mathcal{L}_0 contains the kinetic terms of the W^\pm , Z^0 , γ and Higgs bosons. It also includes their corresponding mass terms, except for the massless photon. It is analogue to the Lagrangian (1.26) described at the beginning of section 1.3.1. The fundamental difference is that the gauge field masses - and also the fermions masses - are not introduced by hand but are a direct consequence of the $SU(2)_L \otimes U(1)_Y$ spontaneous symmetry breaking. The remaining terms in (1.43) describe the fermion-boson (\mathcal{L}_{FB}), fermion-Higgs (\mathcal{L}_{FH}), boson-boson (\mathcal{L}_{BB}), boson-Higgs (\mathcal{L}_{BH}) and Higgs-Higgs (\mathcal{L}_{HH}) interactions. Of particular interest is the interaction Lagrangian between the fermions and the Higgs particle \mathcal{L}_{FH} :

$$\mathcal{L}_{\text{FH}} = -g_f \cdot \bar{\psi}_f H \psi_f \stackrel{(1.41)}{=} -\frac{m_f}{v} \cdot \bar{\psi}_f H \psi_f \tag{1.45}$$

Together with (1.41), it expresses that the interaction between the fermions and the Higgs particle is proportional to the fermion mass.

In summary, the masses of the Standard Model fundamental particles - leptons, quarks and gauge bosons - are generated through their interaction with the scalar background Higgs field which arises from the electroweak spontaneous symmetry breaking.

Some physical quantities can be predicted from the Higgs Mechanism in the Standard Model. Using the electroweak Fermi constant with $\hbar = c = 1$:

$$G_F = 1.16639 \cdot 10^{-5} \text{ GeV}^{-2} \tag{1.46}$$

the vacuum expectation value is:

$$v = \left(\sqrt{2}G_F\right)^{-\frac{1}{2}} \sim 246 \text{ GeV} \tag{1.47}$$

The charged and neutral electroweak coupling constants are defined as:

$$\begin{aligned}
g = g_W &= \frac{e}{\sin \theta_W} = 2 \left(\sqrt{2}G_F\right)^{\frac{1}{2}} \cdot m_W \\
g' = g_Z &= \frac{g_W}{\cos \theta_W} = \frac{e}{\sin \theta_W \cos \theta_W} = 2 \left(\sqrt{2}G_F\right)^{\frac{1}{2}} \cdot m_Z
\end{aligned} \tag{1.48}$$

It comes directly that $m_Z = \frac{m_W}{\cos\theta_W}$. In definitive, from (1.47) and (1.48), the gauge bosons masses are:

$$m_W = \frac{1}{2}vg_W \quad , \quad m_Z = \frac{1}{2}vg_Z \quad \text{and} \quad m_\gamma = 0 \quad (1.49)$$

The gauge bosons masses together with the Weinberg angle θ_W have to be measured experimentally and recent results give [1]:

$$\begin{aligned} m_W &= 80.425 \text{ GeV}/c^2 \\ m_Z &= 91.188 \text{ GeV}/c^2 \\ \sin^2\theta_W &\simeq 0.231 \end{aligned} \quad (1.50)$$

From (1.41) and (1.47), the fermions masses can be expressed as:

$$m_f = vg_f = \left(\sqrt{2}G_F\right)^{-\frac{1}{2}} \cdot g_f \quad (1.51)$$

in such a way that the coupling between the fermions and the Higgs particle is, in accord with (1.48):

$$g_f = \left(\sqrt{2}G_F\right)^{\frac{1}{2}} \cdot m_f = \frac{e}{2\sin\theta_W} \cdot \frac{m_f}{m_W} \quad (1.52)$$

In definitive, in the Standard Model, the electroweak gauge bosons and fermions couplings to the Higgs particle written in terms of e , θ_W and m_W or G_F are proportional to their mass, as shown in table 1.4:

	e , θ_W and m_W	G_F
g_W	$\frac{e}{\sin\theta_W m_W} \cdot m_W$	$2 \left(\sqrt{2}G_F\right)^{\frac{1}{2}} \cdot m_W$
g_Z	$\frac{e}{\sin\theta_W m_W} \cdot m_Z$	$2 \left(\sqrt{2}G_F\right)^{\frac{1}{2}} \cdot m_Z$
g_f	$\frac{1}{2} \frac{e}{\sin\theta_W m_W} \cdot m_f$	$\left(\sqrt{2}G_F\right)^{\frac{1}{2}} \cdot m_f$

Table 1.4: Couplings of the W^\pm , Z^0 bosons and fermions to the Higgs particle, expressed in terms of e , θ_W and m_W (*left column*) and the Fermi constant G_F (*right column*). All couplings are proportional to their respective mass.

The Higgs boson mass is given by (see § 1.3.1 and 1.3.2):

$$m_H = v\sqrt{2\lambda} \quad (1.53)$$

and cannot be predicted due to the unknown parameter λ . Actually, it is the unique unknown parameter while, at it has been demonstrated, all couplings are fixed by the masses of the particles. This is a consequence of the Higgs mechanism *sui generis*. However, an upper limit can be set by requiring that all interactions, including the Yukawa couplings of the fermions to the Higgs field and the self-interaction of the Higgs field with itself, should remain weak between the $SU(2) \otimes U(1)$ symmetry breaking scale - which is the vacuum expectation value v - and the unification scale $\Lambda \sim 1$ TeV [4]. The Higgs self-coupling λ appearing in the renormalization-group equations should not increase too much in this energy range giving a significant upper bound on λ and, as a consequence of (1.53), on the Higgs mass. On the other hand, a lower bound can also be set by requiring the vacuum stability [4, 5]. Indeed, the Yukawa coupling involving t -quarks increases proportionally with the top mass. In the same time, the top-loop corrections reduce the parameter λ as m_t grows. If m_t exceeds a certain threshold, λ becomes negative together with the self-energy potential, implying that the ground state is no longer stable. To avoid instability, the Higgs mass must exceed a minimal value for a given top mass.

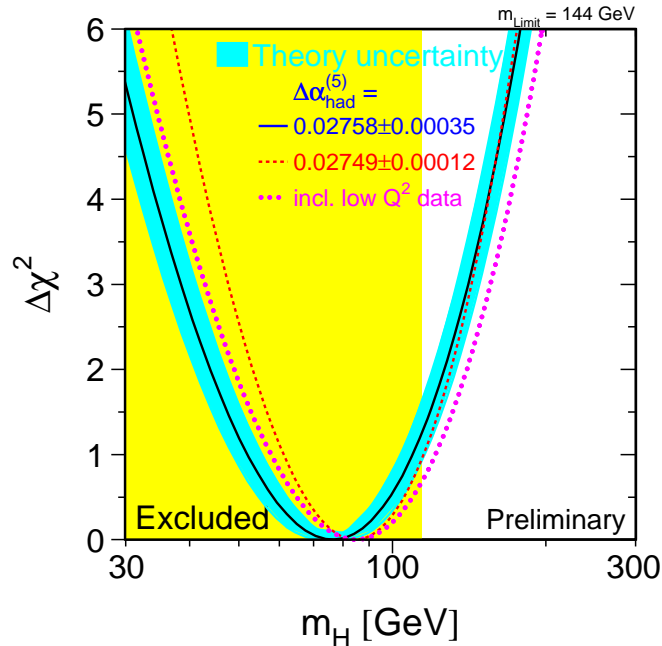


Figure 1.8: $\Delta\chi^2$ of the fit of all electroweak data as a function of the Higgs mass. The high precision measurements are performed at LEP, SLD, CDF and D0 [6].

Figure 1.8 shows the $\Delta\chi^2$ of the fit of all electroweak data as a function of the Higgs mass, assuming the consistency of the Standard Model. The data are derived from high precision measurements performed at LEP, SLD, CDF and D0 [6]. The hypothesis $m_H \leq 182 \text{ GeV}/c^2$ is confirmed at 95% CL in the LEP experiments, indicating a preference for a light Higgs. The direct searches for a Higgs boson at LEP have nevertheless excluded values $m_H < 114 \text{ GeV}/c^2$ [7]. New searches at the LHC proton collider will explore the entire canonical Higgs mass range. In definitive, if the Standard Model is valid up to an energy value near the Planck scale $\Lambda_P \sim 1.22 \cdot 10^{19} \text{ GeV}$, the Higgs mass should be in the window $114 < m_H < 182 \text{ GeV}/c^2$. Discovering a Higgs particle with a mass out of this window would be a hint for New Physics.

1.3.4 Higgs production

The most relevant Standard Model Higgs production mechanisms in hadrons collisions are quickly described in this section [3, 8]. The corresponding Feynman diagrams are pictured in figure 1.9:

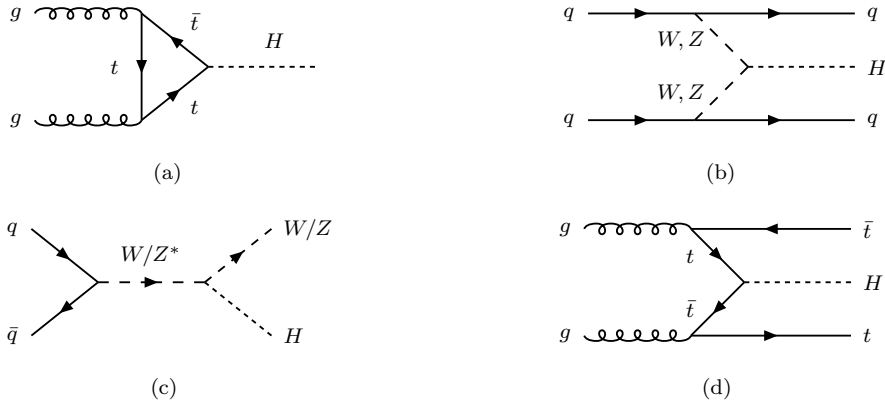


Figure 1.9: Dominant Standard Model Higgs production mechanisms in hadrons collisions: gluon fusion (a), W/Z vector boson fusion (b), W/Z associated production (c) and $t\bar{t}$ associated production (d).

The predominant mechanism is the gluon fusion $gg \rightarrow H$. It involves a quark loop in which the quarks couple to the gluons on the one hand and the Higgs particle on the other hand. As the coupling between the quark and the Higgs particle is proportional to the quark mass and as the t -quark is largely heavier than the other quarks, its presence in the loop is totally favoured.

Another mechanism is the vector boson fusion $qq \rightarrow qq VV \rightarrow qq H$ ($V = W, Z$) in which two incoming quarks emit two W or two Z which annihilate to create a Higgs particle. The cross-section is smaller than the gluon fusion but becomes comparable for large Higgs masses ($m_H \sim 1 \text{ TeV}/c^2$). Nevertheless, the process has the advantage to be more easily recognizable due to the presence of the two outgoing quarks which fragment to create jets in the final state.

The other mechanisms described here are the W/Z and the $t\bar{t}$ associated productions. In the W/Z associated production $q\bar{q} \rightarrow V^* \rightarrow V H$ ($V = W, Z$), an incoming $q\bar{q}$ pair annihilates to create an off-shell vector boson W/Z^* which deexcites by emission of a Higgs particle. This phenomena is also called *Higgs-strahlung* due to its similarity with the electromagnetic Bremsstrahlung in which an excited electron recovers its fundamental state by emission of a photon. In the $t\bar{t}$ associated production $gg \rightarrow t\bar{t}t\bar{t} \rightarrow t\bar{t}H$, two gluons create a $t\bar{t}$ pair each. A t from a pair annihilates with the \bar{t} from the other pair to create a Higgs particle, remaining a $t\bar{t}$ pair. Here again, the presence of top quarks is totally dominant. The cross-sections of the associated production mechanisms are also lower than the gluon fusion mechanism and are of interest particularly for light Higgs bosons. Nevertheless, they show some clear signatures for Higgs identification. Indeed, leptonic decays of the associated W/Z boson let appear one (or two) isolated lepton(s) with large transverse momentum in the final state. Similarly to the vector boson fusion, the associated $t\bar{t}$ production results in the presence of jets in the final state.

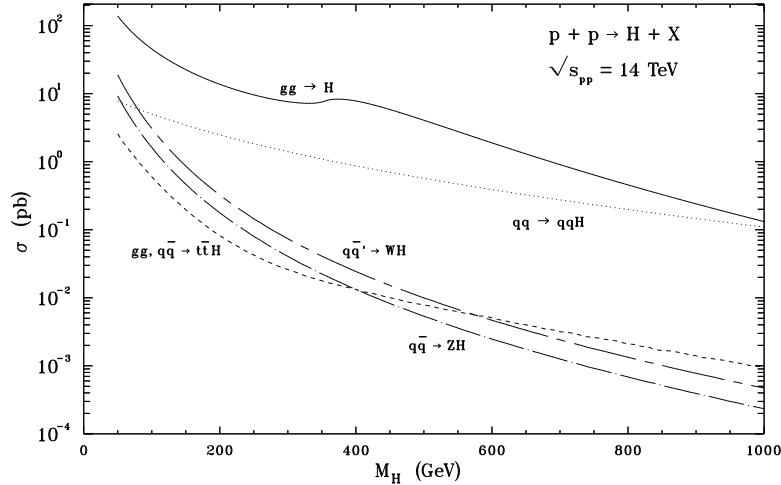


Figure 1.10: Standard Model Higgs production cross-section as a function of the Higgs mass m_H for the dominant production mechanisms in p - p collisions at $\sqrt{s} = 14 \text{ TeV}$. Parton distribution functions CTEQ6M and $m_t = 175 \text{ GeV}/c^2$ are used.

Figure 1.10 shows the cross-sections of the described Higgs production mechanisms as a function of the Higgs mass m_H in p - p collisions at $\sqrt{s} = 14$ TeV. Calculations includes improved knowledge of the parton distribution functions (CTEQ6M) due to recent analysis in the deep inelastic domain, next-to-leading order QCD corrections (except for the $t\bar{t}$ associated process) and recent precision measurements of the t -quark mass $m_t = 175$ GeV/ c^2 .

1.3.5 Higgs decays

Vector boson decays

The widths of the Higgs decays into two vector bosons $Z^0 Z^0$ or $W^+ W^-$ are given as [2, 3]:

$$\Gamma(H \rightarrow VV) = \delta_V \cdot \frac{G_F}{16\sqrt{2}\pi} m_H^3 \cdot \sqrt{1 - 4x_V} \cdot (1 - 4x_V + 12x_V^2) \quad (1.54)$$

where $x_V = m_V^2/m_H^2$ and $\delta_V = 2$ and 1 for $V = W^\pm$ and Z^0 respectively. The coupling strength of the Higgs particle to the electroweak gauge bosons is proportional to the boson mass m_V (eq. (1.48)):

$$g_V = 2 \left(\sqrt{2} G_F \right)^{\frac{1}{2}} \cdot m_V \quad (1.55)$$

The leptonic decays of the Z^0 bosons provides a very good signature of the presence of a Higgs boson through the channel $H \rightarrow Z^0 Z^0 \rightarrow l^+ l^- l^+ l^-$. If the Higgs mass is below the two bosons invariant mass, it can nevertheless decay into a VV^* pair, where V^* is an off-shell virtual vector boson. $\Gamma(H \rightarrow Z^0 Z^{0*})$ becomes relevant for $m_H > 140$ GeV/ c^2 .

Fermionic decays

The Higgs particle coupling with a fermion is proportional to the fermion mass (eq. (1.41) and (1.47)):

$$g_f = \left(\sqrt{2} G_F \right)^{\frac{1}{2}} \cdot m_f \quad (1.56)$$

The heavy mass of the t -quark with respect to the other flavours and to the leptons implies that the Higgs decays mainly into a $t\bar{t}$ quarks pair. However, if the Higgs mass is below the threshold $m_H < 2m_t \simeq 350$ GeV/ c^2 , this mode is suppressed and the Higgs decays dominantly into a $b\bar{b}$ pair. Introducing a color factor \mathcal{N}_c (equal to 3 for quarks, else 1), the width of the Higgs decay into fermions is given as [2, 3]:

$$\Gamma(H \rightarrow f\bar{f}) = \mathcal{N}_c \cdot \frac{G_F}{4\sqrt{2}\pi} m_f^2 m_H \cdot \left(1 - \frac{4m_f^2}{m_H^2} \right)^{\frac{3}{2}} \quad (1.57)$$

The QCD radiative corrections for Higgs decays into $b\bar{b}$ pairs can be found in [9]. They become very interesting in the mass range $80 < m_H < 160 \text{ GeV}/c^2$ because they reduce the decay width by a factor $\sim 2\text{-}3$.

Photonic decay

Although the null mass of the photon implies no possible coupling with the Higgs particle, the Higgs decay into two photons is possible through loop processes in the Standard Model. These include W bosons or fermions, mainly t -quarks rather than light quarks or leptons. The corresponding Feynman diagrams are pictured in figure 1.11:

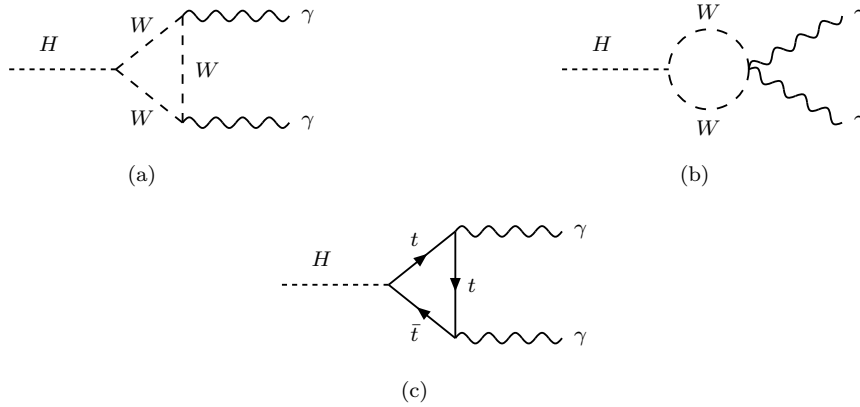


Figure 1.11: Feynman diagrams of the principal Higgs decays into two photons involving triangular W bosons (a), circular W bosons (b) and triangular t -quark (c) loop processes.

The complicate calculation of the $H^0 \rightarrow \gamma\gamma$ width involves dimensional regularization of the infinities arising from the loop and gives [3, 10]:

$$\Gamma(H \rightarrow \gamma\gamma) = \frac{\alpha^2 G_F}{128\sqrt{2}\pi^3} m_H^3 \cdot \left| \sum_i \mathcal{N}_c e_i^2 F_i \right|^2 \quad (1.58)$$

For Higgs mass values $m_H \ll 160 \text{ GeV}/c^2$, it can be approximated to:

$$\Gamma(H \rightarrow \gamma\gamma) = \frac{\alpha^2 G_F}{128\sqrt{2}\pi^3} m_H^3 \cdot \left(\frac{4}{3} \mathcal{N}_c e_t^2 - 7 \right)^2 \quad (1.59)$$

The corresponding branching ratio is small - always below 0.3% in the interesting mass window $80 < m_H < 160 \text{ GeV}/c^2$ - but provides a clean signature due to the two photons presence in the final state. QCD radiative corrections can obviously be applied only for top quarks loops but improve the result by only a factor $< 3\%$ [11].

Gluonic decay

As the gluons are not massive, the Higgs decay into gluons is similar to the two photons decay. However, since gluons couple only to quarks and not to vector bosons, only the t -quark loop contributes to the $H \rightarrow gg$ decay. The constant $\alpha \mathcal{N}_c e_i^2$ in (1.58) has to be replaced by the strong coupling constant α_s and a factor 2 has to be added to render for the different final state particles such that:

$$\Gamma(H \rightarrow gg) = \frac{\alpha_s^2 G_F}{64\sqrt{2}\pi^3} m_H^3 \cdot \left| \sum_i F_i \right|^2 \quad (1.60)$$

For Higgs mass values $m_H \ll 160 \text{ GeV}/c^2$, it can also be approximated to:

$$\Gamma(H \rightarrow gg) = \frac{\alpha_s^2 G_F}{36\sqrt{2}\pi^3} m_H^3 \cdot \left[1 + \left(\frac{95}{4} - \frac{7\mathcal{N}_F}{6} \right) \frac{\alpha_s}{\pi} \right] \quad (1.61)$$

where \mathcal{N}_F is the number of active flavours. The branching ratio is about 40 times higher than for the two photons. However, the signature is less clean, making this process less interesting. This is due to the fact that, during the fragmentation, the gluons create jets at a less important rate than those coming directly from the partons of the hadronic collisions. The QCD radiative corrections, which include the ggg and $gq\bar{q}$ final states, increase the partial width by $\sim 65\%$.

The branching ratios of the Standard Model Higgs decays described here are represented as a function of the Higgs mass m_H in figure 1.12 (*left*):

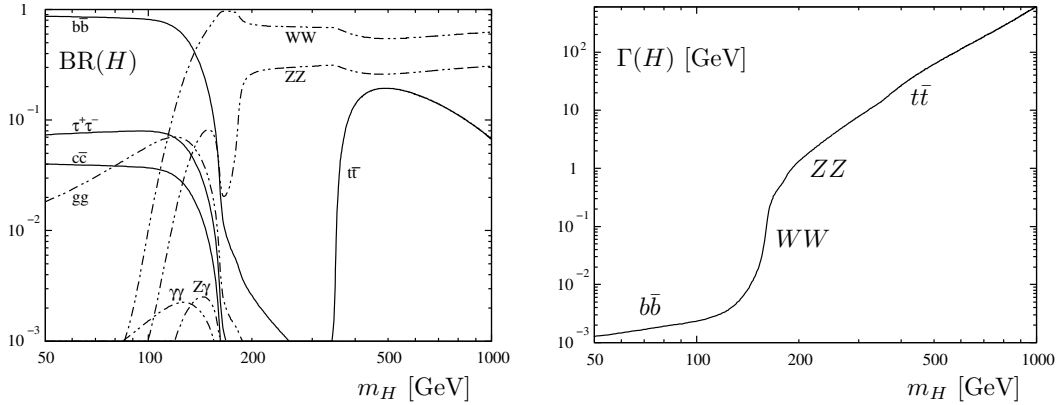


Figure 1.12: Standard Model Higgs branching ratios $\text{BR}(H)$ of the principal decay channels as a function of the Higgs mass m_H (*left*). Width $\Gamma(H)$ of the Higgs particle as a function of the Higgs mass m_H (*right*).

In the Higgs mass range $50 < m_H < 180 \text{ GeV}/c^2$, the dominant decay mode is into $b\bar{b}$. The decays into gauge bosons WW^* and ZZ^* , one boson being virtual, are also important in this window. Above $180 \text{ GeV}/c^2$, i.e. above the WW and ZZ thresholds, the two gauge bosons decays are dominant. The decay into $t\bar{t}$ quarks pairs becomes also important above the $t\bar{t}$ threshold, i.e. $m_H > 350 \text{ GeV}/c^2$. Decays into less massive fermions $H \rightarrow \tau^+\tau^-$ and $H \rightarrow c\bar{c}$ and into gluons also have to be taken into account below $140 \text{ GeV}/c^2$, although the $b\bar{b}$ decay mode dominates in this region. For instance, at $m_H = 120 \text{ GeV}/c^2$, the branching ratios are 68% for $b\bar{b}$, 3,1% for $c\bar{c}$, 6.9% for $\tau^+\tau^-$ and 7% for gg . The decay $H \rightarrow \gamma\gamma$ occurs at a level of only $\sim 0.1\%$ but provides a clear 2-body signature in the final state in the mass range $80 < m_H < 160 \text{ GeV}/c^2$.

The Standard Model Higgs total width is represented as a function of the Higgs mass m_H in figure 1.12 (*right*). Up to $140 \text{ GeV}/c^2$, the main contribution is the $b\bar{b}$ decay and the width is $< 10 \text{ MeV}$. It grows quickly to $\sim 1 \text{ GeV}$ when the virtual and real two gauge bosons channels open up. This narrow value cannot be measured directly. Above $\sim 350 \text{ GeV}/c^2$, the width, which is dominated by the $t\bar{t}$ decay, is larger than 10 GeV and can be resolved experimentally.

Chapter 2

The LHCb Experiment at CERN

One of the challenges of the high energy physicists community is to explore matter at ever lower spatial scale. On the other hand, it has to understand the mechanisms of formation of the Universe at its very earliest instants. These two exciting research domains seem to be dissociated but can actually be studied in parallel. Indeed, during the few fractions of seconds following the Big-Bang, the Universe was quite small so that the energy density and also the temperature were very high. Furthermore, according to the de Broglie principle, a particle with energy E or momentum \vec{p} has a spatial resolution δx given by:

$$\delta x \approx \frac{\hbar}{|\vec{p}|} = \frac{\hbar c}{E}$$

where \hbar is the Planck constant ($\hbar = 6.582 \cdot 10^{-22}$ MeV s). Therefore, high energy experiments allows scientists to approach as more as possible the Big-Bang conditions as well as to study the constituents of matter at a very small scale. Last but not least, there is a third interesting aspect in such experiments which is a consequence of the equivalence between energy and mass as formulated by A. Einstein: $E = mc^2$. Providing high energy allows to produce heavy particles which are accessible only in very specific conditions and to study their properties.

The energy of a particle is the (quadratic) sum of its mass energy, which is an intrinsic feature of the particle, and of its kinetic energy:

$$E^2 = (mc^2)^2 + (\vec{p}c)^2 = m^2c^4 + \vec{p}^2c^2$$

When an electric field \vec{E} is applied on a particle with charge q , it undergoes a force $\vec{F} = q\vec{E}$ which accelerates it according to $\vec{F} = m\vec{a}$. The idea of high energy physics experiments consists in colliding particles with increased kinetic energy in order to obtain high energy in the center-of-mass of the system. Two regimes are

commonly used to provide such interactions. The first one is the fixed target regime where an accelerated particle is thrown on another one at rest. The second one is the frontal collision regime where the two particles are accelerated in the opposite directions and pushed the one on the other. This method has the advantage to provide higher center-of-mass energy but is disadvantaged by the fact that a lower number of interactions is observed. The concept of luminosity \mathcal{L} is introduced to characterize an accelerator. It is proportional to the beams intensities and inversely proportional to their section. As we will see later, beams are discontinuous and constituted of packets of particles called *bunches*. The luminosity is defined as:

$$\mathcal{L} = \frac{n_1 \cdot n_2}{A} \cdot b \cdot f$$

where n_i is the number of particles per bunch in the beam i , A the beam section, b the number of bunches in each beam and f the revolution frequency. Associated to the interaction cross-section σ , it defines the interaction rate ν according to:

$$\nu [\text{s}^{-1}] = \sigma [\text{cm}^2] \cdot \mathcal{L} [\text{cm}^{-2} \text{s}^{-1}]$$

Two types of accelerators are usually implemented: the linear and the circular accelerators. The first one is the simplest but is nevertheless restricted by the length of the machine. This problem disappears with a circular implementation in which particles travel in loop in a ring. The beam trajectories are bent by applying a magnetic field in the transversal direction with respect to the orbit plane. However, another problem occurs: following the Maxwell equations, when a relativistic particle is deviated, it emits photons tangentially to its trajectory. This is the *synchrotron effect*. The energy loss depends on the particle but also on its speed v - through the Lorentz relativist factor $\gamma = (1 - (v/c)^2)^{-\frac{1}{2}}$ - and on the curvature radius as γ^4/r . There is therefore a limitation due to the concurrence between the gain in energy from the acceleration and the loss by synchrotron radiation. In electron colliders, this limit stands around 100-200 GeV and has already been reached at LEP. The new generation of colliders uses hadrons for which the limit is around 100 TeV. In figure 2.1 is presented the evolution of electron and hadron colliders in terms of center-of-mass energy during the last century.

2.1 The Large Hadron Collider

The CERN (Conseil Européen pour la Recherche Nucléaire) is located near Geneva across the boarder between Switzerland and France. This institution was founded in 1954 by 12 European countries and has grown up to 20 member states nowadays. The huge size and complexity of high energy particle physics experiments and also

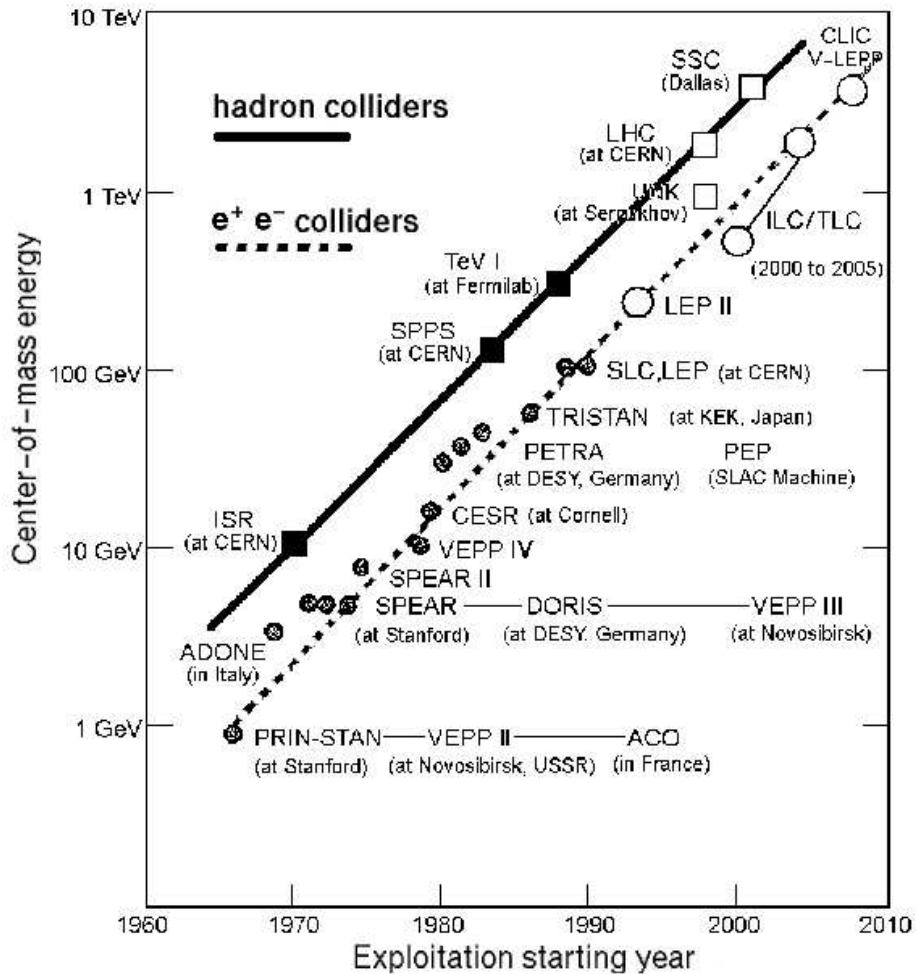


Figure 2.1: Center-of-mass energy evolution in e^+e^- and hadrons colliders. The SSC project has been abandoned.

their very high cost were the principal motivations for the creation of an international collaboration.

The Large Hadron Collider (LHC) is a 27 km circular accelerator build in the tunnel of the ancient LEP collider and will be operative in the current of 2007. It is the last link of a chain of machines in which protons are accelerated up to a kinetic energy of 7 TeV. The whole complex is described in figure 2.2. At first, protons are accelerated by a linear accelerator (LINAC) up to 50 MeV. Then, two successive circular accelerators boost the particles up to 1 GeV (Booster PSB) and 26 GeV (Proton Synchrotron PS). The protons enter a third circular accelerator (Super Proton Synchrotron SPS) in order to reach an energy of 450 GeV. The proton beam is then

separated into two parts which enter the LHC in two separate concentric beams and in the opposite directions, and which are accelerated until they reach an energy of 7 TeV each. Each beam is constituted of packets of $\sim 10^{11}$ protons called *bunches*. These are separated in time by 25 ns giving a nominal LHC bunch crossing frequency of 40 MHz. They travel at almost the speed of light, hence the distance between two packets is 7.5 m. In a ring of 27 km, 3'600 bunches can be placed but LHC plans to use only 2'808 due to the complexity of the injection system. In order to keep the particles along the circular trajectory, a strong magnetic field of 8.3 T is applied. It is provided by a single superconducting magnet operating at a cryogenic temperature of 1.9 K which embedded the two beam pipes. Also shown in figure 2.2 are the four interaction points where are located the CERN experiments. At these points, the protons collide at a center of mass energy $\sqrt{s} = 14$ TeV giving a nominal luminosity $\mathcal{L}^{\text{LHC}} = 10^{34} \text{ cm}^{-2} \text{ s}^{-1}$.

Maintaining such a value is a challenge due to several undesirable phenomena which tend to perturb the system. The first limitation is due to mechanical instabilities in keeping a very well focused beam at the collision point. The transversal section of the two beams is $\sim 17 \mu\text{m}$ rms, which requires a focusing capability of the magnet of the same order. The second limitation is a physical constraint. Due to its positive charge, a bunch from a beam emits an electromagnetic field which deflects the protons belonging to the opposite beam. The protons are therefore pushed back from each other at each crossing. These deflections accumulate turn after turn in such a way that the beams have to be refurbished in counterpart of the possible particle loss in order to keep exactly the required beam density. Thirdly, the electromagnetic field also disturbs the trajectory of particles of the succeeding bunches in the same beam. This is called the *electromagnetic wake-field* and it can also lead to particle loss. Countermeasures have to be taken in order to reduce this effect.

At interaction point IP1 and IP5 stand ATLAS (A Toroidal LHC Apparatus System) and CMS (Compact Muon Solenoid) respectively [13, 14]. They are two general-purpose experiments which aim to study several subjects in high energy particles physics, in particular the electroweak interaction symmetry breaking through the Higgs mechanism. The detectors are designed to discover the Higgs particle as well as a host of new particles, such as supersymmetric partners of the standard family of elementary particles, and therefore adopt a 4π geometry. The collisions will also produce a large amount of top quarks, W^\pm and Z^0 bosons and will be a B physics factory. At IP2 stands ALICE (A Large Ion Collider Experiment) which is dedicated to the study of quark-gluon plasma (QGP), a new state of matter rising in heavy ions collisions at high energy [15]. For that purpose, the LHC also provides Pb-Pb collisions. The fourth LHC experiment is LHCb (Large Hadron Collider Beauty experiment) located at IP8 [16]. Its goal is the understanding of the matter-antimatter asymmetry in the Universe through the study of CP violation in B -mesons systems.

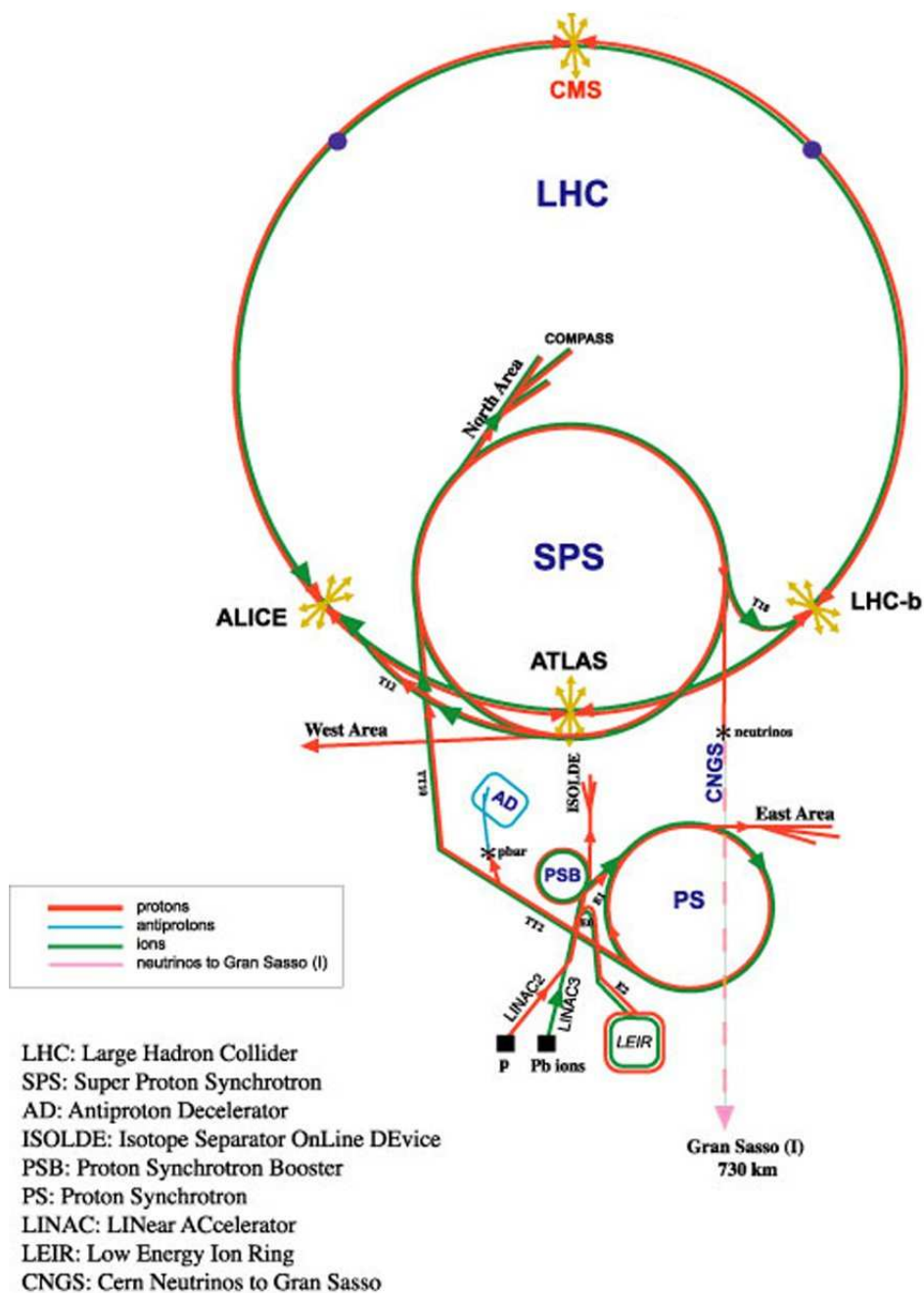


Figure 2.2: The LHC accelerator complex (not to scale) [12].

2.2 The LHCb experiment

The LHCb experiment is optimized to exploit the large number of b -quarks produced at LHC in order to make precision studies of CP violation and other rare phenomena in B -hadron decays [17, 18]. In order to obtain an average of one p - p interaction per crossing, the LHCb luminosity is set to $\mathcal{L}^{\text{LHCb}} = 2 \cdot 10^{32} \text{ cm}^{-2} \text{ s}^{-1}$. This reduced value compared to the LHC nominal luminosity is achieved by less focusing the beams locally. In p - p collisions, the predominant production mechanism of $b\bar{b}$ quarks pairs is the gluon fusion. At first order, the protons partons radiate two gluons which interact together to create a pair of quarks. Another important mechanism is the quark fusion where a quark and an antiquark from the protons annihilate to form a gluon which creates a pair of quarks. These two mechanisms are pictured in figure 2.3:



Figure 2.3: Dominant $b\bar{b}$ quarks pairs production mechanisms in p - p collisions.

The estimated $b\bar{b}$ production cross-section is $\sigma_{b\bar{b}} = 500 \mu\text{b}$ at $\sqrt{s} = 14 \text{ TeV}$ giving a production rate of 100 kHz. At this energy, the b - and \bar{b} -hadrons are emitted predominantly in the same forward or backward cone in the p - p center-of-mass referential. Figure 2.4 shows the correlation between the polar emission angles θ_b and $\theta_{\bar{b}}$ of such b -particles, defined with respect to the beam axis in the p - p rest frame, as simulated by the PYTHIA event generator. This property is exploited for the flavour tagging but also for the detector geometry. It is a single-arm spectrometer with a forward angular coverage from about 15 mrad to 300 (250) mrad in the bending (non-bending) plane. In terms of the pseudorapidity η defined as:

$$\eta = -\ln \left(\tan \frac{\theta}{2} \right)$$

this corresponds to a range comprised between 1.9 (2.1) and 4.9.

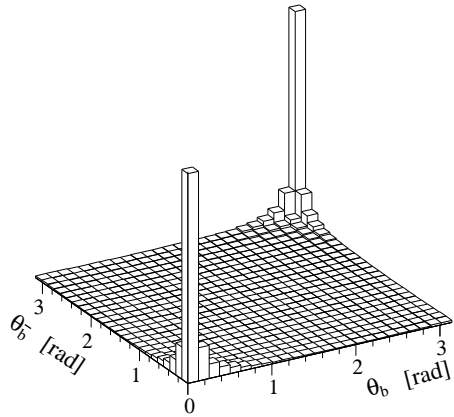


Figure 2.4: Polar angles of the b - and \bar{b} -hadrons calculated by the PYTHIA event generator.

LHCb stands at Interaction Point 8 previously allocated to the DELPHI experiment during the LEP era. In order to avoid expensive infrastructure modifications, the dimensional characteristics of the detector have been adapted to the existing cavern. The detector layout is presented in figure 2.5. A right-handed coordinate system is defined with the interaction point at origin, z along the beam axis and x and y being the horizontal and vertical coordinates in the beam axis transverse plane respectively. The detector is ~ 20 m long (z -axis) and ~ 10 m wide (x - and y -axis). It consists of a vertex detector system used to reconstruct vertices displaced from the interaction point, a magnet and a four tracking stations for the measurement of charged particles momentum, Cherenkov detectors for particle identification, an electromagnetic calorimeter, a hadron calorimeter and a muon detector. Not shown in figure 2.5 are the front-end readout electronics and the data acquisition system. A further description of each sub-system is given hereafter.

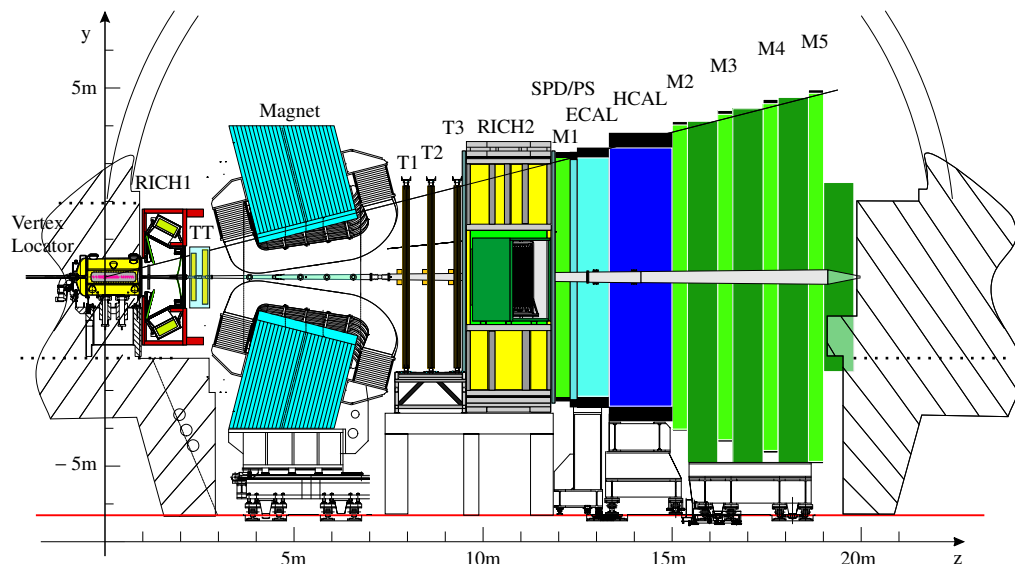


Figure 2.5: Layout of the LHCb detector in the non-bending (vertical) plane [18].

2.2.1 Vertex Locator

The Vertex Locator (VeLo) is a solid-state detector that provides precise measurements of the primary and secondary vertices close to the interaction region [19]. The b -hadrons lifetime $\tau_B \sim 1.5 \cdot 10^{-12}$ s and their Lorentz boost parameter $\gamma \sim 10 - 100$ let them cover a distance $d = \gamma c \tau$ of a few centimeters, decaying thereby predominantly inside the VeLo. Their decay products tracks should converge to a vertex

displaced from the interaction point. A precise track reconstruction in this region is therefore important to get reliable informations on the b -hadrons decay lengths and their decay products impact parameters.

When a charged particle crosses a semiconductor, it loses an energy ΔE used to create N pairs of electron-hole. The necessary energy for a pair creation $w = \frac{\Delta E}{N}$ depends only, at first approximation, on the semiconductor nature but not on the incident particle characteristics ($w = 3.62$ eV for silicon). Applying an electric field on the semiconductor moves the created charges, giving birth to an electric current which can be amplified and exploited. The measurement of this impulse is the base of the detection principle.

The VeLo layout consists of 21 stations disposed along the beam (z -axis), each composed of two $220 \mu\text{m}$ thick n -on- n silicon strip detectors. These are positioned perpendicularly to the beam and measure the circular r and radial ϕ coordinates of charged particles passage (see figure 2.6). Each r and ϕ disk consists of two half-circular sensors with 2'048 strips each, as presented in figure 2.7, giving a total number of channels of $2'048 \cdot 2 \cdot 2 \cdot 21 = 172'032$. An average of 7 stations are crossed by a track. The tracks are reconstructed from the polar coordinates collected in at least three stations. The spatial resolution depends on the number of tracks but is in average of $42 \mu\text{m}$ on the z -axis and $10 \mu\text{m}$ in the x - y transverse plane. The impact parameter resolution is $\sigma_{IP} < 30 \mu\text{m}$ for high transverse momentum particles. The precision on the decay length is $\sim 300 \mu\text{m}$ which corresponds to ~ 10 - 100 fs on the proper time of flight.

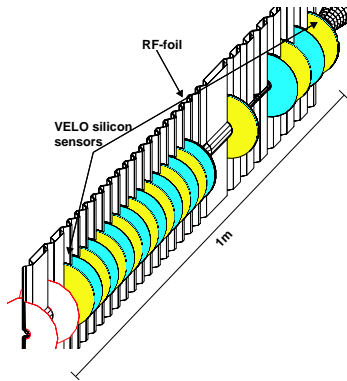


Figure 2.6: Arrangements of silicon sensors along the beam axis with the RF-foil, which separates the LHC vacuum from the detector vacuum. The first two disks (blank) belong to the Pile-Up system [18].

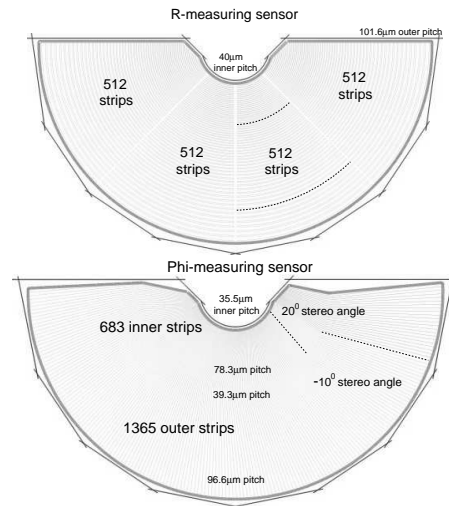


Figure 2.7: r (up) and ϕ (down) sensor layouts. Some strips are indicated with dotted lines for illustration [18].

The radial distance from the beam being smaller than the aperture required by the LHC during injection, the stations must be retractable. For that purpose, they are mounted in Roman Pots. Inside the detector, the beam pipe is replaced with a thin aluminium box which separates the LHC vacuum from the VeLo vacuum. It also acts as a shield against RF pick up from the beam. The assembled detector is shown in figure 2.8:

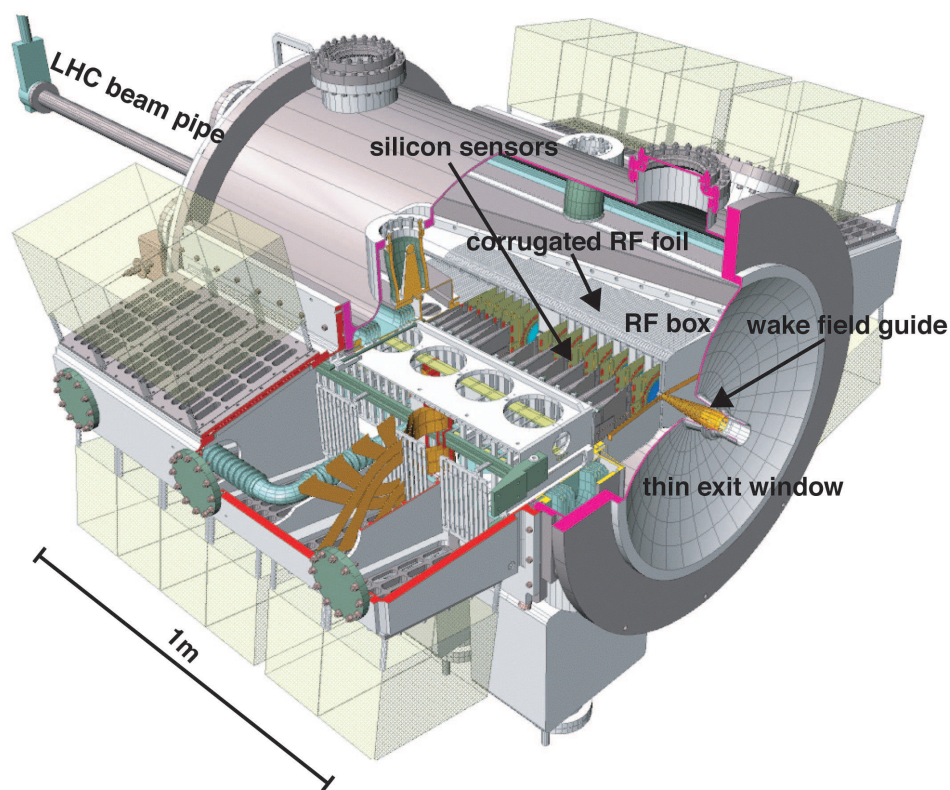


Figure 2.8: The VELO detector assembled. The vacuum vessel with the silicon sensors and the RF box is shown [18].

In figure 2.6, two blank disks placed upstream of the 21 stations can be seen. This is the Pile-Up Veto counter. It counts the number of primary vertices in order to suppress events containing multiple p - p interactions in a single bunch-crossing during the Level-0 trigger (see § 2.2.8). 80% of double interactions are rejected while 95% of single interactions are kept. Simulations have exhibited a primary vertex reconstruction with a resolution of 1 mm along the z -axis.

2.2.2 Magnet

The LHCb magnet is a dipole solenoid which provides an integral magnetic field of 4 Tm with high homogeneity with a maximal value of 1.1 T [20]. It is oriented vertically and its polarity can be inverted in order to reduce systematic errors in CP-violation measurements that could result from a left-right asymmetry of the detector. It consists of two trapezoidal coils made of 50 tons of aluminium conductors and bent at 45° on the two transverse sides (see figure 2.9). They are arranged inside a 1'450 tons iron yoke. The pole faces are shaped in both vertical and horizontal planes to follow the detector acceptance. The VeLo - which stands in the upstream part of the detector with respect to the magnet - benefits from the fringe magnetic field to allow an early momentum analysis for the trigger process.

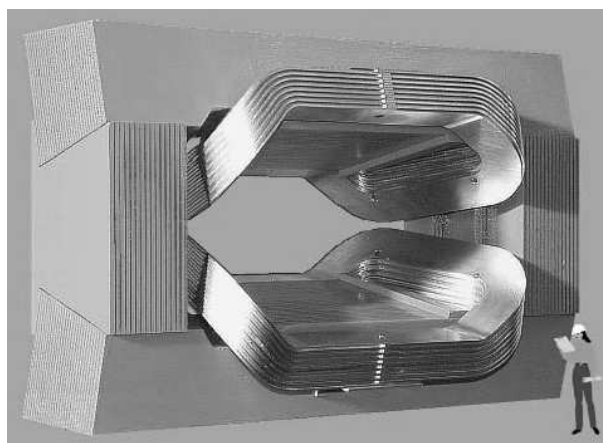


Figure 2.9: The LHCb magnet.

2.2.3 RICH detectors

Two Ring Imaging CHerenkov detectors (RICH) provide hadron identification [21]. The Cherenkov effect appears when a charged particle traverses a transparent medium with refraction index n at a speed v larger than the speed of light in this medium $v > c/n$. The consequence is an asymmetric polarization of the medium along the particle path created by the electric field of the charged particle. During a time interval Δt , the particle travels a distance $v \cdot \Delta t$ while the radiation propagates $c/n \cdot \Delta t$. As shown in figure 2.10, this produces a cone of light - called *Cherenkov light* - which aperture angle θ is given by:

$$\cos \theta = \frac{c/n \cdot \Delta t}{v \cdot \Delta t} = \frac{c}{nv} = \frac{1}{\beta n} \quad \text{with} \quad \beta = \frac{v}{c}$$

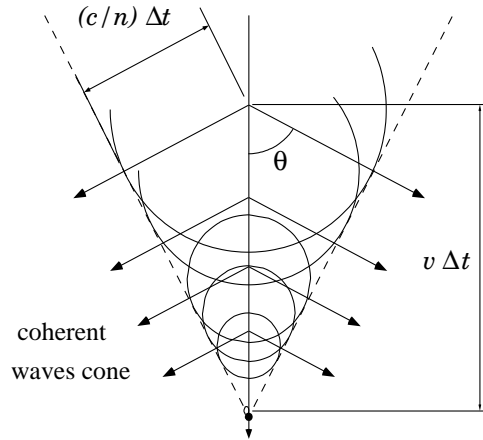


Figure 2.10: Cherenkov cone of light [22].

The image is captured by pixelated Hybrid Photon Detectors (HPD). Particles with low momentum between 1 and 60 GeV/ c are identified by the RICH1 located upstream of the LHCb magnet between the VeLo and the TT. It consists of silica aerogel ($n = 1.03$) and fluorocarbon C₄F₁₀ gas radiators ($n = 1.0014$). Higher momentum particles (up to ~ 100 GeV/ c) are identified by the RICH2 detector situated downstream of the magnet just after the tracking stations T1-T3. It is filled with a CF₄ radiator ($n = 1.0005$).

2.2.4 Tracking system

The tracking system provides efficient reconstruction and precise momentum measurements of charged tracks [23, 24]. It also indicates track directions for ring reconstruction in the RICH and informations for the Level-1 and High Level triggers. It consists of four stations. The first one is the Trigger Tracker (TT) located between the RICH1 and the LHCb magnet. It aims to assign transverse momentum informations to large impact parameter tracks for the Level-1 trigger. Furthermore, it is used in the offline analysis to reconstruct the trajectories of long-lived neutral particles that decay outside of the volume of the VeLo and of low-momentum particles that are bent out of the acceptance of the experiment before reaching the other tracking stations. The TT is made of four silicon layers arranged in two pairs. The first and fourth layers have vertical readout strips, while the second and third layers strips are rotated by a stereo angle of $+5^\circ$ and -5° respectively. Between the magnet and the RICH2 stand the three other tracking stations T1-T3 which are split in Inner and Outer Trackers. As for the TT station, silicon strip sensors are used in the inner part due to the expected high track density. For the Outer Tracker, layers of straw drift-tubes are used where each drift cell has an inner diameter of 5 mm.

The drift gas is a Ar/CF₄/COF₂ mixture for an optimal drift speed. The expected momentum resolution is $\sim 0.3\%$ for momenta from 5 to 200 GeV/ c , limited mainly by multiple scattering.

2.2.5 Calorimeters

The calorimeters identify photons, electrons and hadrons and provide measurements of their position and energy [25]. These informations are used for the Level-0 trigger and have to be supplied with sufficient selectivity and very short latency. The ultimate performances for hadron and electron identification are obtained during the offline analysis.

The Scintillator Pad Detector (SPD) plane is the first part of the calorimeter system. It is located downstream from the RICH2 and aims to reduce the high E_T π^0 tail background for the electron Level-0 trigger. The Pre-Shower (PS) stands just after the SPD. It allows to separate between photon and electron electromagnetic showers and to reject the high background of charged pions. Both SPD and PS are 15 mm thick scintillators which are separated from each other by a 12 mm thick lead wall. Then, the Electromagnetic CALorimeter (ECAL) measures the energy of photons and electrons. It is a structure of 2 mm thick lead sheets interspersed with 4 mm thick scintillator plates and uses the recent development of the Shashlik technology. Finally, the Hadronic CALorimeter (HCAL) measures the energy of hadrons. It is a structure of 4 mm thick scintillating tiles placed parallel to the beam every 16 mm of iron.

2.2.6 Muon detector

The Muon detector provides informations mainly for the Level-0 trigger and also for the offline muon identification [26]. The earliest trigger level requires the candidate muons to have high transverse momentum. These fundamental requirements are imposed by the fact that muons are present in the final states of many CP-sensitive B decays. The long muons lifetime $\tau_\mu = 2.2 \mu\text{s}$ and their low interaction probability allow them to traverse the whole LHCb detector. Therefore, the muon chamber is located at the end of the sub-detectors chain. It consists of a special station M1 placed upstream of the calorimeters which measures the transverse momentum for the Level-0 trigger plus four other stations M2-M5 located after the HCAL along the beam axis. The stations are made of multi-wire proportional chambers (MWPC) and are interspersed with iron shields to attenuate hadrons, electrons and photons. To trigger, a candidate muon must hit all 5 muon stations and have a momentum larger than 5 GeV/ c . Hits in the first two stations are used to calculate the candidate muon transverse momentum.

2.2.7 Front-end electronics and data acquisition system

The Beetle [27] is a front-end chip developed for the VeLo and the IT data acquisition systems of LHCb. It collects the charges from 128 detector channels at a rate of 40 MHz (25 ns samples). Due to the heavy radiation in the LHCb cavern, this chip is made with rad-hard technology in order to work for several years. After collection, the 128 analogue levels corresponding to an event are preamplified and shaped. They are stored in one of the 187 cells of the pipeline at an average rate of 1 MHz awaiting for a Level-0 trigger accept. Once it occurs, the data are passed through a 16 stages derandomizing buffer, multiplexed and transmitted to the Level-1 off-detector electronics. This part stands in the counting room, a radiation free area at about 60 m from the detector, in such a way that standard components can be used. Except for the VeLo, data are transmitted through optical fibers. In the specific case of the VeLo, the data transmission is done in analogue mode via copper lines. The line induces a loss of the amplitude, modifications in the frequency spectrum and possible electric noise pick-up. Therefore, a differential transmission is used and a line driver is inserted between the Beetle and the line to amplify the analogue signal and also to correct the frequency response of the system.

The Level-1 off-detector electronics was originally developed for the VeLo but is now adopted by other sub-detectors such as the tracking system (TT, IT and OT), the calorimeters (ECAL and HCAL) and the muon detector. Its common name is Trigger ELectronics Level-1 board (TELL1) [28]. It aims to synchronize the events data dispatched over several links, to check the data integrity, to perform zero suppression and to find clusters. In order to suit all the configurations requested by the different sub-systems, it accepts input mezzanine cards containing either analogue inputs with Fast Analog-to-Digital Converters (FADC) or optical receivers. Field Programmable Gate Arrays (FPGA) are used to implement processing algorithms. The data are transferred to the Level-1 trigger through Gigabit Ethernet connections at an average rate of 40 kHz. The last stage of data processing is the High Level Trigger where the complete event is reconstructed (see § 2.2.8).

The whole LHCb experiment is controlled by a specific system, the Timing and Fast Control (TFC) [29], based on the LHC Timing, Trigger and Control (TTC) system [30]. It differs from the other LHC experiments because it has to support two levels of high rate triggers. It provides clocks and fast signals such as trigger decisions, reset and synchronization commands via an optical transmission system.

The Experiment Control System (ECS) [31] is in charge of the configuration, control and monitoring of all the components of the online system. It communicates the running parameters such as pedestal values, temperatures, etc... to the different subsystems. It is also used to transmit debugging and error signals.

2.2.8 LHCb trigger system

At LHC, a p - p collision occurs every 25 ns. Knowing that a typical event at LHCb with informations from all the sub-detectors requires about 25 kBytes for storage after zero-suppression [32], recording every events would lead to a huge rate of 1 TBytes per second. This is clearly not achievable and a procedure has to be applied in order to reject uninteresting events and keep only the most relevant. This is the task of the trigger system [33].

The nominal LHC bunch crossing rate is 40 MHz. At a luminosity of $\mathcal{L}^{\text{LHCb}} = 2 \cdot 10^{32} \text{ cm}^{-2} \text{ s}^{-1}$, 25% of these interactions are considered as visible, which means that they produce at least two charged particles with sufficient hits in the VeLo and the tracking system to be reconstructible. This rate decreases to ~ 100 kHz by considering only the events containing a $b\bar{b}$ pair. Furthermore, only 15% have at least one B -meson with all its decay products contained in the LHCb detector acceptance. The branching ratio of B -mesons used for CP violation studies is typically of $\mathcal{O}(10^{-3})$ leading to an acceptable rate of a few events per second. This reduction is achieved by the LHCb trigger system which is split in three stages: Level-0 (L0), Level-1 (L1) and the High Level Trigger (HLT). L0 is implemented in custom electronics, while L1 and HLT are software triggers executed on a cluster of 1'800 CPUs farm located in the counting room.

An overview of the sub-detectors contributions to the three trigger levels is shown in figure 2.11 and a short description of the selection criteria applied in each stages is given hereafter.

Level-0 trigger

The L0 trigger reduces the 40 MHz LHC bunch crossing rate down to 1 MHz. At this rate, the readout of every LHCb sub-systems could in principle be done, allowing their participation to the Level-1 trigger decision. Its latency, which is the time elapsed between a p - p interaction and the arrival of the decision, is fixed to $4 \mu\text{s}$. It includes the time-of-flight, cable length and all delays in the L0-electronics plus a $2 \mu\text{s}$ delay for the data processing. Motivated by the fact that large mass B -hadron decays give a lepton, a photon or a hadron with large transverse energy E_T or momentum p_T , L0 reconstructs:

- the highest E_T electron, photon and hadron clusters in the calorimeters (SPD, PS, ECAL and HCAL)
- the two highest p_T muons in the Muon detector (M1-M5)

To be accepted, an event has to provide an electron with $E_T > 2.8$ GeV, a photon with $E_T > 2.6$ GeV and a hadron with $E_T > 3.6$ GeV, plus a single muon

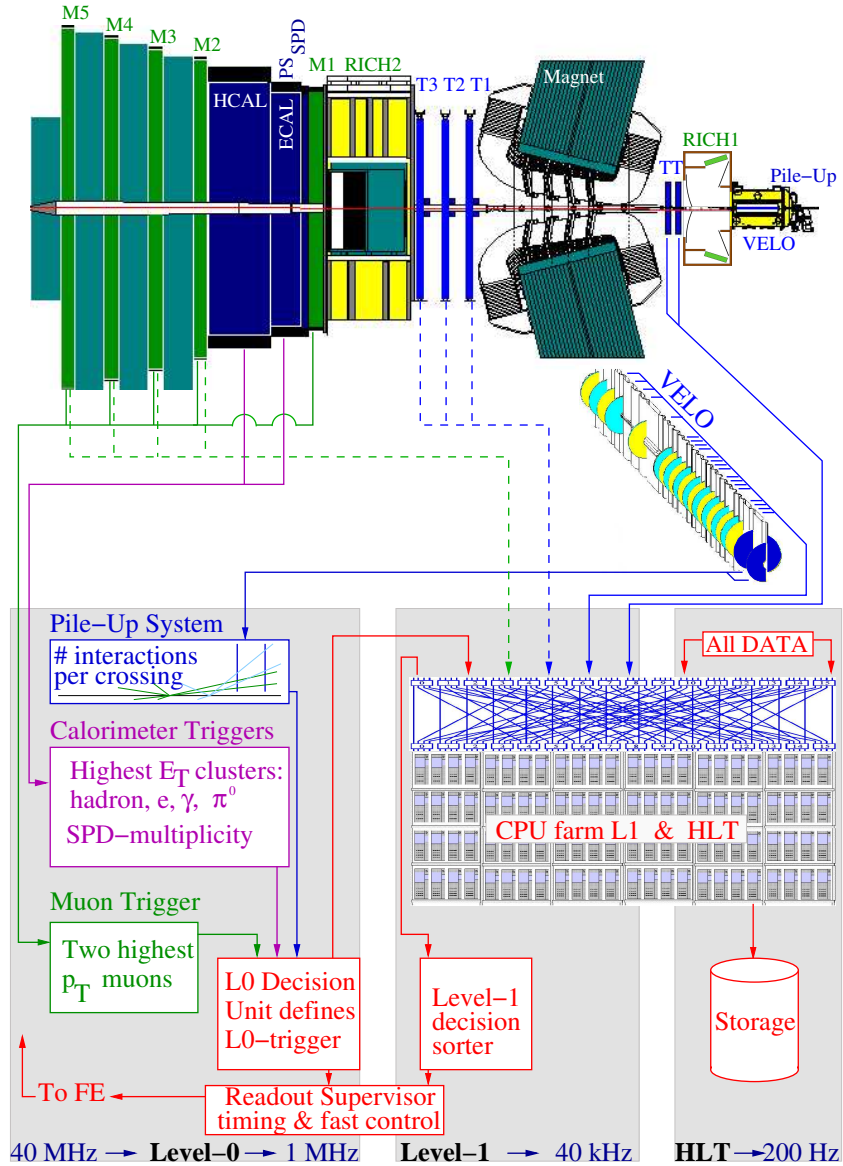


Figure 2.11: Overview of the sub-detectors contributions to the three trigger levels. The SPD, PS, ECAL and HCAL are used to reconstruct the hadron, e , γ and π^0 with the largest E_T , the charged particle multiplicity, and the total energy. Stations M1-M5 are used to reconstruct the two highest p_T muons. The Pile-Up system included in the VeLo discards events with multiple interactions. L0 decreases the event rate from 40 MHz to 1 MHz. Informations from the VELO, TT, and L0 are used for the L1 trigger which reduces the rate to 40 kHz. Full event reconstruction using data from all sub-detectors except the RICH are used for the HLT. A final rate of 200 Hz is obtained for storage.

with $p_T > 1.1$ GeV or several muons with $p_T > 1.3$ GeV. The Pile-Up system, located in the VeLo (see § 2.2.1), acts as a veto to eliminate events with multiple visible interactions. In addition, global event variables such as charged track multiplicities ensure that the selection is based on b -signatures rather than large combinatorics. All the informations are finally collected by the Level-0 Decision Unit (L0DU) which delivers a decision to the Readout Supervisor every 25 ns.

Level-1 trigger

The L1 trigger reduces the 1 MHz L0 output rate to a maximum of 40 kHz. The events selection is based on tracks with large transverse momentum and significant impact parameter with respect to the primary vertex. The L1 algorithm uses informations from the L0 trigger, the VeLo and the TT. Tracks in the VeLo are reconstructed (see § 2.2.1) and matched to the L0 muons or Calorimeter clusters for identification. Secondary vertices with an impact parameter comprised between $150 \mu\text{m}$ and 3 mm are sought, which is a hint for B -hadron decays. The fringe magnetic field between the VeLo and the TT allows to determine their momenta. All sub-systems used for the L1 trigger use the TELL1 board (see § 2.2.7) to store the data in the L1-buffer and to perform zero-suppression and formatting. The L1 trigger delivers a decision to the Readout Supervisor for each event with a variable latency.

High level trigger

The HLT reaches an output rate of 200 Hz. It uses data from all sub-detectors except the RICH. The algorithm performs a second reconstruction of the VeLo tracks and the primary vertex after the L1 trigger one. These tracks are then matched to the ones in the tracking stations T1-T3 with a fast pattern recognition program. The final selection is a combination of confirming the L1 decision with better resolution and selection cuts dedicated to channels which are considered as specially important for the physics analysis.

The HLT and L1 trigger run concurrently on the same processor nodes. L1 has a latency constrained by the trigger system requirements and takes the priority over the HLT algorithm. They use respectively about $\sim 55\%$ and 25% of the computing resources, leaving $\sim 20\%$ to fully reconstruct events accepted by the HLT, including the particle identification, before storage.

In summary, the LHCb trigger aims to reduce the number of events from the 40 MHz nominal LHC bunch crossing rate to a more manageable rate of 200 Hz. In terms of storage facilities, 25 kBytes are necessary for an event after zero-suppression [32]. At the nominal LHC rate, this would lead to 1 TBytes/s which,

as previously said, is not conceivable. L0 and L1 reduce successively this throughput to 25 GBytes/s and 1 GBytes/s respectively. After the HLT, a reasonable rate of 5 MBytes/s is finally reached.

Notice:

The trigger system given in the above description has been modified since the development presented in this thesis was performed. In the final configuration, the L0 trigger is conserved as described while the L1 trigger has been integrated in the HLT which is therefore the second and last level of trigger of LHCb [34]. The HLT aims to reduce the 1 MHz L0 output rate to 2kHz. It consists of a C++ application running on the Event Filter Farm (EFF), which contains about 1'800 computing nodes. It has access to all sub-detectors data, but given the 1 MHz output rate of the L0 trigger and the limited CPU power available, it rejects the bulk of the events by using only part of the full information.

The flow-diagram of the different trigger sequences in the HLT is pictured in figure 2.12. Basically, it is a succession of four so-called “alleys”. At the start of an alley, it is checked if the L0 trigger was based on either the muon system, the HCAL or the ECAL. Most L0 triggers ($\sim 85\%$) are only selected due to one L0 trigger type and hence are only processed by one alley. The others are selected by multiple triggers and are consequently processed by several alleys. The first aim of the alleys is to confirm the L0 objects with better resolution by matching them to at least one tracking sub-detector, i.e. the VeLo and/or the tracking stations T1-T3. If the L0 object is confirmed, additional candidate B -decay tracks are reconstructed using the VeLo informations. For each alley, a summary containing informations about the tracks and vertices responsible for the trigger is written to storage for accepted events. Finally, the inclusive and exclusive selections use cuts on invariant mass and precise pointing cuts to a primary vertex to reduce the rate down to 2 kHz, corresponding to 50 MBytes/s, the rate at which the data are stored for further analysis.

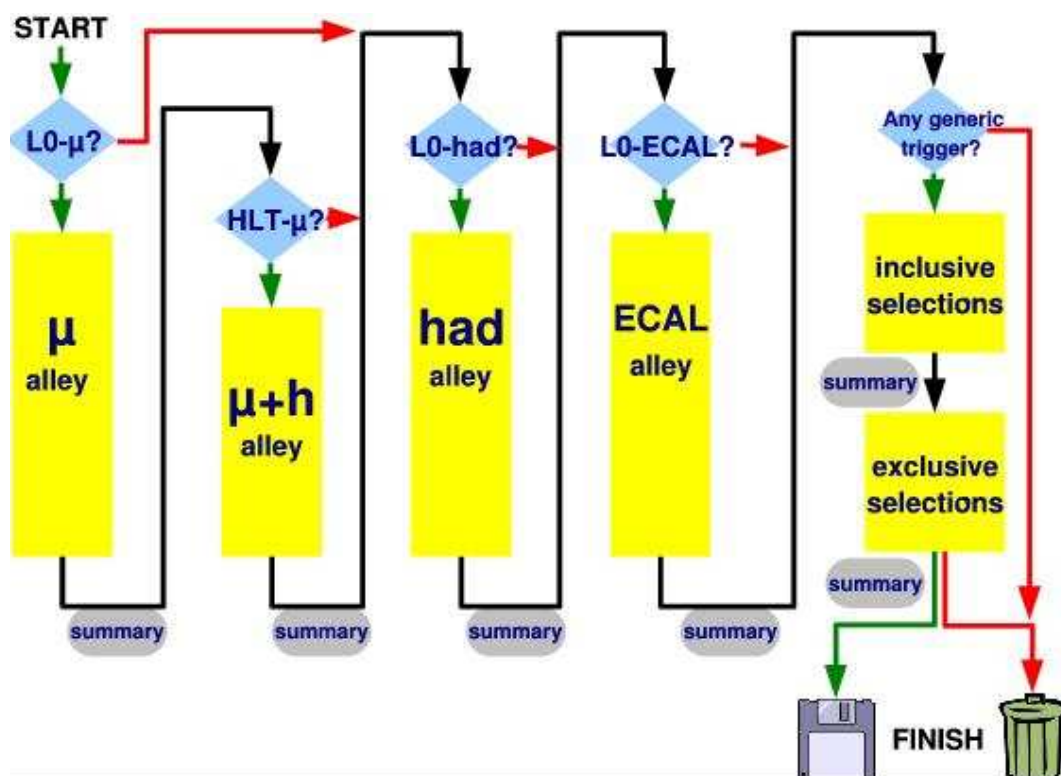


Figure 2.12: Flow-diagram of the different trigger sequences in the HLT. The four “muon”, “muon + hadron”, “hadron” and “ECAL” alleys and the final inclusive and exclusive selections (yellow squares) are implemented in reconstruction algorithms.

Chapter 3

Higgs boson search in LHCb

3.1 Introduction

One of the actual greatest challenges in High Energy Physics is the discovery of the Higgs boson. As explained in § 1.3.1, 1.3.2 and 1.3.3, the Higgs boson is responsible for the mass generation of the Standard Model particles through the mechanism of Spontaneous Symmetry Breaking. Its mass is not known and cannot be predicted by the theory. However the recent results of LEP at CERN have shown a lower limit $m_{H^0} > 114 \text{ GeV}/c^2$. Likewise, below $\sim 150 \text{ GeV}/c^2$, the Higgs decay into two b -quarks $H^0 \rightarrow b\bar{b}$ dominates. In the Higgs rest frame, the two quarks are emitted back-to-back. During the so-called “parton shower”, gluons are emitted from the b -quarks and a string is formed in-between them due to the strong interaction manifestation. When the string fragments, hadrons are created - among which those containing the b - and \bar{b} -quarks - and propagate under the form of jets, as pictured in figure 3.1 At LHC, p - p collisions produce particles with a high longitudinal boost. Because of this, a considerable part of the light Higgs ($\sim 30\%$) are emitted under quite small polar angles and fit inside the LHCb acceptance $1.8 < \eta < 4.9$. Furthermore the LHC luminosity will be increased only progressively during the four first years of exploitation until it reaches its nominal value $\mathcal{L}^{\text{LHC}} = 10^{34} \text{ cm}^{-2} \text{ s}^{-1}$. The LHCb experiment will profit from its nominal luminosity $\mathcal{L}^{\text{LHCb}} = 2 \cdot 10^{32} \text{ cm}^{-2} \text{ s}^{-1}$ from the beginning, with a potentiality for the discovery of the Standard Model Higgs boson that will be discussed in the following.

The aim of this research work is precisely to assess the feasibility to observe such a light Higgs boson at LHCb by using the detector capability to identify b -hadrons. In our case, this information will be used to reconstruct b -jets. The study is focused on the mechanisms in which the Higgs boson is produced in association with a gauge boson decaying leptonically $H^0 + W^\pm \rightarrow b\bar{b} + \ell \nu_\ell$ and $H^0 + Z^0 \rightarrow b\bar{b} + \ell^+ \ell^-$ (see figure 1.9 (c)) for Higgs masses in the range 100 - 130 GeV/c^2 . The gauge

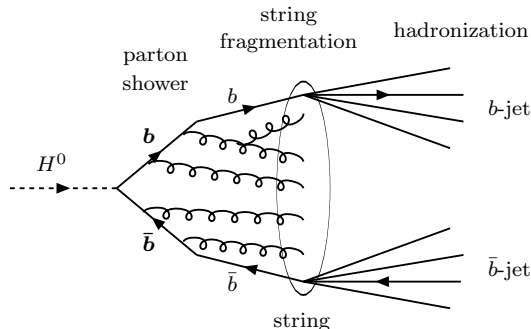


Figure 3.1: Representation of the Higgs decay $H^0 \rightarrow b\bar{b}$. During the parton shower, gluons are emitted and form a string together with the b -quarks. The string fragments and its components hadronize under the form of b -jets containing the b -hadrons. Low p_T b -jets present an energy loss with respect to the initial b -quarks.

bosons decay produces hard leptons quite often isolated from the b -jets. Hence, an isolated lepton with high transverse momentum is required in order to reject the large QCD background. Two different jet reconstruction algorithms are used. The cone algorithm considers a specific seed around which a virtual cone is built. Jets are computed using the particles contained in the cone. The K_T algorithm reconstructs jets by associating particles with nearly parallel momenta considering that they belong to the same jet.

In parallel to the Higgs signal, several important background channels which also provide two b -quarks and an isolated lepton ($t\bar{t} \rightarrow W^+b W^-\bar{b}$, the irreducible backgrounds $Z^0 + W^\pm \rightarrow b\bar{b} + \ell\nu_\ell$ and $Z^0 + Z^0 \rightarrow b\bar{b} + \ell^+\ell^-$, $W^\pm + b$ -jets, $Z^0 + b$ -jets and generic $b\bar{b}$) are also studied. The idea is to find observables which behave differently for backgrounds and Higgs signal and to exploit these differences. In particular, we will use neural network techniques to discriminate background from signal.

Section 3.2 presents the general scheme for the production of Monte Carlo events for the Higgs signal and backgrounds with a description of the parameters used for the generator. The LHCb detector fast simulation is described in section 3.3. The events selection procedure is presented in section 3.4. In particular, the selection of the lepton from the associated gauge boson W^\pm/Z^0 is discussed in § 3.4.2 and the successive cuts applied to select the signal events are enumerated in § 3.4.3. The jet reconstruction algorithms are described in section 3.5 together with a comparison of their performances in terms of Higgs mass resolution. In section 3.6, a jet energy

correction procedure is presented. In particular, the origin of the observed energy loss in low transverse momentum jets is studied. Section 3.7 reports investigations for discriminant topological variables in perspective of their use in the framework of neural network techniques to further reject the background. During this study, we observed an asymmetry in the MC events between the b - and \bar{b} -jets pseudorapidity distributions for $Z^0 \rightarrow b\bar{b}$ events in the irreducible background. This will be discussed in § 3.7.1. The reconstruction of the primary off-shell gauge boson is attempted and kinematics discriminant observables in its referential are explored in § 3.7.2. The neural network strategy is presented in section 3.8; the performances for $t\bar{t}$ and irreducible backgrounds suppression are reported in § 3.8.3.

3.2 Generation of Higgs and background events with PYTHIA

For this study, the standalone computer program PYTHIA version 6.325 [35] is used to generate signal and background events. Proton-proton collisions are simulated at a center-of-mass energy $\sqrt{s} = 14$ TeV. The generator uses the string fragmentation scheme (MSTJ(1)=1) according to the Lund model [36] and allows initial-state (MSTP(61)=1) and final-state (MSTP(71)=1) QCD and QED radiations. It includes up to next-to-leading order QCD corrections. A multitude of event types can be produced by setting the different configuration parameters offered by the software. In accord with the LHCb generator group, the settings presented in table 3.1 are used. MSTP(2) is used to set a second order calculation mode for α_s . With MSTP(33) a K factor is included in hard cross-sections for parton-parton interaction by shifting $\alpha_s(Q^2)$ to $\alpha_s(K \cdot Q^2)$. MSTP(51) specifies the parton density functions used for the calculations. The Les Houches Accord Parton Density Functions LHAPDF version 4 CTEQ4L library is activated [37]. MSTP(82) affects the structure of multiple interactions. PARP(82) sets the regularization scale p_{T0} of the transverse momentum spectrum for multiple interactions at the reference energy scale defined by PARP(89) and with the degree of energy rescaling given by PARP(90). PARJ(13-17) are probability parameters which determine the spin of mesons when formed in fragmentation or decays.

The physics processes allowed in the simulation are specified by the MSUB parameters. Among these, of particular interest are MSUB(91-94) which concern the elastic scattering, the single and double diffractions and MSUB(95) which allows low p_T scattering in soft QCD processes. The absence of low p_T production can lead to divergent cross-sections.

In order to check the consistency of our setup with the official LHCb one [38], we have generated a set of 10^6 events for the physics processes listed in table 3.2. The

parameter	value	explanation
MSTP(2)	2	2 nd -order running α_s
MSTP(33)	3	$\alpha_s(Q^2) \rightarrow \alpha_s(K \cdot Q^2)$ where K is PARP(33)
MSTP(51)	19170	CTEQ4L LHAPDF
MSTP(52)	2	choice of external PDF
MSTP(82)	3	structure of multiple interactions
MSTP(128)	2	resonance decay products not stored
PARP(82)	3.47	p_{T0} regularization scale
PARP(89)	14000.0	reference energy scale
PARP(90)	0.174	degree of energy rescaling term
PARJ(13)	0.750	probability that a charm or heavier meson has spin 1
PARJ(14)	0.162	probability that a spin 0 meson is produced with an orbital angular momentum 1, for a total spin 1
PARJ(15)	0.018	probability that a spin 1 meson is produced with an orbital angular momentum 1, for a total spin 0
PARJ(16)	0.054	probability that a spin 1 meson is produced with an orbital angular momentum 1, for a total spin 1
PARJ(17)	0.090	probability that a spin 1 meson is produced with an orbital angular momentum 1, for a total spin 2

Table 3.1: PYTHIA 6.325 most relevant configuration parameters used for the events generation in accord with the LHCb production group. These settings are contained in the options file `$GAUSSOPTS/PythiaSettings.opts`.

parameters given in table 3.1 are used, in particular the CTEQ4L LHAPDF library. A second similar set using the CTEQ6L LHAPDF library has also been produced. The production cross-sections are compared to the ones obtained by the LHCb production working group for the same processes with the same generator and the CTEQ6L LHAPDF library [38]. The results presented in table 3.2 are in accordance with the official LHCb ones which ensures the consistency of our generation system.

As previously mentioned, for the Higgs study, we concentrate exclusively on the associated production in which a W^\pm or a Z^0 is produced together with a H^0 (see figure 1.9 (c)). The H^0 is produced with a mass $m_{H^0} = 115 \text{ GeV}/c^2$ (unless otherwise specified). The leptonic decay of the gauge boson offers a signature with one isolated lepton with high transverse momentum. On the other side, the Higgs boson decays into two b -jets. The event topology is therefore an isolated lepton and two b -jets with

MSUB	process	cross-section in [mb]		
		Lausanne		LHCb prod.WG
		CTEQ4L	CTEQ6L	CTEQ6L
11	$f_i + f_j \rightarrow f_i + f_j$ (QCD)	10.49	9.403	12.37
12	$f_i + \bar{f}_i \rightarrow f_j + \bar{f}_j$	0.0106	0.0087	0.0092
13	$f_i + \bar{f}_i \rightarrow g + g$	0.0082	0.0086	0.0080
28	$f_i + g \rightarrow f_i + g$	12.28	11.63	11.20
53	$g + g \rightarrow f_i + \bar{f}_i$	0.784	0.818	0.75
68	$g + g \rightarrow g + g$	31.13	32.85	30.39
86	$g + g \rightarrow J/\Psi + g$	0.056	0.057	0.066
87	$g + g \rightarrow \chi_{0c} + g$	0.496	0.527	0.61
88	$g + g \rightarrow \chi_{1c} + g$	0.124	0.137	0.15
89	$g + g \rightarrow \chi_{2c} + g$	0.532	0.575	0.66
91	elastic scattering	22.21	22.21	22.21
92	single diffraction (XB)	7.151	7.151	7.151
93	single diffraction (AX)	7.151	7.151	7.151
94	double diffraction	10.19	10.19	10.19
95	low- p_T scattering	0	0	0
106	$g + g \rightarrow J/\Psi + \gamma$	0.00115	0.00115	0.00096
Total		102.6	102.7	102.9

Table 3.2: Comparison of the PYTHIA 6.325 production cross-sections obtained in Lausanne with the CTEQ4L and CTEQ6L LHAPDF libraries (*columns 3 and 4*) and by the LHCb production working group with the CTEQ6L LHAPDF library (*column 5*) for several physics processes. The parameters given in table 3.1 are used.

high p_T in the final state. Unfortunately, several event types without Higgs boson offer a similar topology. In order to deal with such backgrounds and to discriminate them from the signal, these are also generated and studied. However only the most relevant channels in terms of cross-sections are considered. The channels chosen for signal and background are enumerated in table 3.3.

The first considered background is $t\bar{t}$ with the two quarks decaying almost exclusively into a $b\bar{b}$ pair and two W bosons. A high p_T lepton can be present in the final state when one of the two W bosons decays leptonically. The t -quark is generated with a mass $m_t = 175 \text{ GeV}/c^2$. In this study, we have not considered indirect lepton production which can occur in W^\pm hadronic decays of the kind $W \rightarrow q_1\bar{q}_2 \rightarrow \ell + X$. Anyway, these should be suppressed by the fact that the lepton should have a low transverse momentum and should not be isolated. In the case of channels Z^0W^\pm and Z^0Z^0 , the Z^0 plays the role of the H^0 when it decays into two b -quarks. The remaining gauge boson can decay leptonically. The fact that the two

type	MSUB	description	special
$H^0 Z^0$	24	$f_i + \bar{f}_i \rightarrow Z^0 + H^0$	$m_{H^0} = 115 \text{ GeV}/c^2$ (PMAS(25,1))
$H^0 W^\pm$	26	$f_i + \bar{f}_j \rightarrow W^\pm + H^0$	
$t \bar{t} (W^+ b W^- \bar{b})$	81	$q + \bar{q} \rightarrow t + \bar{t}$	$m_t = 175 \text{ GeV}/c^2$ (PMAS(6,1))
	82	$g + g \rightarrow t + \bar{t}$	
$Z^0 W^\pm$	23	$f_i + \bar{f}_j \rightarrow Z^0 + W^\pm$	
$Z^0 Z^0$	22	$f_i + \bar{f}_i \rightarrow Z^0 + Z^0$	
$W^\pm + b\text{-jets}$	2	$f_i + \bar{f}_j \rightarrow W^\pm$	
$\gamma^*/Z^0 + b\text{-jets}$	1	$f_i + \bar{f}_i \rightarrow \gamma^*/Z^0$	
$b \bar{b}$	81	$q + \bar{q} \rightarrow b + \bar{b}$	$m_b = 4.8 \text{ GeV}/c^2$ (PMAS(5,1))
	82	$g + g \rightarrow b + \bar{b}$	

Table 3.3: Signal and background production channels with the corresponding PYTHIA process numbers MSUB. In the right column are given the H^0 , t - and b -quarks generation masses and the corresponding PYTHIA parameters.

parameter	value	explanation
MSTP(2)	1	1 st -order running α_s
MSTP(33)	0	no factor is included in hard cross-section for parton-parton interactions
MSTP(51)	7	CTEQ5L (leading order)
MSTP(52)	1	choice of PYTHIA internal PDF
MSTP(82)	3	structure of multiple interactions
MSTP(128)	0	resonance decay products stored
PARP(82)	3.47	see table 3.1
PARP(89)	14000.0	
PARP(90)	0.174	
PARJ(13)	0.750	
PARJ(14)	0.0	
PARJ(15)	0.0	
PARJ(16)	0.0	
PARJ(17)	0.0	

Table 3.4: PYTHIA 6.319 configuration parameters used for the $b\bar{b}$ events generation.

b -quarks come from a single particle Z^0 - instead of two like for $t\bar{t}$ - renders these backgrounds very difficult to discriminate from the signal. That is why this is called *irreducible* background. In the two channels $W^\pm + b$ -jets and $\gamma^*/Z^0 + b$ -jets, the isolated lepton comes from the gauge boson decay while the b -quarks arise directly from the initial parton shower. The last background channel $b\bar{b}$ has by far the most important production cross-section. However, it is largely attenuated by the fact that the lepton resulting from the parton shower is either absent or does not satisfy the isolation requirements (see § 3.4.2). The b -quark has a mass $m_b = 4.8 \text{ GeV}/c^2$ for the generation. The $b\bar{b}$ events were produced in a different way from the other channels. Due to the largely dominant cross-section, it is necessary to have a huge number of events of this type at disposal. The generation was performed on a CPU farm with the version 6.319 of PYTHIA. In order to optimize the production yield, the configuration parameters were also different and are given in table 3.4.

In the second column of table 3.5, the inclusive production cross-sections σ_{incl} at leading order for the signal and the background are given. It concerns all events which contain the required primary particles independently of their decay modes. Therefore the two b -jets and the isolated lepton are not always present in the final state and such interesting events have to be extracted specifically. The generation efficiency can be increased by requiring the generator to force the production of such particles in the final states by specifying the allowed decay modes of the primary particles. This is done for the Higgs and gauge bosons. The generator provides the following branching ratios for the considered decay channels:

$$\begin{cases} \text{BR}(H^0 \rightarrow b\bar{b}) & = 72.40\% \\ \text{BR}(Z^0 \rightarrow e^+ e^-) & = 3.37\% \\ \text{BR}(Z^0 \rightarrow \mu^+ \mu^-) & = 3.37\% \\ \text{BR}(W^+ \rightarrow e^+ \nu_e) & = 10.86\% \\ \text{BR}(W^+ \rightarrow \mu^+ \nu_\mu) & = 10.86\% \\ \text{BR}(Z^0 \rightarrow b\bar{b}) & = 15.20\% \end{cases}$$

The t -quark decay into a W and a b -quark is not specified but this channel is quite exclusive as $\text{BR}(t \rightarrow W^+ b) = 99.82\%$ in our generation. For the $t\bar{t}$ background, the two W^\pm bosons are not forced to decay leptonically. Otherwise, the W^\pm or Z^0 leptonic decays are restricted to the electrons and muons channels.

The branching ratios $\text{BR}(W^+ \rightarrow \tau^+ \nu_\tau)$ and $\text{BR}(Z^0 \rightarrow \tau^+ \tau^-)$ are 10.74% and 3.37% respectively. The τ has a short lifetime ($\tau_\tau \simeq 290 \text{ fs}$) and decays $\sim 30\%$ leptonically. This limits considerably the probability to find an isolated lepton in the final state. Furthermore, such a lepton should be observed *not prompt*, that is with a significant impact parameter with respect to the interaction point. Finally, being heavier than the other leptons, the τ should be produced with a reduced

	$\sigma_{\text{incl.}}$ [pb]	specific requirements	$\sigma_{\text{red.}}$ [pb]	$N_{\text{events/year}}$	$N_{\text{events}}^{\text{gen.}}$
<i>Signal</i> ($m_{H^0} = 115$ GeV/ c^2)					
$H^0 Z^0$	0.81	$H^0 \rightarrow b\bar{b}$, $Z^0 \rightarrow \ell^+ \ell^-$ ($\ell = e$ or μ)	$3.97 \cdot 10^{-2}$	79	$(1 \cdot 10^6)$
$H^0 W^\pm$	1.48	$H^0 \rightarrow b\bar{b}$, $W \rightarrow \ell \nu_\ell$ ($\ell = e$ or μ)	$2.33 \cdot 10^{-1}$	466	$(1 \cdot 10^6)$
Total	2.29		$2.73 \cdot 10^{-1}$	545	$3 \cdot 10^6$
<i>Background</i>					
$t\bar{t}$ ($W^+b W^-\bar{b}$)	570.82		570.82	$1.1 \cdot 10^6$	$2 \cdot 10^7$
$Z^0 W^\pm$	26.92	$Z^0 \rightarrow b\bar{b}$, $W \rightarrow \ell \nu_\ell$ ($\ell = e$ or μ)	$8.88 \cdot 10^{-1}$	1776	$1 \cdot 10^6$
$Z^0 Z^0$	11.86	$Z^0 \rightarrow b\bar{b}$, $Z^0 \rightarrow \ell^+ \ell^-$ ($\ell = e$ or μ)	$5.71 \cdot 10^{-1}$	1142	$5 \cdot 10^6$
$W^\pm + b$ -jets	$1.59 \cdot 10^5$	$W \rightarrow \ell \nu_\ell$ ($\ell = e$ or μ)	$3.46 \cdot 10^4$	$6.9 \cdot 10^7$	$6 \cdot 10^7$
$\gamma^*/Z^0 + b$ -jets	$7.55 \cdot 10^4$	$Z^0 \rightarrow \ell^+ \ell^-$ ($\ell = e$ or μ) CKIN(1)=12	$1.10 \cdot 10^4$	$2.2 \cdot 10^7$	$4 \cdot 10^7$
$b\bar{b}$	$4.90 \cdot 10^8$	CKIN(1)=30	$5.12 \cdot 10^7$	$1.0 \cdot 10^{11}$	$6.2 \cdot 10^9$

Table 3.5: Inclusive production cross-sections at leading order $\sigma_{\text{incl.}}$ for Higgs signal and background channels giving $b\bar{b}\ell$ (column 2). Specific requirements used for the events generation for each channel and the resulting reduced cross-sections $\sigma_{\text{red.}}$ (column 3 and 4). Number of events expected per LHCb year with an integrated luminosity $\mathcal{L}_{\text{int.}}^{\text{LHCb}} = 2 \cdot 10^3 \text{ pb}^{-1}$ (column 5) and number of events generated for the study (column 6). The Higgs boson is produced with a mass $m_{H^0} = 115 \text{ GeV}/c^2$.

momentum which should prevent it from passing the isolation cuts (see § 3.4.2). For these reasons, it has been decided to neglect the W^\pm and Z^0 leptonic decays into τ .

In the $\gamma^*/Z^0 + b$ -jets background, the Drell-Yan process is also included. A non negligible fraction of such events provides an isolated lepton with high p_T . A lower cutoff $\hat{m} = \sqrt{\hat{s}} = 12$ GeV (CKIN(1)=12) is set on the reference energy scale to attenuate the off- Z^0 resonance. In the same way, another lower cutoff $\hat{m} = \sqrt{\hat{s}} = 30$ GeV (CKIN(1)=30) is set for the $b\bar{b}$ background in order to force the b -jets and the lepton to have sufficiently large p_T . These requirements are summarized in the third column of table 3.5. Their use leads to the reduced cross-sections σ_{red} , given in the fourth column. The LHCb luminosity is $\mathcal{L}^{\text{LHCb}} = 2 \cdot 10^{32} \text{ cm}^{-2} \text{ s}^{-1} = 2 \cdot 10^{-4} \text{ pb}^{-1} \text{ s}^{-1}$. Assuming an annual LHCb performing activity of $\sim 30\%$ (1 year $\simeq 3 \cdot 10^7$ s), the integrated luminosity per year reaches $\mathcal{L}_{\text{int.}}^{\text{LHCb}} = 2 \cdot 10^3 \text{ pb}^{-1}$. In the fifth column are presented the number of events expected during one LHCb year activity for each type of events according to the reduced cross-sections σ_{red} . The corresponding number of events generated for this study are given in the sixth column for comparison. For $H^0 Z^0$ and $H^0 W^\pm$, two separate sets of 10^6 events were produced in order to get specific informations about each type. The principal signal analysis was nevertheless performed on a mixed set of $3 \cdot 10^6$ $H^0 Z^0$ and $H^0 W^\pm$ events, the proportion of each type being dictated by their respective cross-section. In any case, the number of signal events generated exceeds the number of events expected per year by a factor $\sim 10^3$ which gives statistical reliability to the analysis. The same observation is valid for the $Z^0 Z^0$ and $Z^0 W^\pm$ backgrounds. For the $W^\pm + b$ -jets, $\gamma^*/Z^0 + b$ -jets and $t\bar{t}$ channels, the equivalent number of LHCb years simulated are about 1, 2 and 18 respectively. In return, only a small fraction $\sim 6\%$ of LHCb year of $b\bar{b}$ production is available due to the relatively huge cross-section.

3.3 LHCb fast simulation

A previous work on the search for a Higgs boson in LHCb [40] aimed to assess the relevant detector effects contributions to the dijet mass resolution. These were implemented in a fast simulation in order to be able to switch them off and to study them individually for the signal and backgrounds. The LHCb geometrical acceptance was reproduced by selecting only particles emitted inside a forward conical ring with inner and outer radii $\theta_{\text{min}} = 15$ mrad and $\theta_{\text{max}} = 300$ mrad respectively. It also included the Level-0 trigger approximated with a four-vector level parametrization. The resolution on the impact parameter and on the primary vertex reconstruction were reproduced by gaussian smearing of the four-vectors delivered by PYTHIA with parameters inferred from the full simulation. The dependence of the primary vertex resolution with the number of primary charged tracks in the event was included. Furthermore, the precision in its measurements as a function of its distance from

the first measurement station was also implemented as a function of the track momentum. The 4 Tm integrated magnetic field average effect was reproduced by providing a p_T kick to the charged particles. Finally, the calorimeter energy resolution was also simulated by smearing the particles energy with values inferred from the full simulation results. This parametrization took implicitly into account the global effects of the calorimeter segmentation and the shower shape. The Pile-Up system was not explicitly implemented. Nevertheless, multiple interactions per bunch crossing are anyway suppressed as the LHCb luminosity is tuned in order to provide single interactions per bunch crossing. Furthermore, the fast simulation assumed perfect particle identification and provided the possibility to exclude or to keep neutrini. Some relevant topological variables such as the impact parameter of tracks, the dijet transverse momentum and the dijet mass in minimum bias events were compared between the fast and a full simulations (SICB based on GEANT3) with fair agreement.

For a Higgs boson produced with $m_{H^0} = 115 \text{ GeV}/c^2$, the contribution of the intrinsic width $\Gamma_{H^0} \simeq 3 \text{ MeV}$ (see figure 1.12) to the dijet mass resolution can be ignored. At four-vector level, it was demonstrated that the dominant contributions come from the LHCb geometrical acceptance restriction and the subsequent loss of particles outside the detector ($\sim 5\%$), from errors in jet reconstruction including particles coming from the underlying event ($\sim 14\%$) and from the escape of neutrini ($\sim 26\%$), leading to a total resolution $\text{FWHM}_{M_{jj}}/M_{jj} \sim 30\%$ ¹. Including the fast simulation, the contribution of the calorimeters to the energy resolution can be considered as minor and the overall contribution of the remaining effects cited above - except the magnetic field - are estimated of the order of 10%. Finally, it was shown that the effect of the magnet is not negligible, increasing the dijet mass resolution by another 18%.

In the present work, the fast simulation is restricted to the LHCb geometrical acceptance, with the possibility to reject or keep neutrini for specific tests. As in [40], the pyramidal feature of the LHCb detector (15 – 300 mrad in the bending plane and 15 – 250 mrad in the non-bending plane (see § 2.2)) is approximated by a forward conical ring centered on the z -axis and corresponding to the spectrometer dimension in the bending plane. The LHCb detector geometrical acceptance is therefore featured in terms of the polar angle θ :

$$15 < \theta < 300 \text{ mrad} \tag{3.1}$$

¹When the dijet mass distribution is parametrized with a gaussian best fit, the resolution can be expressed as $\sigma_{M_{jj}}/M_{jj}$ where $\sigma_{M_{jj}} = \text{FWHM}_{M_{jj}}/2\sqrt{2\ln 2}$ is the standard deviation.

3.4 Events selection procedure

3.4.1 Preselection

The preselection is a set of technical cuts with the aim to ensure the presence of two b -hadrons and a lepton with important p_T , falling in a region close to the LHCb acceptance. In order to allow future boundaries effects studies, we require, in a first step, an acceptance in θ a bit larger than (3.1):

- two b -hadrons in $0 < \theta < 400$ mrad
- at least one lepton e^\pm or μ^\pm with $p_T > 4$ GeV/ c in $0 < \theta < 400$ mrad

The considered b -hadrons are enumerated in table 3.6 with their PYTHIA identification code, their quark composition and their spin. The preselected events are stored on disk in order to gain efficiency for the subsequent analysis.

3.4.2 Associated boson tagging from isolated lepton

The gauge boson leptonic decay in the two kinds of signal events H^0W^\pm and H^0Z^0 provides one or two leptons with high transverse momentum. The detection and selection of such leptons is therefore crucial in order to distinguish these events. In this section, we describe the basic idea which will be used in the event selection.

The first step consists in the preselection of *prompt* e^\pm and μ^\pm with a small impact parameter ($IP < 30$ μm) with respect to the interaction point. Indeed, the gauge boson W^\pm/Z^0 is produced in association with the H^0 at the interaction point and its short lifetime implies that its decay products are also emitted from a region very close to the interaction point. Furthermore, the leptons must stand inside the LHCb acceptance and have a relatively large transverse momentum ($p_T > 10$ GeV/ c).

The second step consists in the identification of events in which the associated gauge boson is a Z^0 . For that purpose, all the possible pairs of leptons with same flavour and opposite charge (e^+e^- or $\mu^+\mu^-$) are combined among the preselected leptons. For each couple, the dilepton energy-momentum is reconstructed by the addition of the leptons four-vectors $p_{\text{dilepton}}^\mu = p_{\ell^+}^\mu + p_{\ell^-}^\mu$ and the dilepton mass M_{dilepton} is evaluated. If at least one dilepton has a mass in the Z^0 mass window, chosen as:

$$76 < M_{\text{dilepton}} < 106 \text{ GeV}/c^2, \quad (3.2)$$

the event is tagged as a Z^0 -associated event. In the opposite case, the fact that no pair of leptons satisfies this criterion does not necessarily imply that the gauge boson is a W^\pm . Indeed the second lepton of a Z^0 could be emitted outside the LHCb

		PYTHIA code	quark composition	spin			PYTHIA code	quark composition	spin
Mesons	B^0	511	$d\bar{b}$	0	Baryons	Σ_b^-	5112	ddb	1/2
	\bar{B}^0	-511	$b\bar{d}$	0		$\bar{\Sigma}_b^-$	-5112	$\bar{d}\bar{d}\bar{b}$	1/2
	B^+	521	$u\bar{b}$	0		Λ_b^0	5122	udb	1/2
	B^-	-521	$b\bar{u}$	0		$\bar{\Lambda}_b^0$	-5122	$\bar{u}\bar{d}\bar{b}$	1/2
	B_s^0	531	$s\bar{b}$	0		Σ_b^0	5212	udb	1/2
	\bar{B}_s^0	-531	$b\bar{s}$	0		$\bar{\Sigma}_b^0$	-5212	$\bar{u}\bar{d}\bar{b}$	1/2
	B_c^+	541	$c\bar{b}$	0		Σ_b^+	5222	uub	1/2
	B_c^-	-541	$b\bar{c}$	0		$\bar{\Sigma}_b^+$	-5222	$\bar{u}\bar{u}\bar{b}$	1/2
	η_b	551	$b\bar{b}$	0		Σ_b^{*-}	5114	ddb	3/2
	B^{*0}	513	$d\bar{b}$	1		$\bar{\Sigma}_b^{*-}$	-5114	$\bar{d}\bar{d}\bar{b}$	3/2
	\bar{B}^{*0}	-513	$b\bar{d}$	1		Σ_b^{*0}	5214	udb	3/2
	B^{*+}	523	$u\bar{b}$	1		$\bar{\Sigma}_b^{*0}$	-5214	$\bar{u}\bar{d}\bar{b}$	3/2
	B^{*-}	-523	$b\bar{u}$	1		Σ_b^{*+}	5224	uub	3/2
	B_s^{*0}	533	$s\bar{b}$	1		$\bar{\Sigma}_b^{*+}$	-5224	$\bar{u}\bar{u}\bar{b}$	3/2
	\bar{B}_s^{*0}	-533	$b\bar{s}$	1					
	B_c^{*+}	543	$c\bar{b}$	1					
	B_c^{*-}	-543	$b\bar{c}$	1					
	Υ	553	$b\bar{b}$	1					

Table 3.6: b -hadrons considered in the study with their PYTHIA identification code, their quark composition and their spin. The difference between Σ_b^0 and Λ_b^0 is in the light quarks spin alignment with the b -spin.

acceptance escaping the detection. Therefore, if the condition (3.2) is not fulfilled, the event is tagged as a *not Z^0 -associated* event.

At this point, no supplementary condition is required for a Z^0 -associated event. An isolation criterion is imposed only for leptons in *not Z^0 -associated* events. The leptons are often isolated from the other final state particles and, in particular, from the b -jets coming from the Higgs decay. Two different methods have been studied and compared in order to insure the lepton isolation from the jets.

The first method consists in specifying a minimal distance between the candidate lepton and the two b -jets or, more precisely, the two b -hadrons to speed up the procedure. This criterion is applied before the b -jets reconstruction and their four-vectors are thereby not known yet. Nevertheless, it is possible that during the real data analysis, the procedure would be inverted. We introduce here the notion of

distance as it will be frequently used in the rest of this work. The distance ΔR_{ij} between to entities i and j is defined in the (η, ϕ) phase space as:

$$\Delta R_{ij} = \sqrt{(\eta_i - \eta_j)^2 + (\phi_i - \phi_j)^2} \quad (3.3)$$

η is the pseudorapidity:

$$\eta = -\ln \left(\tan \frac{\theta}{2} \right) \quad (3.4)$$

θ and ϕ are respectively the polar and azimuthal angles with respect to the LHCb z -axis. As it will be shown in § 3.5, we anticipate that an optimal distance parameter $R_{\text{cone}} = 0.6$ should be adopted for the jets reconstruction using the cone algorithm and $R_{K_T} = 0.6$ for the K_T algorithm. Furthermore, according to figure 3.5 (*right*) and 3.7 (*right*), the typical distance between a b -hadron and its corresponding b -jet is smaller than 0.1. A minimal value of ~ 0.7 should therefore be sufficient to insure that the lepton is isolated from the jets. We have chosen:

$$\Delta R(\text{candidate lepton} - b\text{-hadron}) > 0.75 \quad (3.5)$$

The second method is inspired from what is done by the CDF collaboration [39]. A cone of radius $R_{\text{cone}} = 0.4$ is constructed around the candidate lepton direction exactly like in the cone algorithm (see § 3.5.1). The additional energy deposited in the cone is compared to the lepton energy. The isolation condition is fulfilled if:

$$\frac{E_{\text{cone}}}{E_{\text{candidate lepton}}} < 10\% \quad (3.6)$$

In both methods, if several leptons are considered as isolated in the sense of (3.5) or (3.6), the highest- p_T lepton is finally selected as the candidate tag.

An analysis based on a set of 38'384 $H^0 W^\pm$ and $H^0 Z^0$ events has been performed in order to compare the efficiency of both methods. It results that 5'024 events are tagged as Z^0 -associated events. The Monte Carlo truth informations show that only 9 of these are in reality $H^0 W^\pm$ events with a dilepton mass satisfying by accident the condition (3.2). It remains 5'015 events (99.82%) correctly interpreted as $H^0 Z^0$ events. Concerning the *not* Z^0 -associated events (events without dilepton mass satisfying (3.2)), 29'424 contain a candidate lepton which satisfies the isolation condition (3.5). The MC truth exhibits that 29'411 of them (99.96%) are really originating from the associated gauge boson. In turn, using the CDF lepton isolation criterion (3.6), only 26'007 events have a candidate lepton among which 25'998 (99.97%) really come from the W^\pm/Z^0 .

In definitive, both methods offer similar and very good efficiency for the isolated lepton identification. However, in practice, the method “à la CDF” implies more calculation resources and rejects events which are fairly accepted by the other method. It is therefore considered as a second choice. Nevertheless, the possibility to use this criterion to discriminate particular kinds of background should be envisaged in further studies.

3.4.3 Selection cuts

In this section, we present the sequence of selection criteria applied in order to extract signal events.

1. “ N_{jj+lep} ” selection

This stage of the selection process consists in imposing the nominal acceptance (3.1) for all the considered particles. In particular, we require:

- two b -hadrons in the acceptance
- at least one e^\pm or μ^\pm in the acceptance, with $p_T > 10 \text{ GeV}/c$ and produced with impact parameter $IP < 30 \mu\text{m}$
 - if *not* Z^0 -associated event: $\Delta R(\text{lepton} - b\text{-hadron}) > 0.75$

The b -hadrons, which are necessary for the b -jets reconstruction with the cone algorithm (see § 3.5.1), have to stand inside the LHCb acceptance. At this point, the lepton isolation process described in § 3.4.2 is performed. It requires a *prompt* lepton with a minimal distance from the b -hadrons in the sense of (3.3) when the event is tagged as *not* Z^0 -associated. All this procedure is executed before the b -jets reconstruction.

2. Jet invariant mass:

The next selection step is performed after the b -jets reconstruction (see § 3.5). It consists precisely in requiring a minimal invariant jet mass consistent with the parent b -quark. Although the nominal mass should be close to $m_b = 4.8 \text{ GeV}/c^2$, a reduced value for reconstructed mass is accepted. This is justified by the fact that some b -hadron decay particles can be lost outside the jet cone and that neutrino escape the detection (and other generic resolution effects). Therefore, the b -jet invariant mass must satisfy:

- $M_{b\text{-jet}} > 3 \text{ GeV}/c^2$

3. No jet cone overlap:

The following cut aims at discarding ambiguous situations where the two cones overlap. As it will be explained in § 3.5.1 and § 3.5.3, the cone algorithm constructs a cone of radius $R_{\text{cone}} = 0.6$ around each b -hadrons direction. A minimal distance:

- $\Delta R(b\text{-hadrons}) > 2 \cdot R_{\text{cone}} = 1.2$

is therefore required between the two b -hadrons. As it will be seen later, the cone algorithm forbids particles double counting in any case, even if the cones overlap.

4. “ $\mathbf{p}_T^{\ell_1}$ ” cut:

In order to be able to compare with the results published in [40], a supplementary cut on the highest- p_T isolated lepton ℓ_1 transverse momentum is optionally performed:

- $p_T^{\ell_1} > 20 \text{ GeV}/c$

5. “ $\mathbf{E}_T^{\text{miss}}$ ” cut:

The last selection concerns *not* Z^0 -associated events exclusively. Such events are predominantly of type $H^0 W^\pm$ with a neutrino coming from the W^\pm leptonic decay which escapes detection. Another possibility is the case of $H^0 Z^0$ events in which one of the two leptons from the Z^0 escapes detection. In both cases, one gauge boson decay product is missing which leads to a significant total transverse energy loss. We require:

- if *not* Z^0 -associated event: $E_T^{\text{miss}} > 20 \text{ GeV}$

In table 3.7, we give the number of remaining signal and background events expected per LHCb year in the interesting mass window $80 < M_{\text{jj}} < 120 \text{ GeV}/c^2$ after each step of the selection procedure previously described. The preselection is already very efficient for the $W^\pm + b$ -jets, $\gamma^*/Z^0 + b$ -jets and $b\bar{b}$ backgrounds where the number of events are decreased by a factor $\sim \mathcal{O}(10^3)$ while the signal is only reduced by a factor ~ 15 with respect to the initial number of events presented in the fifth column of table 3.5. The $t\bar{t}$ is also reduced by a factor ~ 150 . The first selection “ $N_{\text{jj} + \text{lep}}$ ” is also very efficient, in particular for the dominant $b\bar{b}$ background which is decreased by a factor $\sim \mathcal{O}(10^5)$ while 2/3 of the signal is rejected. The next cuts on the jet mass and the distance between jets are not very significant. The significance² after each of these steps remains constant and low ($S/\sqrt{B} \simeq 0.33$). The stronger requirement $p_T^{\ell_1} > 20 \text{ GeV}/c$ has quite no effect on the signal and background

²Throughout this work, the significance is defined as S/\sqrt{B} where S is the number of signal events and B the number of background events in the Higgs mass window $80 < M_{\text{jj}} < 120 \text{ GeV}/c^2$.

		1	2	3	4	5 - a	5 - b	5
	Preselection $0 < \theta < 400$ mrad $P_T^{\text{lep}} > 4$ GeV/ c	$N_{\text{jj+lep}}$ $15 < \theta < 300$ mrad $P_T^{\text{lep}} > 10$ GeV/ c $\Delta R(\text{lep.-}b\text{-had.}) > 0.75$ $IP_{\text{lep}} > 30$ μm	$M_{b\text{-jet}} > 3$ GeV/ c^2	$\Delta R(b\text{-had.}) > 1.2$	$P_T^{\ell_1} > 20$ GeV/ c	<i>not</i> Z^0 - <i>associated</i> $E_T^{\text{miss}} > 20$ GeV	Z^0 - <i>associated</i>	Total
		$80 < M_{\text{jj}} < 120$ GeV/ c^2						
<i>Signal</i>								
$H^0 Z^0$	5.3	2.3	2.3	2.2	2.2	0.7	1.2	1.9
$H^0 W^\pm$	30.6	10.8	10.6	10.3	9.4	8.1	0	8.1
Total	35.9	13.1	12.9	12.5	11.6	8.8	1.2	10.0
<i>Background</i>								
$t \bar{t}$	7007	726	700	677	597	547	5	552
$Z^0 W^\pm$	87.6	14.8	14.7	14.2	12.1	10.5	0	10.5
$Z^0 Z^0$	34.4	8.1	8.0	7.8	6.9	1.9	3.5	5.4
$W^\pm + b\text{-jets}$	29533	40.3	40.3	40.3	35.6	33.3	0	33.3
$\gamma^*/Z^0 + b\text{-jets}$	22746	61.1	56.1	55.6	52.2	14.3	29.7	44.0
$b \bar{b}$	$1.25 \cdot 10^8$	597	597	597	0	0	0	0
Total	$1.25 \cdot 10^8$	1447	1416	1392	704	607	38	645
S/\sqrt{B}		0.34	0.34	0.33	0.44	0.36	0.19	0.39

Table 3.7: Number of signal and background events expected per LHCb year in the Higgs mass window $80 < M_{\text{jj}} < 120$ GeV/ c^2 after each of the successive selection cuts described in § 3.4.3.

channels, except $b\bar{b}$ which is totally suppressed. Obviously, this has to be considered with precaution as only 22 days of LHCb production are simulated for this channel. Nevertheless, this affects the significance which is increased to $S/\sqrt{B} = 0.44$ with 11.6 signal events left. Our results are somehow different compared to [40] in which similar cuts led to $S/\sqrt{B} = 0.59$. The last cut on the transverse missing energy decreases more or less in the same way signal and backgrounds by $\sim 10\text{-}15\%$, except channel $Z^0 Z^0$ which is reduced by $\sim 20\text{-}25\%$. This finally reduces the significance to $S/\sqrt{B} = 0.39$. As we will see later, supplementary cuts should be performed in order to improve this value.

In figures 3.2 to 3.4, we present the histograms of some relevant variables, obtained from the Monte Carlo truth, after the previous selections applied to 10^6 generated event. The cut from the shown variable was removed.

In figure 3.2 are presented the Higgs momentum $|\vec{p}^{H^0}|$ (*left*) and transverse momentum $p_T^{H^0}$ (*right*) distributions for events accepted after the selection procedure. The topology of such signal events with a high transverse momentum for the Higgs is confirmed here with a most probable value $p_T^{H^0} \simeq 60 \text{ GeV}/c$.

The Higgs decay products kinematic variables are also shown in figure 3.3. The b -quarks are considered directly after the Higgs decay and before the parton shower, without any differentiation between the quark and the antiquark. The right plot shows that they carry a considerable part of the Higgs transverse momentum as the most probable value is around $p_T^{b\text{-quark}} \simeq 50 \text{ GeV}/c$.

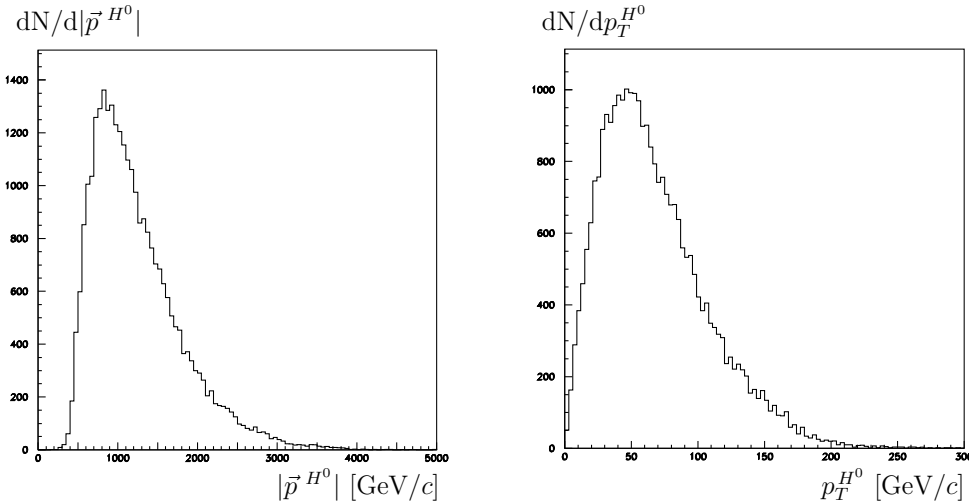


Figure 3.2: Higgs momentum $|\vec{p}^{H^0}|$ (*left*) and transverse momentum $p_T^{H^0}$ (*right*) distributions for events accepted after the selection procedure. The informations are obtained from the MC truth.

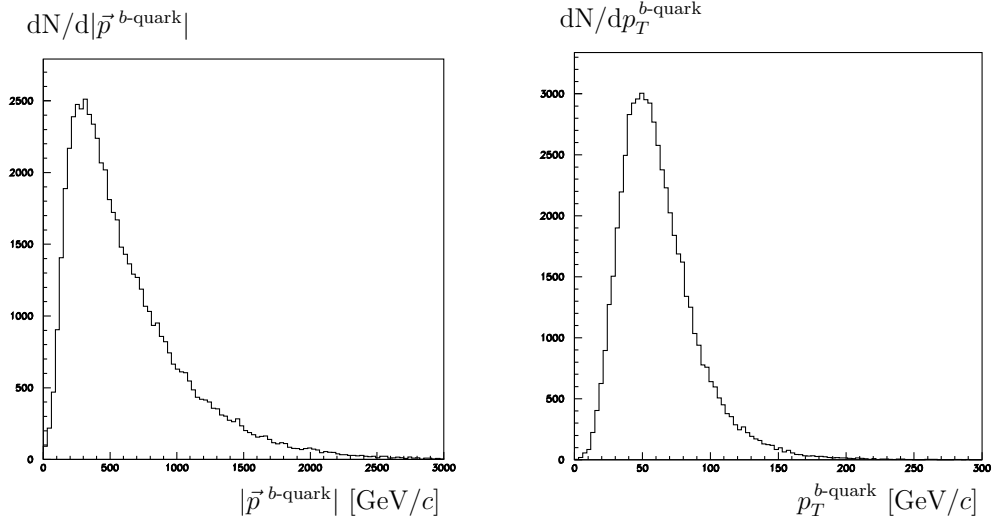


Figure 3.3: b -quarks from the Higgs decay $H^0 \rightarrow b\bar{b}$ momentum $|\vec{p}^{b\text{-quark}}|$ (*left*) and transverse momentum $p_T^{b\text{-quark}}$ (*right*) distributions for events accepted after the selection procedure. The quarks are considered directly after the Higgs decay and before the parton shower. The plots cumulate the quark and antiquark information (from MC truth) without any differentiation.

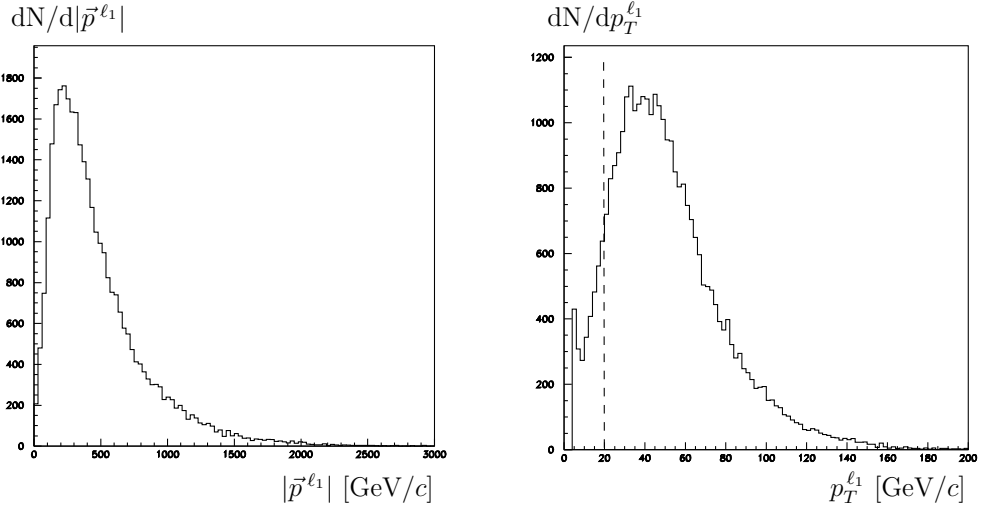


Figure 3.4: Isolated lepton momentum $|\vec{p}^{\ell_1}|$ (*left*) and transverse momentum $p_T^{\ell_1}$ (*right*) distributions for events accepted after the selection procedure. On the right plot is specified the position of the special fourth selection cut $p_T^{\ell_1} > 20$ GeV/ c .

Finally, the description of the interesting hard process components kinematics is completed with the presentation of the isolated lepton momentum and transverse momentum in figure 3.4. The Higgs associated events topology predicts a high transverse momentum for the associated boson, subsequently transferred to the descendant lepton. This is confirmed in the right plot where the most probable value is $p_T^{\ell_1} \simeq 50 \text{ GeV}/c$.

3.5 Jet reconstruction algorithms

In this study, only the Higgs decay $H^0 \rightarrow b\bar{b}$ is considered. After string fragmentation, the b -quarks hadronize into b -hadrons whose decay give birth to structures collimated around the initial b -hadrons directions, the b -jets. This section describes the two jet reconstruction algorithms used for the study: the cone and the K_T or ‘‘Durham’’ algorithms. Their performances in terms of dijet mass resolution are compared.

3.5.1 Cone algorithm

The principle of the cone algorithm is to consider that a jet is contained in a virtual cone of radius R_{cone} constructed around a predefined direction. In this study, we have chosen the direction of the b -hadrons, as given by their momenta \vec{p}_b and $\vec{p}_{\bar{b}}$. This choice is motivated by the fact that LHCb is specifically developed to recognize such b -hadrons. Furthermore, the distribution of the distance between the b -quark and the b -hadron in the (η, ϕ) phase space (see eq. (3.3)) from the Monte Carlo truth analysis shows a small average value $\langle \Delta R \rangle \simeq 0.02$ (see figure 3.5 (*left*)). This implies that the hadronization process does not change the b -quark direction in a significant way which is a supplementary argument in favour of this choice.

In practice, the algorithm first considers the particle with the highest transverse momentum among the two b - and \bar{b} -hadrons and associates it to the first cone axis \vec{p}_A^1 . The pseudorapidity defined in (3.4) and the azimuthal angle (η_A^1, ϕ_A^1) are calculated. For each particle n emitted inside the LHCb acceptance (3.1) and appearing in the final state - except the isolated lepton(s) (see § 3.4.2) and the neutrini - (η_n, ϕ_n) are also evaluated. The particle n is associated to the jet if:

$$\sqrt{(\eta_n - \eta_A^1)^2 + (\phi_n - \phi_A^1)^2} \leq R_{\text{cone}} \quad (3.7)$$

The second b -jet is constructed similarly around the remaining seed \vec{p}_A^2 with (η_A^2, ϕ_A^2) , but with the difference that particles already associated to the first b -jet are discarded. This restriction is adopted in order to deal with possible cone overlapping

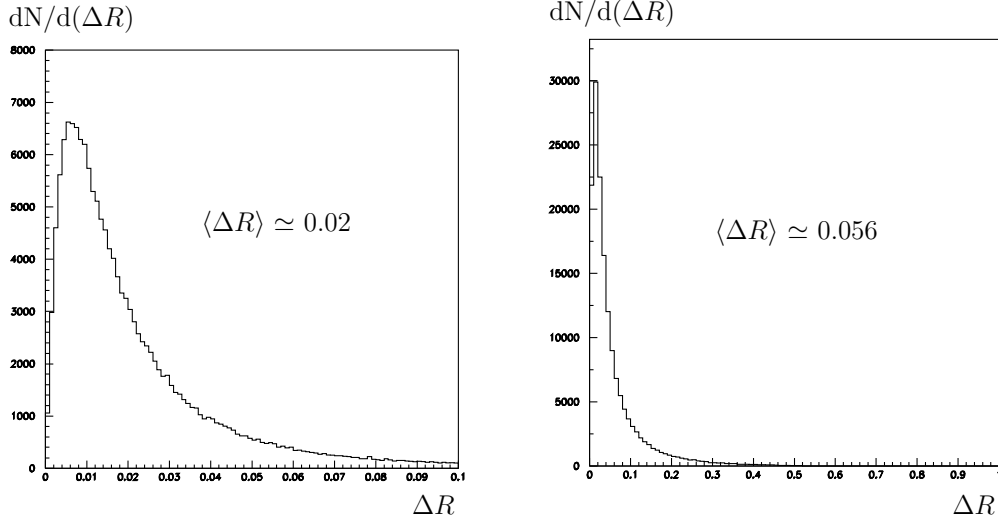


Figure 3.5: Distribution of the distance ΔR between the b -quark and the b -hadron. The informations are obtained from the MC truth (*left*). Distribution of the distance ΔR between the initial cone axis predefined by the b -hadron direction (from MC truth) and the b -jet reconstructed by the cone algorithm (*right*).

in the case of large values of R_{cone} and to avoid subsequent particle double counting. The jets energy-momentum p_J^1 and p_J^2 are finally calculated by summing the four-vectors of the final particles included in each jet:

$$\begin{aligned}
 p_J^1 &= (E_J^1, \vec{p}_J^1) = \sum_{n \in \text{jet1}} (E_n^1, \vec{p}_n^1) \\
 p_J^2 &= (E_J^2, \vec{p}_J^2) = \sum_{n \in \text{jet2}} (E_n^2, \vec{p}_n^2)
 \end{aligned}
 \tag{3.8}$$

At the end of the process, the directions of the initial cone axis should therefore differ slightly from the resulting jets directions as it is represented schematically in figure 3.6. Figure 3.5 (*right*) shows precisely the distribution of the distance ΔR in (η, ϕ) between the initial cone axis defined as the b -hadron direction (from MC truth) and the corresponding reconstructed b -jet with a small average value $\langle \Delta R \rangle \simeq 0.056$.

3.5.2 K_T or “Durham” algorithm

The K_T algorithm [41, 42] is an iterative clustering algorithm inherited from the JADE and “Durham” algorithms developed to reconstruct jets in e^+e^- collisions. In this case, the initial state is purely electromagnetic and all the final state hadrons are

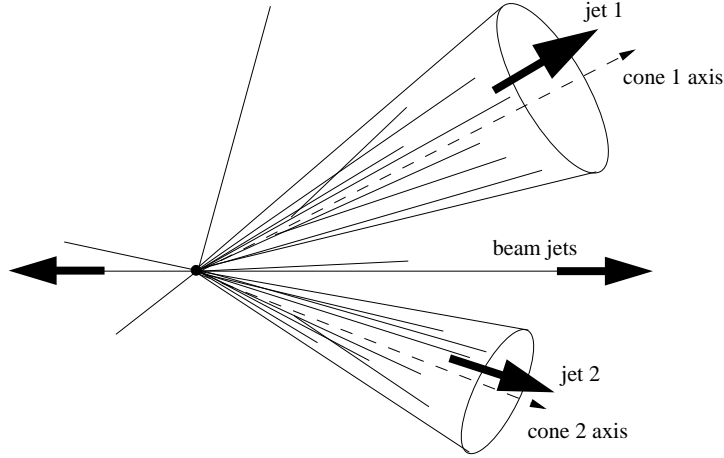


Figure 3.6: Representation of jets reconstruction using the cone algorithm. The predefined cone axis and the resulting jets directions are shown.

associated with the hard scattering process. In hadron-hadron collisions, only one active parton from each incident hadron participates in the hard scattering process. The remaining partons undergo soft interactions and their resulting hadrons are part of what is called the *underlying* event. These are in first approximation uncorrelated with the interesting hard process. Furthermore, these particles plus the initial state radiation produce characteristic jets with small p_T but large longitudinal momentum called beam jets. In contrast, jets arising from the hard process have typically large p_T and quite small longitudinal momentum.

The hard scattering process is moving in the parton-parton rest frame along the beam axis. The K_T algorithm insures invariance under boosts along this axis by using the transverse momentum p_T or energy E_T , the pseudorapidity η defined in (3.4) and the azimuthal angle ϕ as natural variables.

The initial point of the algorithm consists in considering each final state particle emitted in the LHCb acceptance (3.1) as a *protojet*. The idea is that protojets with nearly parallel momenta should be joined as they should belong to the same jet. The algorithm should also determine when the merging should cease so that the obtained protojet is considered as a jet. The merging criterion depends on a parameter R_{K_T} introduced by Ellis and Soper [43] which is similar to R_{cone} in the cone algorithm.

In practice, the K_T algorithm operates recursively as follows:

1. For each protojet i , define the closeness to the beam axis z :

$$d_{ib} = E_{Ti}^2 R_{K_T}^2$$

and, for each pair of protojets ij , define the distance:

$$d_{ij} = \min(E_{Ti}^2, E_{Tj}^2) \Delta R_{ij}^2 \quad \text{where} \quad \Delta R_{ij}^2 = (\eta_i - \eta_j)^2 + (\phi_i - \phi_j)^2$$

2. Find the minima $\min(d_{ib})$ and $\min(d_{ij})$ in both sets.
3. If $\min(d_{ib}) < \min(d_{ij})$, $d_{\min} = \min(d_{ib})$ and the protojet i is considered as a complete jet.
4. If $d_{\min} = \min(d_{ij}) < \min(d_{ib})$, $d_{\min} = \min(d_{ij})$ and the two protojets i and j are merged into a new protojet k following the covariant E recombination scheme ³ in which the energy-momentum four-vector are added:

$$p_k^\mu = p_i^\mu + p_j^\mu$$

5. Go to step 1.

Each time a jet is completed, a scale factor $y(n)$ corresponding to the number of completed jets n is evaluated:

$$y(n) = d_{\min}/E_{\text{tot}}^2$$

In the *inclusive* mode, the clusterization procedure continues until there are no more protojets and results in a set of jets with successively larger $d_{ib} = E_{Ti}^2 R_{KT}^2$. Inside each jet, all particles have respective distances smaller than R_{KT} while the respective distance between jets is larger than R_{KT} , exactly like with the cone algorithm. In figure 3.7 (*left*) is presented the average number of jets obtained by the K_T algorithm per event for values of R_{KT} between 0.1 and 2.4. A jet is counted if it satisfies $p_T > 5 \text{ GeV}/c$ or $E > 100 \text{ GeV}$. The K_T algorithm can also be used in *exclusive* mode in which the number of final jets N_{jets} is predefined. In this mode, the iteration stops when all couple of jets ij satisfies $d_{ij} > d_{\text{cut}}$ where $d_{\text{cut}} = y(N_{\text{jets}})$ acts as a resolution parameter.

In this study, as explained in § 3.4.2, an event is tagged either as a *not* Z^0 - or as a Z^0 -associated event with respectively one or two isolated leptons. The K_T

³Two other recombination schemes are also possible: the p_T - and the p_T^2 -weighted schemes. In these cases, the merging is done via:

$$\left\{ \begin{array}{l} p_{Tk} = p_{Ti} + p_{Tj} \\ \eta_k = (p_{Ti}\eta_i + p_{Tj}\eta_j)/p_{Tk} \\ \phi_k = (p_{Ti}\phi_i + p_{Tj}\phi_j)/p_{Tk} \end{array} \right. \quad \text{and} \quad \left\{ \begin{array}{l} p_{Tk}^2 = p_{Ti}^2 + p_{Tj}^2 \\ \eta_k = (p_{Ti}^2\eta_i + p_{Tj}^2\eta_j)/p_{Tk}^2 \\ \phi_k = (p_{Ti}^2\phi_i + p_{Tj}^2\phi_j)/p_{Tk}^2 \end{array} \right.$$

respectively. The particularity of both these schemes is that they produce massless jets.

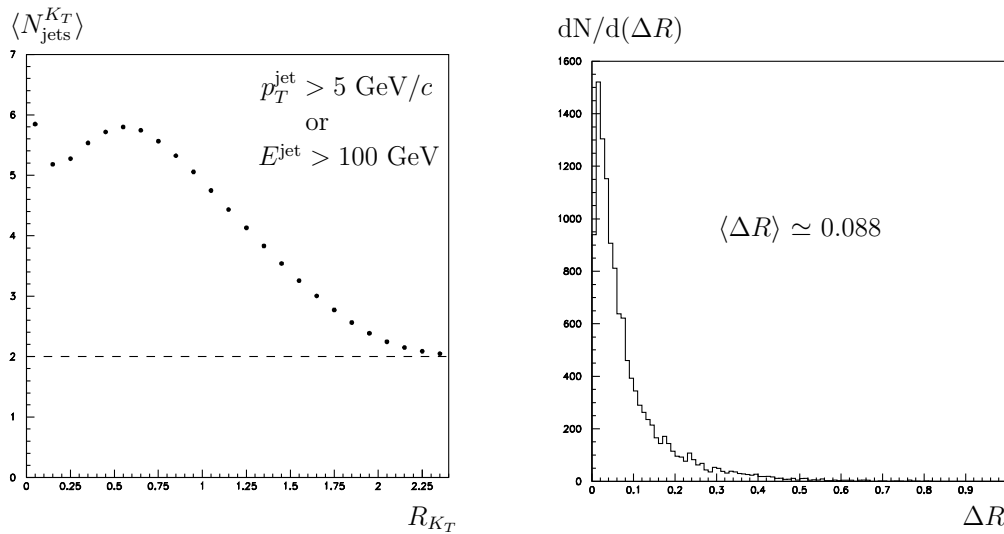


Figure 3.7: Average number of jets per event obtained by the K_T algorithm as a function of R_{K_T} . A jet is counted if $p_T > 5 \text{ GeV}/c$ or $E > 100 \text{ GeV}$ (*left*). Distribution of the minimal distance ΔR between the b -hadron and the corresponding K_T -jet (*right*).

algorithm interprets an isolated high p_T lepton as a jet compound of a single particle. Therefore, the isolated lepton(s) is (are) discarded by hand from the initial set of protojets.

The distance ΔR in (η, ϕ) is calculated between each obtained K_T jets and the two b -hadrons. The two K_T jets which give the minimal ΔR are assimilated to the two b -jets. The distribution of the minimal distance ΔR between the b -hadron and the corresponding selected K_T jet is shown in figure 3.7 (*right*). The fact that the b -tagging must subsequently be applied to identify the b -jets implies that there is no *a priori* particular advantages in choosing the K_T algorithm with respect to the cone algorithm, if one requests that both jets are tagged. The interest might come in case we wish to generalize to a “single tag” jet analysis to increase the selection efficiency.

3.5.3 Cone and K_T algorithms comparison

For both cone and K_T algorithms, the definition of jet depends on the parameter R_{cone} and R_{K_T} . In a sense, it has to fit at best the aperture of the physical jet. When it is too low, some particles belonging to the jet are not taken into account in the reconstruction, the resulting jet mass being therefore undervalued. Conversely, when it is too large, particles which do not really come from the original b -quark

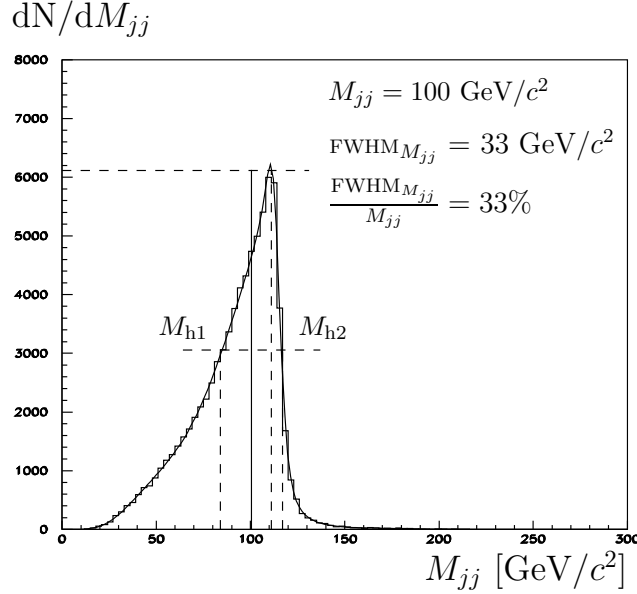


Figure 3.8: Example of dijet mass distribution obtained with the cone algorithm for $R_{cone} = 0.6$. A smooth fit [44] is performed to determine the central value and the full width at half maximum.

are counted in the jet overestimating the jet mass. This affects directly the dijet reconstruction, in particular the mass distribution which is distorted by a misplaced peak value M_{jj} and/or by an increased width $\text{FWHM}_{M_{jj}}$.

Both algorithms are optimized by requiring the best dijet mass resolution, i.e. the minimal value of $\text{FWHM}_{M_{jj}}/M_{jj}$ as a function of R_{cone} and R_{KT} . The dijet energy-momentum is obtained by adding the four-vectors of the two jets found by the algorithm:

$$p_{jj}^{\mu} = p_{j_1}^{\mu} + p_{j_2}^{\mu} \quad \Rightarrow \quad M_{jj} = \sqrt{p_{jj}^{\mu} \cdot p_{jj\mu}} \quad (3.9)$$

An example of dijet mass distribution dN/dM_{jj} obtained with the cone algorithm with $R_{cone} = 0.6$ is shown in figure 3.8. For non-optimal values of R , non-negligible tails affect the standard deviations. A smooth fit [44] of the distribution is therefore performed on which are determined the mean peak value M_{jj} and the full width at half maximum $\text{FWHM}_{M_{jj}}$. The procedure consists first in finding the maximum of the fit curve. Then the masses M_{h1} and M_{h2} corresponding to the fit values at half maximum are evaluated. The distribution parameters are finally obtained via:

$$M_{jj} = \frac{M_{h1} + M_{h2}}{2} \quad (3.10)$$

$$\text{FWHM}_{M_{jj}} = M_{h2} - M_{h1}$$

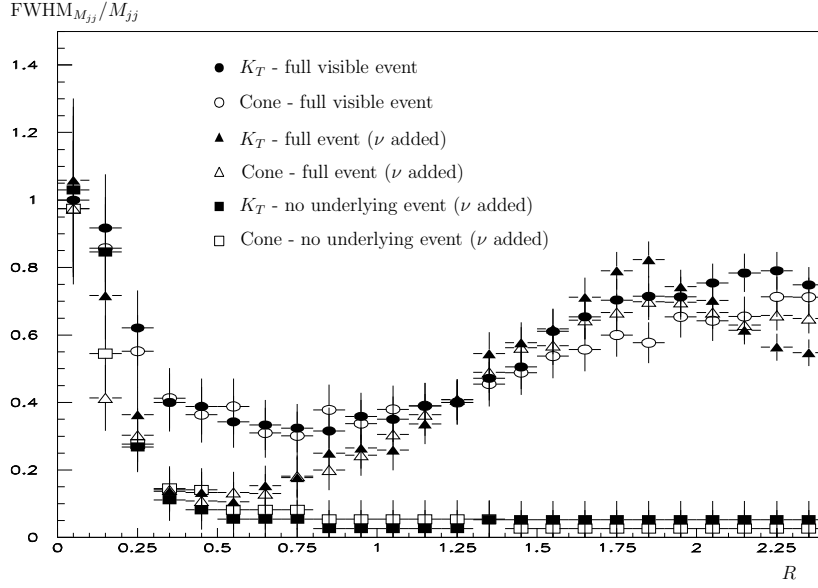


Figure 3.9: Dijet mass resolution for $H^0 \rightarrow b\bar{b}$ events as a function of the parameters R_{K_T} and R_{cone} for the K_T (\bullet , \blacktriangle , \blacksquare) and cone (\circ , \triangle , \square) algorithms respectively. The results are shown for the full visible event, the full event including neutrini and without the underlying event.

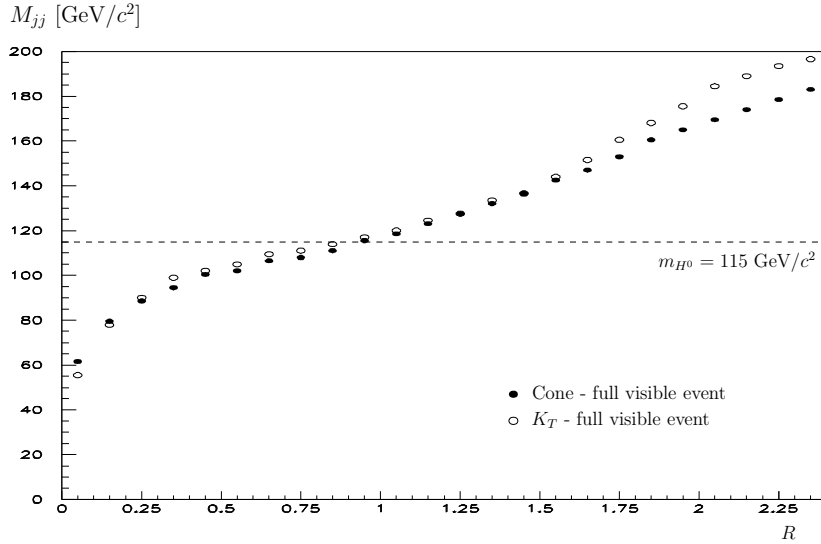


Figure 3.10: Dijet mass distribution central value M_{jj} as a function of the parameters R_{cone} and R_{K_T} for the cone (\bullet) and K_T (\circ) algorithms respectively, for the full visible event.

The performances of both algorithms were tested for several values of R_{cone} and R_{K_T} between 0.1 and 2.4. The results in terms of dijet mass resolution are presented in figure 3.9. They are very similar for both algorithms with a low resolution of $\sim 30\%$ in the $R_{cone, K_T} \in [0.5, 1.0]$ region. The cone algorithm is easier and faster at execution and, as a matter of fact, is adopted for the rest of the analysis with $R_{cone} = 0.6$. The same exercise was performed by adding the neutrino informations from the MC truth to the full visible event. Obviously the resolution is improved, in particular in the interesting region where it reaches $\sim 15\%$. For large value of R , the collection of particles not belonging to the interesting hard process becomes harmful for the resolution. Finally, figure 3.9 also shows the results obtained without the underlying event. In this case, the jet mass cannot be overestimated and the resolution remains very good ($\sim 5\%$) even for large values of R .

Besides, the dijet mass distribution central value is affected by the value of R_{cone} and R_{K_T} . Figure 3.10 shows its displacement around the generated Higgs mass $m_{H^0} = 115 \text{ GeV}/c^2$. As expected, this value is almost reached for $R \simeq 1.0$. Here again, both algorithms behave very similarly except in the uninteresting region $R > 1.7$. The selected value $R_{cone} = 0.6$ decreases the mean peak value to $M_{jj} = 100 \text{ GeV}/c^2$. This will be taken into account in the jet energy correction procedure presented in the next section.

3.6 Jet energy correction

Figure 3.1 represents the Higgs decay $H^0 \rightarrow b\bar{b}$, followed by the parton shower with emission of gluons and the string formation. After the string fragmentation, hadrons are formed and emitted in jets. The energy carried by the two initial quarks before the parton shower is expected to be recovered in the jets. Instead, we observe an energy loss after the reconstruction of b -jets with low transverse momentum. Indeed, the ratio $E^b/E^{b\text{-jet}}$ between the energies of the initial b -quark before parton shower and its corresponding b -jet is expressed as a function of $p_T^{b\text{-jet}}$ in figure 3.11 (*left*). The quark and flavour informations are obtained from the MC truth and the jets are reconstructed by the cone algorithm with $R_{cone} = 0.6$. For $p_T^{b\text{-jet}} \simeq 30 \text{ GeV}/c$, about 90% of the energy is recovered while only 70% for $p_T^{b\text{-jet}} \simeq 10 \text{ GeV}/c$. An hyperbolic fit (3.11) can be performed in order to parameterize the energy loss:

$$\frac{E^b}{E^{b\text{-jet}}} = f(p_T) = a + \frac{b}{(p_T^{b\text{-jet}} - c)} \quad \text{with:} \quad \begin{cases} a &= 0.979 \pm 9.703 \cdot 10^{-4} \\ b &= 2.963 \pm 5.193 \cdot 10^{-2} \\ c &= 2.736 \pm 1.044 \cdot 10^{-1} \\ \chi^2 &= 16.88 \quad N_p^{\text{fit}} = 95 \end{cases} \quad (3.11)$$

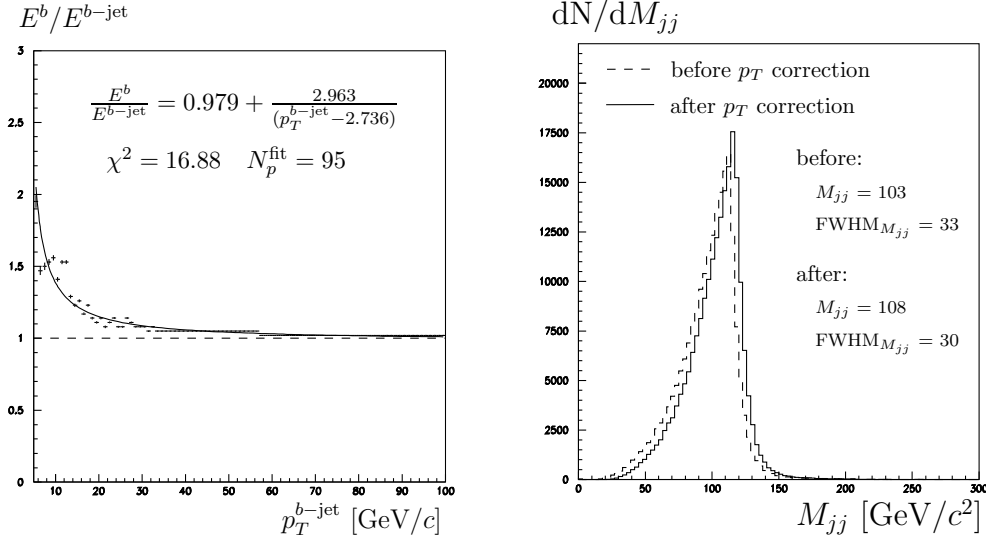


Figure 3.11: Hyperbolic fit of the ratio $E^b/E^{b\text{-jet}}$ as a function of $p_T^{b\text{-jet}}$ for b -jets reconstructed by the cone algorithm with $R_{\text{cone}} = 0.6$ (*left*). Dijet mass distribution with $R_{\text{cone}} = 0.6$ before and after p_T hyperbolic correction (*right*).

The b -jet energy-momentum and, by the fact, the mass can be corrected depending on the jet transverse momentum by the inversion of (3.11):

$$\begin{aligned}
 E_{\text{corr.}}^{b\text{-jet}} &= E^{b\text{-jet}} \times f(p_T) \\
 \vec{p}_{\text{corr.}}^{b\text{-jet}} &= \vec{p}^{b\text{-jet}} \times f(p_T) \\
 m_{\text{corr.}}^{b\text{-jet}} &= m^{b\text{-jet}} \times f(p_T)
 \end{aligned}
 \tag{3.12}$$

This affects the dijet mass distribution shown before and after p_T hyperbolic correction in figure 3.11 (*right*). The central value is displaced toward the original Higgs generated mass while the width is reduced improving slightly the resolution from 32% to 28%.

The end of this section aims to understand the origin of such energy loss in low- p_T b -jets reconstruction. As it concerns low- p_T jets, it is not likely that neutrino are responsible for it. An analysis taking into account only the final state particles originating from the interesting hard process - that is without the underlying event - but including neutrino (from MC truth) exhibits similar results than in figure 3.11 (*left*). This demonstrates that neutrino are not responsible for this behaviour in a dominant way.

Another explanation is a loss of particles outside the detector acceptance. Indeed, when the b -hadron seed is emitted close to the boundaries, the constructed cone can

lay partially outside the acceptance. In order to examine this hypothesis, three regions in θ are considered: $\theta < 50$ mrad, $50 < \theta < 250$ mrad and $\theta > 250$ mrad. The study is performed without underlying event and including neutrini. The b -hadrons are required to be in $15 < \theta < 330$ mrad. Two cases are envisaged: in the first one we only consider particles in the acceptance to build the jets, in the second we consider all the particles. The ratio $E^b/E^{b\text{-jet}}$ evaluated as a function of $p_T^{b\text{-jet}}$ for the three regions is presented in figure 3.12. We observe that the acceptance restriction has almost no influence in the middle region as expected, but also in the region close to the beam. The effect is significant only in the outer region. In definitive, low- p_T jets emitted near the upper limit of the acceptance are not well reconstructed as some particles are lost outside the detector.

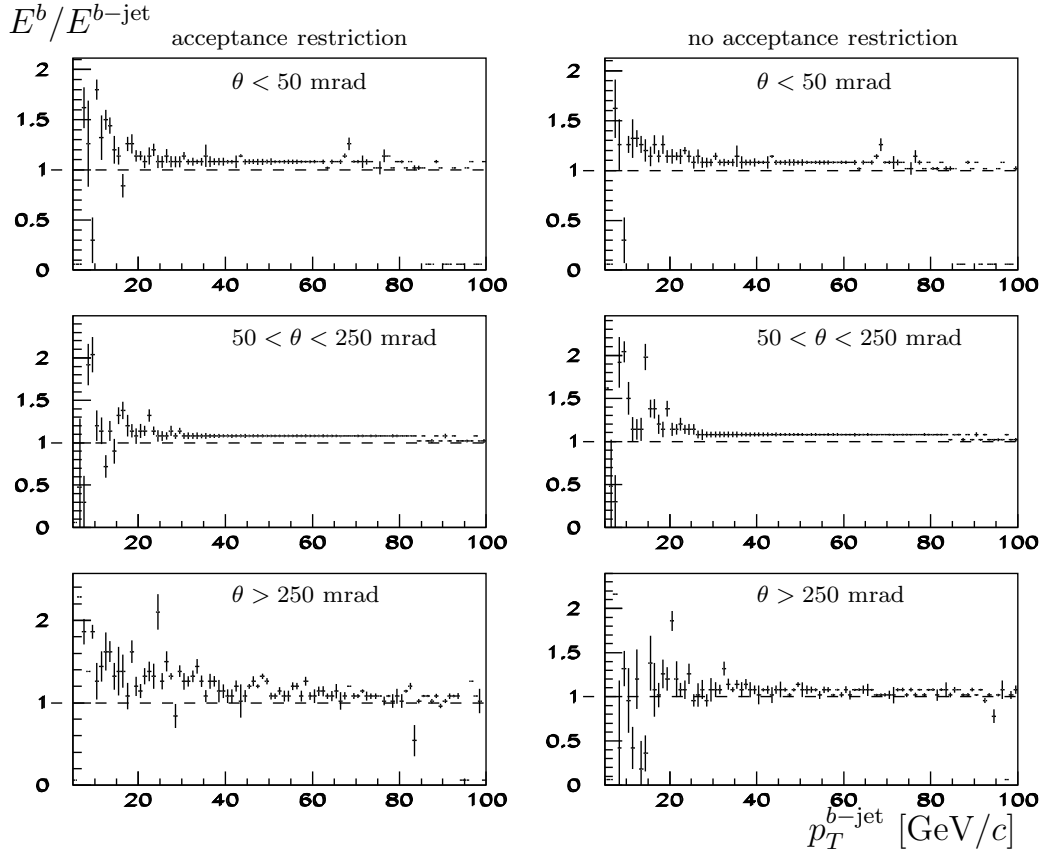


Figure 3.12: Ratio $E^b/E^{b\text{-jet}}$ as a function of $p_T^{b\text{-jet}}$ for b -hadrons emitted in the three regions $\theta < 50$ mrad, $50 < \theta < 250$ mrad and $\theta > 250$ mrad. On the left, jets are reconstructed using only final particles which fall inside the LHCb acceptance. On the right, this restriction is removed.

Another reason for degradation of the b -jet information is the presence of extra jets due to parton shower. For verification, the extra jet four-vector $p_{\text{extra jet}}^\mu$ is defined as:

$$p_{\text{extra jet}}^\mu = p_{H^0}^\mu - p_{j_1}^\mu - p_{j_2}^\mu \quad (3.13)$$

where $p_{H^0}^\mu$ is obtained from the MC truth and $p_{j_1}^\mu$ and $p_{j_2}^\mu$ are reconstructed without the underlying event and including neutrino. For this study no acceptance restriction is required. Finally a third jet $p_{j_3}^\mu$ is reconstructed with the cone algorithm in the direction $\vec{p}_{\text{extra jet}}$ exactly like the two others.

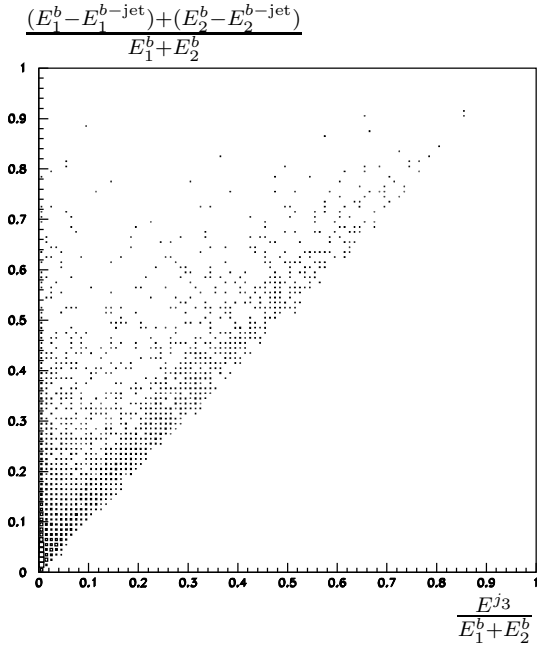


Figure 3.13: Correlation between the third reconstructed jet energy and the energy loss with respect to the initial b -quarks energy $\alpha \frac{E^{j_3}}{E_1^b + E_2^b}$ vs $\frac{(E_1^b - E_1^{b\text{-jet}}) + (E_2^b - E_2^{b\text{-jet}})}{E_1^b + E_2^b}$, for events containing at least one b -jet with low transverse momentum below 30 GeV/ c .

Figure 3.13 represents the correlation between the third jet energy and the energy loss with respect to the initial b -quarks energy in the two b -jets. Only events with at least one low- p_T b -jet ($p_T^{b\text{-jet}} < 30$ GeV/ c) are considered and the energy loss is defined as $(E_1^b - E_1^{b\text{-jet}}) + (E_2^b - E_2^{b\text{-jet}})$. A correlation band at $\sim 45^\circ$ confirms that a third jet is present. A vertical strip is visible at $E^{j_3} \simeq 0$. In this case, no physical jet really exists in the $\vec{p}_{\text{extra jet}}$ direction which might imply the presence of more than one extra-jet.

In conclusion, the origin of the energy loss in low- p_T b -jets reconstruction is mainly the loss of energy out of the detector in the upper limit of the acceptance. A specific jet correction as a function of $\theta^{b\text{-jet}}$ could therefore be envisaged in addition to the correction as a function of p_T (see eq. (3.11)). The resolution is also degraded by the presence of extra jets carrying part of the energy elsewhere.

3.7 Investigations for discriminant variables

The kinematics selections 1 - 4 in § 3.4.3 associated to the lepton isolation requirements in § 3.4.2 lead to a low value of 0.44 for the significance (see table 3.7). These

cuts are more or less equivalent to those applied in [40] in the first steps of the analysis leading to $S/\sqrt{B} = 0.59$. Although small differences exist between the two studies (the events generation is performed using PYTHIA 6.134 and the selection criteria are applied in a slightly different order in [40]), the gap is too important and our selections have to be improved or completed to better reduce the background.

For that purpose, it has been decided to try the usage of neural networks. A neural network is a stand-alone machine which accepts several variables in input and outputs a unique answer. During a preliminary phase, it has to be trained with events for which the output answer is known. Once trained, it should provide the probability on whether an unknown event should be considered as signal or background.

The essential part of the work consists in finding the adequate observables. These should in the most promising case behave or, at least, be correlated differently for signal and background. Anyway, the hope is that the differences could be detected by the neural network and exploited for the discrimination.

The next two sections discuss about the search for such appropriate discriminant variables. In particular, the observed asymmetry between the b -jets pseudorapidity η_b and $\eta_{\bar{b}}$ distributions for the irreducible backgrounds involving $Z^0 \rightarrow b\bar{b}$ decays is detailed in § 3.7.1. Section 3.7.2 presents differences between signal and background in the b -dijet polar angle $\theta_{jj}^{(V^*)}$ distributions in the primary off-shell gauge boson $V^* = W^{\pm*}$ or Z^{0*} rest frame. The V^* decays into a Higgs (a Z^0) and an associated gauge boson for the signal (resp. background). The difficulty precisely comes from the escape of the neutrino from the W^\pm decay which has to be reconstructed artificially. The study about background discrimination using neural networks is finally presented in section 3.8. The neural network structure and calculation are described in § 3.8.1 and 3.8.2. The results for $t\bar{t}$ and irreducible background reduction are discussed in § 3.8.3.

3.7.1 $Z^0 \rightarrow b\bar{b}$ decay products pseudorapidity asymmetry

The Electroweak theory predicts an asymmetry between the b -jets pseudorapidity distributions in the irreducible backgrounds Z^0W^\pm and Z^0Z^0 - which involve Z^0 decay into $b\bar{b}$ - which disappears in the signal H^0W^\pm/Z^0 channels. This effect is present in PYTHIA as shown in figure 3.14. This section aims to explain the origin of such asymmetries which could be exploited for the background discrimination. We have done a detailed study based on single $q\bar{q} \rightarrow Z^0 \rightarrow b\bar{b}$ events for which a similar phenomenon is observed.

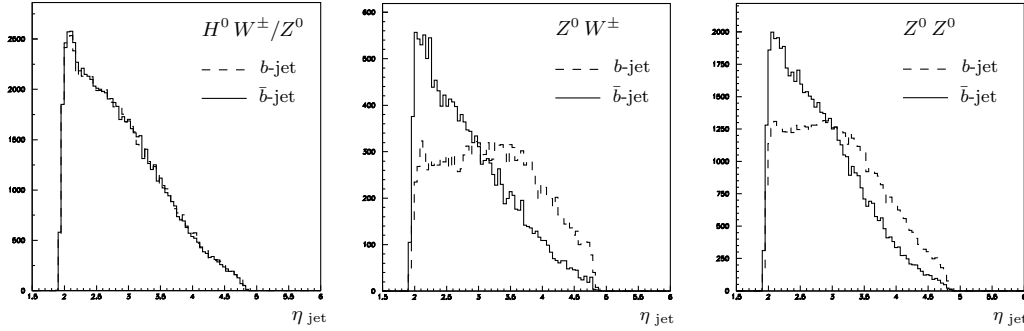


Figure 3.14: b - and \bar{b} -jets pseudorapidity distributions for signal H^0W^\pm/Z^0 (left) and irreducible backgrounds Z^0W^\pm (middle) and Z^0Z^0 (right). The b - and \bar{b} -flavours are known from the MC truth.

The LHCb detector geometry imposes that only events in which the hard process is produced in the forward direction with respect to the interaction point are considered. In Z^0Z^0 events, the primary off-shell Z^{0*} boson is produced via $q\bar{q}$ annihilation. When the quark flavour is light (u or d), the quark q predominantly comes directly from one of the two protons while the antiquark \bar{q} is produced in the quark sea, as pictured in figure 3.15. It results that the quark is more “rapid” than the antiquark and that it provides the major part of the Z^{0*} momentum.

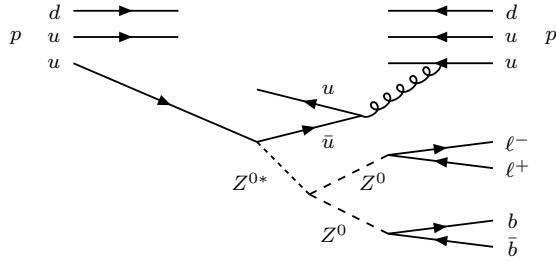


Figure 3.15: Schema of Z^0Z^0 event production in p - p collision. In this example, the off-shell gauge boson is produced via light $q\bar{q}$ annihilation. The quark u comes directly from the incoming proton while the \bar{u} is produced in the quark sea. It is more “rapid” than the antiquark and therefore provides the major part of the Z^{0*} momentum.

In our specific $q\bar{q} \rightarrow Z^0$ study, the Z^0 boson is also emitted preferentially in the same direction than the quark and, as exclusively forward Z^0 are observed in these events, light quarks propagate more often forward than backward. For the heavier flavours (c , s , b or t), as both q and \bar{q} are produced in the quark sea, such asymmetry vanish. Table 3.8 shows the proportion of Z^0 parent quarks emitted forward and backward with respect to the Z^0 momentum for every flavours, as predicted by PYTHIA. The fact that u - and d -quarks are lighter and that the quark comes directly from the proton at first order implies that $u\bar{u} \rightarrow Z^0$ and $d\bar{d} \rightarrow Z^0$ are very frequent (88.3%).

QF	flavour	N_{events}	forward	backward
1	d	169044 (32.2%)	131082 (77.5%)	37962 (22.5%)
2	u	294481 (56.1%)	252980 (85.9%)	41501 (14.1%)
3	s	36699 (7.0%)	18395 (50.1%)	18304 (49.9%)
4	c	24681 (4.7%)	12422 (50.3%)	12259 (49.7%)
5	b	118 (< 0.1%)	55 (46.6%)	63 (53.4%)
6	t	0	0	0
total	<i>down</i>	205861 (39.2%)	149532 (72.6%)	56329 (27.4%)
total	<i>up</i>	319162 (60.8%)	265402 (83.1%)	53760 (16.9%)
total		525023	414934 (79.0%)	110089 (21.0%)

Table 3.8: Proportion of Z^0 parent quarks emitted forward and backward with respect to the Z^0 momentum for every flavours in $q\bar{q} \rightarrow Z^0$ events, as predicted by PYTHIA 6.319 with CTEQ5L (see table 3.4).

A difference between the H^0 and the Z^0 bosons is that the H^0 is a spin 0 particle while Z^0 has spin 1. The asymmetry studied here is a phenomenon similar to the one analyzed in the $e^+e^- \rightarrow Z^0 \rightarrow \ell^+\ell^-$ process at LEP, PEP and DESY. It was shown that, even if the electron beams are not polarized longitudinally, the probability that the Z^0 spin is aligned with the e^+ is different than for the e^- , leading to a non-zero Z^0 average polarization [45]. In our specific case $q\bar{q} \rightarrow Z^0 \rightarrow b\bar{b}$, we consider the interaction Lagrangian \mathcal{L}_{qZ} between Z^0 and quarks which has different components for left- and right-handed *up* and *down* quarks:

$$\begin{aligned}
\mathcal{L}_{qZ} = \sum_i \left[& - u_{Li}^+ \tilde{\sigma}^\mu u_{Li} \left(\frac{e}{\sin(2\theta_W)} \right) Z_\mu \cdot \left(1 - \frac{4}{3} \sin^2 \theta_W \right) \right. \\
& + u_{Ri}^+ \sigma^\mu u_{Ri} \left(\frac{e}{\sin(2\theta_W)} \right) Z_\mu \cdot \frac{4}{3} \sin^2 \theta_W \\
& + d_{Li}^+ \tilde{\sigma}^\mu d_{Li} \left(\frac{e}{\sin(2\theta_W)} \right) Z_\mu \cdot \left(1 - \frac{2}{3} \sin^2 \theta_W \right) \\
& \left. - d_{Ri}^+ \sigma^\mu d_{Ri} \left(\frac{e}{\sin(2\theta_W)} \right) Z_\mu \cdot \frac{2}{3} \sin^2 \theta_W \right] \quad (3.14)
\end{aligned}$$

From (3.14) result the differential transition rates per unit of $\cos \theta$, where θ is the angle between the direction of the quark momentum and the Z^0 spin, for *down* quarks:

$$\frac{d\Gamma(d_i\bar{d}_i)}{d\cos\theta} = \frac{3G_F M_Z^3}{32\sqrt{2}\pi} \left[\left(1 - \frac{2}{3} \sin^2 \theta_W \right)^2 (1 - \cos\theta)^2 + \left(\frac{2}{3} \sin^2 \theta_W \right)^2 (1 + \cos\theta)^2 \right] \quad (3.15)$$

and up quarks:

$$\frac{d\Gamma(u_i\bar{u}_i)}{d\cos\theta} = \frac{3G_F M_Z^3}{32\sqrt{2}\pi} \left[\left(1 - \frac{4}{3}\sin^2\theta_W\right)^2 (1 - \cos\theta)^2 + \left(\frac{4}{3}\sin^2\theta_W\right)^2 (1 + \cos\theta)^2 \right] \quad (3.16)$$

By integration over $\cos\theta$, we obtain the forward and backward decay partial widths:

$$\begin{aligned} \Gamma_{d_i\bar{d}_i} \left(0 < \theta < \frac{\pi}{2}\right) &= \frac{G_F M_Z^3}{32\sqrt{2}\pi} \left(1 - \frac{4}{3}\sin^2\theta_W + \frac{32}{9}\sin^4\theta_W\right) = 5.486 \cdot 10^{-2} \text{ GeV} \\ \Gamma_{d_i\bar{d}_i} \left(\frac{\pi}{2} < \theta < \pi\right) &= \frac{G_F M_Z^3}{32\sqrt{2}\pi} \left(7 - \frac{28}{3}\sin^2\theta_W + \frac{32}{9}\sin^4\theta_W\right) = 3.122 \cdot 10^{-1} \text{ GeV} \\ \Gamma_{d_i\bar{d}_i} &= \Gamma_{d_i\bar{d}_i} \left(0 < \theta < \frac{\pi}{2}\right) + \Gamma_{d_i\bar{d}_i} \left(\frac{\pi}{2} < \theta < \pi\right) = 3.671 \cdot 10^{-1} \text{ GeV} \end{aligned}$$

and

$$\begin{aligned} \Gamma_{u_i\bar{u}_i} \left(0 < \theta < \frac{\pi}{2}\right) &= \frac{G_F M_Z^3}{32\sqrt{2}\pi} \left(1 - \frac{8}{3}\sin^2\theta_W + \frac{128}{9}\sin^4\theta_W\right) = 7.147 \cdot 10^{-2} \text{ GeV} \\ \Gamma_{u_i\bar{u}_i} \left(\frac{\pi}{2} < \theta < \pi\right) &= \frac{G_F M_Z^3}{32\sqrt{2}\pi} \left(7 - \frac{56}{3}\sin^2\theta_W + \frac{128}{9}\sin^4\theta_W\right) = 2.133 \cdot 10^{-1} \text{ GeV} \\ \Gamma_{u_i\bar{u}_i} &= \Gamma_{u_i\bar{u}_i} \left(0 < \theta < \frac{\pi}{2}\right) + \Gamma_{u_i\bar{u}_i} \left(\frac{\pi}{2} < \theta < \pi\right) = 2.848 \cdot 10^{-1} \text{ GeV} \end{aligned}$$

with $\sin^2\theta_W = 0.2324$. The probabilities that the Z^0 is produced with the spin parallel to the quark and the antiquark can be evaluated:

$$\begin{aligned} \mathcal{P}(Z^0 \text{ spin} \parallel d_i) &= \mathcal{P}_{d_i\bar{d}_i} \left(0 < \theta < \frac{\pi}{2}\right) = \frac{\Gamma_{d_i\bar{d}_i} \left(0 < \theta < \frac{\pi}{2}\right)}{\Gamma_{d_i\bar{d}_i}} = 15.0\% \\ \mathcal{P}(Z^0 \text{ spin} \parallel \bar{d}_i) &= \mathcal{P}_{d_i\bar{d}_i} \left(\frac{\pi}{2} < \theta < \pi\right) = \frac{\Gamma_{d_i\bar{d}_i} \left(\frac{\pi}{2} < \theta < \pi\right)}{\Gamma_{d_i\bar{d}_i}} = 85.0\% \end{aligned} \quad (3.17)$$

$$\begin{aligned} \mathcal{P}(Z^0 \text{ spin} \parallel u_i) &= \mathcal{P}_{u_i\bar{u}_i} \left(0 < \theta < \frac{\pi}{2}\right) = \frac{\Gamma_{u_i\bar{u}_i} \left(0 < \theta < \frac{\pi}{2}\right)}{\Gamma_{u_i\bar{u}_i}} = 25.1\% \\ \mathcal{P}(Z^0 \text{ spin} \parallel \bar{u}_i) &= \mathcal{P}_{u_i\bar{u}_i} \left(\frac{\pi}{2} < \theta < \pi\right) = \frac{\Gamma_{u_i\bar{u}_i} \left(\frac{\pi}{2} < \theta < \pi\right)}{\Gamma_{u_i\bar{u}_i}} = 74.9\% \end{aligned} \quad (3.18)$$

From (3.17) and (3.18) and using the results of table 3.8, we derive the probabilities, for up and $down$ flavours, that the Z^0 spin is oriented forward and backward:

$$\begin{aligned} \mathcal{P}(Z^0 \text{ spin forward})|_{f_i\bar{f}_i} &= \mathcal{P}(f_i\bar{f}_i) \times \\ &[\mathcal{P}(f_i\bar{f}_i \text{ forward}) \cdot \mathcal{P}(Z^0 \text{ spin} \parallel f_i) + \mathcal{P}(f_i\bar{f}_i \text{ backward}) \cdot \mathcal{P}(Z^0 \text{ spin} \parallel \bar{f}_i)] \end{aligned} \quad (3.19)$$

$$\mathcal{P}(Z^0 \text{ spin backward})|_{f_i \bar{f}_i} = \mathcal{P}(f_i \bar{f}_i) \times [\mathcal{P}(f_i \bar{f}_i \text{ forward}) \cdot \mathcal{P}(Z^0 \text{ spin} \parallel \bar{f}_i) + \mathcal{P}(f_i \bar{f}_i \text{ backward}) \cdot \mathcal{P}(Z^0 \text{ spin} \parallel f_i)] \quad (3.20)$$

The numerical results presented in table 3.9 show that there is a preference for the Z^0 spin to be directed backward with respect to the Z^0 momentum.

flavour	$\mathcal{P}(Z^0 \text{ spin}) _{f_i \bar{f}_i}$	
	forward	backward
$d_i \bar{d}_i$	13.4%	25.8%
$u_i \bar{u}_i$	20.4%	40.4%
total	33.8%	66.2%

Table 3.9: Probability that the Z^0 spin is oriented forward and backward with respect to the Z^0 momentum for the Z^0 parents flavour *up* and *down*.

After the Z^0 production, its decay into $b\bar{b}$ is considered. The probabilities that the b -quark is emitted forward and backward in the Z^0 referential are obtained by combination of (3.19) and (3.20) with (3.17) derived from the interaction Lagrangian between Z^0 and *down* quarks:

$$\mathcal{P}(b \text{ forward})|_{f_i \bar{f}_i} = \mathcal{P}(Z^0 \text{ spin} \parallel b) \cdot \mathcal{P}(Z^0 \text{ spin forward})|_{f_i \bar{f}_i} + \mathcal{P}(Z^0 \text{ spin} \parallel \bar{b}) \cdot \mathcal{P}(Z^0 \text{ spin backward})|_{f_i \bar{f}_i} \quad (3.21)$$

$$\mathcal{P}(b \text{ backward})|_{f_i \bar{f}_i} = \mathcal{P}(Z^0 \text{ spin} \parallel b) \cdot \mathcal{P}(Z^0 \text{ spin backward})|_{f_i \bar{f}_i} + \mathcal{P}(Z^0 \text{ spin} \parallel \bar{b}) \cdot \mathcal{P}(Z^0 \text{ spin forward})|_{f_i \bar{f}_i} \quad (3.22)$$

The obtained probabilities exposed in table 3.10 show a preference for the b -quark to be produced in the forward direction in the Z^0 rest frame. This is in agreement with the b -quark pseudorapidity distribution $\eta_b^{(Z^0)}$ in the Z^0 referential obtained from a set of 525'023 $Z^0 \rightarrow b\bar{b}$ events and presented in figure 3.16.

By transposing this phenomenon in the laboratory rest frame in which exclusively forward gauge bosons are observed, these observations are also in accord with the irreducible backgrounds distributions presented in figure 3.14 in which the b -jet is in average more rapid than the \bar{b} -jet.

flavour	$\mathcal{P}(b) \big _{f_i \bar{f}_i}$	
	forward	backward
$d_i \bar{d}_i$	23.9%	15.3%
$u_i \bar{u}_i$	37.4%	23.4%
total	61.3%	38.7%

Table 3.10: Probability for the b -quark from $Z^0 \rightarrow b\bar{b}$ to be emitted forward and backward in the Z^0 rest frame when the Z^0 is produced via *down* and *up* quarks annihilation.

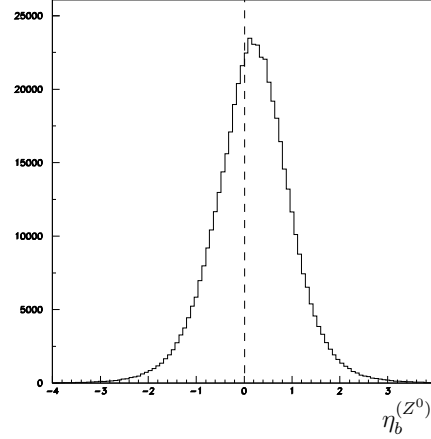


Figure 3.16: Distribution of the b -quark pseudorapidity $\eta_b^{(Z^0)}$ in the Z^0 referential for a set of $Z^0 \rightarrow b\bar{b}$ events. The b is emitted in the forward direction of the Z^0 boson 60.5% of the cases while only a fraction 39.5% goes in the backward direction.

3.7.2 Primary boson reconstruction

This section aims to exploit the event kinematics to suggest a way to reconstruct the primary off-shell gauge boson decaying into the Higgs and an associated gauge boson. Figure 3.17 (*left*) represents the primary boson $V^* = W^{\pm*}$ or Z^{0*} decay into a Higgs and an associated gauge boson $V = W^\pm$ or Z^0 , themselves decaying subsequently following $H^0 \rightarrow b\bar{b}$ and $V \rightarrow \ell_1 \ell_2$.

The primary boson is reconstructed from the two b -jets on one part, and from the two leptons on the other:

$$p_{H^0}^\mu = p_{jj}^\mu = p_{J_1}^\mu + p_{J_2}^\mu \quad (3.23)$$

$$p_V^\mu = p_{\ell_1}^\mu + p_{\ell_2}^\mu \quad (3.24)$$

$$p_{V^*}^\mu = p_{jj}^\mu + p_V^\mu = p_{J_1}^\mu + p_{J_2}^\mu + p_{\ell_1}^\mu + p_{\ell_2}^\mu \quad (3.25)$$

As previously explained, an event is considered either as Z^0 - or *not* Z^0 -associated depending on whether a lepton pair is compatible with the Z^0 mass or not (see § 3.4.2). For Z^0 -associated events, both leptons are known and the primary boson four-vector

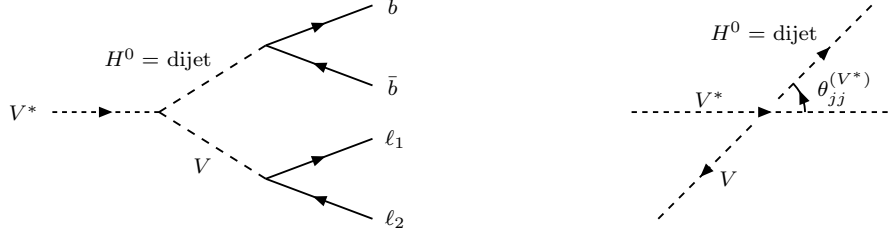


Figure 3.17: Primary off-shell gauge boson V^* decaying into $H^0 \rightarrow b\bar{b}$ and an associated gauge boson $V \rightarrow \ell_1 \ell_2$ (*left*). $V^* \rightarrow H^0 + V$ in the V^* rest frame with the b -dijet polar angle with respect to the V^* direction $\theta_{jj}^{(V^*)}$ (*right*).

is easily reconstructed. The situation is more complicated for *not Z^0 -associated* events as only one isolated lepton ℓ_1 is known. Most of these events have a W^\pm associated boson which decays into $\ell \nu_\ell$, the neutrino escaping detection. The starting point is to assume that the V^* is emitted longitudinally along the z -axis with a quasi-null transverse momentum:

$$\vec{p}_{TV^*} = \vec{p}_{TV} + \vec{p}_{TH^0} \simeq 0 \quad \Rightarrow \quad \vec{p}_{TV} = -\vec{p}_{TH^0} \quad (3.26)$$

The primary boson transverse momentum p_{TV^*} distribution for *not Z^0 -associated* events is shown in figure 3.18 (*left*). It is obtained by combination of the Higgs and associated gauge bosons informations from the Monte Carlo truth. Its value is quite small - $p_{TV^*} \leq 25$ GeV/ c in about 75% of the cases - compared to the Higgs one (see fig. 3.2 (*right*)). Following assumption (3.26), the Higgs and associated gauge bosons transverse momenta should be equal in magnitude. This is confirmed in figure 3.18 (*right*) which clearly shows a correlation between p_{TH^0} and p_{TV} for *not Z^0 -associated* events. In the transverse plane, the gauge boson decay implies $\vec{p}_{TV} = \vec{p}_{T\ell_1} + \vec{p}_{T\ell_2}$. The unknown lepton transverse momentum can be extracted:

$$\vec{p}_{T\ell_2} = \vec{p}_{TV} - \vec{p}_{T\ell_1} \stackrel{(3.26)}{=} -\vec{p}_{TH^0} - \vec{p}_{T\ell_1} = -\vec{p}_{TJ_1} - \vec{p}_{TJ_2} - \vec{p}_{T\ell_1} \quad (3.27)$$

Considering the associated boson four-vector:

$$p_V^\mu = p_{\ell_1}^\mu + p_{\ell_2}^\mu = (E_{\ell_1} + E_{\ell_2}, \vec{p}_{\ell_1} + \vec{p}_{\ell_2})$$

its invariant mass is:

$$\begin{aligned} m_V^2 &= (E_{\ell_1} + E_{\ell_2})^2 - (\vec{p}_{\ell_1} + \vec{p}_{\ell_2})^2 \\ &= \underbrace{E_{\ell_1}^2 - \vec{p}_{\ell_1}^2}_{=m_{\ell_1}^2} + \underbrace{E_{\ell_2}^2 - \vec{p}_{\ell_2}^2}_{=m_{\ell_2}^2} + 2E_{\ell_1}E_{\ell_2} - 2\vec{p}_{\ell_1} \cdot \vec{p}_{\ell_2} \end{aligned} \quad (3.28)$$

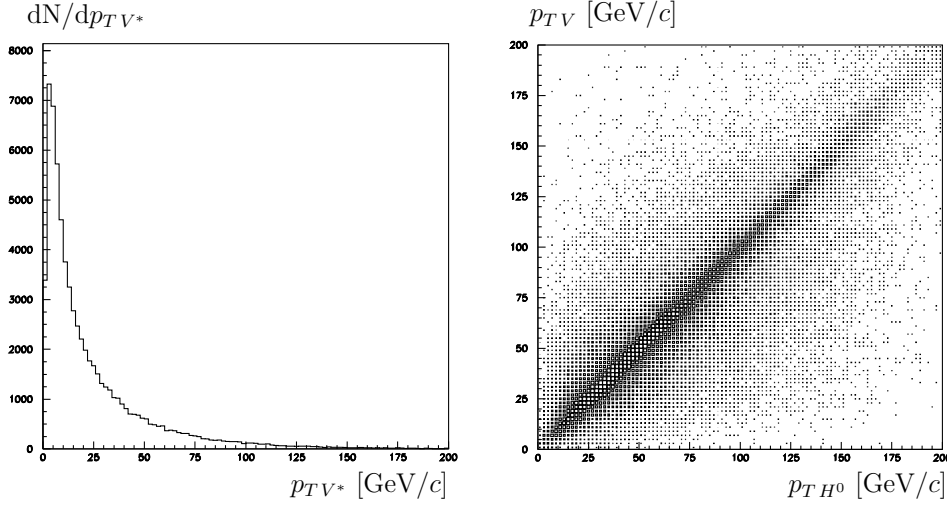


Figure 3.18: Primary boson transverse momentum p_{TV^*} distribution for *not* Z^0 -associated events (*left*). Correlation between the Higgs boson and the associated gauge boson transverse momenta “ p_{TH^0} vs p_{TV} ” for *not* Z^0 -associated events (*right*). The informations are obtained from the MC truth.

Neglecting the mass of the second lepton $m_{\ell_2} = 0$:

$$E_{\ell_2} \simeq |\vec{p}_{\ell_2}| = \sqrt{p_{T\ell_2}^2 + p_{z\ell_2}^2} \quad (3.29)$$

With $\vec{p}_{\ell_1} \cdot \vec{p}_{\ell_2} = \vec{p}_{T\ell_1} \cdot \vec{p}_{T\ell_2} + p_{z\ell_1}p_{z\ell_2}$, (3.28) becomes:

$$m_V^2 = m_{\ell_1}^2 + 2E_{\ell_1} \sqrt{p_{T\ell_2}^2 + p_{z\ell_2}^2} - 2\vec{p}_{T\ell_1} \cdot \vec{p}_{T\ell_2} - 2p_{z\ell_1}p_{z\ell_2} \quad (3.30)$$

Squaring (3.30) and using (3.27), we obtain a 2nd-degree equation in $p_{z\ell_2}$ with solutions:

$$p_{z\ell_2}^{\pm} = \frac{4Ap_{z\ell_1} \pm \sqrt{16E_{\ell_1}^2 [A^2 - 4p_{T\ell_2}^2 (E_{\ell_1}^2 - p_{z\ell_1}^2)]}}{8(E_{\ell_1}^2 - p_{z\ell_1}^2)} \quad (3.31)$$

$$\text{where:} \quad A = m_V^2 - m_{\ell_1}^2 + 2\vec{p}_{T\ell_1} \cdot \vec{p}_{T\ell_2}$$

According to the respective reduced cross-sections for signal channels $H^0 W^{\pm}$ and $H^0 Z^0$ (see table 3.5), the V mass is set to $m_V = 86\% \cdot m_W + 14\% \cdot m_Z \simeq 82 \text{ GeV}/c^2$ for the calculations. With the second lepton energy (3.29) and momentum (3.27) and (3.31), the two solutions for the primary off-shell gauge boson four-vectors $p_{V^*}^{\pm\mu}$

in (3.25) can be reconstructed. We define $\theta_{jj}^{(V^*)}$ as the b -dijet polar angle in the V^* referential (see figure 3.17 (*right*)). For *not* Z^0 -associated events, two solutions $\theta_{jj}^{(V_\pm^*)}$ are considered instead of a unique one for Z^0 -associated events. Obviously, only one of the two is suitable but cannot be distinguished. The distributions of $\cos(\theta_{jj}^{(V^*)})$ for the signal $H^0 W^\pm/Z^0$ and the irreducible backgrounds $Z^0 Z^0$ and $Z^0 W^\pm$ classified following *not* Z^0 - and Z^0 -associated events are shown in figure 3.19. Noticeable differences between signal and backgrounds encourage the use of this variable for background discrimination. Furthermore, the same study with a Higgs mass equal to the Z^0 one ($m_{H^0} = 91 \text{ GeV}/c^2$) was performed in order to ensure that the observed differences were due to the spin structure of the event and not to the mass difference between H^0 and Z^0 and brought to the same conclusion.

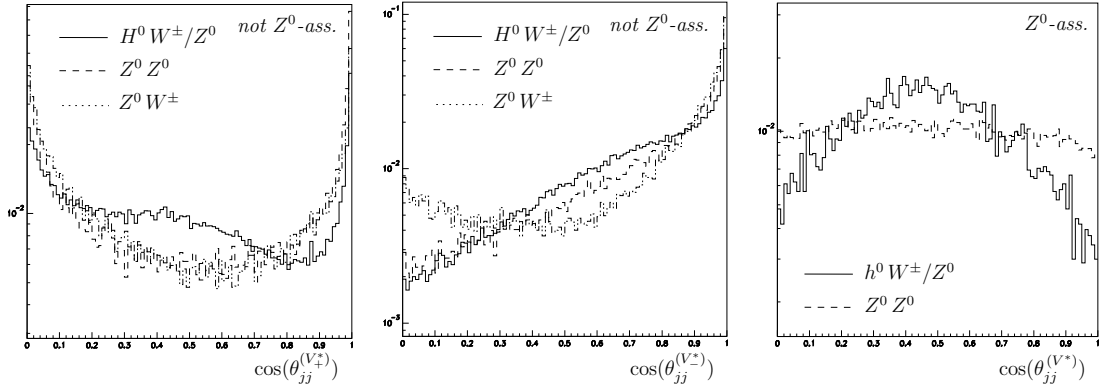


Figure 3.19: Cosine of the b -dijet polar angle in the primary boson V^* rest frame for the signal $H^0 W^\pm/Z^0$ and the irreducible backgrounds $Z^0 Z^0$ and $Z^0 W^\pm$ classified following *not* Z^0 - and Z^0 -associated events. In the first case, the results for the two solutions (3.31) are given.

3.8 Background discrimination using neural networks

We have evaluated the usage of neural network techniques to discriminate the background from the signal on the events that passed the selection procedure described in § 3.4. The criteria seen so far being too weak to use standard cuts, the hope is that some correlations could be detected by a neural network and exploited for background discrimination. The method consists in giving a set of suitable parameters to a neural network which is trained with Monte Carlo events to give an answer 1

for signal and 0 for background. Once trained it should be able to provide an answer (a probability) for an event to be a signal or a background.

3.8.1 Multi-Layer Perceptron

In practice, the neural network chosen is a Multi-Layer Perceptron (MLP) implemented in the MLPfit package [46] whose routines are called in a standalone program.

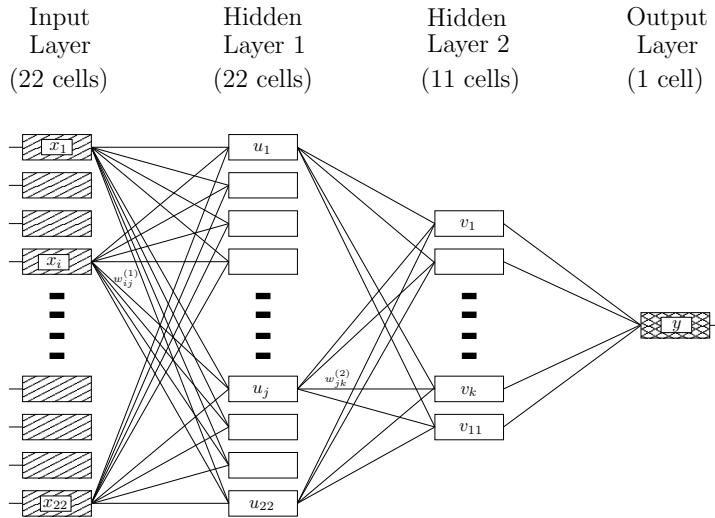


Figure 3.20: Schema of the Multi-Layer Perceptron with the input layer containing 22 cells corresponding to the 22 input parameters, the two hidden layers (22 and 11 cells) and the output layer giving the neural network answer.

A schema of the MLP is presented in figure 3.20. Our baseline configuration contains four layers: the input layer (22 cells), two hidden layers (22 and 11 cells) and the output layer (1 cell). The 22 cells at the input correspond to the selected 22 event parameters (see § 3.8.2). Each of the 22 cells x_i in the input layer is connected to the 22 cells u_j of the hidden layer 1 with a weight $w_{ij}^{(1)}$. The neuron j in this layer computes a linear combination of the neurons of the previous layer with a bias $w_{0j}^{(1)}$, which is then passed through a transfer function F according to:

$$u_j = F \left(w_{0j}^{(1)} + \sum_i w_{ij}^{(1)} x_i \right)$$

The same procedure is then applied in the successive layers up to the output layer. The transfer function of the output neuron is linear $F(t) = t$ whereas it is a sigmoid $F(t) = \frac{1}{1+e^{-t}}$ for the hidden neurons.

Before utilization, the neural network is trained during the so-called *learning* or *testing* phase. The 22 parameters of an equal number p of known signal and background events are successively passed to the neural network together with the desired answer $t_p = 1$ for signal and $t_p = 0$ for background. A loop over all the $2 \times p$ events is called an *epoch* or a *cycle*. The MLP output o_p is compared to t_p and the weights w_{ij} , initially set to random numbers between -0.5 and 0.5, are updated at each epoch in order to minimize the error:

$$E = \sum_p e_p = \sum_p \frac{1}{2} \omega_p (o_p - t_p)^2 \quad (\text{where } \omega_p = 1 \text{ usually})$$

Several learning methods are available in MLPfit. All consist in the computation of $\partial E / \partial w_{ij} = \sum_p \partial e_p / \partial w_{ij}$ called the *back-propagation of the errors*. The Broyden, Fletcher, Goldfarb and Shanno (BFGS) method based on the mathematical theory of unconstrained minimization is adopted [47]. The learning method operating parameters are given in table 3.11.

MLP parameter	value	description
L_{method}	6	BFGS learning method
η	0.1	learning parameter
d	0.992	decay parameter ($\eta \rightarrow \eta \cdot d^{\text{epoch}}$)
ϵ	0.1	momentum factor
δ	0.0	flat spot elimination factor
N_{reset}	1000	number of epochs after which the search direction is reset to steepest descent
τ	3.0	line search precision parameter
λ	1.0	regularization parameter

Table 3.11: MLPfit learning method operating parameters.

3.8.2 MLP input parameters

The 22 MLP input patterns chosen in this work are enumerated in table 3.12. Several kinematic variables of the two b -jets j_1 and j_2 and of the isolated lepton 1 are selected. j_1 (resp. j_2) is defined as the b -jet with highest (resp. lowest) transverse momentum. The “ b -jet 1 + b -jet 2 + isolated lepton 1” transverse momentum is selected as it represents the fundamental components of the signal hard process, in particular for $H^0 W^\pm$, while, for $t\bar{t}$, the hard process contains at least an additional lepton. In the same optics, kinematic variables of the total visible event - in

pattern	variable	description
1	m_{j_1}	b -jet 1 mass
2	E_{j_1}	b -jet 1 energy
3	m_{j_2}	b -jet 2 mass
4	E_{j_2}	b -jet 2 energy
5	$p_{T j_1}$	b -jet 1 transverse momentum
6	$p_{T j_2}$	b -jet 2 transverse momentum
7	η_{j_1}	b -jet 1 pseudorapidity
8	η_{j_2}	b -jet 2 pseudorapidity
9	$ \vec{p}_{\ell_1} $	isolated lepton 1 momentum
10	$p_{T \ell_1}$	isolated lepton 1 transverse momentum
11	E_{ℓ_1}	isolated lepton 1 energy
12	$p_{T (j_1+j_2+\ell_1)}$	“ b -jet 1 + b -jet 2 + isolated lepton 1” trans. momentum
13	$p_{T \text{tot}}$	total visible event transverse momentum
14	m_{tot}	total visible event mass
15	E_{tot}	total visible event energy
16	$m_{(\text{tot}-\ell_1)}$	“total visible event - isolated lepton 1” mass
17	$\Delta R(j_1 - \ell_1)$	distance in (η, ϕ) between b -jet 1 and isolated lepton 1
18	$\Delta R(j_2 - \ell_1)$	distance in (η, ϕ) between b -jet 2 and isolated lepton 1
19	$\cos(\theta_{\ell_1}^{(jj)})$	cosine of isolated lepton 1 polar angle in the b -dijet RF
20	$\cos(\theta_{j_1}^{(jj)})$	cosine of b -jet 1 polar angle in the b -dijet RF
21	$\cos(\theta_{jj}^{(V_+^*)})$	cosine of b -dijet polar angle in the reconstructed primary boson V_+^* RF (see § 3.7.2)
22	$\cos(\theta_{jj}^{(V_-^*)})$	cosine of b -dijet polar angle in the reconstructed primary boson V_-^* RF (see § 3.7.2)

Table 3.12: MLP 22 input patterns. j_1 (j_2) is defined as the b -jet with highest (lowest) transverse momentum. *Notice:* For Z^0 -associated events, patterns 21 and 22 are identical as $\theta_{jj}^{(V_+^*)} = \theta_{jj}^{(V_-^*)} = \theta_{jj}^{(V^*)}$ (see § 3.7.2).

particular the transverse momentum - are also selected. The distance $\Delta R(j_1 - \ell_1)$ (resp. $\Delta R(j_2 - \ell_1)$) in (η, ϕ) between b -jet 1 (resp. 2) and the isolated lepton are chosen. In figure 3.21 are presented the scatter plots between these two variables for 30'000 events of $H^0 W^\pm/Z^0$ signal and $t\bar{t}$ background. For the signal, the scatter plot shows that the lepton is preferentially emitted near the b -jet with lowest p_T while there is no preference for $t\bar{t}$. This fact is exploited by the neural network for the $t\bar{t}$ discrimination.

Of course, small differences also exist between the signal and the irreducible backgrounds, in particular $Z^0 W^\pm$, but essentially due to the difference in mass between H^0 and Z^0 and thus not presented here.

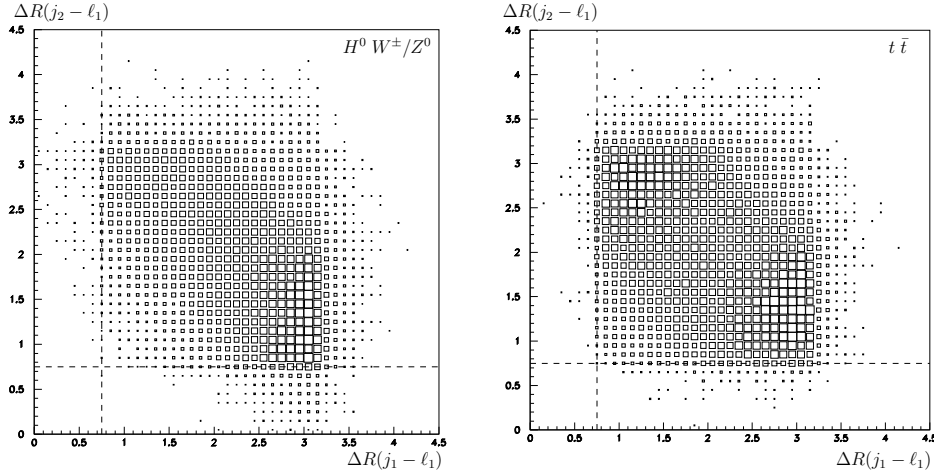


Figure 3.21: Scatter plots “ $\Delta R(j_1 - \ell_1)$ vs $\Delta R(j_2 - \ell_1)$ ” for $H^0 W^\pm/Z^0$ signal and $t\bar{t}$ background (30'000 events each).

In the b -dijet reference frame, the polar angles of the isolated lepton $\theta_{\ell_1}^{(jj)}$ and the first b -jet $\theta_{j_1}^{(jj)}$ distributions are very similar for signal and backgrounds. However, differences occur when their respective cosine are presented in scatter plots like in figure 3.22. The rectangle covering approximately the region $\cos(\theta_{j_1}^{(jj)}) \in [0.0, 1.0]$ and $\cos(\theta_{\ell_1}^{(jj)}) \in [-1.0, -0.6]$ contains a large portion of the signal and is pictured as a reference. $t\bar{t}$ events are somehow more spread out of the rectangle. $Z^0 W^\pm$ events are at contrary better grouped, while signal and irreducible background $Z^0 Z^0$ are again very similar. It must be noticed that care must be taken when we exploit (indirectly) the difference in mass $m_{Z^0} < m_{H^0}$. After the event selection by the neural network, the b -dijet mass distribution (which should be the “deliverable” of the analysis) will be affected by the usage of this information. The two last selected parameters are the cosines $\cos(\theta_{jj}^{(V_\pm^*)})$ of the b -dijet polar angle in the reconstructed primary boson V_\pm^* referential as explained in § 3.7.2. Indeed, for *not* Z^0 -associated

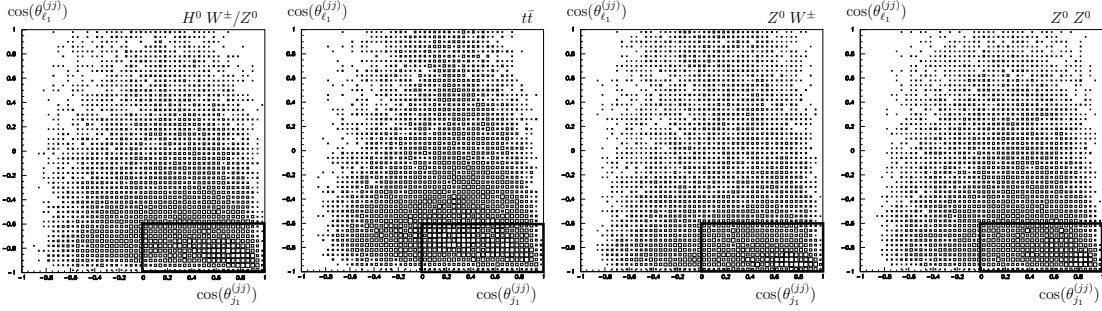


Figure 3.22: Scatter plots “ $\cos(\theta_{j_1}^{(jj)})$ vs $\cos(\theta_{\ell_1}^{(jj)})$ ” for $H^0 W^\pm/Z^0$ signal and $t\bar{t}$, $Z^0 W^\pm$ and $Z^0 Z^0$ backgrounds where $\theta_{j_1}^{(jj)}$ and $\theta_{\ell_1}^{(jj)}$ are the polar angles of the highest p_T b -jet and the isolated lepton 1 in the b -dijet rest frame respectively (15’000 events per each channel).

events, two solutions exist for the associated neutrino and thus for the primary boson. At contrary, for Z^0 -associated events, the primary boson is reconstructed unequivocally from the two b -jets and the two observed leptons which match the Z^0 mass. A unique solution $\theta_{jj}^{(V^*)} = \theta_{jj}^{(V^*)} = \theta_{jj}^{(V^*)}$ therefore exists and patterns 21 and 22 are identical.

3.8.3 Performances for $t\bar{t}$ and irreducible backgrounds suppression with multiple MLPs

In this analysis, we have to discriminate six types of background from the signal. Instead of using a unique neural network for all types of background, it is more suitable to use a dedicated one for each background channel and apply them sequentially. After the selection procedure presented in § 3.4.3, the most important remaining background channel is $t\bar{t}$ (see table 3.7). The starting point is therefore the elaboration of a MLP network to discriminate $t\bar{t}$ from the signal (“HA-TT”). Only events which have a dijet mass included in the Higgs mass window $80 < M_{jj} < 120 \text{ GeV}/c^2$ are considered to train the MLP. The MLP works optimally when the input patterns are comprised between 0 and 1. For this reason, the 22 input parameters are shifted and scaled in this interval. Among the initial $3 \cdot 10^6$ $H^0 W^\pm/Z^0$ and $2 \cdot 10^7$ $t\bar{t}$ events generated for the study (see table 3.5), only 54’838 and 10’044 events respectively remain for the learning and testing operations. Among these, only 94 $t\bar{t}$ events are fortuitously tagged as Z^0 -associated, which is too few to elaborate a specific neural network for this type of events. Therefore, a unique MLP for Z^0 - and *not* Z^0 -associated events is build. It is trained and tested with two independent sets of $2 \times 5’022$ events.

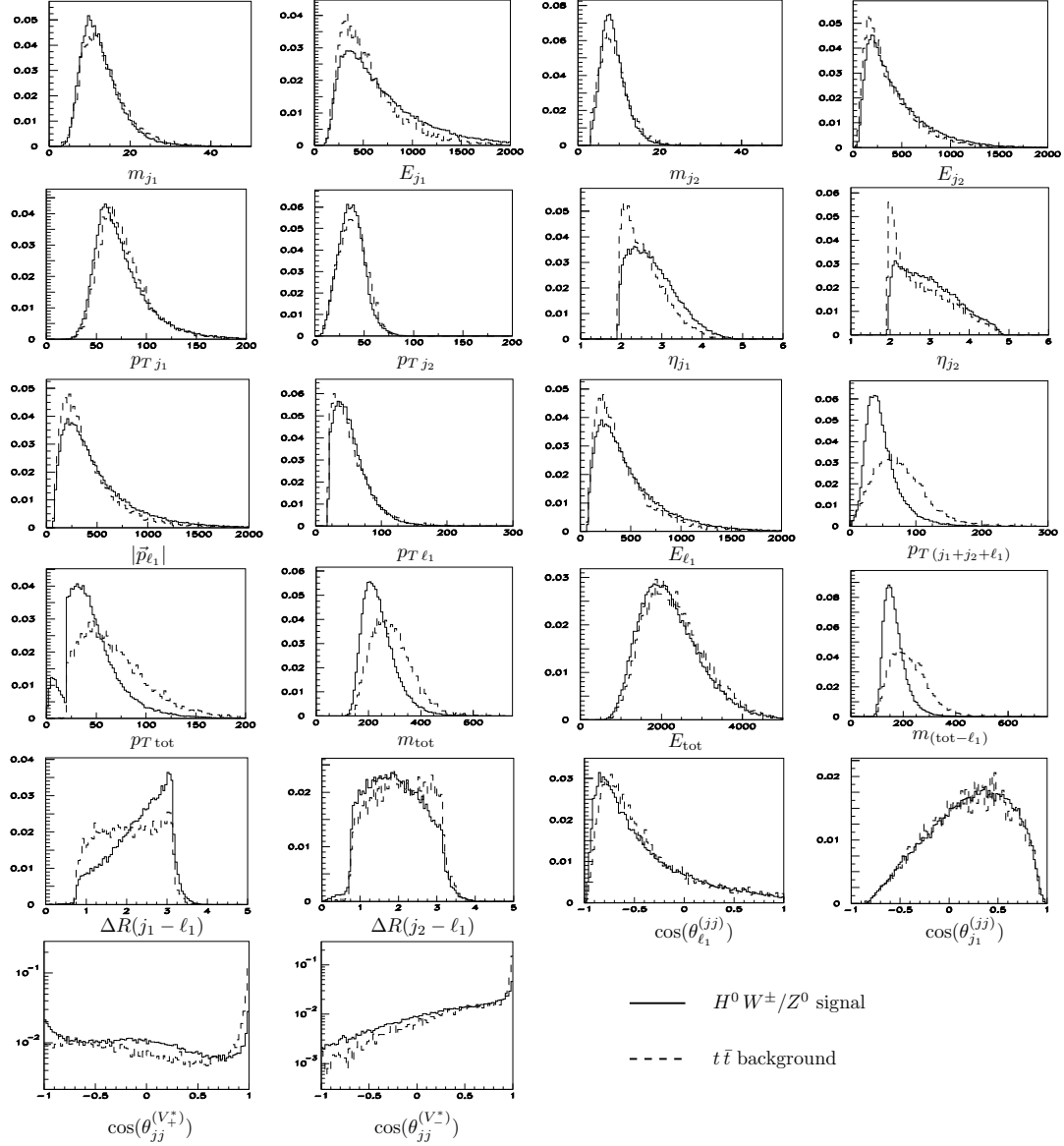


Figure 3.23: Distributions of the 22 MLP input patterns for the signal $H^0 W^\pm/Z^0$ (full line) and $t\bar{t}$ background (dashed line) events. The histograms are normalized to 1.

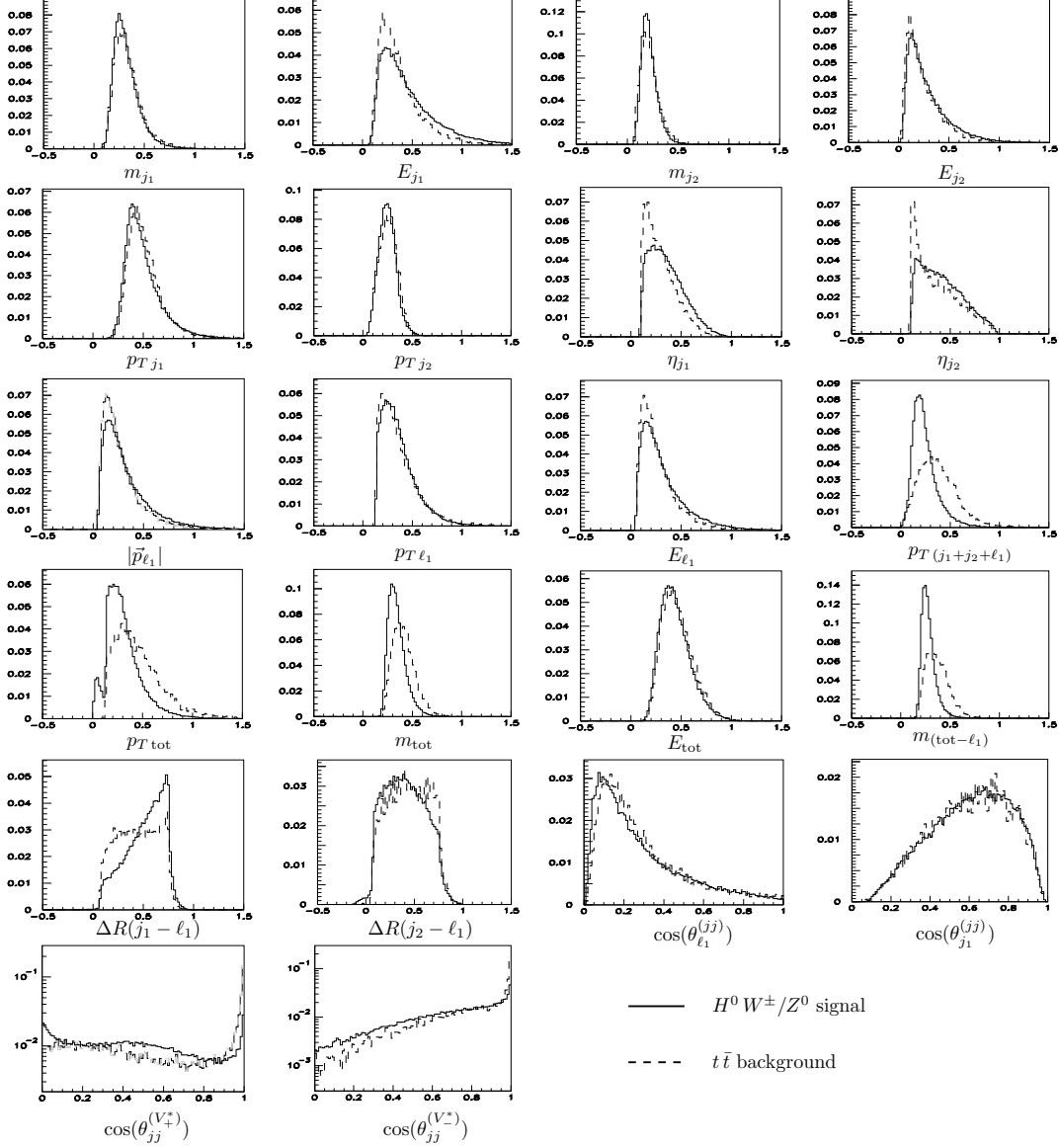


Figure 3.24: Distributions of the 22 MLP input patterns shifted and scaled between 0 and 1 for the signal $H^0 W^\pm / Z^0$ (full line) and $t\bar{t}$ background (dashed line) events. The histograms are normalized to 1.

In figures 3.23 and 3.24, we present the 22 parameters distributions for signal $H^0 W^\pm/Z^0$ and $t\bar{t}$ background with a b -dijet mass in $80 < M_{jj} < 120 \text{ GeV}/c^2$. The histograms are normalized to 1. Furthermore, the histograms are shifted and scaled between 0 and 1 in figure 3.24. Some differences appear in several variable distributions which is encouraging for the use of the neural network. The $p_{T\text{tot}}$ distribution for the signal presents a small peak on the left of the histogram (below $20 \text{ GeV}/c$ in figure 3.23) which is absent for $t\bar{t}$ background. This is due to the “ $E_T^{\text{miss}} > 20 \text{ GeV}$ ” cut applied exclusively on *not* Z^0 -associated events. Almost every $t\bar{t}$ events undergo this cut, which is not the case for signal $H^0 Z^0$.

The “HA-TT” neural network answer distributions during the test phase are presented in black for the signal and in red for the $t\bar{t}$ background in figure 3.25 (*top left*). The back-propagation error for the learning and the testing sets during 500 cycles is also pictured (*bottom left*). An output cut optimization procedure is performed in order to maximize the significance S/\sqrt{B} (fig. 3.25 (*right*)): events are rejected when $\text{OUT}_{\text{HA-TT}} < 0.7$.

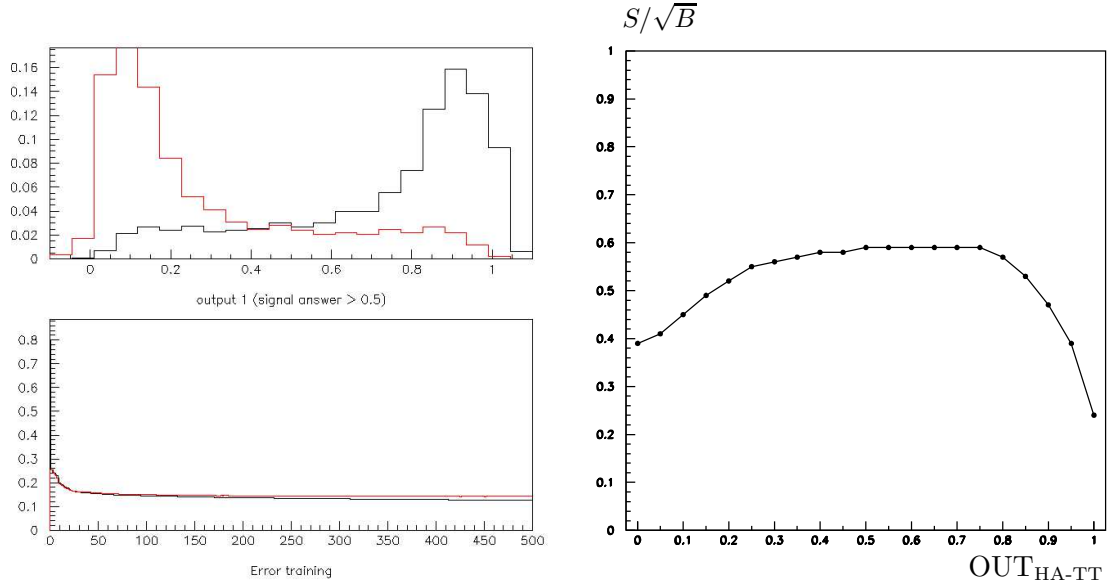


Figure 3.25: “HA-TT” MLP answer distributions for the signal (black) and the $t\bar{t}$ background (red) during the test phase (*top left*). Back-propagation error for the learning (black) and the testing sets (red) during 500 cycles (*bottom left*). S/\sqrt{B} as a function of the cut on $\text{OUT}_{\text{HA-TT}}$ (*right*).

	Number of events per year after the selection cuts described in § 3.4.3		Number of events per year after “HA-TT” neural network ($\text{OUT}_{\text{HA-TT}} > 0.7$)	
		$80 < M_{jj} < 120$		$80 < M_{jj} < 120$
<i>Signal</i>				
$H^0 Z^0$	2.7	1.8	1.9	1.4
$H^0 W^\pm$	11.5	8.1	6.9	5.2
Total	14.2	9.9	8.8	6.6
<i>Background</i>				
$t\bar{t}$	1785.6	552.4	280.4	55.3
$Z^0 W^\pm$	27.6	10.5	17.9	6.9
$Z^0 Z^0$	13.3	5.4	10.0	4.2
$W^\pm + b$ -jets	1351.3	33.4	989.0	21.9
$\gamma^*/Z^0 + b$ -jets	717.8	44.0	578.6	38.5
$b\bar{b}$	48.4	0	0	0
Total	3944.0	645.7	1875.9	126.8
S/\sqrt{B}		0.39		0.59

Table 3.13: Number of signal and background events expected per LHCb year in total and in the Higgs mass window $80 < M_{jj} < 120 \text{ GeV}/c^2$ before and after the “HA-TT” neural network.

In the second and third columns of table 3.13 are reported the number of events expected per LHCb year after the selection procedure described in § 3.4.3. The corresponding b -dijet mass distributions are shown in figure 3.26. In the fourth and fifth columns are presented the number of events after the use of the “HA-TT” neural network. The corresponding b -dijet mass distributions are plotted in figure 3.27. The comparison shows that, in the Higgs mass window $80 < M_{jj} < 120 \text{ GeV}/c^2$, a third of the signal events are rejected while the number of $t\bar{t}$ events is strongly reduced by a factor 10. Including the other background channels, the significance is increased from 0.39 to 0.59. Furthermore, the respective distribution shapes are more or less conserved which confirms that the use of the “HA-TT” neural network is therefore appropriate to discriminate $t\bar{t}$ background from the signal.

After the $t\bar{t}$ discrimination, neural networks should be used to remove the irreducible channels $Z^0 W^\pm$ and $Z^0 Z^0$. The neural networks will be fed with events already accepted by the “HA-TT” MLP. The two background cases are studied independently.

For $Z^0 W^\pm$, only 3’884 *not* Z^0 -associated events with $80 < M_{jj} < 120 \text{ GeV}/c^2$ are available in this study. The “HA-ZW” MLP is therefore trained and tested with two sets of $2 \times 1’942$ *not* Z^0 -associated events during 500 cycles (see figure 3.28 (*top left*)). Only *not* Z^0 -associated events are submitted to this MLP, while Z^0 -associated

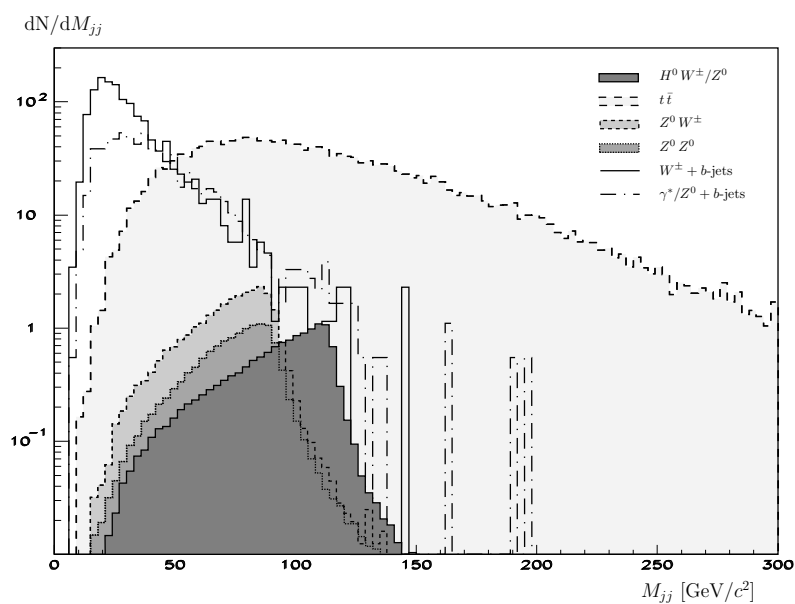


Figure 3.26: Dijet mass distribution for signal and backgrounds after the selection procedure described in § 3.4.3.

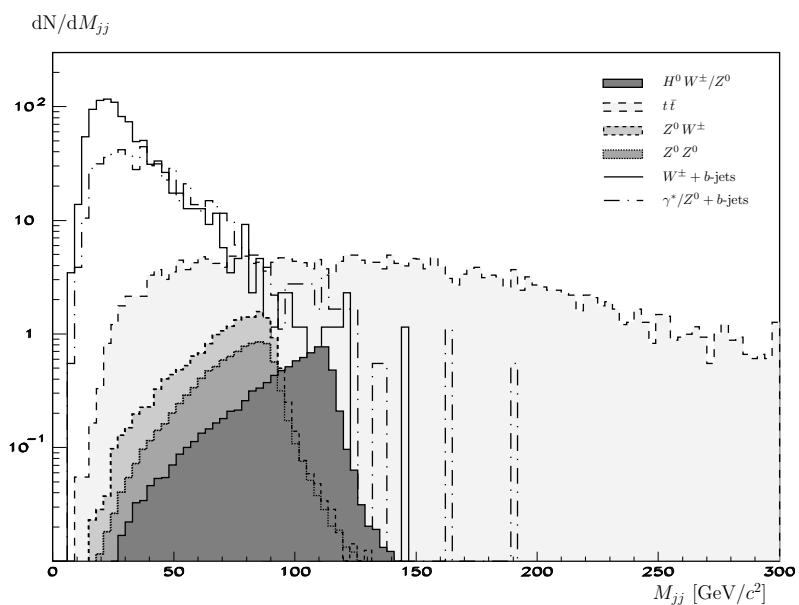


Figure 3.27: Dijet mass distribution for signal and backgrounds after the selection procedure and the “HA-TT” neural network utilization.

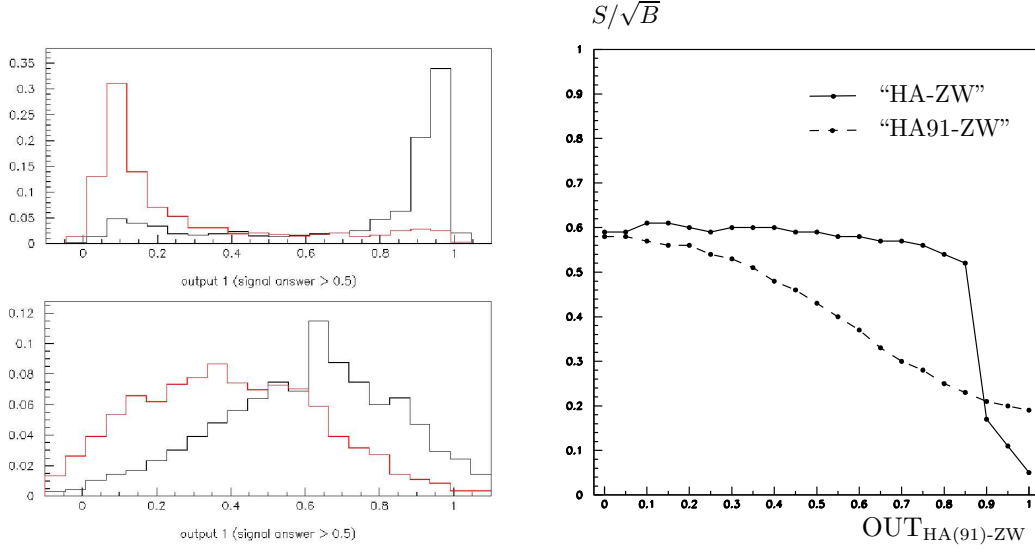


Figure 3.28: “HA-ZW” (*top left*) and “HA91-ZW” (*bottom left*) MLP answer distributions for the signal (black) and the $Z^0 W^\pm$ background (red) during the test phase. S/\sqrt{B} as a function of the cut on $\text{OUT}_{\text{HA}(91)\text{-ZW}}$ (*right*).

events are accepted without any additional test. The “HA-ZW” MLP output cut optimization procedure presented in figure 3.28 (*right*, full line) shows a maximal significance when events with $\text{OUT}_{\text{HA-ZW}} < 0.1$ are discarded. The number of events expected per year at LHCb after this selection are presented in the second and third columns of table 3.14. About 3% of the signal events is lost while $Z^0 W^\pm$ is suppressed by $\sim 40\%$. With the other background channels, the significance is slightly improved with respect to the “HA-TT” MLP alone ($S/\sqrt{B} = 0.61$). However, by looking at the b -dijet mass distributions in figure 3.29, the $H^0 W^\pm/Z^0$ and the $t\bar{t}$ plots (and also in the $Z^0 W^\pm$ one, but in a less significant way) are distorted in the region around the Z^0 boson mass ($\sim 90 \text{ GeV}/c^2$). The distribution shapes are not conserved with respect to figures 3.26 and 3.27. We deduce that the “HA-ZW” MLP reconstructs the b -dijet mass which becomes the dominant discriminant criterion instead of the spin related observables discussed previously, which is not suitable. In order to test this hypothesis, a similar neural network is build with events for which we have set equal masses for H^0 and Z^0 . A set of $3 \cdot 10^6$ $H^0 W^\pm/Z^0$ events with $m_{H^0} = m_{Z^0} = 91 \text{ GeV}/c^2$ was produced. After the selection procedure, they are submitted to the “HA-TT” MLP. Among the remaining 30'361 events with $80 < M_{jj} < 120 \text{ GeV}/c^2$, 3'884 ($2 \times 1'942$) are used to construct the “HA91-ZW” MLP together with the $Z^0 W^\pm$ events, exactly like for the “HA-ZW” MLP calculation. The output of this MLP are presented in figure 3.28 (*bottom left*)

	Number of events per year after “HA-ZW” neural network ($\text{OUT}_{\text{HA-ZW}} > 0.1$)		Number of events per year after “HA-ZZ” neural network ($\text{OUT}_{\text{HA-ZZ}} > 0.2$)	
		$80 < M_{\text{jj}} < 120$		$80 < M_{\text{jj}} < 120$
<i>Signal</i>				
$H^0 Z^0$	1.9	1.4	1.5	1.3
$H^0 W^\pm$	6.4	5.0	5.3	5.0
Total	8.3	6.4	6.8	6.3
<i>Background</i>				
$t \bar{t}$	262.5	51.3	209.9	49.0
$Z^0 W^\pm$	11.7	4.3	5.5	4.6
$Z^0 Z^0$	9.3	3.9	2.9	2.3
$W^\pm + b$ -jets	939.6	15.0	132.2	15.0
$\gamma^*/Z^0 + b$ -jets	564.9	36.8	77.0	31.9
$b \bar{b}$	0	0	0	0
Total	1788.0	111.3	427.5	102.8
S/\sqrt{B}		0.61		0.62

Table 3.14: Number of signal and background events expected per LHCb year in total and in the Higgs mass window $80 < M_{\text{jj}} < 120 \text{ GeV}/c^2$ after the “HA-ZW” (*left*) and “HA-ZZ” (*right*) neural networks.

showing a reduced discrimination efficiency compared to the previous case. Moreover, the “HA91-ZW” MLP output cut procedure which aims to improve the significance (fig. 3.28 (*right*, dotted line) shows that there is no cut value which improves the significance. (It should be clear that we have analyzed the normal set of signal events with $m_{H^0} = 115 \text{ GeV}/c^2$.) Nevertheless, we present the b -dijet mass distributions after the “HA91-ZW” with $\text{OUT}_{\text{HA91-ZW}} > 0.6$ in figure 3.30. The distortion around $\sim 90 \text{ GeV}/c^2$ disappears totally and the shape of figures 3.26 and 3.27 is preserved. This confirms that the “HA-ZW” MLP is principally based on the reconstructed b -dijet mass which is not suitable. The use of such neural network to reject the irreducible background $Z^0 W^\pm$ should therefore be abandoned, while, in principle, the “HA91-ZW” MLP could be used. Unfortunately, in the present configuration, the “HA91-ZW” choice results in a systematic reduction of the significance. Further investigations for suitable discriminant parameters are unavoidable.

For what concerns the $Z^0 Z^0$ irreducible background discrimination, two different MLPs are elaborated for Z^0 - and *not* Z^0 -associated events. They are trained and tested using two sets of $2 \times 2'759$ and $2 \times 2'565$ events with $80 < M_{\text{jj}} < 120 \text{ GeV}/c^2$ during 500 cycles respectively (see figure 3.31 (*left*)). In this case, events are accepted when $\text{OUT}_{\text{HA-ZZ}} > 0.2$ (see the output cut optimization procedure in fig. 3.31 (*right*, full line)) and the number of events expected per LHCb year are reported in the

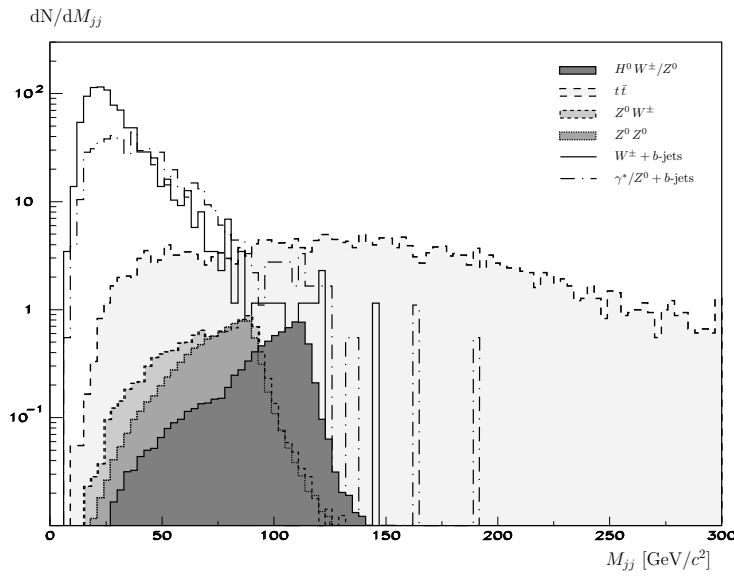


Figure 3.29: Dijet mass distribution for signal and backgrounds after the selection cuts and the utilization of two successive neural networks “HA-TT” and “HA-ZW”.

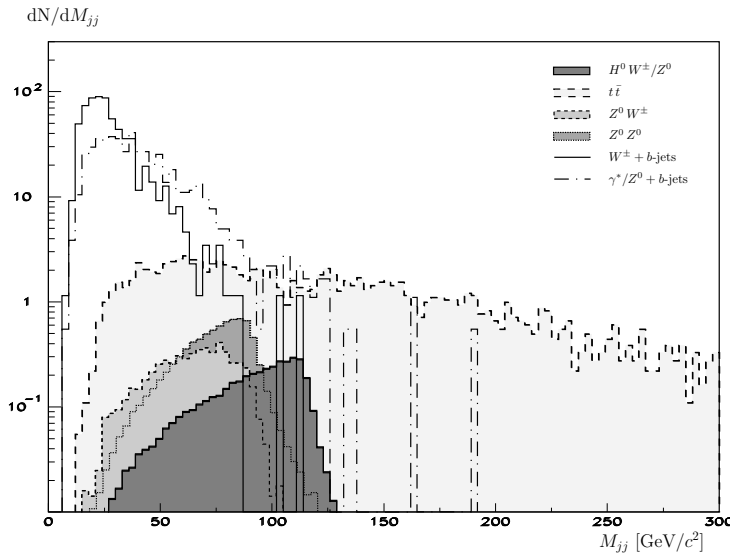


Figure 3.30: Dijet mass distribution for signal and backgrounds after the selection cuts and the utilization of two successive neural networks “HA-TT” and “HA91-ZW”. The second MLP for the irreducible background $Z^0 W^\pm$ is build with signal events generated with a Higgs mass $m_{H^0} = m_{Z^0} = 91 \text{ GeV}/c^2$.

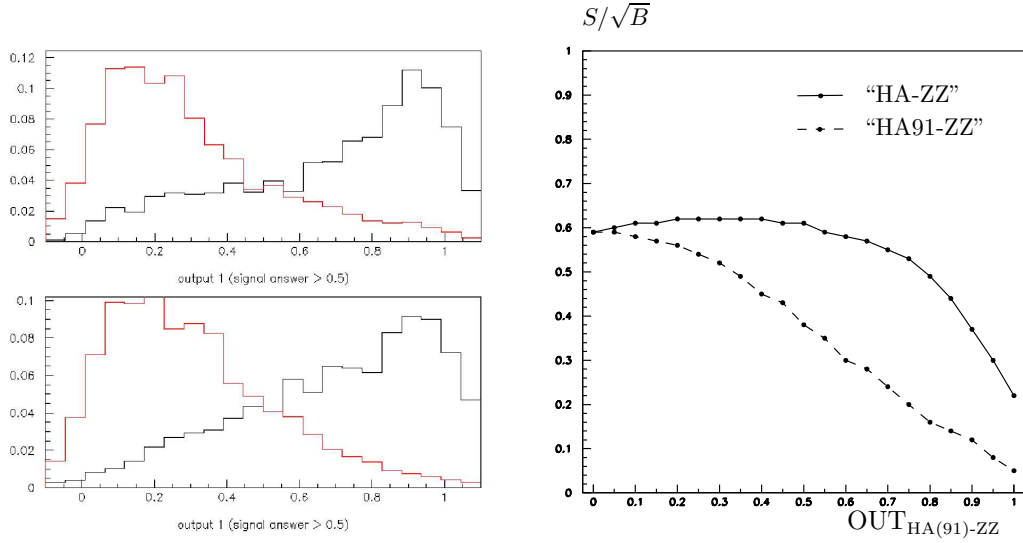


Figure 3.31: “HA-ZZ” MLP answer distributions for the signal (black) and the $Z^0 Z^0$ background (red) during the test phase for Z^0 - (top left) and *not* Z^0 -associated events (bottom left). S/\sqrt{B} as a function of the cut on $\text{OUT}_{\text{HA}(91)\text{-ZZ}}$ (right).

fourth and fifth columns of table 3.14. With respect to “HA-TT”, only 5% of the signal events in the window $80 < M_{\text{jj}} < 120 \text{ GeV}/c^2$ are rejected while $\sim 55\%$ of the $Z^0 Z^0$ event remains. In total, the significance is increased to $S/\sqrt{B} = 0.62$. Once more, the b -dijet mass distributions are strongly distorted as they are truncated below $\sim 80 \text{ GeV}/c^2$ (figure 3.32). This certainly implies that the “HA-ZZ” MLP also uses the b -dijet mass as dominant discriminant criterion. For confirmation, two neural networks are conceived from $Z^0 Z^0$ and signal events generated with $m_{H^0} = m_{Z^0} = 91 \text{ GeV}/c^2$. After the selection cuts and “HA-TT”, $2 \times 3'892$ Z^0 - and $2 \times 2'565$ *not* Z^0 -associated events are available for the learning and testing phases. The results after 500 cycles are shown in figure 3.34. Here again, we observe the reduction in the discrimination power of “HA91-ZZ” compared to “HA-ZZ”. The output cut optimization procedure (fig. 3.31 (right, dotted line)) shows that this neural network is not efficient to improve the significance. We present anyway the b -dijet mass distributions after “HA91-ZZ” with $\text{OUT}_{\text{HA91-ZZ}} > 0.6$ in figure 3.33. In this case, the main effect of “HA-ZZ” which is to reject events with $M_{\text{jj}} < 80 \text{ GeV}/c^2$ is no more present, and the shapes are not very different from figures 3.26 and 3.27. These results indicate that the “HA-ZZ” MLP is not efficient, as it was the case for the “HA-ZW” MLP.

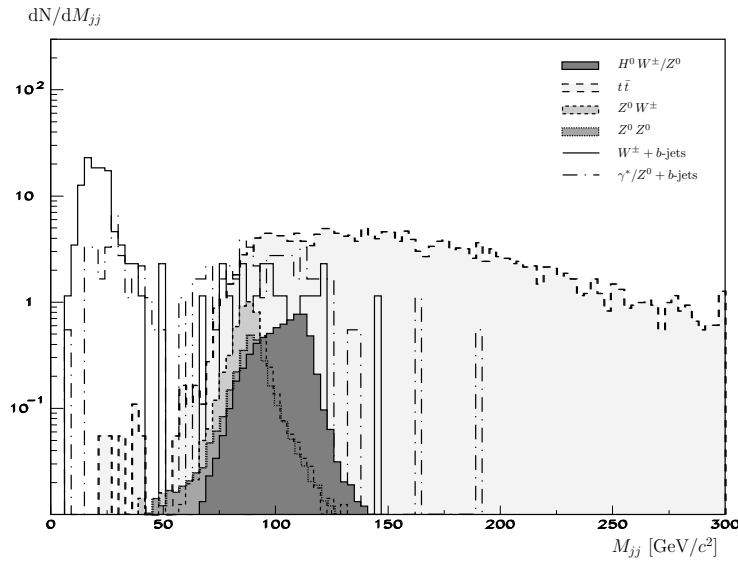


Figure 3.32: Dijet mass distribution for signal and backgrounds after the selection cuts and the utilization of two successive neural networks “HA-TT” and “HA-ZZ”.

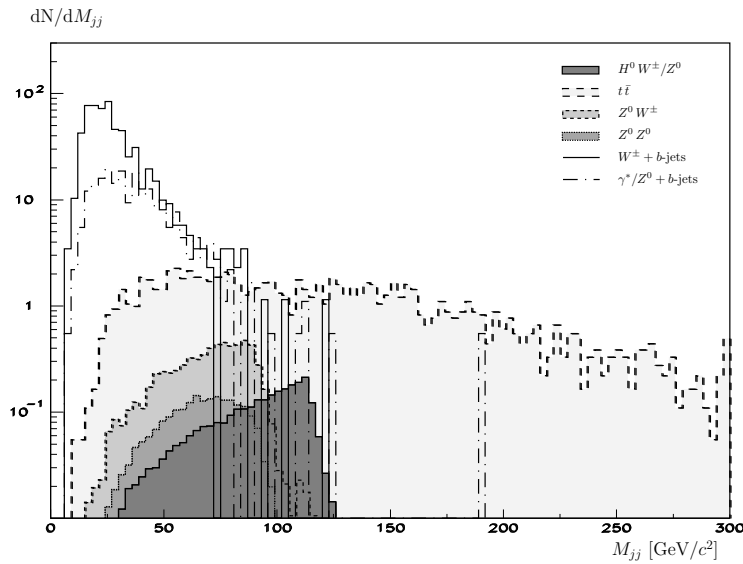


Figure 3.33: Dijet mass distribution for signal and backgrounds after the selection cuts and the utilization of two successive neural networks “HA-TT” and “HA91-ZZ”. The second MLP for the irreducible background $Z^0 Z^0$ is build with signal events generated with a Higgs mass $m_{H^0} = m_{Z^0} = 91 \text{ GeV}/c^2$.

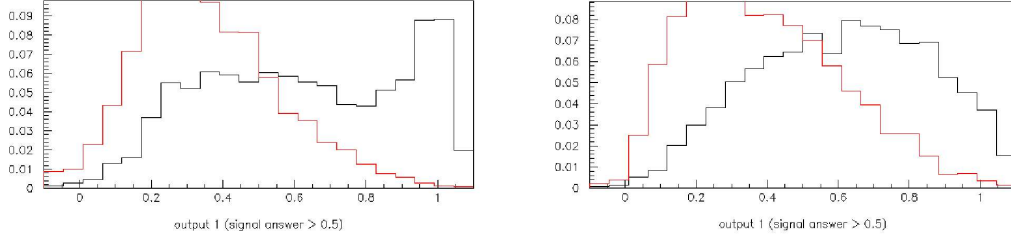


Figure 3.34: “HA91-ZZ” MLP answer distributions for the signal (black) and the $Z^0 Z^0$ background (red) during the test phase for Z^0 - (*left*) and *not* Z^0 -associated events (*left*).

In definitive, the use of neural network turns out to be efficient for $t\bar{t}$ background discrimination. Indeed, this channel is strongly suppressed by a factor 10 leading to a final significance of 0.59. On the other hand, further developments should be performed concerning the irreducible backgrounds suppression with MLPs. For $Z^0 W^\pm$ as for $Z^0 Z^0$, the dominant discriminant criterion seems to be connected with the b -dijet mass resulting in distorted mass distributions. This can be avoided training MLPs with signal events generated with $m_{H^0} = m_{Z^0} = 91 \text{ GeV}/c^2$, but this results in a very low discrimination power. Figures 3.35 and 3.36 represents the signal and the combined backgrounds dijet mass distributions after the selection procedure and respectively before and after the use of the “HA-TT” neural network (see fig. 3.26 and 3.27), as it is expected after one LHCb year acquisition.

Significance comparison with CDF

We now wish to give a comparison of our results with the analysis of the Run II Tevatron data by CDF (CDF II) [39]. CDF presents a search for Higgs bosons decaying into $b\bar{b}$ and produced in association with W^\pm bosons in $p\bar{p}$ collisions at $\sqrt{s} = 1.96 \text{ TeV}$, using a data sample corresponding to an integrated luminosity $\mathcal{L}_{\text{int.}}^{\text{CDF}} = 320 \text{ pb}^{-1}$. The Standard Model $H^0 W^\pm$ production cross-section is $\sigma_{H^0 W^\pm}^{\text{CDF}} = 0.2 \text{ pb}$ for $m_{H^0} = 115 \text{ GeV}/c^2$ at the CDF center-of-mass energy. It results a significance $S/\sqrt{B} = 0.07$ when only one b -jet is tagged and 0.05 for the double-tagged sample. In [39], the $H^0 Z^0$ channel is studied separately and only $t\bar{t}$ and $W^\pm + b$ -jets backgrounds are taken into account. In our case, these same channels for signal and backgrounds after selection (before the “HA-TT”, see table 3.13) give:

$$\left. \frac{S}{\sqrt{B}} \right|_{\text{LHCb}} = \frac{8.1}{\sqrt{552.4 + 33.4}} \simeq 0.33$$

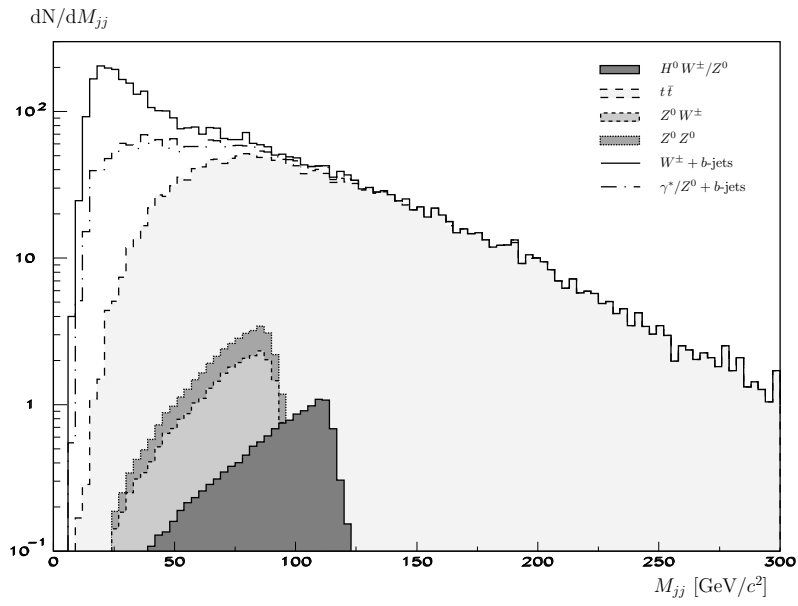


Figure 3.35: Signal and total background dijet mass distributions after the selection procedure described in § 3.4.3.

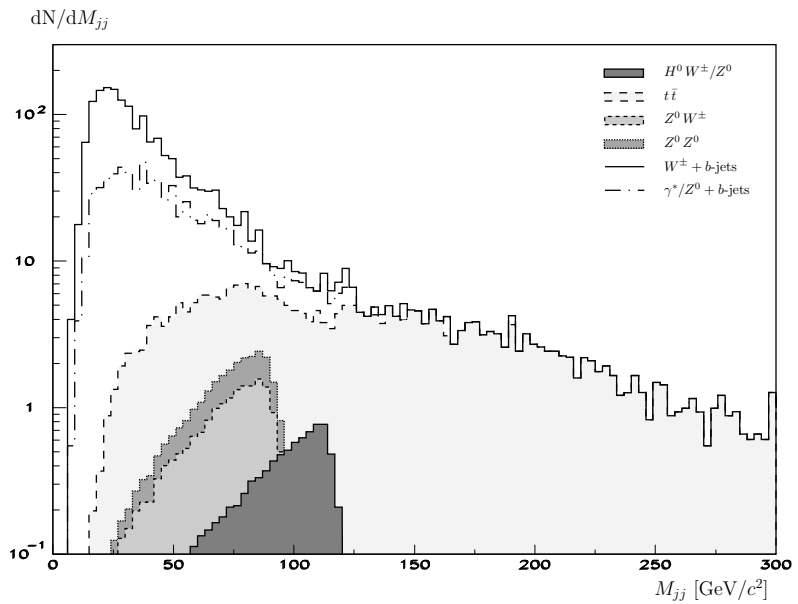


Figure 3.36: Signal and total background dijet mass distributions after the selection procedure and the “HA-TT” neural network utilization.

	CDF	LHCb
$\mathcal{L}_{\text{int.}}$ [pb ⁻¹]	320	$2 \cdot 10^3$
$\sigma_{H^0 W^\pm}$ [pb]	0.2	1.48
$\sigma_{t\bar{t}}$ [pb]	8.6	571
$\sigma_{W^\pm + b\text{-jets}}$ [pb]	$2.6 \cdot 10^4$	$1.6 \cdot 10^5$

Table 3.15: Integrated luminosity and production cross-sections for signal and backgrounds in CDF and LHCb.

which is 6-7 times larger than CDF double-tagged analysis. As presented in table 3.15, LHCb benefits from a higher integrated luminosity and also higher production cross-sections for signal and backgrounds. During one year of activity, LHCb should collect a statistic about 10 times larger than CDF Run II. The significances for the two configurations are:

$$S/\sqrt{B}\Big|_{\text{CDF}} = \frac{\mathcal{L}_{\text{int.}}^{\text{CDF}} \cdot \sigma_S^{\text{CDF}} \cdot f_S^{\text{CDF}}}{\sqrt{\mathcal{L}_{\text{int.}}^{\text{CDF}} \cdot \sigma_B^{\text{CDF}} \cdot f_B^{\text{CDF}}}}$$

$$S/\sqrt{B}\Big|_{\text{LHCb}} = \frac{\mathcal{L}_{\text{int.}}^{\text{LHCb}} \cdot \sigma_S^{\text{LHCb}} \cdot f_S^{\text{LHCb}}}{\sqrt{\mathcal{L}_{\text{int.}}^{\text{LHCb}} \cdot \sigma_B^{\text{LHCb}} \cdot f_B^{\text{LHCb}}}}$$

where $f_{S(B)}^{\text{CDF(LHCb)}}$ is the fraction of signal (background) events selected in CDF (LHCb). From the previous expressions, we obtain:

$$\frac{S/\sqrt{B}\Big|_{\text{LHCb}}}{S/\sqrt{B}\Big|_{\text{CDF}}} = \underbrace{\sqrt{\frac{\mathcal{L}_{\text{int.}}^{\text{LHCb}}}{\mathcal{L}_{\text{int.}}^{\text{CDF}}} \cdot \frac{\sigma_S^{\text{LHCb}}}{\sigma_S^{\text{CDF}}} \cdot \sqrt{\frac{\sigma_B^{\text{CDF}}}{\sigma_B^{\text{LHCb}}}}}_{\simeq 7.45} \times \frac{f_S/\sqrt{f_B}\Big|_{\text{LHCb}}}{f_S/\sqrt{f_B}\Big|_{\text{CDF}}}$$

If we assume similar selection fractions for both experiments ($f_S^{\text{CDF}} \simeq f_S^{\text{LHCb}} \equiv f_S$ and $f_B^{\text{CDF}} \simeq f_B^{\text{LHCb}} \equiv f_B$), the last term is about the unity and the terms with $\mathcal{L}\sigma$ are dominant. For comparison, the LHCb significance inferred from the CDF value is:

$$\frac{S}{\sqrt{B}}\Big|_{\text{LHCb}}^{\text{estimated}} \simeq \underbrace{\frac{S}{\sqrt{B}}\Big|_{\text{CDF}}}_{\simeq 0.05} \times 7.45 \simeq 0.37$$

which is consistent with our result. CDF considers a different interval for the significance calculation ($100 < M_{jj} < 140$ GeV/ c^2). In table 3.16, we give the significance values obtained from our data when the lower bound of the mass window is of 80, 90

	Number of events per year after the selection cuts described in § 3.4.3			Number of events per year after “HA-TT” neural network ($\text{OUT}_{\text{HA-TT}} > 0.7$)		
	$80 < M_{jj} < 120$	$90 < M_{jj} < 120$	$100 < M_{jj} < 120$	$80 < M_{jj} < 120$	$90 < M_{jj} < 120$	$100 < M_{jj} < 120$
<i>Signal</i>						
$H^0 Z^0$	1.8	1.5	1.0	1.4	1.1	0.8
$H^0 W^\pm$	8.1	6.6	4.6	5.2	4.4	3.1
Total	9.9	8.1	5.6	6.6	5.5	3.9
<i>Background</i>						
$t\bar{t}$	552.4	397.4	250.6	55.3	41.9	26.7
$Z^0 W^\pm$	10.5	3.3	0.6	6.9	2.1	0.3
$Z^0 Z^0$	5.4	1.9	0.4	4.2	1.4	0.3
$W^\pm + b$ -jets	33.4	15.0	8.1	21.9	11.5	5.8
$\gamma^*/Z^0 + b$ -jets	44.0	26.4	17.1	38.5	22.6	14.9
Total	645.7	443.9	276.7	126.8	79.4	47.9
S/\sqrt{B}	0.39	0.39	0.34	0.59	0.62	0.57

Table 3.16: Number of signal and background events expected per LHCb year and significance before and after the “HA-TT” MLP discrimination considering three different mass windows $80 < M_{jj} < 120$, $90 < M_{jj} < 120$ and $100 < M_{jj} < 120$ GeV/ c^2 .

and 100 GeV/ c^2 . We can see that the significance remains almost constant, and this before and after the neural network utilization. These considerations indicate that the power of analysis predicted by our study, before the MLP filter, is equivalent to the figure obtained by CDF. We can therefore expect a significant improvement after the neural network discrimination.

Sensitivity assessment using a Toy Monte Carlo

In order to better assess the sensitivity of the present setup to the Higgs signal, we have adopted a Toy Monte Carlo (TMC) method which is used to simulate many “LHCb experiments”. For each “experiment”, we randomly generate a number of events for each type of physics event (signal $H^0 W^\pm/Z^0$, and backgrounds $t\bar{t}$, $Z^0 W^\pm$, $Z^0 Z^0$, $W^\pm + b$ -jets and $\gamma^*/Z^0 + b$ -jets). The background levels are kept at the average values, while the signal level is varied from 2 events/year up to 40/year. We have chosen to consider a statistic accumulated over 6 years at nominal luminosity. For each event, a mass is generated using the (high statistics) distributions obtained after the “HA-TT” MLP cut (see fig. 3.36). The resulting mass plot for each experiment (see an example in fig. 3.37 (*left*)) is then fitted keeping free the number of events of each kind. Note that the position and the width of the Higgs peak are fixed. For each configuration, we generate 400 experiments. An example of distribution giving the deviation from truth of the fitted number of signal events is given in figure 3.37 (*right*).

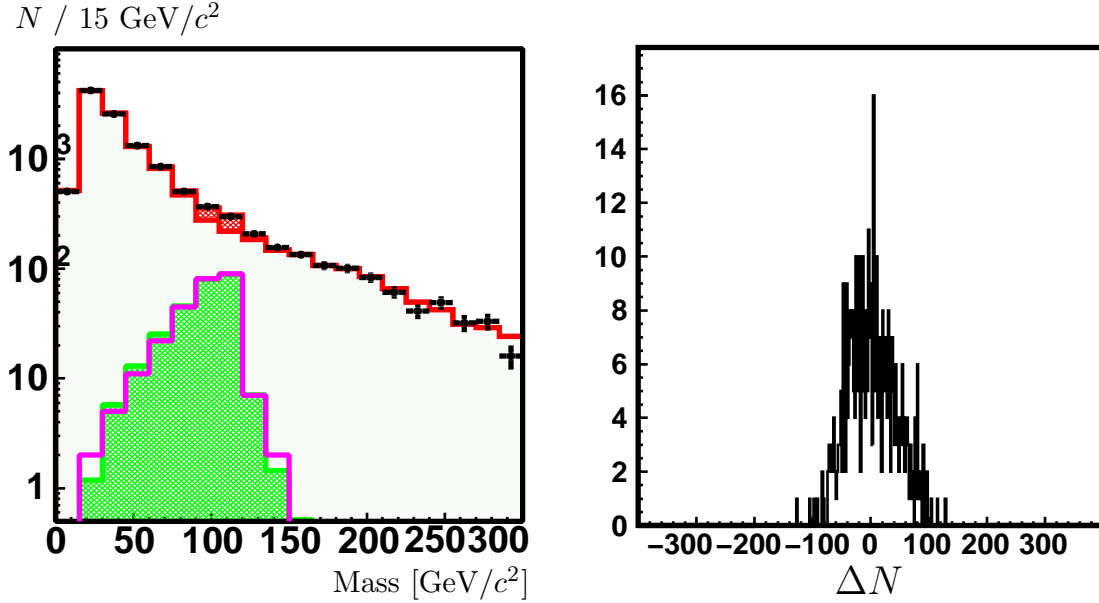


Figure 3.37: Example of mass distribution obtained for one “LHCb experiment”: the black error bars represent the total events generated, with 265 signal events at the bottom in violet. The total fitted distribution is in red with 270 ± 47 signal events (shaded green) (*left*). Deviation ΔN of the number of signal events reconstructed from the number generated, for 400 “LHCb experiments” (*right*). For this plot, 240 signal events on the average have been considered (40 events/year \times 6 years).

In figure 3.38 (*top*), we present the r.m.s. of the deviation histograms as a function of the generated number of events. The total number of events is from 12 (2 events/year \times 6 years) to 240 (40 events/year \times 6 years). Figure 3.38 (*bottom*) shows the corresponding significance N/σ_N .

From this study, we obtain significance values which are consistent with the naïve event counting used before. The improvement from the “shape” information in the fit is marginal.

Assuming that all the kinds of background can be directly measured, except $t\bar{t}$, we have also fitted the mass distributions keeping free only the signal and the $t\bar{t}$ contributions. No significant improvement is observed, as the fit is dominated by the fluctuations of the $t\bar{t}$.

In conclusion, with the present setup, it is in principle possible to reach a significance of 4σ after 6 years of running, if the physics yield is about 3 times the Standard Model prediction.

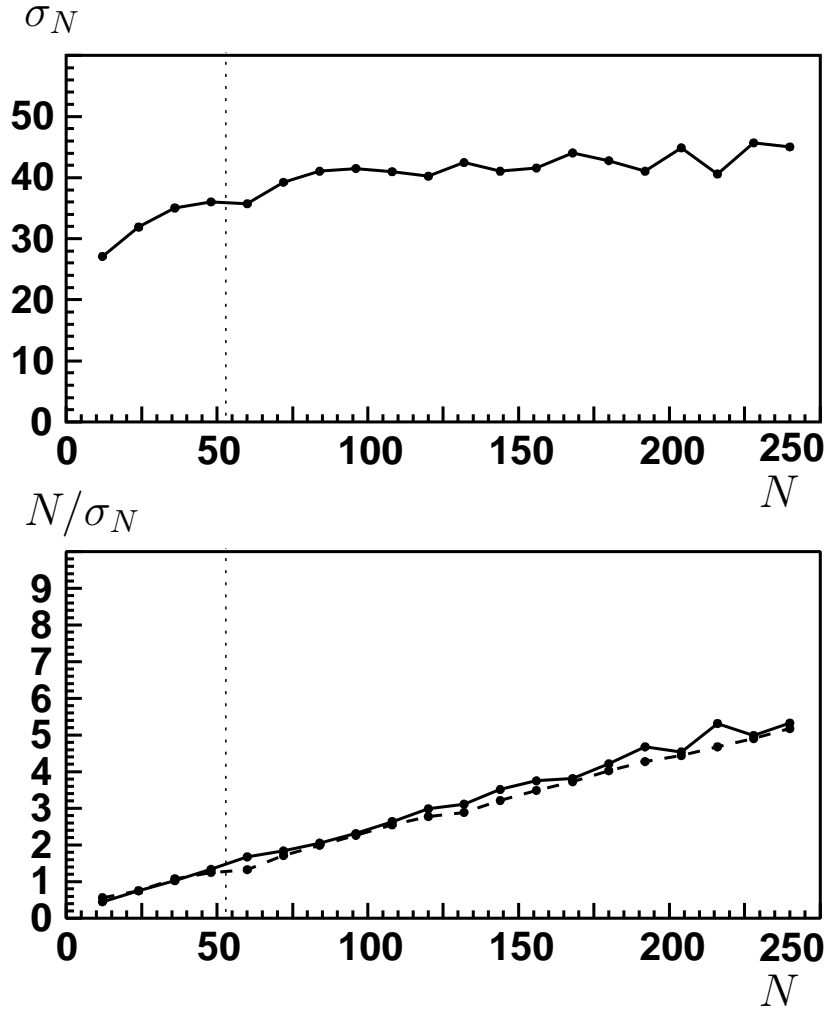


Figure 3.38: R.m.s of the deviation of the number of signal events reconstructed from the number generated, as a function of the total number N of signal events generated (*top*). The corresponding significance N/σ_N , where σ_N is the r.m.s. of the deviation histograms seen before (full line) or the error resulting from the fit (dotted line) (*bottom*). The vertical dotted line represents the Standard Model prediction for 6 LHCb years for the total number of signal events.

3.9 Conclusion

The aim of this work was to assess the feasibility to observe a light Higgs boson at LHCb by using the detector capability to identify b -hadrons. We focused the study on the mechanisms in which the Higgs boson is produced in association with a gauge boson decaying leptonically $H^0 + W^\pm \rightarrow b\bar{b} + \ell\nu_\ell$ and $H^0 + Z^0 \rightarrow b\bar{b} + \ell^+\ell^-$ for $m_{H^0} = 115 \text{ GeV}/c^2$. In parallel to the Higgs signal, several important background channels which also provide two b -quarks and an isolated lepton were studied.

Signal and background events were produced with the standalone computer program PYTHIA version 6.325 (except generic $b\bar{b}$ with 6.319). The generator was set to simulate proton-proton collisions at a center-of-mass energy $\sqrt{s} = 14 \text{ TeV}$ in the LHCb conditions.

The geometrical acceptance of the LHCb spectrometer was approximated by a forward conical region centered on the z -axis and corresponding to the detector acceptance in the bending plane. Thanks to the Monte Carlo truth, we have been able to study the effects of the energy loss because of the presence of neutrini in the event and also the effects due to the particles of the underlying event (particles not directly associated to the hard phenomenon under study).

The “cone” and the “ K_T ” algorithms were used to reconstruct jets and to recover the information of the $H^0 \rightarrow b\bar{b}$ decay products. The parameters of the two algorithms (R_{cone} and R_{K_T}) were optimized to give the best b -dijet mass resolution $\text{FWHM}_{M_{jj}}/M_{jj}$. The results of the two algorithms were similar and we have chosen the cone algorithm with $R_{cone} = 0.6$ ($\text{FWHM}_{M_{jj}}/M_{jj} \sim 30\%$) for the rest of the study.

A jet energy correction procedure was studied in order to compensate for the observed energy loss in low transverse momentum jets, which was parametrized by the hyperbolic function (3.11). A Monte Carlo truth analysis exhibited that neutrini are not responsible in a dominant way for the energy loss. We showed that the loss of particles outside the acceptance affects the reconstruction of jets falling close to the outer region of the detector ($\theta > 250 \text{ mrad}$). The presence of extra jets from the parton shower is also a major reason for the degradation of the b -jet information.

An event selection procedure was elaborated to insure the presence of two b -hadrons from the Higgs decay. The request of a prompt isolated lepton is used to tag the W^\pm or Z^0 gauge boson produced in association with the Higgs. Concerning the selection of the lepton, which is important to reject the large QCD background, we have tested two methods. The first one requires a minimal distance $\Delta R > 0.75$ in the (η, ϕ) phase space between the lepton and each of the two b -hadrons. The second requires that the energy deposited in a cone of radius $R = 0.4$ centered on the candidate lepton does not exceed 10% of the lepton energy. Both methods offered similar and very good efficiency (in more than 99% of the cases, the candidate lepton

is really originating from the associated gauge boson), and the first one was chosen for our study. The events selection led to a significance $S/\sqrt{B} = 0.39$.

In order to improve the events selection efficiency, we have adopted a neural network technique. For that purpose, we have investigated for discriminant variables between signal and background. In particular, we have studied in detail the observed asymmetry in MC events between the b - and \bar{b} -jets pseudorapidity distributions for the irreducible background. In these events, the b -hadrons come from the $Z^0 \rightarrow b\bar{b}$ decay. According to the Electroweak theory, it was shown that the spin 1 of the Z^0 (the Higgs is a spin 0 particle) is responsible for this asymmetry. We have also developed a technique to reconstruct the primary off-shell gauge boson $V^* = W^{\pm*}$ or Z^{0*} , which decays into a Higgs and an associated gauge boson $V = W^\pm$ or Z^0 , themselves decaying subsequently following $H^0 \rightarrow b\bar{b}$ and $V \rightarrow \ell_1 \ell_2$. We showed that the b -dijet polar angle $\theta_{jj}^{(V^*)}$ in the V^* rest frame behaves differently for the signal and irreducible background.

The neural networks were implemented in Multi-Layer Perceptrons with 22 input parameters. In a first time, we have elaborated the ‘‘HA-TT’’ MLP to discriminate the $t\bar{t}$ background (the most important one after the standard selection cuts). It was found to be efficient with an increase of the significance to $S/\sqrt{B} = 0.59$. Subsequently to the ‘‘HA-TT’’, we have used two distinct ‘‘HA-ZW’’ and ‘‘HA-ZZ’’ MLPs to reject the irreducible background. They turned out to be inadequate, despite of a slight improvement of the significance ($S/\sqrt{B} \simeq 0.61$), as they both base their discrimination efficiency on the reconstructed b -dijet mass criterion. Indeed, the b -dijet mass distributions (fig. 3.29 and 3.32) are distorted in the region close to the Z^0 mass. In order to avoid the discrimination on the mass, we have elaborated the ‘‘HA91-ZW’’ and ‘‘HA91-ZZ’’ MLPs, both trained with signal events generated with a Higgs mass $m_{H^0} = m_{Z^0} = 91 \text{ GeV}/c^2$. Unfortunately, in the present configuration, they systematically led to a reduction of the significance and were by the fact discarded. Further investigations for suitable variables to be used by these MLPs should be performed.

Finally, we have adopted a Toy Monte Carlo method to better assess the sensitivity of our setup to the Higgs signal. With the present setup which includes MLP discrimination, we conclude that it is in principle possible to reach a significance of 4σ after 6 years of running (see fig. 3.38), if the physics yield is about 3 times the Standard Model prediction.

Chapter 4

Tests on the VeLo analogue transmission line with the TELL1 prototype RB3

4.1 Introduction

The Beetle 1.3 [27] is a front-end chip which has been developed for the Vertex Locator (VeLo) and for the Inner Tracker (IT) data acquisition system of LHCb [19]. Its goal is to collect the charges from 128 channels of a detector at a rate of 40 MHz (25 ns samples). Due to the heavy radiation in the LHCb cavern, this chip is made with rad-hard technology in order to work for several years. After collection, the 128 analogue levels corresponding to an event are stored in one of the 187 cells of the pipeline. In the presence of a Level-0 trigger accept (L0A), the data are multiplexed and transmitted to the Level-1 off-detector electronics called TELL1 [28]. The actual TELL1 logic block diagram is represented in figure 4.1.

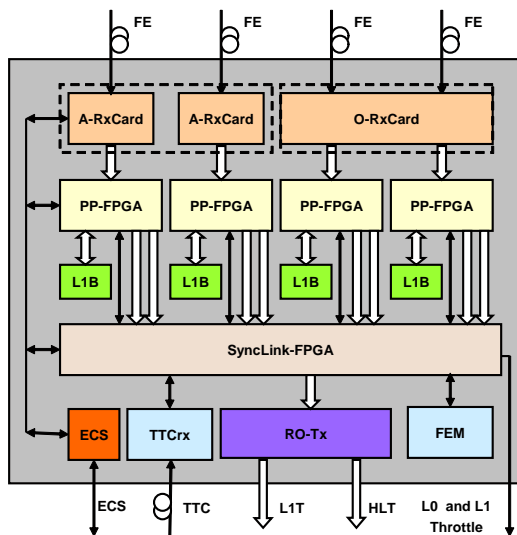


Figure 4.1: TELL1 logic block diagram.

The TELL1 board will stand in a radiation free area at about 60 m from the detector, in such a way that we are not constrained to use rad-hard components.

In the case of the VeLo, the data transmission is done in analogue mode, via copper lines of 60 m length. The line induces a loss of the amplitude, modifications in the frequency spectrum and possible electric noise pick-up. Therefore, a differential transmission is used and a line driver is inserted between the Beetle and the line to amplify the analogue signal and also to correct the frequency response of the system.

The TELL1 prototype used for the tests and described in this document is the Readout Board 3, RB3 [48]. It is a 40MHz device which can be equipped with up to four FADC cards, each receiving 4 input lines. In our case, the RB3 is equipped with a unique 4-links FADC mezzanine card receiving the data from a unique front-end chip. The 8-bit ADC samples the incoming analogue signal of the four links each 25 ns. For that purpose, a dedicated 40 MHz clock is provided for each ADC channel and a delay scan has to be done for each configuration in order to determine the optimal sampling point. The ADC output must be subsequently synchronized to the RB3 main clock. The so-called “synchronization and pre-processing” FPGAs are dedicated to this goal: upon a L0A, the data from the four links are written into dual clock FIFOs, each using their respective ADC time domain, and are subsequently read with the RB3 board clock. The four link data are then merged in order to form 32-bit words, which are subsequently sent to the “L1 trigger” FPGA in charge to prepare the data structure for the transmission via S-link [49]. A PC with S-link receiver is used to collect the data.

The goal of the tests made in Lausanne is to gain experience with RB3 and improve the performances of the analogue transmission line by studying several configurations. In particular, in § 4.3, we study frequency “pre-compensation”, by filtering at the level of the line driver, and “post-compensation”, by equalization at the end of the line just before the ADC. The pre-compensation is preferred because in general it has a better immunity to high frequency pick-up from the line. In § 4.4 we present the measurements of different contributions to the common and random noise of the system. In particular we estimate the effects of the pipeline non-uniformity and the noise due to the 60 m line.

4.2 Experimental setup

4.2.1 Front-End Electronics setup

The Beetle 1.3 [27] is the 2003 version of a rad-hard on-detector chip which has been developed for LHCb by the University of Heidelberg. It fulfills the requirements of the Vertex Locator (VeLo) and the Inner Tracker (IT) acquisition system (see § 2.2.7). As previously said, the Beetle collects the deposited charges from 128 detector channels corresponding to an event, after preamplification and shaping.

They are then stored at a rate of 40 MHz in one of the 187 cells of a pipeline. Once a L0A occurs, they are passed through a 16 stages derandomizing buffer. In order to characterize the events, 16 information pseudo-digital bits (PDB) are inserted before the analogue signal data stream. A part of this “header” is the Pipeline Column Number (PCN) which represents the position of the event data in the pipeline. Eight bit are therefore necessary to define the PCN ($2^7 = 128 < 187 < 256 = 2^8$). The remaining 8 PDB of the header represent the “I” word giving informations about the Beetle settings and status. Two modes of data transmission can be selected:

1. The $16+128=144$ data samples are transmitted over a single link. The duration of an event data transmission is therefore $144 \cdot 25 \text{ ns} = 3.6 \mu\text{s}$.
2. The 144 data samples are transmitted over four links. Each link carries $4+32=36$ samples. In this way, the duration of an event readout is four times less: $36 \cdot 25 \text{ ns} = 900 \text{ ns}$.

In our tests, we use the single link mode for settings purpose because it provides an overall view of the Beetle data frame, but we use the four links mode for the final measurements because this will be the configuration in LHCb. A representation of the 4-links output mode with the header pseudo-digital bits is shown in figure 4.2:

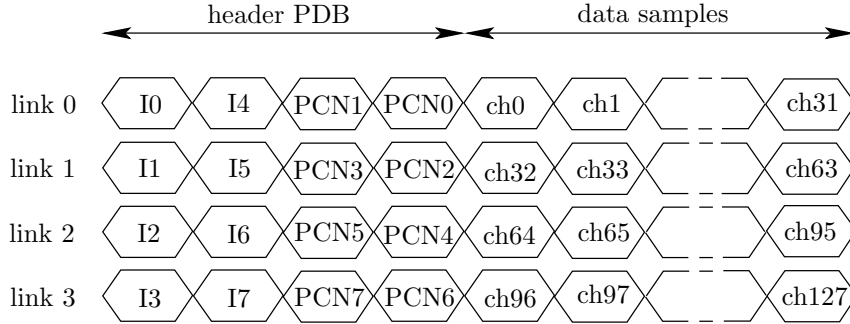


Figure 4.2: Beetle 1.3 4-links output mode. $I(7 : 0)$ represents the I word carrying the Beetle internal registers settings. $PCN(7 : 0)$ is the Pipeline Column Number which value is comprised between 0 and 186.

In the setup in Lausanne, we do not have Silicon sensors to connect to the front-end chip. A charge injection system is therefore used to simulate charge collection. The channels 0, 1, 2, 3, 4, and 5 in link 0, and 122, 123, 124, 125, 126, and 127 in link 3 are bonded to the injection system. The larger capacity of these channels with respect to the non-bonded ones implies an increase of the pedestal values and the noise as we can see in figure 4.3.

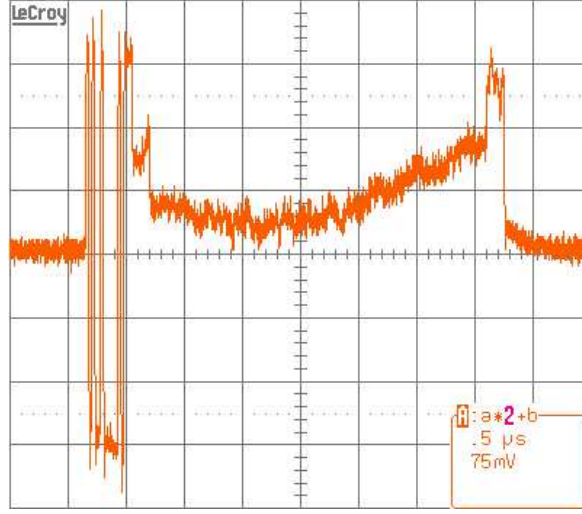


Figure 4.3: Beetle “frame” without charge injection readout of the 128 channels mode. At the beginning, after the header, and at the end, the channels bonded to the injection capacitances are visible.

The input capacity of the injection system is ~ 3 pF and the injected pulse has an amplitude corresponding to a charge injection of ~ 3.5 fC ($\simeq 22'000$ electrons). Assuming a width of $200 \mu\text{m}$ for the VeLo Silicon sensors [50], this corresponds to the average charge deposited by a minimum ionizing particle. It is important to say that we consider the average probability for the loss of energy according to the Landau distribution ($\left.\frac{dE}{d(\rho x)}\right|_{\text{min}}^{\text{Si}} = 1.664 \text{ MeV} \cdot \text{g}^{-1} \cdot \text{cm}^2$ and $\rho_{\text{Si}} = 2.33 \text{ g} \cdot \text{cm}^{-3}$) [51]. Other people consider instead the most probable value of the Landau distribution for the loss of energy in the matter. In this case, the calibration below has to be multiplied by ~ 0.7 .

In figure 4.4, we show the analogue signal directly at the output of the Beetle. A charge injection of ~ 1 MIP was present at the third channel. The measurement is done with a 2 GHz oscilloscope equipped with 0.7 pF active probes. A 200 MHz frequency cut is applied and a set of ~ 4000 events is recorded. A pedestal subtraction evaluated over ~ 1000 events without pulse injections is applied. The average amplitude is calculated (over $4 \times \sim 1000$ events) for the four possible configurations of the two last PDB of the header which are distinguishable on the figure. We can see that an internal crosstalk effect is already present at the level of the Beetle. It propagates only in the next 25 ns sample and seems to have equal amplitude after the header and after the pulse ($\sim 8\%$). The Beetle contains several registers for voltage settings and setup functionalities which are managed by a LabView code running on a PC, connected to the Beetle through an I2C interface.

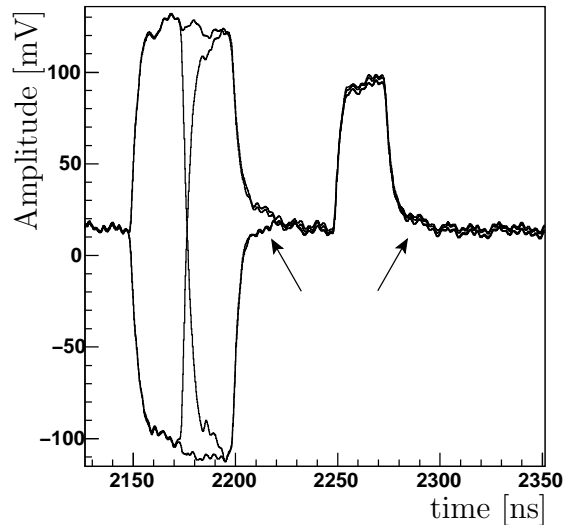


Figure 4.4: Analogue signal measured at the Beetle output with a 2 GHz oscilloscope equipped with 0.7 pF active probes and with a 200 MHz frequency cut. A charge equivalent to ~ 1 MIP is injected in the third channel. The four curves represent the average over ~ 1000 events for the four possible PDB of the header in link 0 after pedestal subtraction. A tail follows each signal (see arrows), corresponding to a crosstalk larger than 5% height at middle of the 25 ns window.

4.2.2 Off-Detector Electronics setup

The Level-1 off-detector electronics Readout Board version 3 RB3 [48] has been developed as a prototype of TELL1 [28] (see § 2.2.7). For our tests, a unique 4-links FADC card is needed on the RB3 to digitize the data from a unique Beetle chip. The analog-to-digital converter AD9057 [52] has an acceptance dynamic range between +2 V and +3 V. Therefore, the analogue signal after amplification is shifted by a pre-defined offset in order to adjust finely the baseline within the ADC acceptance window. This is done through an 8-bit voltage-output digital-to-analog converter Max521 [53] controlled by the RB3 logic.

The ADC samples the incoming analogue signal at a rate of 40 MHz and digitizes it into 8-bit. The four analogue lines may have different relative delays of the order of a few nanoseconds. A dedicated programmable delay between 0 and 24 ns is used to adjust the ADC strobes to the input analogue signal independently for each link. These four delays were initially provided by a PHOS4 chip [54], the ideal adjustment being determined through a delay scan for each link. An important result of our tests was the discovery that the PHOS4 was not a reliable device. Therefore, it has been decided to bypass it: in our tests, the ADC clocks have been derived from the common 40 MHz RB3 clock and delayed externally by cable-delay boxes. In the

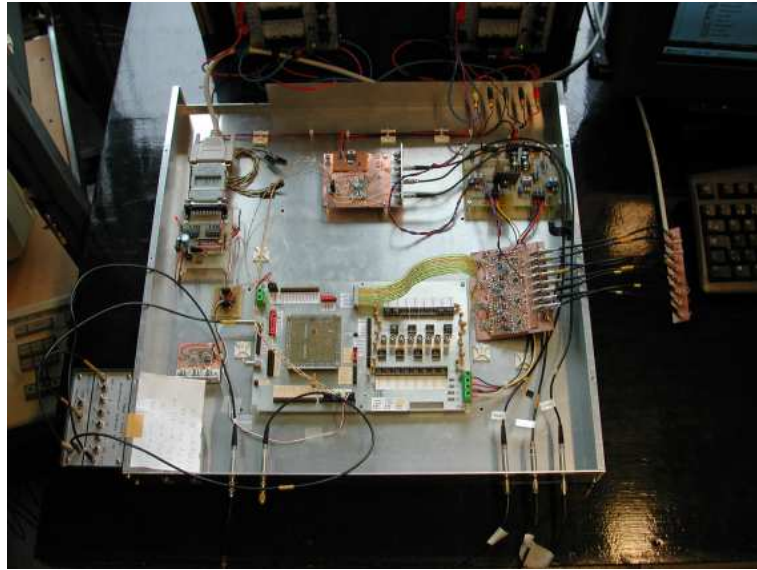


Figure 4.5: A picture of the setup with a Beetle 1.3.

TELL1, the programmable delay will be obtained by an ad hoc circuitry based on Phase-Locked Loops (PLL) implemented in the FPGAs.

A Synchronization and Pre-Processing (SPP) FPGA¹ is dedicated to each FADC card. In the simplified version of the firmware adopted for our tests, once a L0A signal occurs, the 8-bit data of the four links are stored in four dual clocks FIFO, each controlled by their own ADC clock and then re-synchronized to the common board clock.

For each link, the first four incoming bits carrying the pseudo-digital informations are extracted and treated separately from the analogue data samples. The PCN is reconstructed and compared to the PCNs coming either from the Front-End Emulator (FEM) or from another link. The error flags resulting from this test and other event informations are collected to form two 32-bit words. At the output of the SPP FPGA, an event is characterized by these two words, followed by the 32 channels data words (see figure 4.6).

Zero-suppression is not performed in this version of the firmware. The consequence is that the SPP FPGA output rate is too high for the rest of the board, leading to a saturation of the Level-1 Trigger (L1T) FPGA FIFO, which is the next step in the data flow. In order to solve the problem, a sampling system that reduces the number of events down to an acceptable level is implemented in the SPP FPGA.

¹Altera Apex EP20K200BC-356 [55]

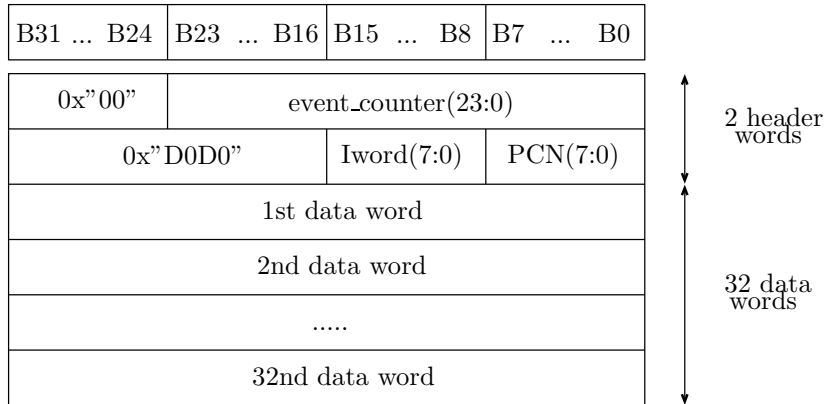


Figure 4.6: SPP FPGA output event format.

The L1T FPGA² receives the data words coming from the four SPP FPGAs. It reformats the events and sends them to a S-link transmitter mezzanine card where they are finally exported to a PC for acquisition and analysis via the S-link.

In the final version of the TELL1, the 40 MHz clock and the L0A are derived from the Timing, Trigger and Control system (TTC). For this purpose, a specific place is reserved for the TTC receiver (TTCrx) mezzanine card [56]. Another place is foreseen for the Front-End Emulator (FEM) chip, which is a Beetle 1.3 (without detector). Synchronized by the TTC system and in the absence of errors, front-end chips and FEM should behave the same, which can be checked by PCN comparison. However, during our tests, these two chips are bypassed and clock and trigger are provided by a programmable multi-channel pulse generator SEQSI³ [57]. The RB3 contains several registers to set the functionalities of the board. These are programmed through an I2C-USB interface controlled by a PC [58]. In figure 4.7, we show a picture of the RB3 setup in the laboratory of Lausanne.

4.2.3 Performances of the RB3 system

- As previously said, we have encountered important difficulties with the programmable delay PHOS4. Although this chip has been tested and used several times, the implemented delay is not always correctly interpreted. In our case, it was very difficult to set the ADC sampling point reliably. TELL1 will implement a circuitry on the FPGA using Phase-Locked Loops (PLL) to generate a fast clock and shift registers for clock dividing.

²Altera Apex EP20K100QC-240 [55]

³SEQSI: SEQuencer for use in Silicon readout Investigation

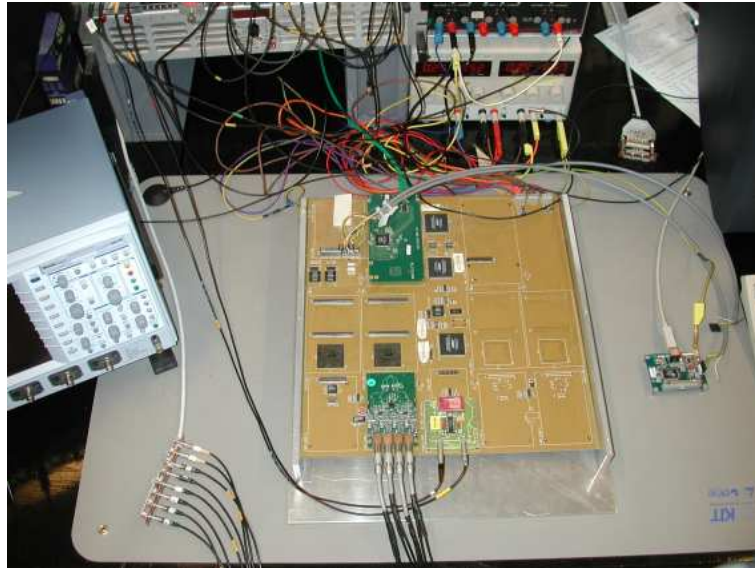


Figure 4.7: A picture of the setup with RB3. The FADC card is at the bottom of the motherboard and the S-link at the top.

- Due to our inexperience in the VHDL coding, we spent several months in programming the synchronization tasks. The main problem was to handle time domain conflicts between the writing and reading of the FIFO. This happens specially during the routing simulation in which the FPGA internal signal transmission delays are taken into account and are of the same order than the delay between the writing and reading clocks.
- The S-link was performing well. Nevertheless, it is a non-standard device. It has been abandoned for a Gigabit Ethernet transmission system with a data nominal link output of 1 kBytes @ 20 kHz i.e. 20 MBytes/s.

4.3 Studies of the 60 m transmission line

4.3.1 Cable choice and performances

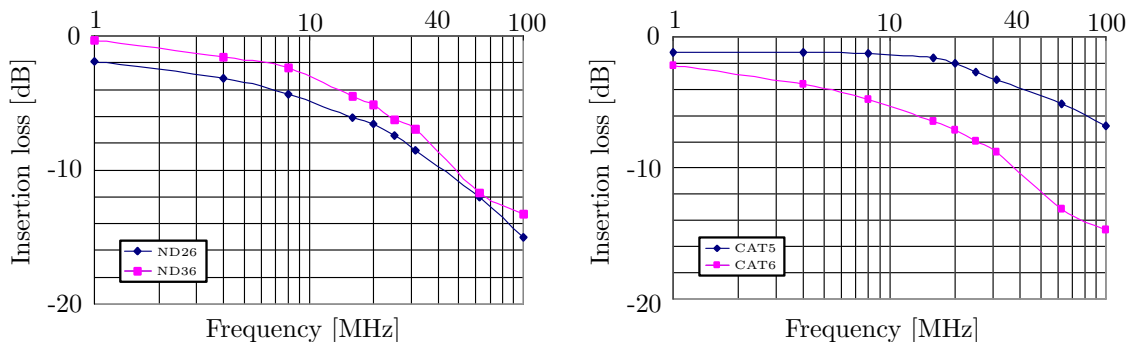
Some tests have been made to select the best compromise given by four cable types: ND26P, ND36P, CAT5 and CAT6. The technical features of the cables are summarized in table 4.1. A serious advantage of the CAT6 with respect to the others is that the four twisted pairs are shielded individually, providing a better protection against RF pick-up and crosstalk. Secondly, the CAT family has lower external diameters (~ 5 mm) than the ND (~ 15 mm) which simplifies the connections.

	ND26P	ND36P	CAT5	CAT6
Number of pairs	13	18	4	4
Shield	global Al	global Al	global Al	individual Al
External diameter [mm]	14	15.5	5.3	5.8
Impedance [Ω]	120	120	100	100
Price per pair [CHF/m]	0.38	0.33	0.53	0.35

Table 4.1: Technical features of the tested cables.

However, if we consider the diameter of a single pair, the difference is not significant because we have less than 4 mm for the ND while it is ~ 3 mm for the CAT. Concerning the price per pair, the four types are similar, the CAT5 being the most expensive. Knowing that we need 5'376 links for the readout of the VeLo detector, the use of 60 m CAT6 lines will cost $5'376 \cdot 0.35 \cdot 60 \simeq 113$ kCHF (without connectors).

Some more detailed physical performances have to be taken into account for the selection. For that purpose, the insertion loss and the propagation delays have been measured. As it can be seen in figure 4.8, the CAT5 provides less attenuation at 40 MHz (~ -4 dB) than the three other cables (~ -10 dB). The lowest propagation delay - necessary time for the analogue signal to travel through the line - is given by the CAT6 cable (~ 250 ns), and also the very lowest propagation delay skew, which is the maximal difference of propagation delays between the pairs. Over 60 m, we measured a propagation delay skew of ~ 1.7 ns to be compared to more than 6 ns for the other cables.

Figure 4.8: Insertion loss for the ND26P and ND36P (*left*) and for the CAT5 and CAT6 (*right*) 60 m lines measured in the laboratory of Lausanne.

The Near End Crosstalk (NEXT) and the Far End Crosstalk (FEXT) are the “capacitive + inductive” crosstalks measured at the input and the output of a neighbour pair respectively. These quantities must be related to the insertion loss. In particular, the Attenuation to Crosstalk Ratio (ACR) is the difference between the insertion loss and the NEXT, which can be interpreted as a signal-to-noise ratio considering only the noise induced by a neighbour pair. In a similar way, the Equal Level Far End Crosstalk (ELFEXT) is defined as the difference between the insertion loss and the FEXT.

The NEXT is measured at several frequencies between 1 and 100 MHz. The results are shown in figure 4.9. The curves obtained with the ND36P, the CAT5 and the CAT6 are quite similar (~ -50 dB at 40 MHz) while the attenuation is less important with the ND26P (~ -30 dB at 40 MHz). The ACR curves are also

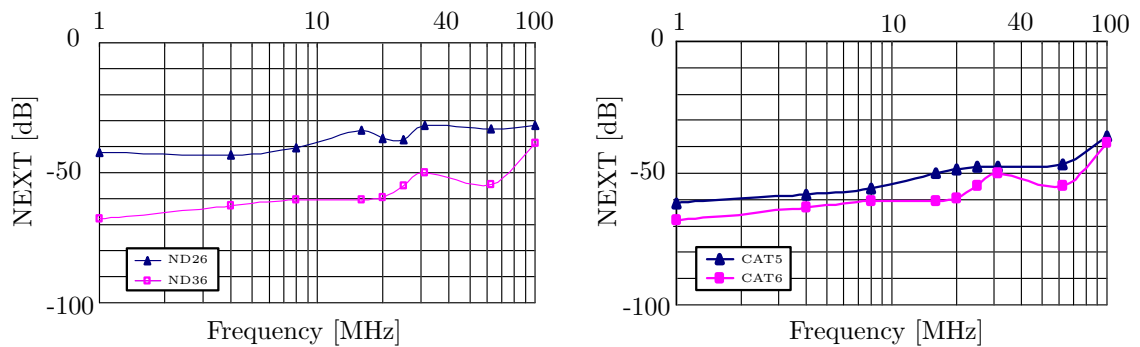


Figure 4.9: Near End Crosstalk (NEXT) for the ND26P and ND36P (*left*) and for the CAT5 and CAT6 (*right*) 60 m lines measured in Lausanne.

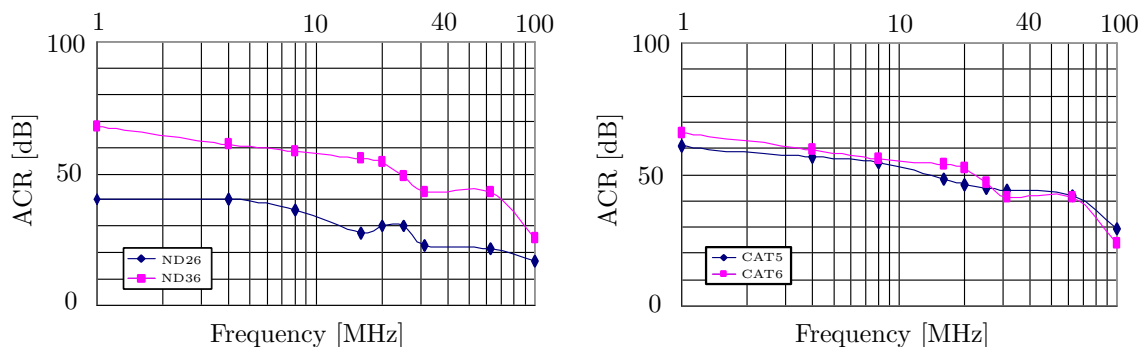


Figure 4.10: Attenuation Crosstalk Ratio (ACR) for the ND26P and ND36P (*left*) and for the CAT5 and CAT6 (*right*) 60 m lines measured in Lausanne.

equivalent at 40 MHz (~ 40 dB), except for the ND26P where it is only of the order of 20 dB (see figure 4.10). The FEXT curves are represented in figure 4.11. The best results are obtained with the CAT family and specially with the CAT6 (~ -65 dB at 40 MHz). This is reported to the ELFEXT which is also greater with the CAT5 and the CAT6 lines (see figure 4.12). In particular, it is ~ 50 dB at 40 MHz while it is only ~ 30 dB with the ND cables.

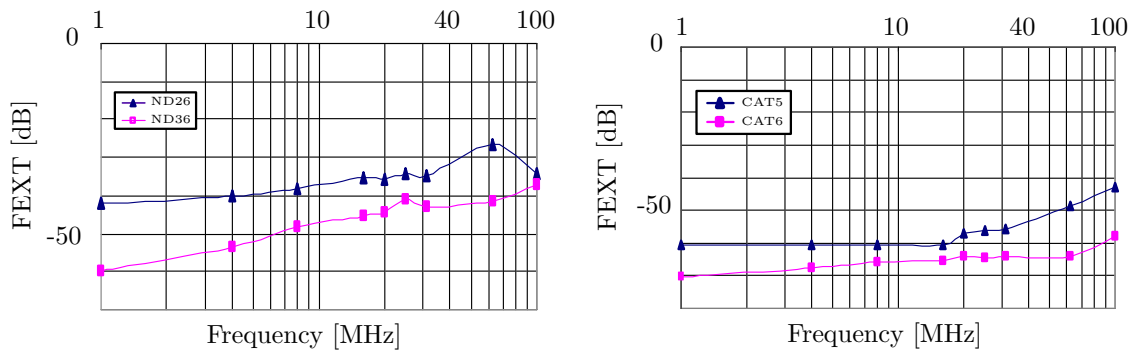


Figure 4.11: Far End Crosstalk (FEXT) for the ND26P and ND36P (*left*) and for the CAT5 and CAT6 (*right*) 60 m lines measured in Lausanne.

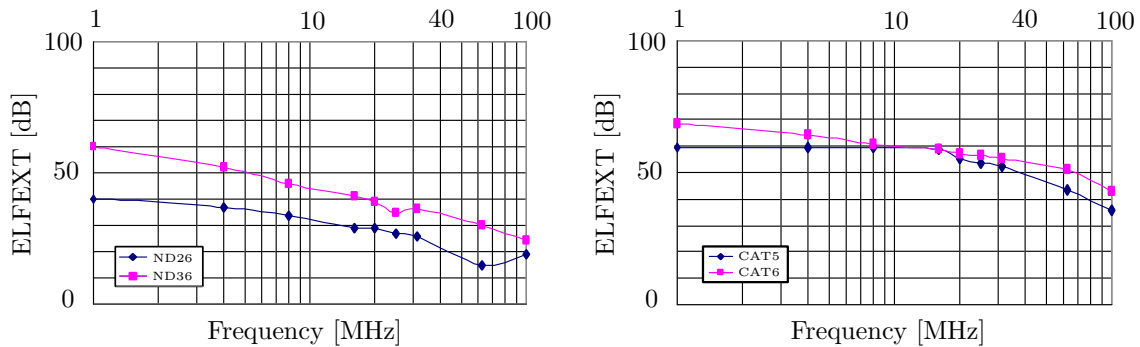


Figure 4.12: Equal Level Far End Crosstalk (ELFEXT) for the ND26P and ND36P (*left*) and for the CAT5 and CAT6 (*right*) 60 m lines measured in Lausanne.

The results of these measurements are summarized in table 4.2. All these considerations lead to the choice of CAT6. The decisive parameters are the lowest propagation delay skew and the high values for the ACR and ELFEXT. The quite low price and easy availability are also in favour of this cable.

	ND26P	ND36P	CAT5	CAT6
Insertion loss at 40 MHz [dB]	-9.16	-8	-4	-10
Propagation delay [ns]	300	300	300	250
Propagation delay skew [ns]	6.5	11.0	6.1	1.7
ACR at 40 MHz [dB]	23	40	43	41
ELFEXT at 40 MHz [dB]	23	34	50	54

Table 4.2: Physical performances of the tested cables (60 m lines).

4.3.2 Gain and Frequency compensation

We will now discuss the active elements of the transmission line. We have tested several schemes of drivers and receivers. For our first tests in July 2003 (prototype 1), the analogue signal gain compensation was obtained in the line driver, while the frequency compensation was done in the receiver after the line. The driver is composed of three stages (see figure 4.13) and uses AD8042 Op-Amps. The first stage acts on both polarities and is an inverting amplifier. On the second stage, the inverted polarity is subtracted to the non-inverted one. The resulting unipolar signal is then amplified. On the last stage, we use an inverting and a non-inverting amplifier to reconstruct the differential signal. The gain per polarity is ~ 6.3 leading to a global gain $G \simeq 12.6$ for the driver 1.

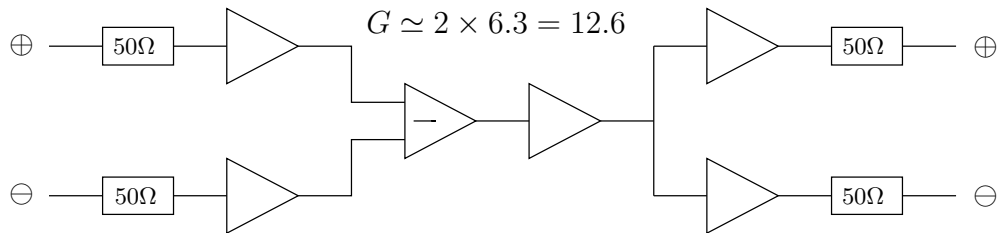


Figure 4.13: Schematics of the driver 1.

The receiver 1 contains four stages, three of them being used for frequency response correction calculated to match the cable loss (see figure 4.14). The first stage acts as a differentiator to have an unipolar signal. It is followed by a non-inverting amplifier ($G_1 \simeq 1$) with a feedback which is the first correction pole. The first stage is integrated in an AD8130 device. The second correction pole is done in the second stage where a non-inverting amplifier ($G_2 \simeq 1.15$) with a feedback is integrated in

an OPA680 device. The third stage acts like the second one but with $G_3 \simeq 2$. The last stage of the receiver is dedicated to reconstruct a bipolar output and is integrated in a HTA1212 device with a gain $G_4 \simeq 1$. The global gain of the receiver is thus $G_{tot} \simeq 2.3$.

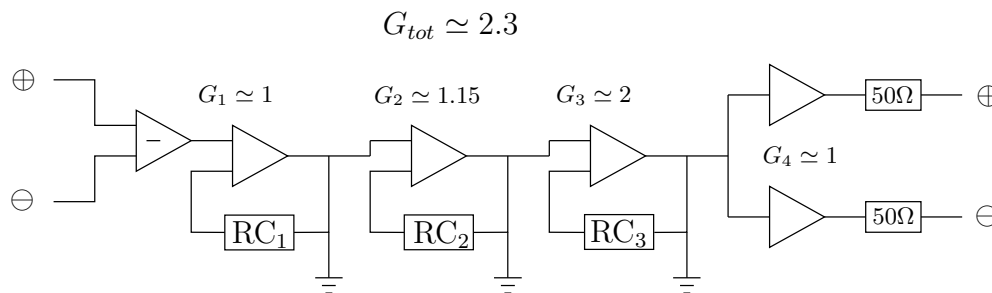


Figure 4.14: Schematics of the receiver 1. RC indicates a feedback network.

The overall measured gain of the line comprising the line driver 1, the 60 m cable and the receiver 1 is $G \simeq 12.4$. A problem appeared with this configuration. The response to a 25 ns square pulse provided by a functions generator shows a quite large tail in the next window of 25 ns. We will call this effect *crosstalk* or *residual amplitude*. The crosstalk factor for this configuration is $\sim 8\%$. We observed that the Op-Amp bandwidth was far from our needs. Similarly, we found that when the pulse was provided by the Beetle (see figure 4.15), the crosstalk was even larger ($\sim 16\%$). The presence of a 50Ω resistance on both inputs of the line driver acts as a 50Ω load to ground for the Beetle. As the offset of the Beetle baseline is non zero, some current is pulled out of the Beetle leading to a non-optimal use of the front-end chip. The raising and falling times in this configuration are already of ~ 9.8 ns and ~ 9.2 ns. It was then decided to redesign the whole system.

The second version of the line driver and receiver was released in November 2003. The main change was made on the line driver because the two 50Ω resistances are removed and replaced by a single 100Ω resistance connecting the two input polarities (see figure 4.16). A capacitive coupling is inserted between the Beetle and the amplifiers. In this configuration, there is no current flowing from the Beetle output and the ground. Therefore, the front-end chip can operate correctly. The raising and falling times are reduced respectively to ~ 3.8 ns and ~ 4.8 ns, significantly reducing the contribution to crosstalk. The inserted capacitance acts as a high-pass filter with a frequency cut at ~ 1600 Hz. The gain for each polarity is ~ 7 implying a total gain $G \simeq 14$ for this second version. The AD8042 amplifiers used in the driver 1 are replaced by two HFA1135.

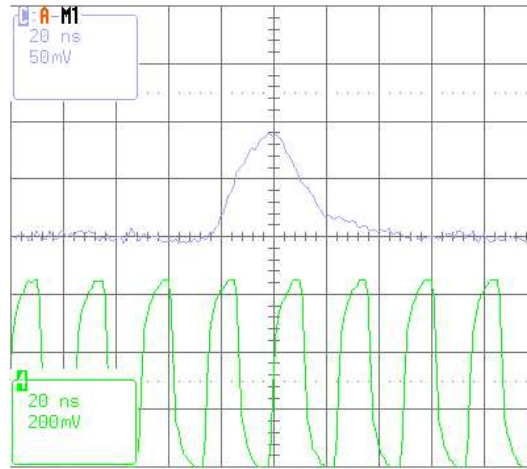


Figure 4.15: The top signal is the response of the driver 1 with the receiver 1 (link 0) to a 25 ns pulse provided by the Beetle. The bottom is the clock which drives the ADC by its rising edge. The time scale is 20 ns per division.

The design of the receiver 2 is the same than in the first version except that the OPA680 amplifiers are replaced with faster AD8056 in the second and the third stages, leading to a global gain for the receiver of $G \simeq 2.42$. The measured gain of the 60 m line with the line driver 2 and the receiver 2 is $G \simeq 12.08$ (~ 6.04 per polarity), similar to prototype 1.

At this point of the development, a first trial of pre-compensation was also applied, by adding a capacitor C_{out} in parallel to the output resistance of the line driver. An advantage of this solution is that the optimal value of the capacitance can be tuned quickly. Depending on the value of the capacitance, it is possible to obtain over- or under-shoot in the analogue signal after 25 ns. For instance, the crosstalk factor was considerably reduced to less than 5% with $C_{out} = 270$ pF (see figure 4.17).

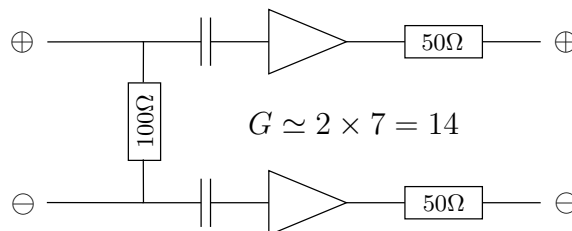


Figure 4.16: Schematics of the driver 2 with the capacitive coupling.

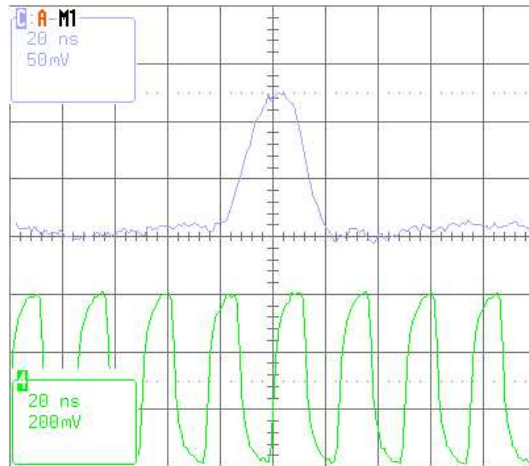


Figure 4.17: Time-domain response of the driver 2 ($C_{out} = 270$ pF) with the receiver 2 (link 0) with a 25 ns pulse from the Beetle. The time scale is 20 ns per division.

The good results obtained with the pre-compensation in the driver 2 led to a reconceptualization for the analogue signal compensation in January 2004. The idea of compensating the signal in the receiver was abandoned for the benefit of a unique pre-compensation. The idea is also that a post-compensation should not be used in order to avoid amplification of possible RF noise pick-up from the line. The third version contains two corrections in the driver (see figure 4.18). A ~ 120 pF capacitance is put in parallel to the output resistance of the driver. The HFA1135 amplifiers are replaced by AD8011 in which a second correction is inserted as in

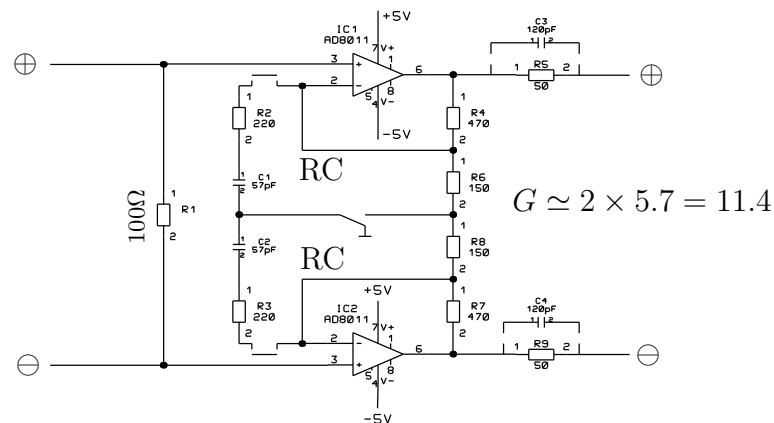


Figure 4.18: Schematics of the driver 3 and 4. RC indicates a feedback network.

the Op-Amp feedback. The global gain of the driver 3 is $G \simeq 2 \times 5.7 = 11.4$. A receiver with flat frequency response is associated with it. The crosstalk factor in this configuration is $\simeq 6\%$ with the Beetle connected. The improvement is significant if we remember the $\sim 16\%$ value obtained with the first configuration.

The driver 3-bis is exactly the same than the previous, except that printed circuit and SMD components are used. The fourth and final version of the driver is extended to the use of the four links. Its time-domain response after 60 m (link 0) is represented in figure 4.19.

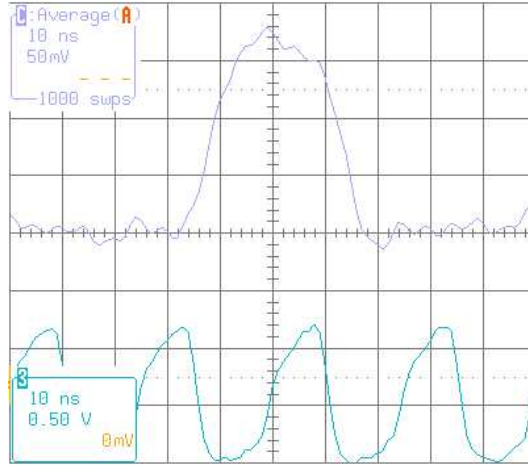


Figure 4.19: Time-domain response of the driver 4 (link 0). The time scale is 10 ns per division.

4.3.3 Performance measurements with the optimal configuration

As it is described in figure 4.21, a Beetle 1.3 controlled by a SEQSI sends analogue data on four links to a RB3. One MIP equivalent charges ($\sim 22'000$ electrons) are injected in the channel 3 in link 0 where the six channels 0, 1, 2, 3, 4 and 5 are bonded. Although the four links mode is used, only the behaviour of the link 0 is studied here. The differential output signals are amplified and pre-compensated on the line driver version 4, with two poles of correction. The signals travel 60 m through an uncoiled CAT6 twisted-pairs line and are collected by four analogue boards on the RB3. At this point, the unipolar signal is formed and digitized on 8-bit. As explained in section 4.2.2, four independent clocks are used to adjust the ADC strobes to the input analogue signals. The ADC sampling phase ϕ_{ADC}^l ($l = 0, 1, 2, 3$) is defined as the time difference between the ADC clock of link l and

the common RB3 clock. A phase scan by steps of 3 ns was made with a ~ 1 MIP pulse injected in channel 3 (resp. 26) for link 0 (resp. 3). For link 1 and 2, as no channels are bonded to the charge injection system, we use a stable bit of the header as the signal (~ 1.5 MIP). The average value over 400 events are calculated. A more accurate scan by steps of 1 ns is subsequently performed in the interesting region ($\phi_{\text{ADC}}^l = 0, \dots 3$ ns and 22, $\dots 25$ ns). The results are shown in figure 4.20. The optimal phase is selected as a compromise between the highest amplitude for the signal and the lowest in the neighbour channels. In particular, a non-zero signal in the preceding channel is an indication of a too late clock phase. According to figure 4.20, the selected ADC sampling phases for the four links are presented in table 4.3. After digitization, the data enter the RB3 for synchronization and formatting before being exported through the S-link for storage and analysis.

link l	0	1	2	3
ϕ_{ADC}^l [ns]	22	19	19	19

Table 4.3: Optimal ADC sampling phase for the four links.

A measurement consists in the acquisition of two distinct 1'000 events runs. The charge injection system is disabled for the first one in order to measure the pedestal amplitudes (pedestal file: $p(c, e)$ where c is the channel number and e the event number) and is reactivated for the second one to simulate particles detection (pulse file: $a(c, e)$). A thousand events is an adequate value to have a low statistical error.

First, an algorithm evaluates the pedestal of the 128 channels with the pedestal file. The pedestals are the baseline amplitudes of each channel taking every parts of the transmission line into account. The pedestal value of each channel $P(c)$ is calculated over $\sim 1'000$ events:

$$P(c) = \frac{1}{1000} \cdot \sum_{e=1}^{1000} p(c, e) \quad \text{for } c = 1, \dots, 128 \quad (4.1)$$

The pedestal shape of the link 0 is presented in figure 4.22 (*left*). The rms values (not represented) are very small (rms $\simeq 0.1$ adc counts) with respect to the global pedestal amplitude (pedestal $\simeq 65$ adc counts). Higher amplitudes due to higher capacitance load on the bonded channels are noticeable in the first 6 bins.

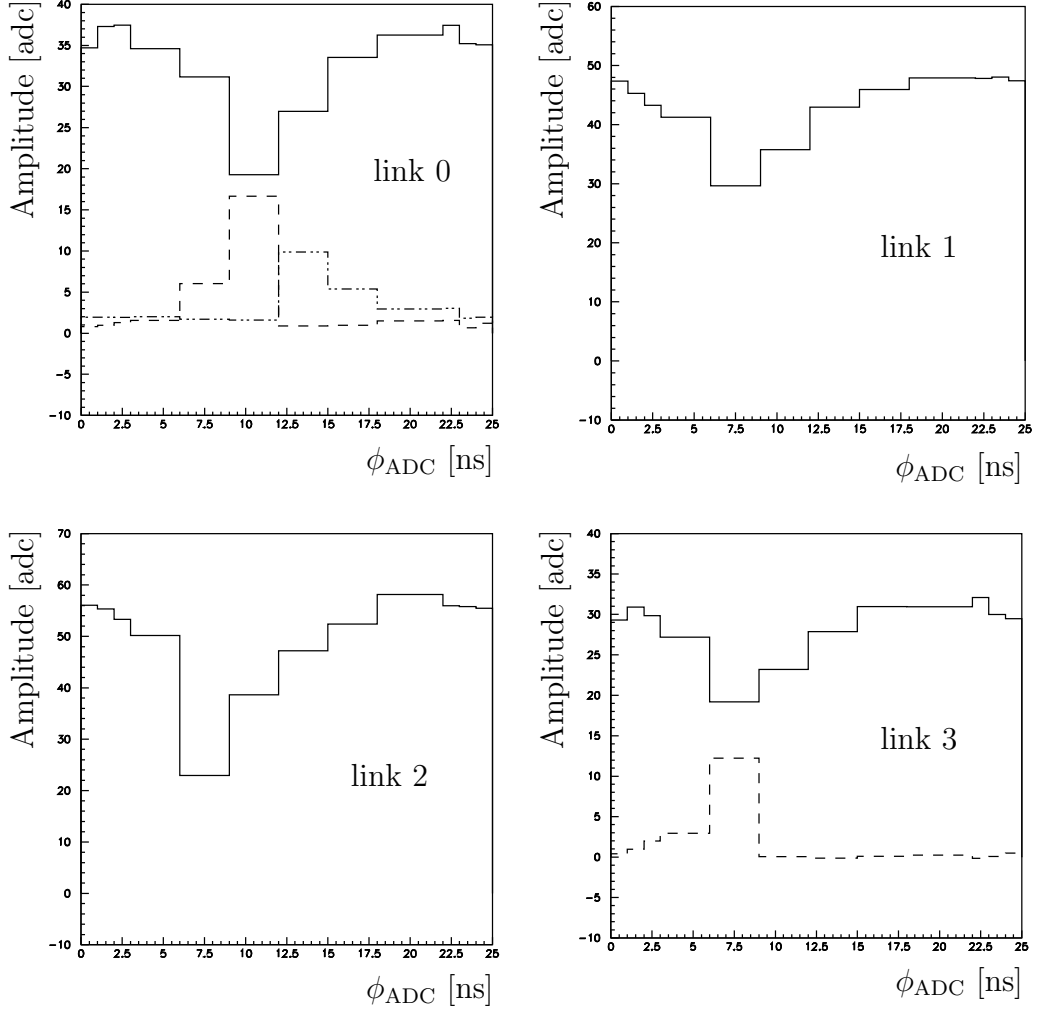


Figure 4.20: Signal amplitude as a function of the ADC sampling phase ϕ_{ADC}^l for the four links $l = 0, 1, 2, 3$. ϕ_{ADC}^l is defined as the time difference between the ADC and the common RB3 clocks. The phase is scanned by steps of 3 ns except between 0 and 3 ns and between 22 and 25 ns where the step is 1 ns. The signal corresponds to ~ 1 MIP in links 0 and 3 while it is ~ 1.5 MIP in links 1 and 2. The previous and the following channels are also shown for link 0, and only the previous for link 3 (dashed line).

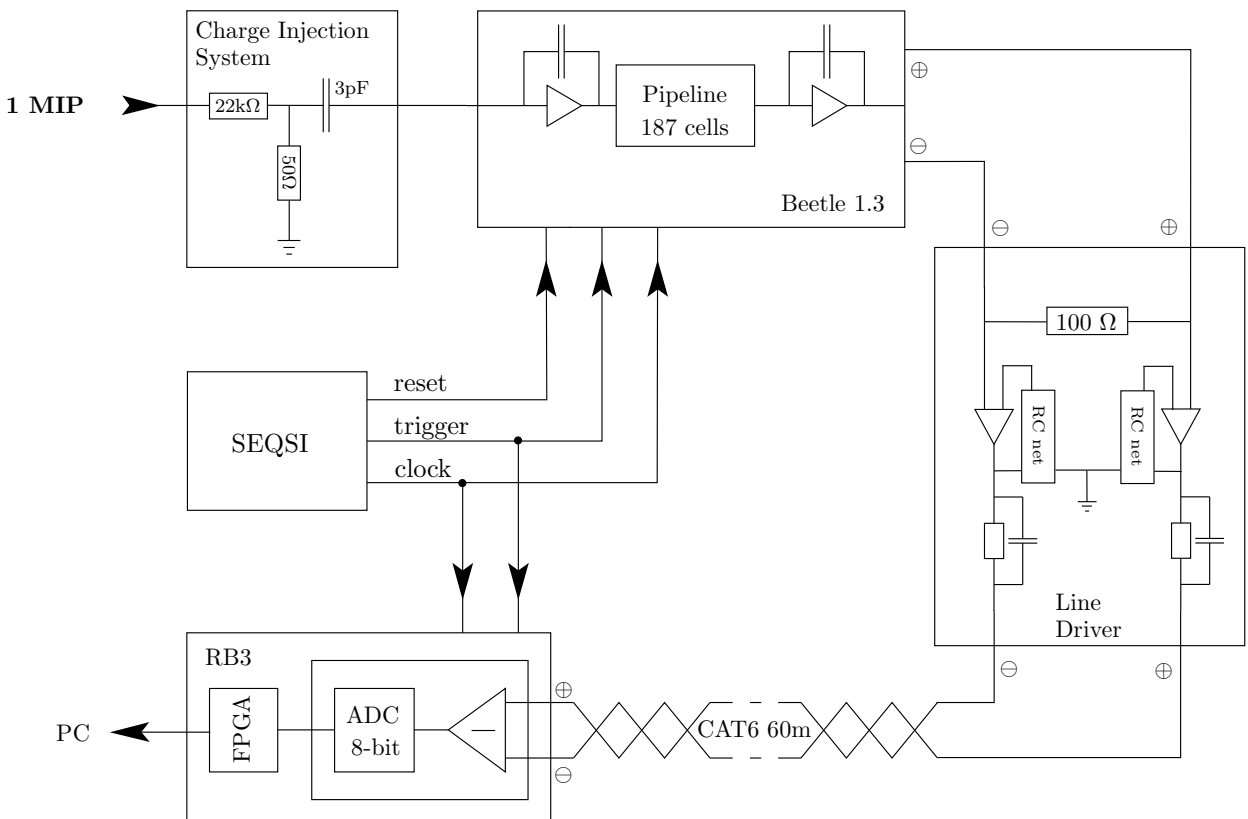


Figure 4.21: Block diagram of the experimental setup.

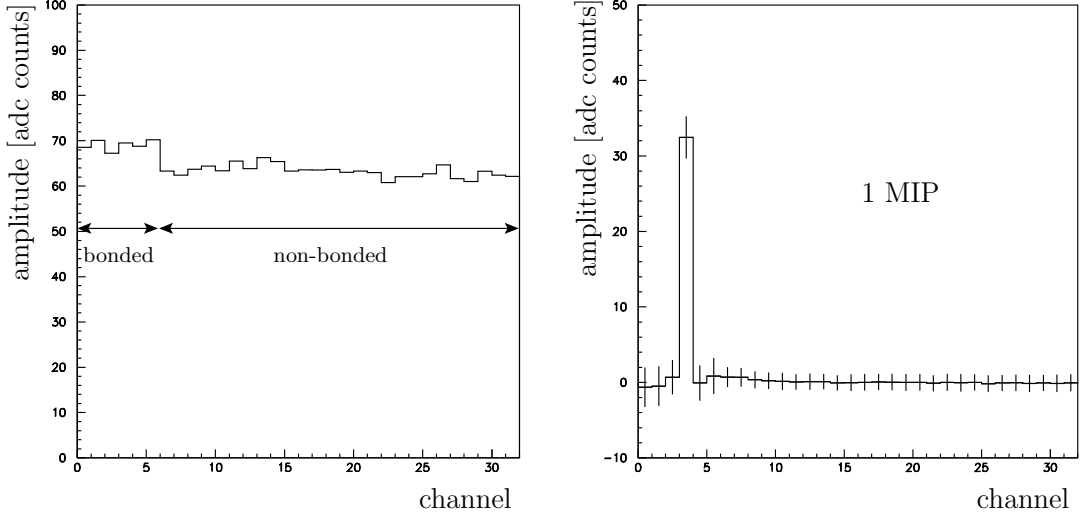


Figure 4.22: Pedestal amplitudes for link 0 (average over 1'000 events) (*left*). Average over 1'000 events with the charge corresponding to ~ 1 MIP injected in channel 3 (*right*).

Then, we perform the analysis of the pulsed data. The first step is the pedestal subtraction. For each channel, the corresponding pedestal amplitude $P(c)$ (eq. (4.1)) is subtracted to the data $a(c, e)$ for event e :

$$A(c, e) = a(c, e) - P(c) \quad \text{for } c = 1, \dots, 128 \text{ and } e = 1, \dots, 1'000 \quad (4.2)$$

The second step consists in the Common Mode Suppression (CMS) which has to be calculated for each event independently. A simple correction for low frequency common noise can be obtained by evaluating the average value $CN(e)$ of the channels data $A(c, e)$ for each link:

$$CN(e) = \frac{1}{C_{nb}} \cdot \sum_{c_{nb}=1}^{C_{nb}} A(c_{nb}, e) \quad (4.3)$$

for C_{nb} non-bonded channels and $e = 1, \dots, 1'000$

It is important to notice that we consider only the non-bonded channels for the common mode calculation. As only six channels are bonded including one pulsed in the link 0, the statistic would have been too low with the bonded channels. Furthermore, as we will see later, the amplitude of the pulse in channel 3 propagates in several next neighbours. These channels must be discarded. Therefore, the

calculation of the common noise in link 0 is done only with the 24 last non-bonded channels. In practice, this way of doing cannot correct for common mode originated at the level of the charge injection system.

The common noise per event (eq. (4.3)) is then subtracted to the recorded data $A(c, e)$ (eq. (4.2)) giving the corrected value $B(c, e)$:

$$B(c, e) = A(c, e) - CN(e) \quad \text{for } c = 1, \dots, 32 \text{ and } e = 1, \dots, 1'000 \quad (4.4)$$

An example of result of the procedure is given in figure 4.22 (*right*), where a pulse equivalent to one MIP was injected in the channel 3. The figure shows the average over 1'000 events. Here again, the rms values are larger in the bonded channels (~ 4 adc counts) than in the non-bonded channels (~ 2 adc counts).

The effect of the CMS algorithm on the non-bonded channels is demonstrated in figure 4.23. The 1'000 amplitude values of channel 12 are represented as a function of channel 22 in a scatter plot. On the left, only the pedestals are subtracted. A correlation between the two channels is clearly noticeable which traduces the presence of low frequency common mode. On the right figure, the CMS algorithm is applied, the result being the vanishing of the correlation. As we will discuss in detail in section 4.4, the main source of common noise originates at the level of the Beetle.

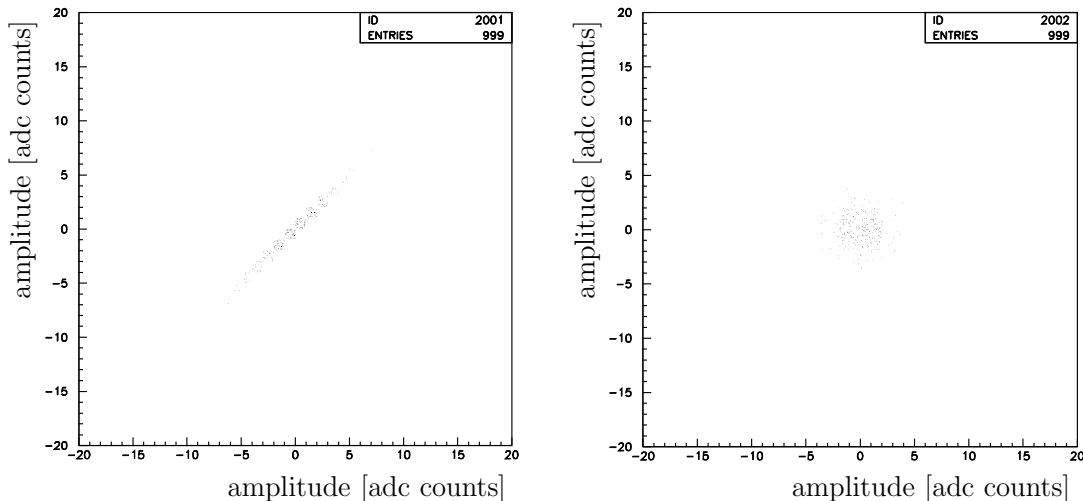


Figure 4.23: Representation of the non-bonded channels 12 *vs* 22 before (*left*) and after (*right*) the common noise suppression.

If we observe the figure 4.22 (*right*), we can guess a residual crosstalk with the adjacent channels. As previously said, the signal shape depends on the frequency compensation network, on the Beetle internal characteristics and on the line. The measured crosstalk depends on the ADC sampling phase which determines at which point the signal shape is sampled. To evaluate the crosstalk, we consider the amplitudes of the four channels following the pulsed channel 3 and compute the four rates $R_i(e)$ for each event:

$$R_i(e) = \frac{B(3+i, e)}{B(3, e)} \quad \text{for } i = 1, \dots, 4 \text{ and } e = 1, \dots, 1'000 \quad (4.5)$$

The distributions of $R_i(e)$ for 1'000 events are shown in figure 4.24. The width of the distributions is due to the residual noise. As it has been optimized, the crosstalk factor is quite low with this configuration in channel 4, the mean value being close to zero $CF_1 \simeq -0.05\%$. The four crosstalk factors are presented in the left column of table 4.4.

	Beetle	Generator
CF_1 [%]	-0.05	-4.5
CF_2 [%]	2.8	4.0
CF_3 [%]	2.1	2.5
CF_4 [%]	2.0	2.8

Table 4.4: Crosstalk factors evaluated with a 25 ns pulse coming from a Beetle (*left*) and from a generator (*right*).

For comparison, we give the contribution to the crosstalk from the line driver and the line only. For this, the Beetle is disconnected and 25 ns pulses with amplitude equivalent to 1 MIP are injected in the line driver with a functions generator. A common noise suppression is not necessary in this case ($CN(e) \simeq 0$). According to eq. (4.5) and (4.4), we use:

$$R_i^{\text{gen}}(e) \simeq \frac{A(3+i, e)}{A(3, e)} \quad \text{for } i = 1, \dots, 4 \text{ and } e = 1, \dots, 1'000 \quad (4.6)$$

The distributions of the $R_i^{\text{gen}}(e)$ in the four 25 ns window next neighbours are presented in figure 4.25 and the mean values in the right column of table 4.4. The crosstalk factors are larger in this case but still lower than 5%. The rms are very low because of the quasi-absence of noise.

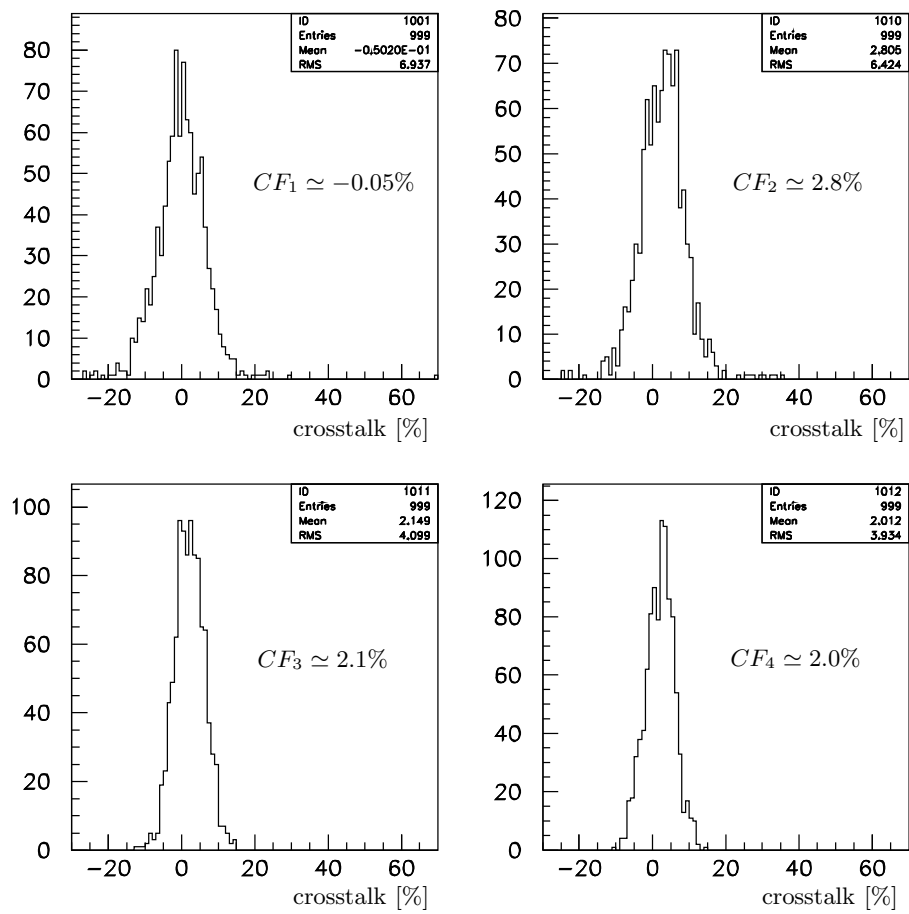


Figure 4.24: Distributions of the crosstalks in % in link 0 for channel 4 (*up left*), 5 (*up right*), 6 (*down left*) and 7 (*down right*). The charge was injected in channel 3.

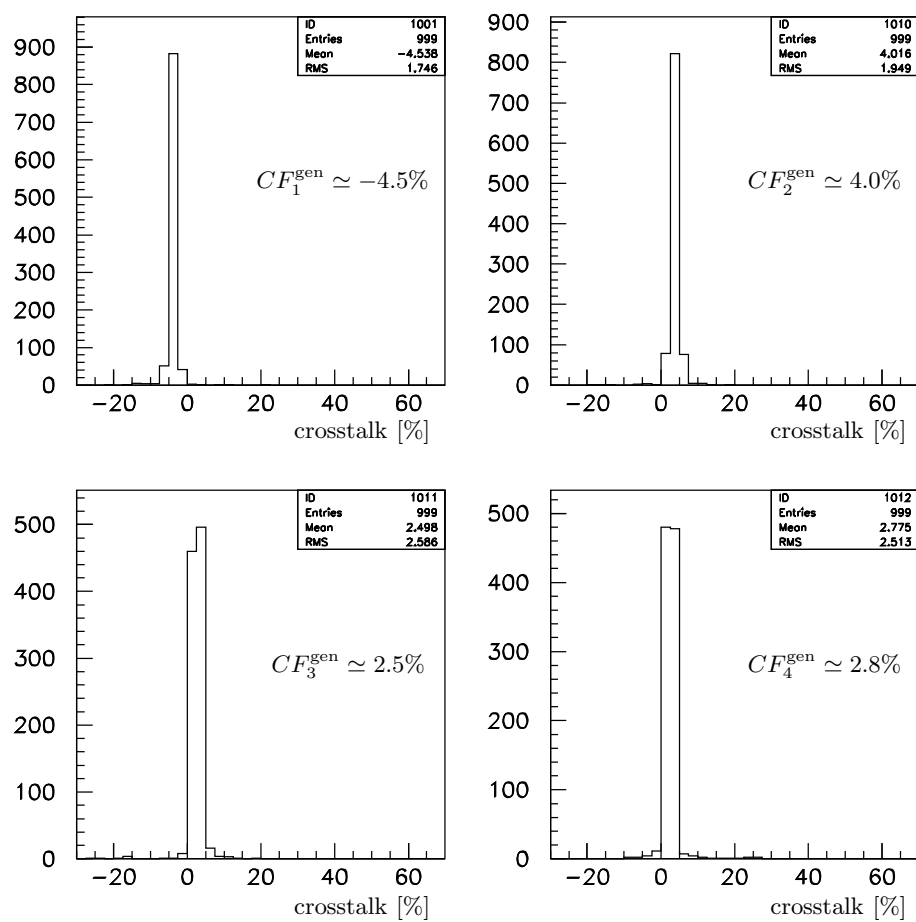


Figure 4.25: Distributions of the crosstalk in % in the four 25 ns window next neighbours with a 25 ns pulse injected from a generator instead of the Beetle.

It is important to emphasize that these factors correspond to the crosstalk induced in the line driver and the 60 m line only. If we consider the three transfer functions of the Beetle φ_B , the line driver φ_D and the line φ_L and a signal S injected at the level of the Beetle, the response S' received on RB3 can be written as:

$$S' = \varphi_L \circ \varphi_D \circ \varphi_B(S) \quad (4.7)$$

The line driver is tuned to correct for deformations induced from the charge collection at the Beetle level until RB3, in such a way that:

$$S' \simeq S \quad \Rightarrow \quad \varphi_L \circ \varphi_D \circ \varphi_B \simeq \mathbb{1} \quad (4.8)$$

On the other hand, for a signal T injected at the line driver level, its response T' on RB3 is:

$$T' = \varphi_L \circ \varphi_D(T) \simeq \varphi_B^{-1}(T) \quad (4.9)$$

according to eq. (4.8). In section 4.2.1, we have seen that crosstalk effects of the order of $\sim 8\%$ are already present at the level of the Beetle (figure 4.4). Therefore, its transfer function $\varphi_B \neq \mathbb{1}$ and $T' \neq T$. The signal is over-compensated in that case.

The signal and pedestal obtained with the Beetle disconnected and connected are shown in figure 4.26. The first measurement gives an estimate of the intrinsic noise of the line. The system is calibrated by the injection of a charge equivalent to 1 MIP, giving a signal of ~ 32.5 adc counts. The intrinsic noise of the system without the Beetle is ~ 0.41 adc leading to $S/N \simeq 79.2$. With the Beetle connected and after CMS, the total noise increases by a factor ~ 2.5 ($\simeq 1.14$ adc counts) thus $S/N \simeq 28.5$. According to an equivalent noise charge of $\sim 1'000$ electrons for a $200 \mu m$ thick silicon strip [59] together with the calibration of 22'000 electrons $\simeq 1$ MIP $\simeq 32.5$ adc counts, the detector contribution to noise should be ~ 1.48 adc counts. The quadratic sum of both contributions leads to:

$$N_{total} = N_{detector} \oplus N_{line} \simeq \sqrt{(1.48)^2 + (1.14)^2} \simeq 1.87 \text{ adc counts}$$

which implies a signal-to-noise ratio reduced to $S/N \simeq 17.4$ which still fulfills the requirements for the VeLo.

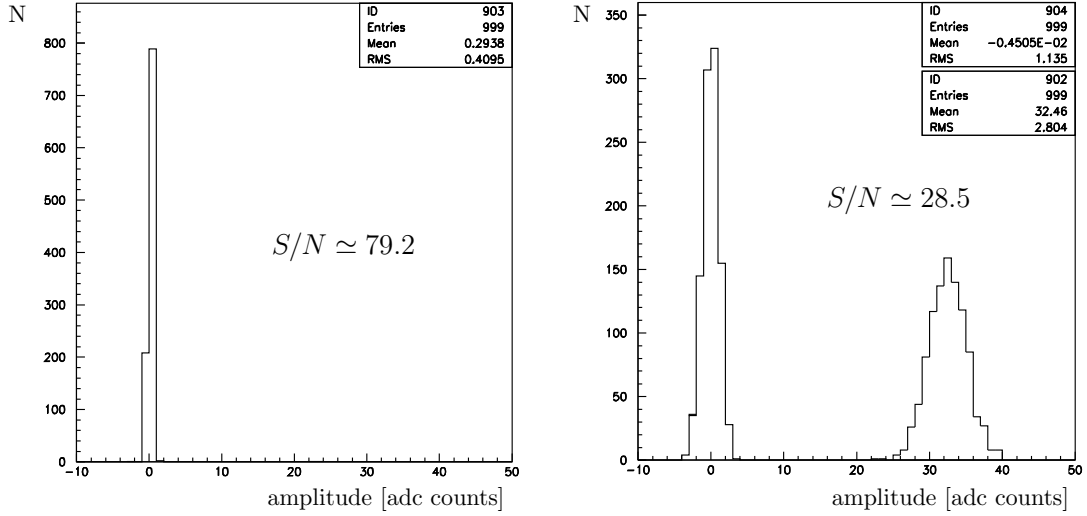


Figure 4.26: Signal and noise without (*left*) and with (*right*) the Beetle connected. In the second case, the noise peak is measured using non-bonded channels. The peak at ~ 32.5 adc counts corresponds to ~ 1 MIP calibration.

4.4 Noise study

4.4.1 Pipeline non-uniformity

The Beetle 1.3 contains a pipeline composed of 128×187 cells which can store up to 187 events waiting for a L0 trigger. If we look at a single channel, the 187 positions in which the sample can be stored can have slightly different capacitance values. This might imply different values of pedestals for the same channel as a function of the position in the pipeline. On top of that, we can have some state machine dependent effects.

As already stated, the position in the pipeline is encoded in the header of the analogue data as the Pipeline Column Number PCN. In the algorithm explained in the previous section, the pedestals are in practice averaged over the 187 pipeline positions. The fluctuations of the pedestal values in a fixed channel as a function of the PCN bring an additional kind of noise to the analogue signal. In figure 4.27, the pedestal structure of the pipeline depending on the channel and the PCN is represented for each link independently. We can notice several ridges and hollows which are common to several neighbour channels along the PCN axis implying correlations between channels on the same link.

More in detail, the pedestal values of channels 18 and 30 in link 0 are shown on the left of figure 4.28. On the right, each of the 187 values of channel 18 are plot as a function of channel 30. The correlation with PCN is apparent. The

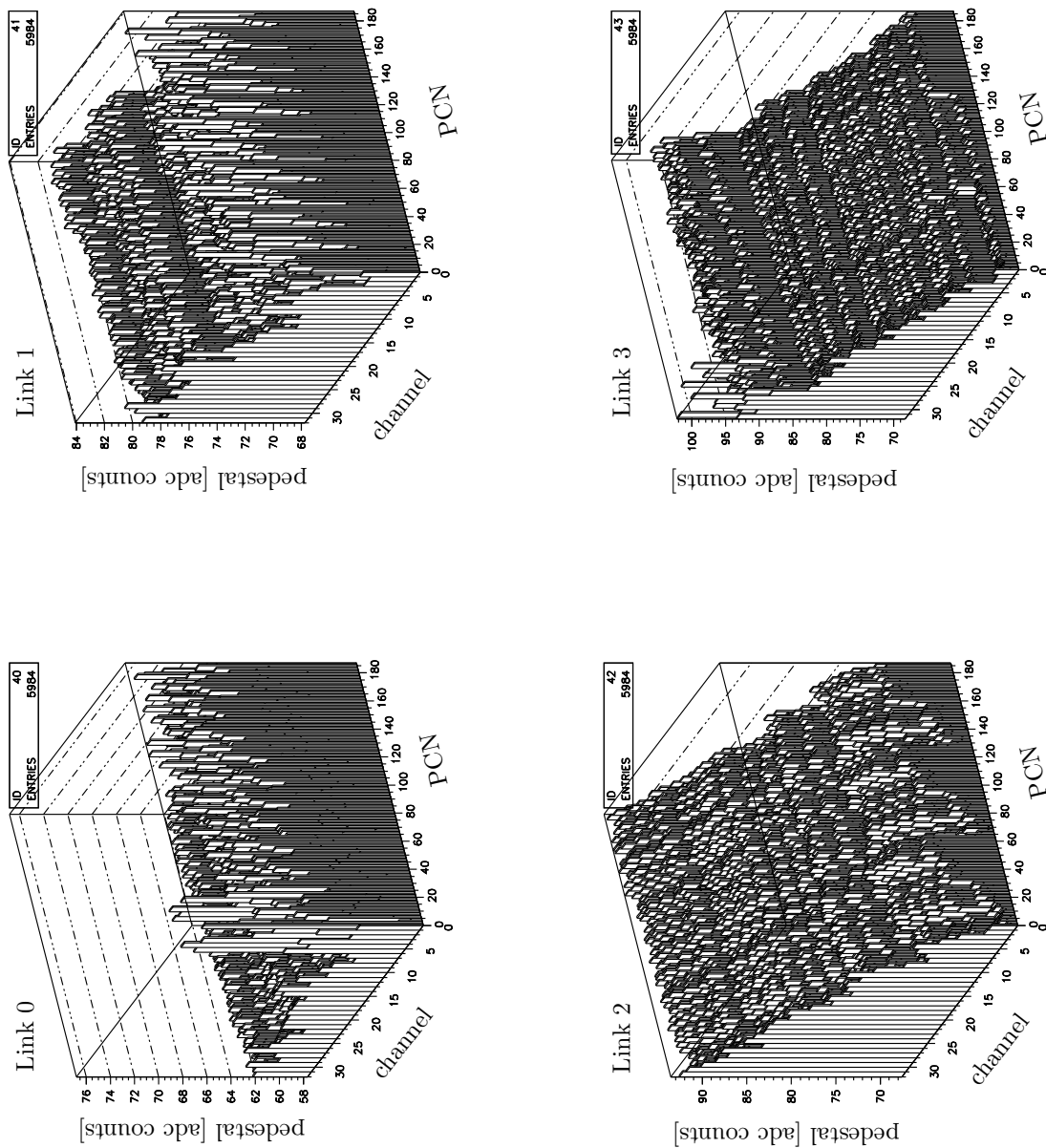


Figure 4.27: Pedestal values as a function of the channel and the Pipeline Column Number PCN for the four links independently.

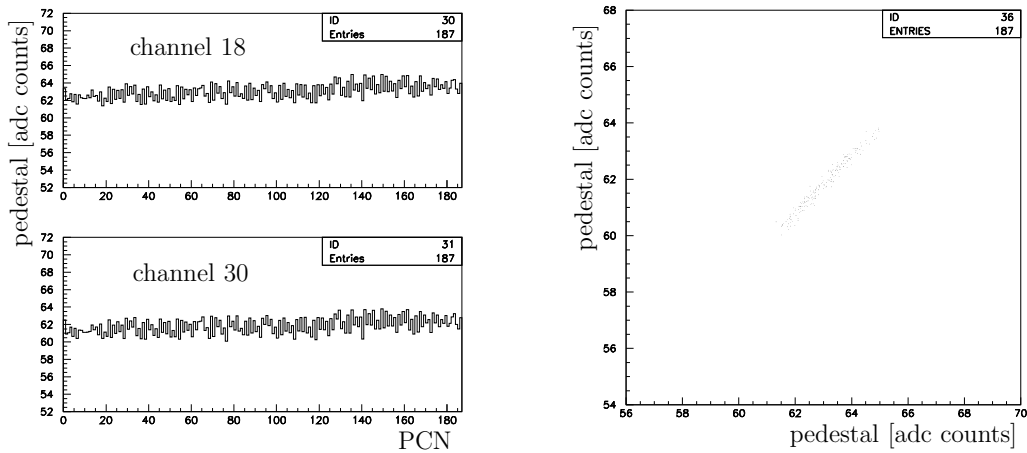


Figure 4.28: Pedestal amplitudes for channels 18 and 30 (link 0) as a function of PCN (*left*) and their correlation (*right*).

fact that the points stand along a $\sim 45^\circ$ line imply that only a general offset exists between the two channels and that their shapes are similar. In principle, looking to this example, we can suppose that a common mode correction procedure will automatically cure the problem. Another example is presented in figure 4.29 for link 3 in which the pedestals of channels 108 and 120 are drawn. Here again, the values are correlated. Figure 4.30 shows the case of channels which do not belong to the same link: channel 48 in link 1 and channel 80 in link 2. The correlation is apparent, a little less accentuated than in the two previous cases in which both

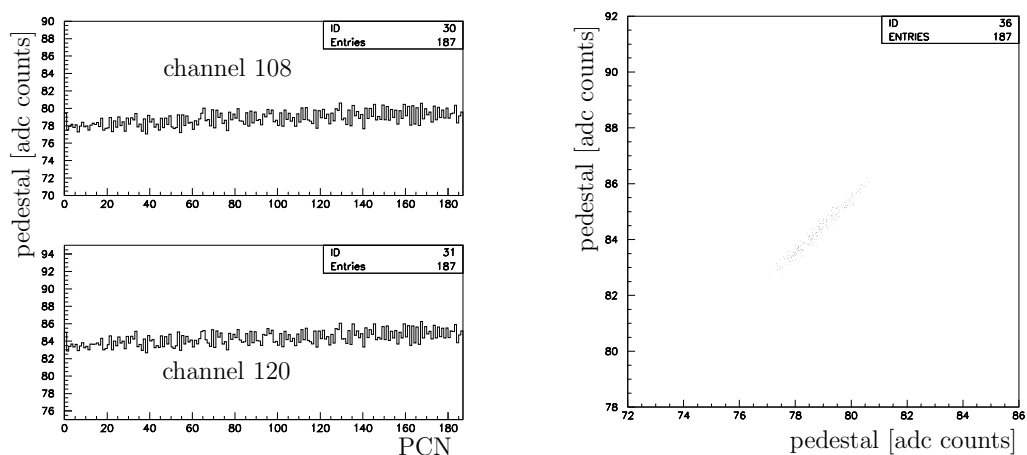


Figure 4.29: Pedestal values correlation between channels 108 and 120 (link 3).

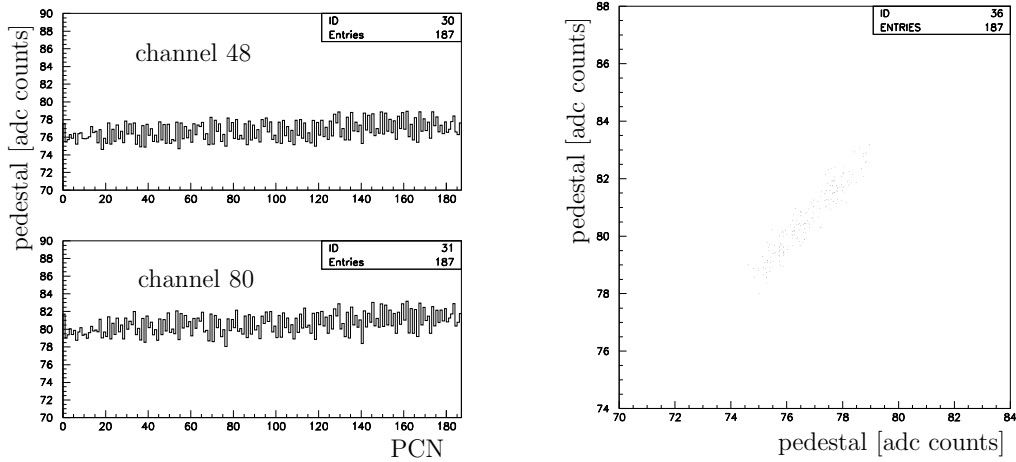


Figure 4.30: Pedestal values correlation between channels 48 (link 1) and 80 (link 2).

channels belong to the same link. In these ideal cases, the noise generated by the pipeline non-uniformity appears like a contribution to the common noise ($\sim 1/2$ of the total, by comparison with the case shown in figure 4.23) and is accounted for in the procedure previously discussed. However, we can find channels in which the pedestal values are less correlated with the others. These channels are found systematically close to the header in the transmission. It is the case for channel 96 - the first of link 3 - which is compared to channel 108 in figure 4.31, clearly showing two baseline levels. The header bits crosstalk influence is suspected to be responsible for this effect and this will be demonstrated in section 4.4.3. Despite of the 2-levels

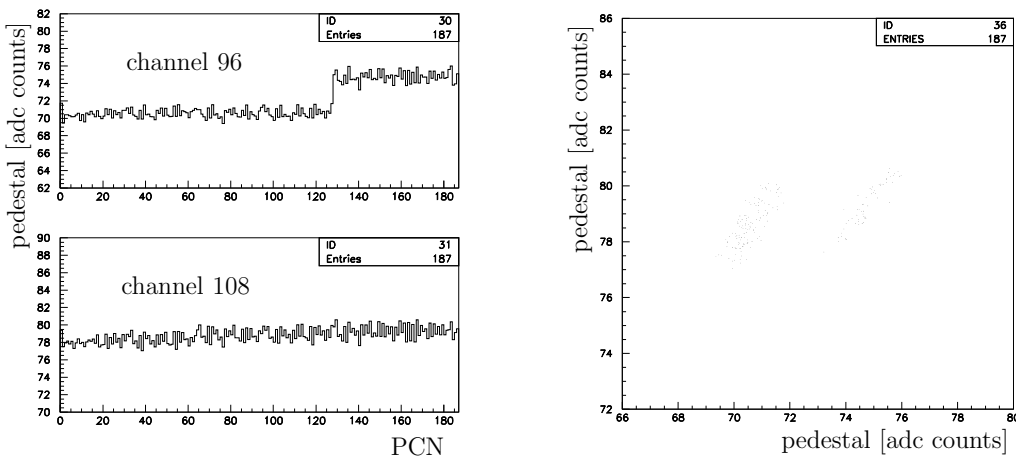


Figure 4.31: Pedestal values correlation between channels 96 and 108 (link 3).

shape in channel 96, both channels are still correlated as it can be seen on the right of figure 4.31. In this case, some procedure more involved than the common mode suppression has to be considered. In principle, a pipeline dependent pedestal subtraction could be used (see section 4.4.3).

In conclusion, applying a pipeline independent pedestal subtraction like it is done in section 4.3.3 cannot cure all the problems. Only a pipeline dependent pedestal subtraction is capable of removing the totality of this source of noise. This is one of the point studied in the next section.

4.4.2 Contributions to noise

In this section, we discuss in more detail the different contributions to the common and random noise in our system with a 60 m line. The random noise cannot be suppressed offline and the only way to decrease its contribution is at the hardware level. If we consider the Beetle 900 ns signal window, any additional noise in a frequency range well below ~ 1 MHz will result in a baseline displacement of the 32 samples which can be suppressed by the common noise correction method explained in section 4.3.3. Furthermore, as it is explained in the previous section, we have observed a common noise component correlated with the Pipeline Column Number. Each component of the line (amplifiers, pipeline, line driver, 60 m line) brings its own contribution to the random as well as to the common noise. The total noise σ_{tot} is the quadratic sum of common and random contributions:

$$\sigma_{tot} = \sigma_{tot}^C \oplus \sigma_{tot}^R \quad (4.10)$$

The common noise contains contributions from the following sources:

- the Beetle input amplifiers indicated with $\sigma_{amplifiers}^C$
- the PCN correlated noise $\sigma_{pipeline}^C$
- the line driver $\sigma_{line\ driver}^C$
- the 60 m line σ_{line}^C

We neglect contributions from the line receiver and ADC on RB3. We can write:

$$\begin{aligned} \sigma_{tot}^C &= \sigma_{amplifiers}^C \oplus \sigma_{pipeline}^C \oplus \sigma_{line\ driver}^C \oplus \sigma_{line}^C \\ \sigma_{amplifiers+line}^C &= \sigma_{amplifiers}^C \oplus \sigma_{line\ driver}^C \oplus \sigma_{line}^C \\ \Rightarrow \quad \sigma_{tot}^C &= \sigma_{amplifiers+line}^C \oplus \sigma_{pipeline}^C \end{aligned} \quad (4.11)$$

with $\sigma_{amplifiers+line}^C$ containing all the contributions except the PCN correlated noise.

On the random side, we have the same sources:

$$\sigma_{tot}^R = \sigma_{amplifiers}^R \oplus \sigma_{pipeline}^R \oplus \sigma_{line\ driver}^R \oplus \sigma_{line}^R \quad (4.12)$$

We will first study the noise in the non-bonded channel 20 which belongs to the link 0 and stands far from the header. The measurement consists in the acquisition of two $N_{events} = 100'000$ events runs for the pedestals calculation and calibration. Considering the 187 possible pipeline cells in which an event can be stored and random triggers, the result of the acquisition is the two sets containing $p(c, PCN, e)$ and $a(c, PCN, e)$ with ~ 500 events per PCN value.

The total amount of noise in channel 20 is estimated by applying a standard Pipeline Independent Pedestal Subtraction (PIPS) as it was described in section 4.3.3, disregarding the PCN.

We then perform a Pipeline Dependent Pedestal Subtraction (PDPS). The pedestal values for each channel and each position in the pipeline $P(c, PCN)$ are calculated:

$$P(c, PCN) = \frac{1}{N_{PCN}^{pedestal}} \cdot \sum_{e=1}^{N_{PCN}^{pedestal}} p(c, PCN, e) \quad (4.13)$$

for $c = 1,..128$ and $PCN = 0,..186$

The pedestal subtraction is performed on the pulsed sample. For each of the $N_{PCN}^{pulse} \simeq 500$ events of the pulsed events set $a(c, PCN, e)$, the pedestal value of the corresponding channel and PCN (eq. (4.13)) is subtracted:

$$A(c, PCN, e) = a(c, PCN, e) - P(c, PCN) \quad (4.14)$$

for $c = 1,..128$ and $PCN = 0,..186$

In figure 4.32, the distribution of the data after pipeline independent (*left*) and dependent (*right*) pedestal subtraction are presented. We have $\sigma_{PIPS}^{tot} \simeq 2.15$ adc counts and $\sigma_{PDPS}^{tot} \simeq 1.92$ adc counts. We estimate the pipeline contribution to the noise of channel 20 to be:

$$\begin{aligned} \sigma_{pipeline}^C &= \sigma_{PIPS}^{tot} \ominus \sigma_{PDPS}^{tot} \\ &\simeq 2.15 \ominus 1.92 \simeq 0.97 \text{ adc counts} \end{aligned} \quad (4.15)$$

It has been shown in section 4.4.1 that channels belonging to the same link and standing far from the header have their pedestal correlated. The pedestal values for channel 20 are represented as a function of the PCN on the left of figure 4.33 and the corresponding distribution on the right. The rms of the distribution also gives an approximative estimation of $\sigma_{pipeline}^C \simeq 0.92$ adc counts, not far from the first estimation given above.

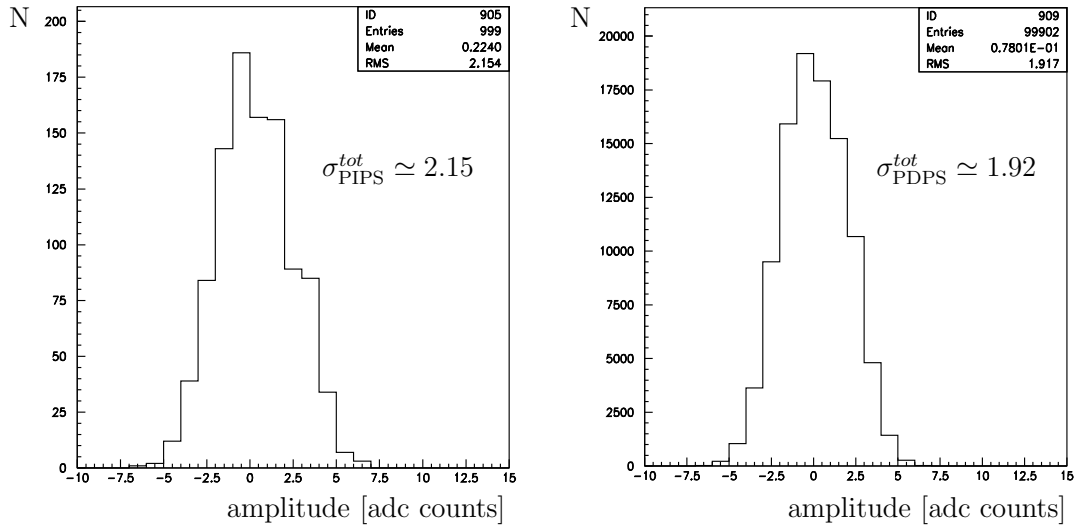


Figure 4.32: Pipeline independent (*left*) and dependent (*right*) pedestal subtraction in channel 20.

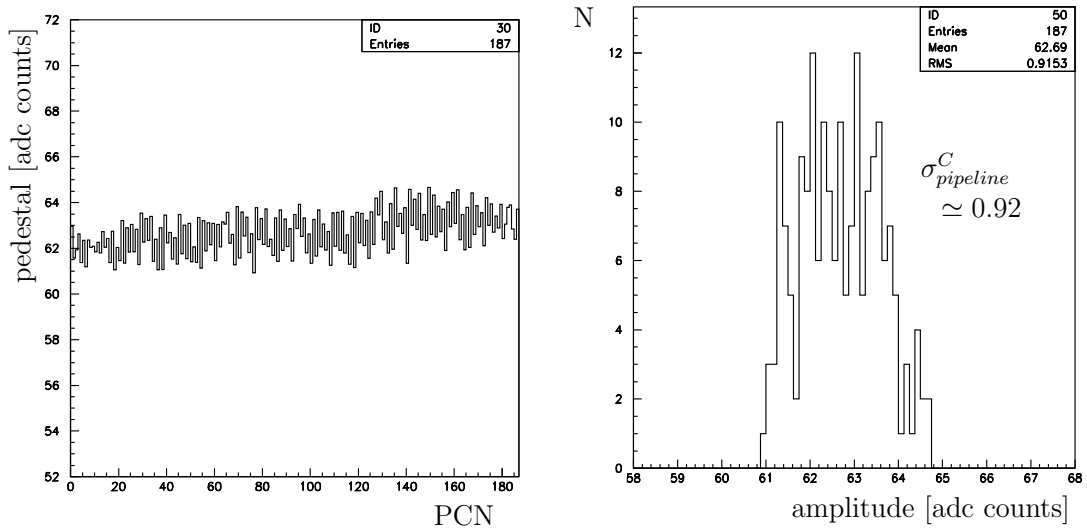


Figure 4.33: Pedestal values of channel 20 as a function of the PCN (*left*) and their distribution (*right*)

We are now ready to consider the effect of the common mode suppression (CMS). As explained in section 4.3.3, the common noise of an event is evaluated over the 24 last non-bonded channels in link 0 (see eq. (4.3)). It must be noticed that the PCN is not important here because it characterizes an event and the correction is

precisely calculated for each event ($e = 1, \dots, 100'000$):

$$CN(e) = \frac{1}{C_{nb}} \cdot \sum_{c_{nb}=1}^{C_{nb}} A(c_{nb}, PCN, e) \quad (4.16)$$

for C_{nb} non-bonded channels

The common noise is then subtracted to the data $A(c, PCN, e)$ obtained from eq. (4.14) for each event e :

$$B(c, PCN, e) = A(c, PCN, e) - CN(e) \quad (4.17)$$

for $c = 1, \dots, 32$

The results for channel 20 after pipeline independent (*left*) and dependent (*right*) pedestal subtraction and common noise suppression are drawn in figure 4.34. The two procedures give very similar results. In practice, with the PIPS, the common noise is suppressed in a single step while, with the PDPS, we first get rid of the pipeline influence and then of the rest of the common noise. The close results ($\sigma_{PIPS}^R \simeq 1.10$ and $\sigma_{PDPS}^R \simeq 1.07$ adc counts) show that a specific processing to correct the noise induced by the PCN effects in channel 20 is not essential and that a standard common noise suppression is therefore sufficient.

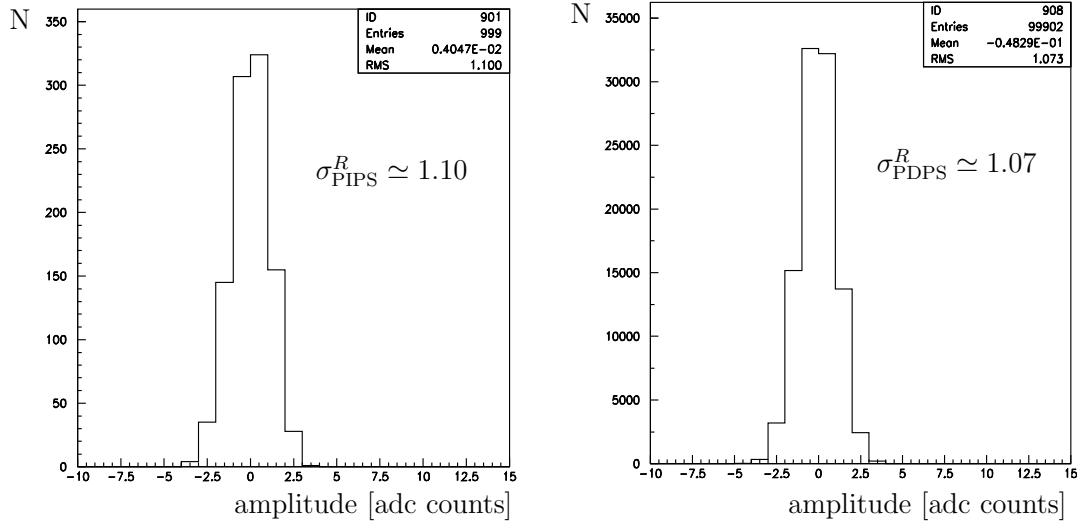


Figure 4.34: Pipeline independent (*left*) and dependent (*right*) pedestal subtraction and common noise suppression in channel 20. The residual fluctuation is interpreted as the random component of the noise. σ_{PIPS}^R contains also a residual from the PCN dependence.

After the PDPS and the CMS procedures, we are left with the random contributions from the line, $\sigma_{\text{PDPS}}^R \simeq 1.07$ adc counts according to relations (4.10) and (4.11). We can now estimate the “not PCN correlated” common noise from the results of figures 4.32 (*right*) and 4.34 (*right*). This corresponds to the amount of noise suppressed by the CMS procedure:

$$\begin{aligned}\sigma_{\text{amplifiers+line}}^C &= \sigma_{\text{PDPS}}^{\text{tot}} \ominus \sigma_{\text{PDPS}}^R \\ &\simeq 1.92 \ominus 1.07 \simeq 1.59 \text{ adc counts}\end{aligned}\quad (4.18)$$

On the other hand, the total common noise σ_{tot}^C is (see eq. (4.11) and (4.15)):

$$\begin{aligned}\sigma_{\text{tot}}^C &= \sigma_{\text{pipeline}}^C \oplus \sigma_{\text{amplifiers+line}}^C \\ &\simeq 0.97 \oplus 1.59 \simeq 1.86 \text{ adc counts}\end{aligned}\quad (4.19)$$

Table 4.5 summarizes the different contributions to noise studied for channel 20 using the calibration $1 \text{ MIP} \simeq 32.5$ adc counts:

$\sigma_{\text{pipeline}}^C \simeq 2.98$		
$\sigma_{\text{amplifiers+line}}^C \simeq 4.89$	$\sigma_{\text{tot}}^C \simeq 5.72$	$\sigma_{\text{PIPS}}^{\text{tot}} \simeq 6.62$
	$\sigma_{\text{PDPS}}^R \simeq 3.29$	$\sigma_{\text{PIPS}}^R \simeq 3.38$

Table 4.5: Contributions to noise for channel 20 in 10^{-2} MIP.

We have to notice that for a channel connected to a silicon sensor, the load induces a greater accumulation of random as well as common noise. This phenomenon is independent from the PCN correlated effects and its influence has to be added to both $\sigma_{\text{amplifiers+line}}^C$ and σ_{PDPS}^R . Therefore, $\sigma_{\text{pipeline}}^C$ becomes negligible compared to $\sigma_{\text{amplifiers+line}}^C$. The conclusion of these tests is that a standard pedestal subtraction and common noise suppression algorithm should be sufficient for channel 20. A particular pipeline dependent pedestal subtraction is not necessary in this case.

4.4.3 Contribution to noise in channels near the header

The situation is different for channels standing just after the header. Even if the system is tuned to obtain the minimal possible crosstalk ($CF < 5\%$), the quick variations in the header pseudo-digital bit has to be added to the pipeline non-uniformity contribution, increasing the common noise. In this paragraph, we study the channel 96 which is the first of link 3. On the left of figure 4.35, the pedestal values corresponding to the 187 positions of the pipeline are represented. On the right, the distribution of these 187 amplitudes is plotted.

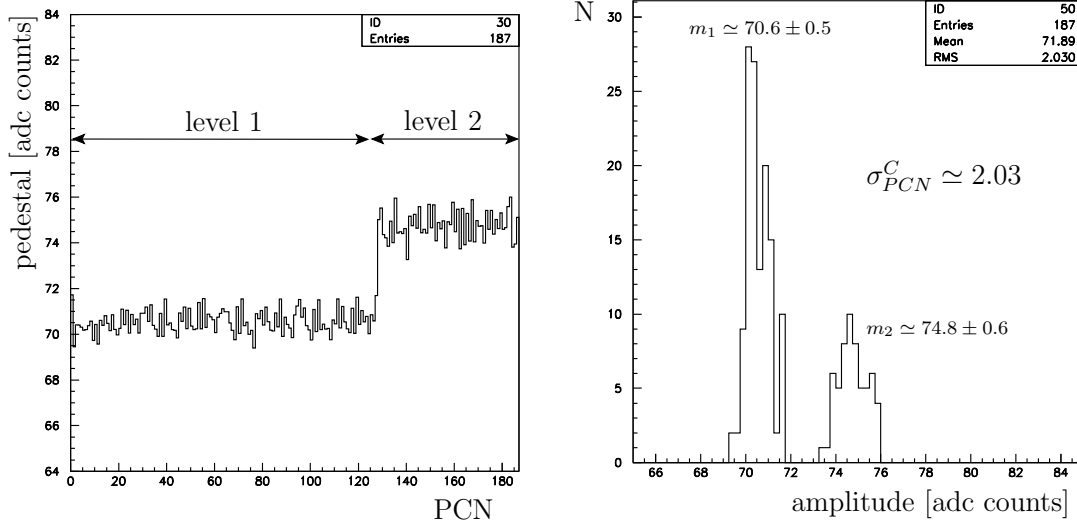


Figure 4.35: Pedestal amplitudes of channel 96 as a function of the PCN (*left*) and their distribution (*right*)

A portion of this pipeline dependent effect could be due to some internal features of the Beetle. We will assume for the moment that this is negligible and try to explain that the 2-levels shape on the figure is due uniquely to the line transmission crosstalk. In section 4.3.3, we have evaluated the crosstalk factors in the four next neighbour channels with and without the Beetle connected. In the first case, these factors depend on the way the common mode is evaluated. In the second, the internal crosstalk features of the Beetle are not taken into account. Table 4.4 summarizes the results obtained with both methods.

A representation of the header pseudo-digital bits (PDB) was shown in figure 4.2. In the third link, the two first PDB are stable: $I(3) = '0'$ and $I(7) = '0'$. The last two PDB are $PCN(7)$ and $PCN(6)$. We remember that the PCN is a value between 0 and 186 coded on 8 bits. Therefore, for $PCN = 0, \dots, 63$, both $PCN(6)$ and $PCN(7)$ are '0' (because $2^6 = 64$). Between 64 and 127, $PCN(7)$ is still '0' ($2^7 = 128$) but $PCN(6)$ is '1'. Finally, from 128 until 186, the situation is inverted: $PCN(6) = '0'$ and $PCN(7) = '1'$.

In the left column of table 4.6, we give the results of a specific set of measurements intended to determine the mean amplitude values of the link 3 header bits H . The zero reference for the PDB amplitudes is set as the average value of the baseline sampled 25 ns before the first header bit:

$$\text{baseline} = 54.0 \pm 1.7 \text{ adc counts}$$

With respect to this baseline value, the amplitudes used for the crosstalk contribu-

tions $h = H - \text{baseline}$ are then -48.2 ± 2.2 for a bit set to '0' and 45.8 ± 2.2 for a bit set to '1' (right column of table 4.6).

binary	H [adc]	h [adc]
'0'	5.8 ± 0.5	-48.2 ± 2.2
'1'	99.8 ± 0.5	45.8 ± 2.2

Table 4.6: Mean amplitudes of the link 3 header bits in adc counts. In the right column, the amplitudes have been shifted by the baseline mean value 54.0 ± 1.7 .

The channel 96 pedestal value $P(96)$ can be expressed as the sum of its intrinsic pedestal $P_{\text{intr}}(96)$, the crosstalk contribution from the header bits $C(96)$ and some Beetle internal features contributions neglected for the moment:

$$P(96) = P_{\text{intr}}(96) + C(96) + \underbrace{\text{Beetle internal features}}_{\text{neglected}}$$

Assuming as a first approximation that the intrinsic pedestal $P_{\text{intr}}(96)$ corresponds to the PCN independent average of channel 96, we have:

$$P_{\text{intr}}(96) = 71.9 \pm 2.0 \text{ adc counts}$$

We now evaluate the crosstalk contribution due to the four header bits on channel 96. In principle, we have to take into account that the first header bit has an influence on the three following ones plus channel 96. The second header bit, which is already affected by the first one, has an influence on the third and fourth bits plus channel 96 and so on for the other header bits, as schematically represented in figure 4.36. The global effect on channel 96 is then:

$$\begin{aligned} C(96) = & h1(c_4 + 2 c_1 c_3 + c_2^2 + 3c_1^2 c_2 + c_1^4) \\ & + h2(c_3 + 2 c_1 c_2 + c_1^3) \\ & + h3(c_2 + c_1^2) + h4 c_1 \end{aligned} \quad (4.20)$$

For crosstalk factors less than 5%, a first order approximation is reasonable:

$$C(96) \simeq c_4 h1 + c_3 h2 + c_2 h3 + c_1 h4 \quad (4.21)$$

The use of the crosstalk factors obtained from both methods mentioned above (table 4.4) with the amplitudes h of the header bits (table 4.6) allows to determine the theoretical pedestal of channel 96 as a function of the three possible header bits configurations in link 3. The results are presented in figure 4.37.

h1	h2	h3	h4	ch96
h1	c_1h1	c_2h1	c_3h1	c_4h1
	$h2+c_1h1$	$c_1(h2+c_1h1)$	$c_2(h2+c_1h1)$	$c_3(h2+c_1h1)$
	$h3+c_2h1+c_1(h2+c_1h1)$	$c_1[h3+c_2h1+c_1(h2+c_1h1)]$	$c_2[h3+c_2h1+c_1(h2+c_1h1)]$	
	$h4+c_3h1+c_2(h2+c_1h1)+c_1[h3+c_2h1+c_1(h2+c_1h1)]$	$c_1(h4+c_3h1+c_2(h2+c_1h1)+c_1[h3+c_2h1+c_1(h2+c_1h1)])$	$c_2(h4+c_3h1+c_2(h2+c_1h1)+c_1[h3+c_2h1+c_1(h2+c_1h1)])$	

Figure 4.36: Crosstalk influence of the header bits on channel 96.

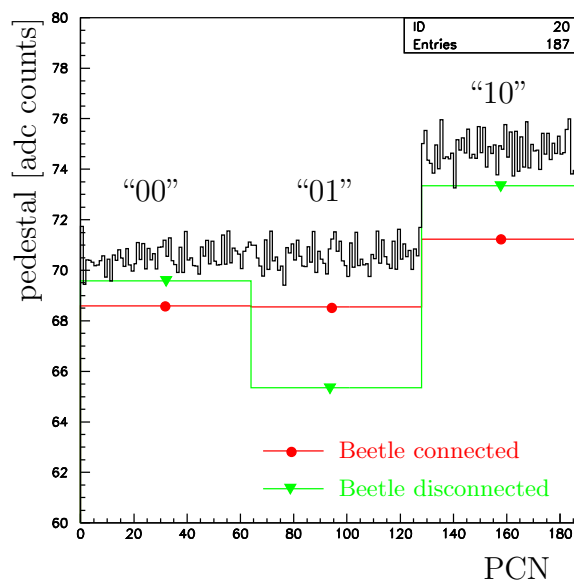


Figure 4.37: Channel 96 pedestal amplitudes as a function of the PCN. Experimental values are plot in black. Theoretical values with crosstalk factors obtained with the Beetle connected and disconnected for the three available $PCN(7 : 6) = "00"$, $"01"$ and $"10"$ configurations are shown with red circles and green triangles respectively.

The use of crosstalk factors obtained with the Beetle connected reproduces quite well the multi-levels shape of the channel 96 pedestal as a function of the PCN although the theoretical predictions are 2-3 adc counts lower than the experimental results. This difference is however comparable with the errors on $P_{\text{intr}}(96)$. It is important to notice that there is a small difference between the levels corresponding to $PCN(7 : 6) = "00"$ and $PCN(7 : 6) = "01"$ which can be explained by the fact that the crosstalk factor in the first next neighbour ($c_1 = -0.05\%$) has a very low influence with respect to the others. The higher level of the last configuration $PCN(7 : 6) = "10"$ is also explainable by the larger crosstalk contribution in the next-to-next neighbour ($c_2 = 2.8\%$). That is the reason why only two levels are distinguishable in figure 4.35 (*left*) although there are in principle three levels. The first two levels from our calculation are both at ~ 68.6 and the third one at ~ 71.2 adc counts. Therefore, the difference of ~ 2.6 adc is not too far from the measured value of ~ 4.2 . On the other hand, using the second set of crosstalk factors obtained with a signal generator, we get a pedestal shape which is inconsistent with the measurement. As explained in section 4.3.3, the Beetle internal crosstalk effects are not taken into account. As the line driver is tuned to compensate for crosstalk coming from the complete system including the Beetle, removing it leads to an over-compensation of the analogue signal. Therefore, the use of these crosstalk factors brings to a wrong result.

We now redo the same analysis performed on channel 20. The 2-levels shape increases the rms of the distribution of figure 4.35 which becomes considerably larger than it was in channel 20. Actually, it contains both contributions of the PCN effect and the header crosstalk. From the distribution, we can estimate a global contribution associated with the PCN, which will be indicated by $\sigma_{\text{pipeline}}^{C+}$:

$$\sigma_{\text{pipeline}}^{C+} = \sigma_{\text{pipeline}}^C \oplus \sigma_{\text{crosstalk}}^C \simeq 2.03 \text{ adc counts} \quad (4.22)$$

In figure 4.38 are represented the distribution of noise in channel 96 after a standard pipeline independent pedestal subtraction (PIPS) (*left*) and after the common mode suppression (CMS) (*right*) over 22 non-bonded channels (100 to 121). As expected, the remaining noise $\sigma_{\text{PIPS}}^R \simeq 1.71$ is larger than what was obtained in channel 20 with the same algorithm ($\sigma_{\text{PIPS}}^R \simeq 1.10$). In figure 4.39, we show the effect of a pipeline dependent pedestal subtraction (PDPS) (*left*) followed by the CMS (*right*).

The total noise amount becomes now comparable to channel 20 with the PIPS method. The total PCN related contribution to common noise can be calculated from the above results:

$$\begin{aligned} \sigma_{\text{pipeline}}^{C+} &= \sigma_{\text{PIPS}}^{\text{tot}} \ominus \sigma_{\text{PDPS}}^{\text{tot}} \\ &\simeq 2.65 \ominus 1.98 \simeq 1.76 \text{ adc counts} \end{aligned} \quad (4.23)$$

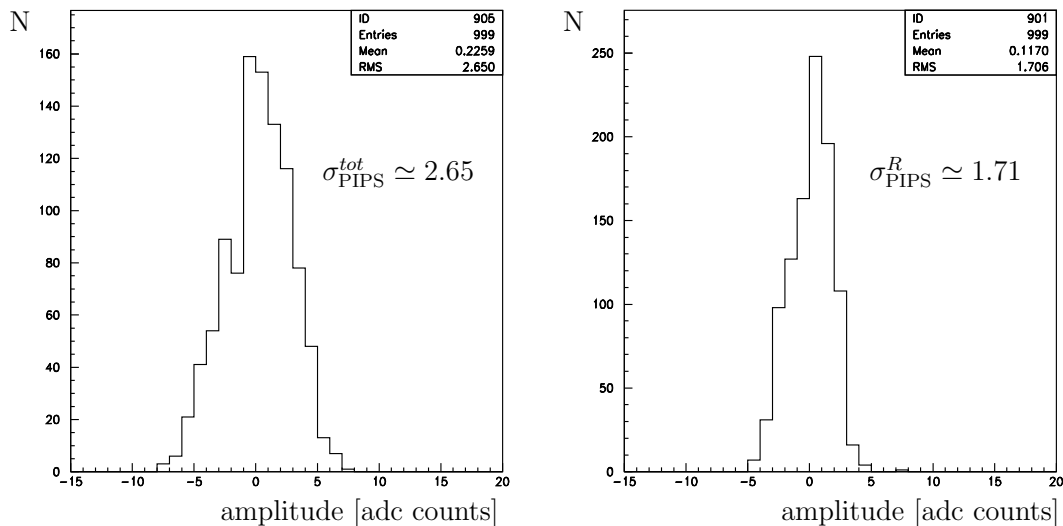


Figure 4.38: Results after pipeline independent pedestal subtraction (*left*) and after common noise suppression (*right*) in channel 96.

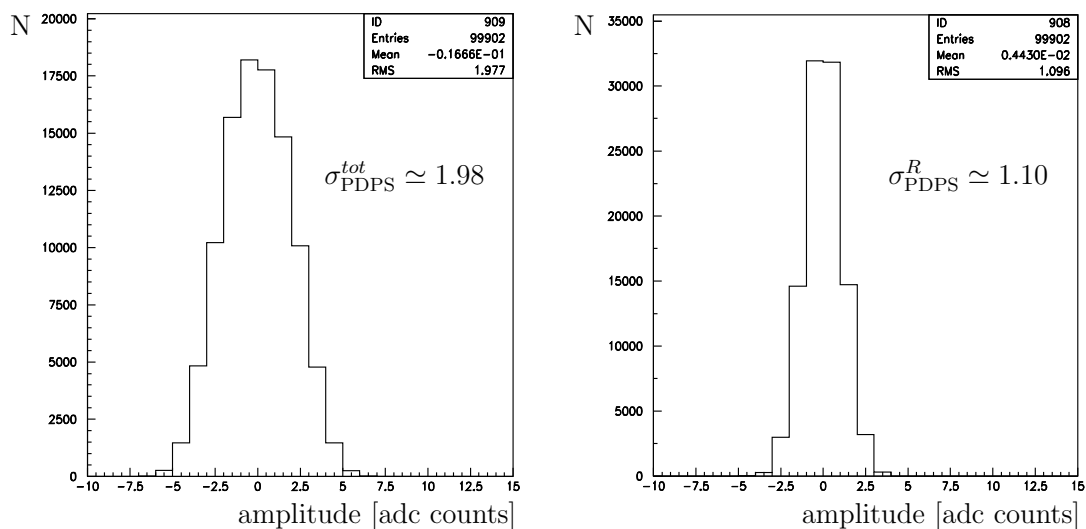


Figure 4.39: Results after pipeline dependent pedestal subtraction (*left*) and after common noise suppression (*right*) in channel 96.

This is consistent with the value inferred from the pedestal dispersion as a function of the PCN. Assuming the same $\sigma_{pipeline}^C \simeq 0.97$ as channel 20, from eq. (4.22), the crosstalk contribution is:

$$\begin{aligned}\sigma_{crosstalk}^C &= \sigma_{pipeline}^{C+} \ominus \sigma_{pipeline}^C \\ &\simeq 1.76 \ominus 0.97 \simeq 1.47 \text{ adc counts}\end{aligned}\quad (4.24)$$

The other contributions to common noise are estimated using eq. (4.18) which gives:

$$\begin{aligned}\sigma_{amplifiers+line}^C &= \sigma_{PDPS}^{tot} \ominus \sigma_{PDPS}^R \\ &\simeq 1.98 \ominus 1.10 \simeq 1.65 \text{ adc counts}\end{aligned}\quad (4.25)$$

close to the ~ 1.59 adc counts for channel 20 (eq. (4.18)). At this point, the total common noise in channel 96 can be calculated from eq. (4.11) incremented by the crosstalk effect:

$$\begin{aligned}\sigma_{tot}^C &= \underbrace{\sigma_{pipeline}^C \oplus \sigma_{crosstalk}^C}_{\sigma_{pipeline}^{C+}} \oplus \sigma_{amplifiers+line}^C \\ &\simeq 1.76 \oplus 1.65 \simeq 2.41 \text{ adc counts}\end{aligned}\quad (4.26)$$

In this channel close to the header, the total common noise is significantly larger than the value of ~ 1.86 adc counts obtained for channel 20 (eq. (4.19)), while the two values of random noise are very close ($\sigma_{PDPS}^R \simeq 1.10$ and 1.07). This confirms that the maximal efficiency of the CMS algorithm is reached.

Table 4.7 summarizes the different contributions to noise studied for channel 96 using the calibration $1 \text{ MIP} \simeq 32.5$ adc counts:

$\sigma_{pipeline}^C \simeq 2.98$		
$\sigma_{crosstalk}^C \simeq 4.52$		
$\sigma_{amplifiers+line}^C \simeq 5.08$	$\sigma_{tot}^C \simeq 7.42$	$\sigma_{PIPS}^{tot} \simeq 8.15$
	$\sigma_{PDPS}^R \simeq 3.38$	$\sigma_{PIPS}^R \simeq 5.26$

Table 4.7: Contributions to noise for channel 96 in 10^{-2} MIP.

In conclusion, even with a crosstalk factor less than 5%, a standard common noise suppression is not very efficient for the channels standing just after the header. In principle, these need specific treatment to reduce the PCN related effects.

4.5 Conclusion

The technical features and physical performances led to the choice of the CAT6 cable for the VeLo 60 m analogue transmission line. This cable is composed of four individually shielded twisted pairs. The low propagation delay (250 ns) and propagation delay skew (1.7 ns) are important parameters for the decision. The insertion loss (-10 dB), the ACR (41 dB) and the ELFEXT (54 dB) at 40 MHz measured in Lausanne are also determinant in favour of the CAT6 line.

Several configurations for the line driver and receiver have been studied for frequency and gain compensation. The best results were obtained with a frequency compensation at the line driver level. This way of doing is preferred to a compensation at the receiver level in order to avoid amplification of possible RF noise pick-up from the line. The chosen driver contains two correction poles: a capacitance in parallel to the output resistance and a RC filter as a feedback network at the level of the amplifiers.

The capacitive injection of a 1 MIP equivalent charge is used for the system calibration giving ~ 32.5 adc counts per MIP. The noise contribution are studied on the non-bonded channels with the Beetle connected (~ 1.14 adc counts $\simeq 3.51 \cdot 10^{-2}$ MIP) or also by disconnecting the Beetle from the rest of the line (~ 0.41 adc counts $\simeq 1.26 \cdot 10^{-2}$ MIP). This leads to a signal-to-noise ratio of ~ 28.5 and ~ 79.2 respectively. The crosstalk factors in the four channels next to the pulsed one were measured. The tuned configuration of the driver brings a low crosstalk factor in the next neighbour of -0.05% while it is of 2.8% , 2.1% and 2.0% in the second, third and fourth next neighbours respectively. All these specifications fulfill the requirements for the VeLo transmission ($CF < 5\%$).

Further studies were made on the contributions to noise in the non-bonded channels. In particular, the aim was to determine if the pipeline non uniformity increases significantly the noise. For that purpose, a pipeline dependent pedestal subtraction (PDPS) was used. The results are different between channels standing far from the header and those which are near the header. In the first case, it has been shown that a standard pipeline independent pedestal subtraction (PIPS) followed by a common mode suppression (CMS) is sufficient to correct for the pipeline non uniformity contribution. In the second case, the overall crosstalk associated to the header bits (Beetle internal features and contribution from the 60 m line) increases significantly the contribution to noise. Therefore, a simple PIPS is no more efficient and a specific procedure to reduce the pipeline influence is needed. The PDPS turned out to be a good way to do it. Another convenient solution can be implemented in a Finite Impulse Response filter (FIR) at the level of the FADC card on the readout board. The correction will therefore stand at the end of the transmission line just after the digitization. This solution has by now already been considered in the TELL1 implementation [28].

List of Figures

1.1	$SU(3)$ representations of the quarks and antiquarks triplets $\mathbf{3}$ and $\bar{\mathbf{3}}$.	3
1.2	Baryons decuplet $\mathbf{10}$ and octet $\mathbf{8}$.	4
1.3	Mesons octet $\mathbf{8}$.	5
1.4	Particle-antiparticle pair creation.	6
1.5	Two CKM-triangles with the Wolfenstein's parameterization.	13
1.6	Global fit of the unitary CKM-triangle with experimental constraints from various measurements.	15
1.7	Representation in the complex plane of the potential $\mathcal{V}(\phi)$ of a massive and self-interacting complex scalar field $\phi = \phi_1 + i\phi_2$ and its projection for $\phi_2 = 0$.	17
1.8	$\Delta\chi^2$ of the fit of all electroweak data as a function of the Higgs mass from high precision measurements at LEP, SLD, CDF and D0.	24
1.9	Dominant Standard Model Higgs production mechanisms in hadrons collisions: gluon fusion, W/Z vector boson fusion, W/Z associated production and $t\bar{t}$ associated production.	25
1.10	Standard Model Higgs production cross-section as a function of the Higgs mass m_H for the dominant production mechanisms in p - p collisions at $\sqrt{s} = 14$ TeV.	26
1.11	Feynman diagrams of the principal Higgs decays into two photons.	28
1.12	Standard Model Higgs branching ratios $\text{BR}(H)$ of the principal decay channels as a function of the Higgs mass m_H . Width $\Gamma(H)$ of the Higgs particle as a function of the Higgs mass m_H .	29
2.1	Center-of-mass energy evolution in e^+e^- and hadrons colliders.	33
2.2	The LHC accelerator complex (not to scale).	35
2.3	Dominant $b\bar{b}$ quarks pairs production mechanisms in p - p collisions.	36
2.4	Polar angles of the b - and \bar{b} -hadrons calculated by the PYTHIA event generator.	36
2.5	Layout of the LHCb detector in the non-bending (vertical) plane.	37
2.6	Arrangements of silicon sensors along the beam axis with the RF-foil and the Pile-Up system.	38

2.7	r and ϕ sensor layouts.	38
2.8	The VELO detector assembled with the vacuum vessel.	39
2.9	The LHCb magnet.	40
2.10	Cherenkov cone of light.	41
2.11	Overview of the sub-detectors contributions to the three trigger levels.	45
2.12	Flow-diagram of the different trigger sequences in the HLT.	48
3.1	Representation of the Higgs decay $H^0 \rightarrow b\bar{b}$ with the parton shower, the string fragmentation and the hadronization.	50
3.2	Higgs momentum $ \vec{p}^{H^0} $ and transverse momentum $p_T^{H^0}$ distributions for events accepted after the selection procedure (MC truth).	65
3.3	b -quarks from the Higgs decay $H^0 \rightarrow b\bar{b}$ momentum $ \vec{p}^{b\text{-quark}} $ and transverse momentum $p_T^{b\text{-quark}}$ distributions for events accepted after the selection procedure.	66
3.4	Isolated lepton momentum $ \vec{p}^{\ell_1} $ and transverse momentum $p_T^{\ell_1}$ distributions for events accepted after the selection procedure.	66
3.5	Distribution of the distance ΔR between the b -quark and the b -hadron. Distribution of the distance ΔR between the initial cone axis predefined by the b -hadron direction and the b -jet reconstructed by the cone algorithm.	68
3.6	Representation of jets reconstruction using the cone algorithm.	69
3.7	Average number of jets per event obtained by the K_T algorithm as a function of R_{K_T} . Distribution of the minimal distance ΔR between the b -hadron and the K_T -jet assimilated to the corresponding b -jet.	71
3.8	Example of dijet mass distribution obtained with the cone algorithm for $R_{cone} = 0.6$	72
3.9	Dijet mass resolution for $H^0 \rightarrow b\bar{b}$ events as a function of the parameters R_{K_T} and R_{cone} for the full visible event, the full event including neutrini and without the underlying event.	73
3.10	Dijet mass distribution central value M_{jj} as a function of the parameters R_{cone} and R_{K_T} for the full visible event.	73
3.11	Hyperbolic fit of the ratio $E^b/E^{b\text{-jet}}$ as a function of $p_T^{b\text{-jet}}$ for b -jets reconstructed by the cone algorithm with $R_{cone} = 0.6$. Dijet mass distribution with $R_{cone} = 0.6$ before and after p_T correction.	75
3.12	Ratio $E^b/E^{b\text{-jet}}$ as a function of $p_T^{b\text{-jet}}$ for b -hadrons emitted in the three regions $\theta < 50$ mrad, $50 < \theta < 250$ mrad and $\theta > 250$ mrad with and without acceptance restriction for the jets reconstruction.	76
3.13	Correlation between the third reconstructed jet energy and the energy loss with respect to the initial b -quarks energy for events with at least one b -jet with $p_T^{b\text{-jet}} < 30$ GeV/ c	77

3.14	b - and \bar{b} -jets pseudorapidity distributions for signal $H^0 W^\pm / Z^0$ and irreducible backgrounds $Z^0 W^\pm$ and $Z^0 Z^0$	79
3.15	Schema of $Z^0 Z^0$ event production in p - p collision.	79
3.16	Distribution of the b -quark pseudorapidity $\eta_b^{(Z^0)}$ in the Z^0 referential for a set of $Z^0 \rightarrow b\bar{b}$ events.	83
3.17	Primary off-shell gauge boson V^* decaying into $H^0 \rightarrow b\bar{b}$ and an associated gauge boson $V \rightarrow \ell_1 \ell_2$. $V^* \rightarrow H^0 + V$ in the V^* rest frame with the b -dijet polar angle with respect to the V^* direction $\theta_{jj}^{(V^*)}$	84
3.18	Primary boson transverse momentum p_{TV^*} distribution for <i>not</i> Z^0 -associated events. Correlation between the Higgs boson and the associated boson transverse momenta for <i>not</i> Z^0 -associated events.	85
3.19	Cosine of the b -dijet polar angle in the primary boson V^* rest frame for the signal $H^0 W^\pm / Z^0$ and the irreducible backgrounds $Z^0 Z^0$ and $Z^0 W^\pm$ classified following <i>not</i> Z^0 - and Z^0 -associated events.	86
3.20	Schema of the Multi-Layer Perceptron.	87
3.21	Scatter plots “ $\Delta R(j_1 - \ell_1)$ vs $\Delta R(j_2 - \ell_1)$ ” for $H^0 W^\pm / Z^0$ signal and $t\bar{t}$ background (30'000 events each).	90
3.22	Scatter plots “ $\cos(\theta_{j_1}^{(jj)})$ vs $\cos(\theta_{\ell_1}^{(jj)})$ ” for $H^0 W^\pm / Z^0$ signal and $t\bar{t}$, $Z^0 W^\pm$ and $Z^0 Z^0$ backgrounds.	91
3.23	Distributions of the 22 MLP input patterns for the signal $H^0 W^\pm / Z^0$ and $t\bar{t}$ background events.	92
3.24	Distributions of the 22 MLP input patterns shifted and scaled between 0 and 1 for the signal $H^0 W^\pm / Z^0$ and $t\bar{t}$ background events.	93
3.25	“HA-TT” MLP answer distributions for the signal and the $t\bar{t}$ background during the test phase. Back-propagation error for the learning and the testing sets during 500 cycles. S/\sqrt{B} as a function of the cut on $\text{OUT}_{\text{HA-TT}}$	94
3.26	Dijet mass distribution for signal and backgrounds after the selection procedure.	96
3.27	Dijet mass distribution for signal and backgrounds after the selection procedure and the “HA-TT” neural network utilization.	96
3.28	“HA-ZW” and “HA91-ZW” MLP answer distributions for the signal and the $Z^0 W^\pm$ background during the test phase. S/\sqrt{B} as a function of the cut on $\text{OUT}_{\text{HA(91)-ZW}}$	97
3.29	Dijet mass distribution for signal and backgrounds after the selection cuts and the utilization of two successive neural networks “HA-TT” and “HA-ZW”.	99
3.30	Dijet mass distribution for signal and backgrounds after the selection cuts and the utilization of two successive neural networks “HA-TT” and “HA91-ZW”.	99

3.31	“HA-ZZ” MLP answer distributions for the signal and the $Z^0 Z^0$ background during the test phase for Z^0 - and <i>not</i> Z^0 -associated events. S/\sqrt{B} as a function of the cut on $\text{OUT}_{\text{HA}(91)\text{-ZZ}}$	100
3.32	Dijet mass distribution for signal and backgrounds after the selection cuts and the utilization of two successive neural networks “HA-TT” and “HA-ZZ”.	101
3.33	Dijet mass distribution for signal and backgrounds after the selection cuts and the utilization of two successive neural networks “HA-TT” and “HA91-ZZ”.	101
3.34	“HA91-ZZ” MLP answer distributions for the signal and the $Z^0 Z^0$ background during the test phase for Z^0 - and <i>not</i> Z^0 -associated events.	102
3.35	Signal and total background dijet mass distributions after the selection procedure.	103
3.36	Signal and total background dijet mass distributions after the selection procedure and the “HA-TT” neural network utilization.	103
3.37	Example of mass distribution obtained for one “LHCb experiment” (Toy Monte Carlo). Deviation of the number of signal events reconstructed from the number generated, for 400 “LHCb experiments”.	106
3.38	R.m.s of the deviation of the number of signal events reconstructed from the number generated, as a function of the total number of signal events generated. The corresponding significance N/σ_N , where σ_N is the r.m.s. of the deviation histograms or resulting from the fit.	107
4.1	TELL1 logic block diagram.	111
4.2	Beetle 1.3 4-links output mode with the Beetle internal registers settings and the Pipeline Column Number.	113
4.3	Beetle “frame” without charge injection readout of the 128 channels mode.	114
4.4	Analogue signal measured at the Beetle output with a 2 GHz oscilloscope equipped with 0.7 pF active probes and with a 200 MHz frequency cut.	115
4.5	A picture of the setup with a Beetle 1.3.	116
4.6	SPP FPGA output event format.	117
4.7	A picture of the setup with RB3.	118
4.8	Insertion loss for the ND26P and ND36P and for the CAT5 and CAT6 60 m lines measured in the laboratory of Lausanne.	119
4.9	Near End Crosstalk (NEXT) for the ND26P and ND36P and for the CAT5 and CAT6 60 m lines measured in Lausanne.	120
4.10	Attenuation Crosstalk Ratio (ACR) for the ND26P and ND36P and for the CAT5 and CAT6 60 m lines measured in Lausanne.	120

4.11	Far End Crosstalk (FEXT) for the ND26P and ND36P and for the CAT5 and CAT6 60 m lines measured in Lausanne.	121
4.12	Equal Level Far End Crosstalk (ELFEXT) for the ND26P and ND36P and for the CAT5 and CAT6 60 m lines measured in Lausanne.	121
4.13	Schematics of the driver 1.	122
4.14	Schematics of the receiver 1.	123
4.15	Response of the driver 1 with the receiver 1 (link 0) to a 25 ns pulse provided by the Beetle with the clock which drives the ADC by its rising edge.	124
4.16	Schematics of the driver 2 with the capacitive coupling.	124
4.17	Time-domain response of the driver 2 ($C_{out} = 270$ pF) with the receiver 2 (link 0) with a 25 ns pulse from the Beetle.	125
4.18	Schematics of the driver 3 and 4.	125
4.19	Time-domain response of the driver 4 (link 0).	126
4.20	Signal amplitude as a function of the ADC sampling phase defined as the time difference between the ADC and the common RB3 clocks for the four links.	128
4.21	Block diagram of the experimental setup.	129
4.22	Pedestal amplitudes for link 0 (average over 1'000 events). Average over 1'000 events with the charge corresponding to ~ 1 MIP injected in channel 3.	130
4.23	Representation of the non-bonded channels 12 <i>vs</i> 22 before and after the common noise suppression.	131
4.24	Distributions of the crosstalks in % in link 0 for channel 4, 5, 6 and 7 for a charge injected in channel 3.	133
4.25	Distributions of the crosstalk in % in the four 25 ns window next neighbours with a 25 ns pulse injected from a generator instead of the Beetle.	134
4.26	Signal and noise without and with the Beetle connected.	136
4.27	Pedestal values as a function of the channel and the Pipeline Column Number PCN for the four links independently.	137
4.28	Pedestal amplitudes for channels 18 and 30 (link 0) as a function of PCN and their correlation.	138
4.29	Pedestal values correlation between channels 108 and 120 (link 3).	138
4.30	Pedestal values correlation between channels 48 (link 1) and 80 (link 2).	139
4.31	Pedestal values correlation between channels 96 and 108 (link 3).	139
4.32	Pipeline independent and dependent pedestal subtraction in channel 20.	142
4.33	Pedestals values of channel 20 as a function of the PCN and their distribution.	142
4.34	Pipeline independent and dependent pedestal subtraction and common noise suppression in channel 20.	143

4.35 Pedestal amplitudes of channel 96 as a function of the PCN and their distribution.	145
4.36 Crosstalk influence of the header bits on channel 96.	147
4.37 Channel 96 pedestal amplitudes as a function of the PCN with the effect of the three available $PCN(7 : 6) = "00"$, $"01"$ and $"10"$ configurations.	147
4.38 Results after pipeline independent pedestal subtraction and after common noise suppression in channel 96.	149
4.39 Results after pipeline dependent pedestal subtraction and after common noise suppression in channel 96.	149

List of Tables

1.1	The Standard Model fundamental particles. The classification contains the three families of leptons and quarks.	2
1.2	The Standard Model fundamental antiparticles.	7
1.3	The four fundamental interactions in the Standard Model with their mediators mass, spin and bearing.	11
1.4	Couplings of the W^\pm , Z^0 bosons and fermions to the Higgs particle. .	23
3.1	PYTHIA 6.325 most relevant configuration parameters used for the events generation in accord with the LHCb production group.	52
3.2	Comparison of the PYTHIA 6.325 production cross-sections obtained in Lausanne with the CTEQ4L and CTEQ6L LHAPDF libraries and by the LHCb production working group with the CTEQ6L LHAPDF library for several physics processes.	53
3.3	Signal and background production channels with the corresponding PYTHIA process numbers MSUB and parameters.	54
3.4	PYTHIA 6.319 configuration parameters used for the $b\bar{b}$ events generation.	54
3.5	Inclusive production cross-sections at leading order for Higgs signal and background channels giving $b\bar{b}\ell$. Specific requirements used for the events generation for each channel and the resulting reduced cross-sections. Number of events expected per LHCb year with an integrated luminosity $\mathcal{L}_{\text{int.}}^{\text{LHCb}} = 2 \cdot 10^3 \text{ pb}^{-1}$ and number of events generated for the study.	56
3.6	b -hadrons considered in the study with their PYTHIA identification code, their quark composition and their spin.	60
3.7	Number of signal and background events expected per LHCb year in the Higgs mass window $80 < M_{j\bar{j}} < 120 \text{ GeV}/c^2$ after each of the successive selection cuts described in § 3.4.3.	64
3.8	Proportion of Z^0 parent quarks emitted forward and backward with respect to the Z^0 momentum for every flavours in $q\bar{q} \rightarrow Z^0$ events, as predicted by PYTHIA 6.319 with CTEQ5L.	80

3.9	Probability that the Z^0 spin is oriented forward and backward with respect to the Z^0 momentum for the Z^0 parents flavour <i>up</i> and <i>down</i> .	82
3.10	Probability for the b -quark from $Z^0 \rightarrow b\bar{b}$ to be emitted forward and backward in the Z^0 rest frame when the Z^0 is produced via <i>down</i> and <i>up</i> quarks annihilation.	83
3.11	MLPfit learning method operating parameters.	88
3.12	MLP 22 input patterns.	89
3.13	Number of signal and background events expected per LHCb year before and after the “HA-TT” neural network.	95
3.14	Number of signal and background events expected per LHCb year after the “HA-ZW” and “HA-ZZ” neural networks.	98
3.15	Integrated luminosity and production cross-sections for signal and backgrounds in CDF and LHCb.	104
3.16	Number of signal and background events expected per LHCb year and significance before and after the “HA-TT” MLP discrimination considering three different mass windows.	105
4.1	Technical features of the tested cables.	119
4.2	Physical performances of the tested cables (60 m lines).	122
4.3	Optimal ADC sampling phase for the four links.	127
4.4	Crosstalk factors evaluated with a 25 ns pulse coming from a Beetle and from a generator.	132
4.5	Contributions to noise for channel 20 in 10^{-2} MIP.	144
4.6	Mean amplitudes of the link 3 header bits in adc counts before and after the baseline mean value shift.	146
4.7	Contributions to noise for channel 96 in 10^{-2} MIP.	150

Bibliography

- [1] Particle Data Group, “Particle Physics Booklet”, CERN, 2004.
- [2] U. Egede, “The search for a standard model Higgs at the LHC and electron identification using transition radiation in the ATLAS tracker”, Lund University, Sweden, LUNFD6/(NFFL-7150), 1997.
- [3] M. Gomez-Bock *et al.*, “Electroweak Symmetry Breaking and Higgs Physics: Basic Concepts”, Journal of Physics: Conference Series 18 p. 74-135, 2005.
- [4] N. Cabibbo *et al.*, “Bounds on the fermions and Higgs boson masses in Grand Unified Theories”, Nucl. Phys. B158 p.295-305, 1979.
- [5] G. Altarelli *et al.*, “Lower limit on the Higgs mass in the Standard Model: An update”, Phys. Lett. B337 p. 141-144, 1994.
- [6] LEP Electroweak Working Group web page, <http://lepewwg.web.cern.ch/LEPEWWG/>
- [7] LEP Collaborations, “Search for the Standard Model Higgs boson at LEP”, Phys. Lett. B565 p. 61-75, 2003.
- [8] Z. Kunszt *et al.*, “Higgs Production at the LHC: an Update on Cross Sections and Branching Ratios”, hep-ph/9611397 v2, 1997.
- [9] L. R. Surguladze, “Quark mass effects in fermionic decays of the Higgs boson in $\mathcal{O}(\alpha_s^2)$ perturbative QCD”, Phys. Lett. B341 p. 60-72, 1994.
- [10] J. F. Gunion *et al.*, “The Higgs Hunters Guide”, Addison-Wesley, 1990.
- [11] B. A. Kniehl, “Higgs phenomenology at one loop in the standard model”, Physics Reports 240 p. 211-300, 1994.
- [12] CERN document server, <http://weblib.cern.ch>
- [13] The ATLAS Experiment web page, <http://atlas.web.cern.ch/Atlas/index.html>

- [14] The CMS Experiment web page, <http://cms.cern.ch/>
- [15] The ALICE Experiment web page, <http://aliceinfo.cern.ch/>
- [16] The LHCb Experiment web page, <http://lhcb.web.cern.ch/lhcb/>
- [17] LHCb Technical Proposal, CERN-LHCC **98-004**.
- [18] LHCb Reoptimized Detector Design and Performance, Technical Design Report, CERN-LHCC **2003-030**.
- [19] LHCb Vertex Locator, Technical Design Report, CERN-LHCC **2001-011**.
- [20] LHCb Magnet, Technical Design Report, CERN-LHCC **2000-007**.
- [21] LHCb RICH, Technical Design Report, CERN-LHCC **2000-037**.
- [22] Physique nucléaire et corpusculaire, Prof. O. Schneider, LPHE, EPFL.
- [23] LHCb Inner Tracker, Technical Design Report, CERN-LHCC **2002-029**.
- [24] LHCb Outer Tracker, Technical Design Report, CERN-LHCC **2001-024**.
- [25] LHCb Calorimeters, Technical Design Report, CERN-LHCC **2000-036**.
- [26] LHCb Muon System, Technical Design Report, CERN-LHCC **2001-010**.
- [27] S. Löchner *et al.*, “The Beetle Reference Manual - Chip Version 1.3, 1.4 and 1.5”, Max Planck Institute for Nuclear Physics, Heidelberg, Germany, LHCb Note **2005-105**.
- [28] G. Haefeli *et al.*, “TELL1: Specification for a common read out board for LHCb”, LHCb Note **2003-007**, IPHE Note **2003-002**.
- [29] R. Jacobson *et al.*, “Timing and Fast Control”, LHCb Note **2001-16**.
- [30] Timing, Trigger and Control (TTC) Systems for the LHC, documentation server, <http://www.cern.ch/TTC/intro.html>
- [31] LHCb Experiment Control System (ECS), documentation server, <http://lhcb-online.web.cern.ch/lhcb-online/ecs/default.htm>
- [32] LHCb Computing, Technical Design Report, CERN-LHCC **2005-019**.
- [33] LHCb Trigger System, Technical Design Report, CERN-LHCC **2003-031**.
- [34] LHCb High Level Trigger web page, <http://lhcb-trig.web.cern.ch/lhcb-trig/HLT/Default.htm>

- [35] PYTHIA web page (Lund University),
<http://www.thep.lu.se/~torbjorn/Pythia.html>
- [36] B. Andersson *et al.*, “Parton fragmentation and string dynamics”,
Lund University, Sweden, Physics Reports 97 p. 31-145, 1983.
- [37] Les Houches Accord Parton Density Function web page,
<http://hepforge.cedar.ac.uk/lhapdf>
- [38] V. Vagnoni, “Validation of PYTHIA 6.3 and LHAPDF 4.1.1”, presented at the
Production and Decay Model Working Group Meeting at CERN, 24th November
2005.
- [39] A. Abulencia *et al.*, “Search for Higgs Bosons Decaying to $b\bar{b}$ and Produced in
Association with W Bosons in $p\bar{p}$ Collisions at $\sqrt{s} = 1.96$ TeV”,
CDF Collaboration, hep-ex/0512051 v2, 2006.
- [40] C. Currat, “Direct search for Higgs boson in LHCb”, IPHE, University of Lau-
sanne, 2001.
- [41] S. Catani *et al.*, “The K_T -clustering algorithm for jets in deep inelastic scat-
tering and hadron collisions”, Phys. Lett. 285 p. 291-299, 1992.
- [42] S. Catani *et al.*, “Longitudinally-invariant K_T -clustering algorithms for hadron-
hadron collisions”, Nucl. Phys. B406 p. 187-224, 1993.
- [43] S. Ellis *et al.*, “Successive combination jet algorithm for hadron collisions”,
Phys. Rev. volume 48 number 7, 1993.
- [44] J. Allison, “Multiquadric radial basis functions for representing multidimen-
sional high energy physics data”, University of Manchester, Computer Physics
Communications 77 p. 377-395, 1993.
- [45] W. N. Cottingham and D. A. Greenwood, “An introduction to the Standard
Model of Particle Physics”, Cambridge University Press, 1998.
- [46] J. Schwindling *et al.*, “MLPfit: a tool for designing and using Multi-Layer
Perceptrons”, DAPNIA/SPP, CEA Saclay, version 1.4, 2000,
schwind.web.cern.ch/schwind/MLPfit/doc/MLPfit.pdf
- [47] R. Fletcher, “Practical Methods of Optimization”, Second Edition, Wiley, 2000.
- [48] Y. Ermoline, “Vertex Detector Electronics: RB3 Specification”, May 2001,
LHCb Note **2001-050**.

- [49] O. Boyle *et al.*, “S-Link Interface Specification”, Edimburg University, 1997.
- [50] “Prototypes”, Physics Department of the University of Liverpool web site,
<http://hep.ph.liv.ac.uk/lhcb/Research/Hardware/Sensors/Prototypes/prototypes.html>
- [51] D. Green, “The Physics of Particle Detectors”, Cambridge University Press, 2000.
- [52] Analogue Devices Data Sheets, “8-bit 40 MSPS/60 MSPS/80 MSPS A/D Converter AD9057”, 2003, www.analog.com
- [53] Maxim Integrated Products, “Max520/Max521, Quad/Octal, 2-Wire Serial 8-Bit DACs with Rail-to-Rail Outputs”, Rev 3, September 1996,
<http://pdfserv.maxim-ic.com/en/ds/MAX520-MAX521.pdf>
- [54] CERN - Microelectronics Group, “PHOS4 - 4 Channel delay generation ASIC with 1 ns resolution”, Datasheet Rev 1.2, February 2000,
http://lhcb-elec.web.cern.ch/lhcb-elec/meetings/lhcbweek_february00/Delay%chip%20SpecificationsV1.pdf
- [55] Altera web site, www.altera.com
- [56] J. Christiansen *et al.*, “TTCrx Reference Manual”, CERN-EP/MIC, Geneva, Switzerland, January 2003.
- [57] M. Morrissey, “SEQSI”, July 1996.
- [58] “DeVaSys USB I2C IO”, <http://www.devasys.com/usbi2cio.htm>
- [59] J. Buytaert, “LHCb Vertex Detector Readout” presented at the 12th International Workshop on Vertex Detectors at Lake Windermere UK, 2003.

Laurent LOCATELLI
Ch. du Treyblanc 4, CH-1006 Lausanne
☎ +41'21'311'79'75 📠 +41'79'285'54'80
✉ Laurent.Locatelli@epfl.ch

Graduate Physicist

Working experiences

- **Research works**

During a PhD thesis at the Ecole Polytechnique Fédérale de Lausanne (EPFL):

- 2004 - 2007 : Study on the feasibility to discover a Higgs boson via jets reconstruction in the LHCb experience at CERN.
- 2002 - 2004 : Development of the vertex locator VeLo analogue transmission line for the LHCb experience at CERN.
- 2001 - 2002 : FPGA programming for the data synchronization on the readout board TELL1 for the LHCb experience at CERN.

- **Teaching**

- 2007 : Teaching substitute in physics, mathematics and computing, 7th - 9th grade, Secondary schools of Béthusy in Lausanne and Montreux-Est.
- 2003 - 2006 : Teaching assistant for Prof. A. Bay lecture “Elementary Particles”, 7th grade, School of Basic Sciences, EPFL.
- 2001 - 2003 : Teaching assistant for practical trainings and laboratories of nuclear physics, 3rd grade, Faculty of Sciences, University of Lausanne.
- 2001 : Teaching substitute in physics, mathematics and computing, 7th - 9th grade, Secondary school of Béthusy in Lausanne.
- 1997 - 2001 : Teaching assistant for practical trainings and laboratories of general physics, 1st grade, Faculty of Sciences, University of Lausanne.

Education

- 2001 - 2007 : PhD thesis in physics at the Ecole Polytechnique Fédérale de Lausanne (EPFL), Switzerland.
“Direct search for Higgs boson in LHCb and contribution to the development of the Vertex Detector”
- 1995 - 2001 : Physicist diploma at the University of Lausanne (UNIL), Switzerland.
“Contribution à un système d’acquisition pour les faisceaux test de LHCb”
- 1991 - 1995 : Swiss federal Maturity, scientific division, Gymnase Auguste Piccard, Lausanne, Switzerland.

Languages

- French (mother tongue), English (fluent), Italian (fluent), German (9 years at school)

Technical knowledges

- Operating systems: Windows, Linux, Mac.
- Programming languages: Fortran, C, C++, Pascal, L^AT_EX, HTML.
- Software: Word, Excel, PowerPoint, Adobe Illustrator, Xfig, GIMP, PAW, ROOT, FileMaker Pro, PYTHIA, MLPfit.
- Hardware: VHDL for FPGA Altera processors programming (HDL Designer, ModelSim, Leonardo, Quartus), I2C.
- Data analysis: Monte Carlo methods, online and offline events reconstruction.

Additional courses

- Various post-graduate lectures in physics at Ecole Polytechnique Fédérale de Lausanne belonging to the “Troisième Cycle de la Physique en Suisse Romande”:
 - “CP Violation Phenomenology”, Tatsuya Nakada.
 - “QCD and Colliders Physics”, Keith Ellis.
 - “Energy resolution in nuclear spectroscopy”, Jean-Francois Loude.
 - “Le Modèle Standard”, Geneviève Belanger.
 - “Modern Analysis Methods in Physics”, Juan Alcaraz.
 - “Théorie Quantique des Champs: une Introduction à la Théorie des Interactions Fondamentales”, Jean-Pierre Derendinger.
- Second Physics Transalpin Seminary “Astroparticles and Cosmology”, 2004, Dolomieu, France.

Publications

- L. Locatelli *et al.*, “Tests on the VeLo analogue line with the TELL1 prototype RB3”, EPFL, LHCb Note 2004-086, 2004.
- G. Haefeli *et al.*, “TELL1: Specification for a common readout board for LHCb”, IPHE note 2003-002, LHCb note 2003-007, 2003.
- G. Haefeli *et al.*, “TELL1: a common data acquisition board for LHCb”, LECC 2003 proceedings, 2003.
- A. Bay *et al.*, “Tests on the L1-electronics board prototype RB2”, IPHE note 2002-008, 2002.

Born on January 17th 1976 in Pompaples (CH), Swiss and Italian, single.